Spin Ladder Models with Cyclic Exchange: A Finite Temperature DMRG Study

Inaugural-Dissertation
zur
Erlangung des Doktorgrades
der Mathematisch-Naturwissenschaftlichen Fakultät
der Universität zu Köln

vorgelegt von

Erik Bartel

aus Mönchengladbach

Köln 2005

Berichterstatter:	Prof. Dr. J. Zittartz Prof. Dr. A. Rosch
Vorsitzender der Prüfungskommission:	Prof. Dr. M. Abd-Elmeguid
Tag der mündlichen Prüfung:	6. Dezember 2005

Contents

Introduction

Strong interactions on a microscopic level can lead to highly non-trivial collective macroscopic behavior. High-temperature superconductivity arising from the complex interplay of electrons in a solid is one such fascinating phenomenon. The essential physics of the superconducting cuprate compounds can be captured by strongly interacting electrons in copper-oxide planes within the three dimensional crystal structure.

Many similarities have been found between the two-dimensional superconducting cuprates and the two-leg ladder compounds which has focused the interest on the ladder systems. The spin ladder is a low-dimensional system of two coupled $S = 1/2$ Heisenberg chains. From the theoretical point of view, it can be considered as a key model exhibiting a whole range of relevant concepts of quasi one-dimensional spin physics like Haldane behavior, dimerization, frustration, critical phases and matrix-product ground states by a careful adaption of the coupling constants. The spin ladder is experimentally realized in a number of materials. One of the most prominent examples, the so called phone number compound $Sr_{14-x}Ca_xCu_{24}O_{41}$ becomes superconducting under pressure for values of $x = 11.5$ and 13.6. Besides, a whole family of cuprate ladder compounds with interesting properties have been synthesized.

Cyclic four-spin interaction terms in addition to the usual nearest-neighbor coupling were surprisingly found to be important to capture the essential physics of real spin ladder systems. On this background, Läuchli et al. [1] proposed a $T = 0$ phase diagram for spin ladders with arbitrary strength of cyclic exchange. They found six distinct phases including spin liquid phases with different dominating short-range ordering and dimerized phases with spontaneously broken Z_2-symmetry. Three second-order and two first-order quantum phase transitions emerge in the model. So far, the complete phase diagram has been subject to only a few $T = 0$ studies. Although a lot of work was done to understand the zero- and finite-temperature physics of the so called rung-singlet phase around the Heisenberg point, no thermodynamic properties for the remaining interesting phases have been given yet. Thermodynamics of the complete phase diagram will be the focus of this work.

Since there is no analytically solvable model amongst the studied spin ladder class, we have to rely on trustworthy numerical methods. The transfer-matrix DMRG (TMRG) is one of the most powerful numerical approaches for finite temperature. It is free of the negative-sign problem or undesirable finite-size effects. For the special demands of the spin model which includes frustration and important physics happening at very low temperatures, there has been the need for a new, optimized TMRG implementation overcoming weaknesses of

available older program code. We combine both, the advantages of a modern object-oriented design and the use of highly-efficient mathematical routines from a performance library, in a new TMRG implementation which preserves up to $m \approx 400$ states and produces low-temperature data with high precision.

Our work with the TMRG algorithm motivated us to further develop the method itself. As the corner transfer-matrix DMRG method brings reasonable advantage over TMRG for classical systems, we have modified the concept for the calculation of thermal properties of one-dimensional quantum systems. We have implemented the novel QCTMRG algorithm and give some test results. A discussion highlighting the advantages and challenges of the new method has been included.

The specific heat capturing important energy scales in the excitation spectrum and the generalized susceptibilities detecting patterns of order are fingerprints of the system at finite temperature. Important conclusions can be drawn about the excitation spectrum. The observation of $T > 0$ data can even provide strong indications for ground-state properties and quantum phase transitions. In the present work, we determine the specific heat for the complete class of spin ladders models with cyclic exchange. A physical interpretation based on the analysis of thermal local expectation values is given. Calculated generalized susceptibilities confirm the existence of broken-symmetry phases and explain the interesting behavior around the first-order quantum phase transitions in the model.

Outline of this thesis

Chapter 1 gives an introduction to the physics of the spin ladder. We start by a short review of experimental realizations of ladder compounds and comment on a future modeling by optical lattices. A general Hamiltonian showing a special duality-invariance is presented. We motivate our interest in cylic four-spin interaction and discuss the $T = 0$ ground-state phase diagram of the spin ladder with cyclic exchange introduced by Läuchli et al. [1].

Chapter 2 gives a description of relevant operators and the Hamiltonian in terms of plaquette operators and provides the spectrum of the plaquette Hamiltonian. We calculate upper bounds to the ground state energy. This is done in terms of variational states of matrix-product type including the different types of order which were proposed for the ladder. The results are discussed and compared with the proposed phase diagram.

Chapter 3 outlines the TMRG method which provides thermodynamic properties of one-dimensional quantum systems and has been used to obtain the results in Chapter 5. The TMRG method combines the Trotter-Suzuki decomposition, the transfer-matrix approach and the density-matrix renormalization group.

In **Chapter 4**, we present the quantum corner-transfer-matrix DMRG (QCTMRG). This new numerical approach has been developed in the framework of this thesis. The algorithmic implementation is shown and some results along with an analysis of the performance are given.

Chapter 5 focuses on the thermodynamic properties of the spin ladder. We present thermal expectation values of relevant operators, the specific heat, and magnetic and generalized susceptibilities of selected points in the different phases of the phase diagram. The results are discussed and an interpretation consistent with the proposed $T = 0$ phase diagram is given.

Chapter 6 draws the conclusion of this thesis and proposes perspectives for further research on the presented topics.

1 Spin ladders

On the way from one to higher dimensions, spin ladder systems arise as an important field of interest in modern solid state physics. Within the past fifteen years a huge effort has been made to understand physical properties from the theoretical as well as from the experimental point of view.

In this chapter, we give theoretical and experimental motivation for studies on spin ladder systems. The spin ladder with nearest-neighbor interaction is introduced as a generic model that shows basic features considered typical for spin ladder models. Yet, for an appropriate description of real spin ladder materials further four-spin couplings have to be added to the model leading to a general 6-parameter model. This general ladder model is self-dual under a certain unitary transformation which provides useful information about the phase behavior. Finally, we motivate the concept of cyclic exchange interaction and introduce the spin ladder with cyclic exchange along with an overview about its $T = 0$ phase diagram.

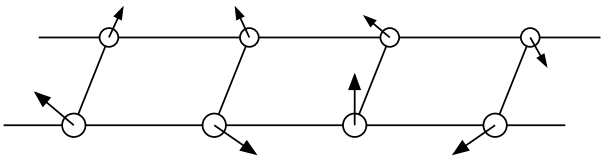

Figure 1.1: Sketch of a two-leg spin ladder.

1.1 Theoretical Motivation

The topological arrangement of spins in form of a ladder (see Fig. 1.1) captures the essential low-temperature physics of a considerable amount of materials. Its physical properties have been brought into connection with the properties of high-T_C superconducting copper oxide compounds [2].

In 1983, Haldane [3, 4] argued that antiferromagnetic chains of integer spin, in contrast to the half-integer case, have an energy gap and their correlations decay exponentially. This conjecture set a focus of interest on the low-temperature properties of one-dimensional spin systems. In this context, Hirsch [5] found the quasi one-dimensional two-leg spin-1/2 ladder to have a finite energy gap in 1988.

One year before, the resonating valence-bond (RVB) state introduced by Anderson [6, 7] was proposed as the ground state of compounds showing high-T_C superconductivity [8] on doping. The RVB state is also described as a spin-liquid because of its purely short-ranged spin correlation and a finite excitation gap. From this background, Dagotto et al. [9] studied two-dimensional spin-1/2 Heisenberg systems of finite size. Starting from a chain they considered ladders with increasing number of legs. It came out as a surprise that even-legged ladders show a finite gap while odd-legged ladders remain critical similar to the spin chain. This observation of a spin-liquid phase in spin ladders triggered hope to find superconductivity in quasi one-dimensional quantum systems where a huge amount of numerical methods for further theoretical research is at hand.

1.2 Experimental realizations

The motivation provided by theorists strongly stimulated experimental efforts to synthesize ladder materials.

1.2.1 Spin ladder compounds

Due to an "enormous experimental effort" [2], spin ladder systems have been realized in several materials since the early 90ies of the last century. For historical reasons, we mention the insulating magnetic salt $(VO)_2P_2O_7$. It has a two-leg vanadium-oxide ladder in its structure which was reported in 1987 by [10]. A spin gap in the spectra found by inelastic neutron scattering experiments [11] seemed to support the picture of a dominant ladder structure. Early theoretical work [12] considered this compound as a possible realization of the spin ladder. However, later inelastic neutron scattering experiments [13] revealed that the compound should be rather modeled by alternating spin chains which are oriented perpendicular to the ladders (see Fig. 1.2). This material exemplifies the subtleties which have to be dealt with when revealing the dominant structures of complex compounds.

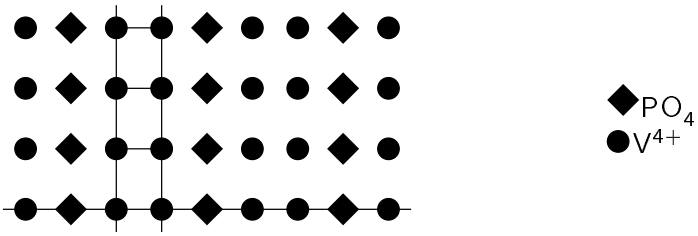

Figure 1.2: Structure of $(VO)_2P_2O_7$. It is rather modeled by alternating spin chains (horizontal line) than by ladders (vertical direction).

The most important realization of spin ladders involve cuprate ladder compounds which allow hole-doping by chemical substitution. In the cuprate ladder compounds, the relevant low-temperature physics happens in two-dimensional planes within the crystal. Here, an edge-sharing arrangement of copper-oxide plaquettes makes up the spin ladder structure (see Fig. 1.3, right). The dominant super-exchange runs via linear Cu-O-Cu paths between adjacent ions and provides a strong Heisenberg coupling between the copper ions. Exchange paths with an angle of 90° contribute only a reduced ferromagnetic interaction because the involved orbitals do not overlap. Thus, intra-leg interaction is small and can usually be neglected. Two families of compounds show such CuO-ladder structures: The cuprate ladder compound $SrCu_2O_3$ and the telephone number compounds $(Ca, Sr, Y, La)_{14}Cu_{24}O_{41}$.

The cuprate ladder compound $SrCu_2O_3$ [14] is considered to be the prototype of a weakly coupled Cu_2O_3 spin ladder. The CuO-planes are separated by layers of strontium ions. A finite spin gap of 420 K was reported and the spin-spin correlation was found to be a few lattice spacings. Further, a series of oxides $Sr_{n-1}Cu_{n+1}O_{2n}$ has been synthesized which contain n-leg ladders confirming the even/odd-effects mentioned above [15].

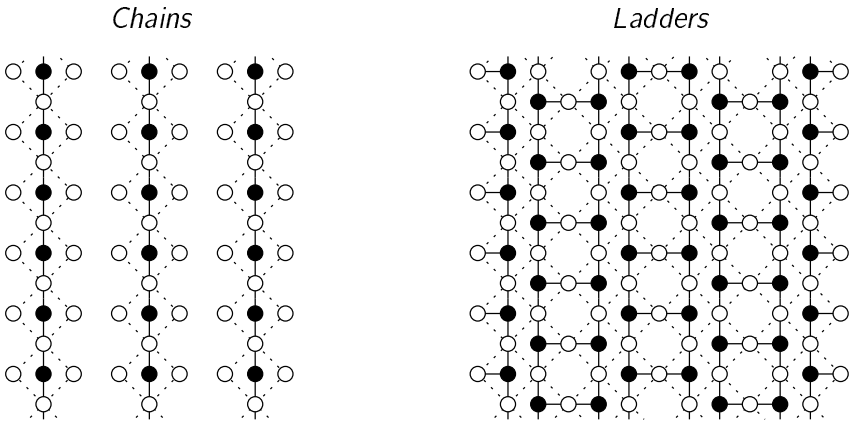

Figure 1.3: Spin chains (left) and ladders (right) arising from two-dimensional arrangement of corner- and edge-sharing copper-oxide plaquettes. Black circles denote copper ions, white circles denote oxygen ions. The dominant super-exchange paths are depicted by straight lines.

The second class of cuprate compounds $(Ca, Sr, Y, La)_{14}Cu_{24}O_{41}$ contain one-dimensional CuO_2 chains, (Ca, Sr, Y, La) layers and two-leg Cu_2O_3 ladders in their crystal structure. Spin chains and ladders interact on different energy scales because in contrast to Fig. 1.3 the super-exchange in the spin chains is mediated via two Cu-O-Cu paths with an angle of 90°. Thus, the behavior of chains and ladder can be studied separately. In contrast to $SrCu_2O_3$ the so-called telephone number compounds can be synthesized at ambient pressure which allow large single crystals to be grown.

Even the undoped compound $Sr_{14}Cu_{24}O_{41}$ is intrinsically doped with 6 holes per unit cell which are distributed between the chains and ladders. This hole ratio can be varied on substituting Sr by Ca. The 'self (hole-)doped' system $Sr_{14-x}Ca_xCu_{24}O_{41}$ becomes superconducting under pressure for values of $x = 13.6$: $T_C \approx 10$K at 3 GPa [16] and $x = 11.5$: $T_C \approx 6.5$K at 4.5 GPa [17]. The (formal) compound $La_6Ca_8Cu_{24}O_{41}$ fulfills the requirement of a true effective spin system since it does not contain holes.

Several other non-superconducting materials ($La_{1-x}Sr_xCuO_{2.5}$, $(Ca, Mg)Cu_2O_3$) have been found which contain ladders. Since in these compounds the interladder exchange coupling is evidently stronger than in the telephone number compounds they are also referred to as "pseudo-ladder"compounds [18, 19, 20]. For a review about further ladder compounds, see [21, 2].

1.2.2 Optical lattices

In recent research, a fascinating perspective for "quantum experiments" on spin systems with a manifold of tunable parameters arose: Ultracold atoms can become trapped by the optical dipol force in externally tuned optical standing waves. The arising systems, the so called optical lattices, can be considered as artificial solids. See [22] for a review.

At temperatures very near to absolute zero temperature bosonic atoms collapse to a single quantum mechanical ground state. This is known as Bose-Einstein condensation. Since the first experimental realization in 1995 (Cornell, Ketterle, and Wieman, Nobel price 2001)[23, 24], a fast growing field of research emerged. For instance, the first fermionic condensate was realized in 2003 [25, 26] bypassing the Pauli exclusion principle by a BCS transition which was originally invented to describe superconductivity. A review on fermionic condensates and basic concepts can be found in [27].

Technically, laser cooling and magnetic evaporative cooling were used to reach ultra-cold temperatures. A further development of the method confines Bose-Einstein condensed atoms in an array of traps. These traps are built by periodic optical dipole potentials which are formed by counter-propagating laser beams. The superposition of two standing wave pairs forms for example a 2D lattice. This optical lattice is tunable in the sense that the periodic potential which controls the tunneling rate between traps can be varied. In addition, the interparticle interaction can be tuned via optically induced Feshbach resonances [28].

The physics of a system of ultracold atoms in an optical lattice is described by the Bose-Hubbard model of an interacting boson gas in a lattice potential. The Hamiltonian

$$H = -J \sum_{<i,j>} \hat{a}_i^\dagger \hat{a}_j + \sum_i \epsilon_i \hat{n}_i + \frac{1}{2} U \sum_i \hat{n}_i (\hat{n}_i - 1) \tag{1.1}$$

includes particle hopping J, a tunable energy offset (ϵ_i) per site, and the boson-boson repulsion U where $\hat{a}_i$, $\hat{a}_i^\dagger$ are the bosonic creation and annihilation operators and $\hat{n} = \hat{a}_i^\dagger \hat{a}_i$ the atomic number operator.

Taking the Bose-Hubbard model as a starting point, a perturbative calculation around states with one atom per site gives the effective spin Hamiltonian. In this fashion, spin systems can be implemented in optical lattices. Even for an experimental realization of a two-leg $S = 1/2$ spin ladder, different setups have been proposed [29, 30].

1.3 Spin ladder with nearest-neighbor interaction

The Heisenberg model [31] describes systems of localized spins with isotropic interaction between nearest neighbors. In terms of the ladder, this means that both, rung and leg interaction terms exist in the Hamiltonian

$$H = J_\parallel \sum_j \left(\mathbf{S}_{1,j} \cdot \mathbf{S}_{1,j+1} + \mathbf{S}_{2,j} \cdot \mathbf{S}_{2,j+1} \right) + J_\perp \sum_j \mathbf{S}_{1,j} \cdot \mathbf{S}_{2,j} \tag{1.2}$$

with two coupling parameters $J_\parallel$ and $J_\perp$, see Fig. 1.4. The indices of the spin operators denote leg and rung number, respectively.

In the antiferromagnetic regime with positive coupling constants, we consider two limiting cases. The leg interaction is set to zero ($J_\parallel = 0$) in the strong-coupling ('strong-rung') limit. Here, the system adopts a gapped phase with singlets on each rung in the ground state. The elementary excitations are triplets with finite energy $J_\perp$. We can regard the

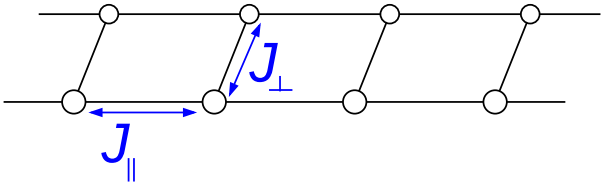

Figure 1.4: Spin ladder with nearest-neighbor two-site exchange.

system as a gas because the excitations are non-interacting. Thermodynamical quantities can be calculated exactly. In the other limiting case ($J_\perp = 0$), the decoupled-chains limit, two independent Heisenberg chains emerge from the ladder model. Thus, we obtain the physics of a spin-1/2 Heisenberg chain. In particular, we know that the system is in a critical phase with algebraically decaying correlations.

Based on this observation, a transition between these two phases is expected at some ratio of the two parameters and several calculations have been performed on this matter. Exact Lanczos-diagonalization of small systems was used in [12] where it was found that the transition happens for $J_\perp/J_\parallel < 0.4$ or smaller. Arguments based on Abelian bosonization [32] suggest that the gap opens for arbitrary small interchain coupling $J_\perp > 0$. Results from a mean field treatment of a flux phase state [33] predict the transition at $J_\perp = 0$ as well as results from various numerical methods which have been considered in [34]. In addition to these works, White et al. [35] proposed a picture of the spin ladder ground state in terms of a short-ranged resonating valence bond (RVB) [7, 36] state. They argued that the mechanism of spin confinement leads to a gap at non-vanishing rung coupling.

The presumably experimentally most relevant point on this parameter line is found at $J_\parallel = J_\perp$, the so-called Heisenberg ladder, where interaction on rungs and legs have the same strength. A spin gap of $\Delta = 0.504 J_\perp$ and a correlation length of $\xi = 3.19(1)$ were calculated by density-matrix renormalization-group (DMRG) [35]. In Fig. 1.5, the gap size can be estimated from magnetic susceptibility data which was obtained by the TMRG method (Chapter 3).

In order to illuminate the influence of dimensionality, it is an interesting extension of the model not to look at two-leg ladders only, but to consider ladders with an arbitrary number n of legs as well. For the Heisenberg-type ladders ($J_\parallel = J_\perp$), this has been done by numerical calculations on the way from one dimension to two dimensions in [9] and, in a more systematic fashion, in [35]. It was found that a significant difference between even and odd-legged ladders exists. While ladders with n even have a finite gap to the excitation spectrum, ladders with odd n are critical. The observed behavior was explained in terms of RVB states: Confinement of free spins exists only in the even-leg case preventing soft modes. However, with increasing number of legs the gap for even-legged ladders decreases. This leads to a gapless spectrum in the infinite-leg limit. Thus, in-between the Heisenberg chain and the two dimensional Heisenberg lattice which both are gapless, we find the Heisenberg ladder with gapped spectrum. Note, however, that the chain has algebraically decaying spin correlations while the 2d lattice is believed to show long-range Néel-order

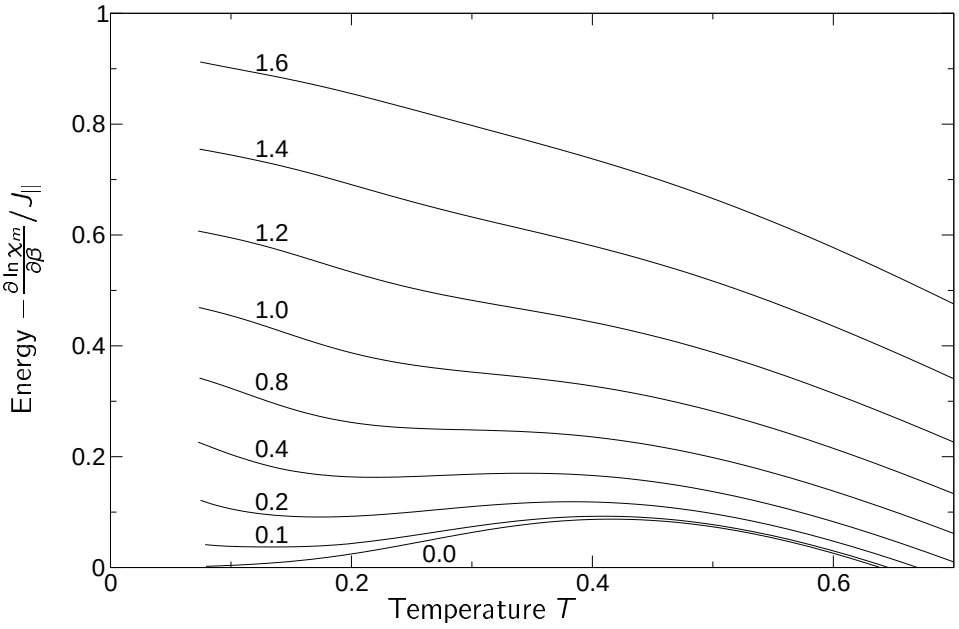

Figure 1.5: Energy gap of Heisenberg ladder. Shown is the temperature dependence of the logarithmic derivative of the magnetic susceptibility with respect to the inverse temperature β for different ratios of coupling constants $J_\perp/J_\|$. The curve should converge to the energy gap for $T \to 0$ [37]. Data from TMRG ($m = 200$).

[38].

Next to the ground state properties and size of the gap, the characteristic features of the low-energy excitations determine the low-temperature behavior of a model. In the case of the ladder, a disordered spin liquid with a Haldane gap is effectively realized. For each $J_\perp \neq 0$ the spinon excitations confine to form triplet (magnon) and singlet excitations. In the dynamical spin susceptibility $\chi''(q, \omega)$, one can see a coherent δ-peak near $q = \pi$ and ω the size of the triplet gap [39]. Thus, the magnons can be considered as "optical" in this case. A refined discussion about spectral properties of spin ladders and a connection to optical experiments is given in [40].

1.4 General Hamiltonian

The spin ladder Hamiltonian of localized spins can be considered as an effective model with exchange interaction emerging from a perturbation theory in the Hubbard model. Because of that it is a natural extension to account for terms arising beyond first order perturbation theory. In addition to the two-site exchange interaction, new interaction terms between the four sites of a plaquette appear as higher-order terms. In analogy to the spin

chain, the two-spin terms are often called bilinear while biquadratic denotes four-spin terms. Note that particle-hole symmetry of the underlying Hubbard model only permits terms with an even number of spins [41].

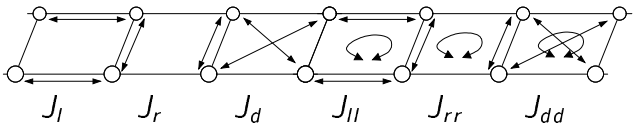

Figure 1.6: Terms in Hamiltonian (1.3).

A most general $SU(2)$-invariant Hamiltonian with additional four-spin exchange

$$\begin{aligned} H &= J_l \sum_j \left(\mathbf{S}_{1,j}\cdot\mathbf{S}_{1,j+1} + \mathbf{S}_{2,j}\cdot\mathbf{S}_{2,j+1}\right) + J_r \sum_j \left(\mathbf{S}_{1,j}\cdot\mathbf{S}_{2,j}\right) \\ &+ J_d \sum_j \left(\mathbf{S}_{1,j}\cdot\mathbf{S}_{2,j+1} + \mathbf{S}_{2,j}\cdot\mathbf{S}_{1,j+1}\right) \\ &+ J_{rr} \sum_j \left(\mathbf{S}_{1,j}\cdot\mathbf{S}_{2,j}\right)\left(\mathbf{S}_{1,j+1}\cdot\mathbf{S}_{2,j+1}\right) \\ &+ J_{ll} \sum_j \left(\mathbf{S}_{1,j}\cdot\mathbf{S}_{1,j+1}\right)\left(\mathbf{S}_{2,j}\cdot\mathbf{S}_{2,j+1}\right) \\ &+ J_{dd} \sum_j \left(\mathbf{S}_{1,j}\cdot\mathbf{S}_{2,j+1}\right)\left(\mathbf{S}_{2,j}\cdot\mathbf{S}_{1,j+1}\right) \end{aligned} \tag{1.3}$$

incorporates all terms respecting reflection symmetry along rungs and legs as well as translational invariance and time reversal symmetry [42]. The interactions are sketched in Fig. 1.6. Besides including exactly solvable points and ring-exchange Hamiltonians emerging from perturbational approaches, this general model exhibits a self-duality described later on. For practical purposes, however, most work done on the spin-ladder with four-spin exchange is restricted to interesting subspaces of the full model,which often still give rise to a rich phase behavior. The model class we will focus on in this thesis is the cyclic four-spin interaction.

1.5 Spin ladder with cyclic four-spin exchange

Cyclic ring exchange was introduced in the context of condensed ^{3}He [43, 44] which solidifies under high pressure at low temperatures. In this exotic lattice, the effective magnetic interaction between the fermionic spin-1/2 ^{3}He atoms is controlled by an atom-atom-exchange process instead of the usual electron exchange in ordinary solids. For these virtual exchange processes, it is energetically cheaper to make three or more particles exchange their places cyclically than to swap places of just two particles in some cases. This results in higher order interaction terms involving more than two sites.

The cyclic ring exchange between the four sites of a plaquette emerges next to the nearest-neighbor interaction in effective spin systems. It can be denoted in terms of permutation operators

$$\begin{aligned} P_\square + P_\square^{-1} &= 4\left[(\mathbf{S}_1\cdot\mathbf{S}_2)(\mathbf{S}_3\cdot\mathbf{S}_4) - (\mathbf{S}_1\cdot\mathbf{S}_3)(\mathbf{S}_2\cdot\mathbf{S}_4) + (\mathbf{S}_1\cdot\mathbf{S}_4)(\mathbf{S}_2\cdot\mathbf{S}_3)\right] \\ &\quad + \mathbf{S}_1\cdot\mathbf{S}_2 + \mathbf{S}_3\cdot\mathbf{S}_4 + \mathbf{S}_1\cdot\mathbf{S}_3 + \mathbf{S}_2\cdot\mathbf{S}_4 + \mathbf{S}_1\cdot\mathbf{S}_4 + \mathbf{S}_2\cdot\mathbf{S}_3 + \frac{1}{4} \end{aligned} \tag{1.4}$$

which indeed rotate a spin configuration in a clockwise and anti-clockwise sense around a plaquette:

$$\left(P_\square + P_\square^{-1}\right)\left|\begin{array}{ccc} 2 & - & 3 \\ | & & | \\ 1 & - & 4 \end{array}\right\rangle = \left|\begin{array}{ccc} 3 & - & 4 \\ | & & | \\ 2 & - & 1 \end{array}\right\rangle + \left|\begin{array}{ccc} 1 & - & 2 \\ | & & | \\ 4 & - & 3 \end{array}\right\rangle$$

On the other hand, spin Hamiltonians arise as effective models from large-U perturbation theory of Hubbard models in crystals. Takahashi [41] was the first to successfully carry out the t/U-expansion of the Hubbard model beyond leading order in two dimensions. In his calculations a fixed relationship

$$J_{ll} = J_{rr} = -J_{dd}$$

between the four-spin interaction terms from Eq. 1.3 appearing in fourth order in t was found. In the framework of the resonating valence bond (RVB) theory, the earlier results of Takahashi were confirmed and expanded to higher orders [45, 46]. While the four-spin interaction for terms up to order $\mathcal{O}(t^4/U^3)$ for an arbitrary lattice topology was given in [41, 45], the result restricted to the two dimensional square lattice was explicitely provided in [46]. In these effective spin models an interaction to next-nearest neighbors arose, too, leading to a coupling between two next-neighboring rungs in the ladder case.

Aiming at a quantitative description in terms of an effective spin model of undoped CuO_2-planes, a direct perturbation expansion starting from a three-band Hubbard model has been performed in [47]. In particular, for the analysis of the quasi-two-dimensional compound La_2CuO_4, the authors stress the relevance of the four-spin coupling as the leading correction to the nearest-neighbor Heisenberg model. The strength of the four-spin coupling reaches about 10% of the rung and leg coupling constant and is, thus, a non-negligible quantity in copper-oxide compounds under study. Experimental studies revealed that it is necessary to account for four-spin exchange terms in order to describe the physical properties of the spin ladder system $(La, Ca)_{14}Cu_{24}O_{41}$[48, 49] correctly.

In this sense, the Hamiltonian with cyclic exchange

$$H = J\sum_{\tau\in\{1,2\},j}\mathbf{S}_{\tau,j}\cdot\mathbf{S}_{\tau,j+1} + J\sum_j \mathbf{S}_{1,j}\cdot\mathbf{S}_{2,j} + J_{\text{cyc}}\sum_j\left(P_\square + P_\square^{-1}\right) \tag{1.5}$$

is believed to capture the effective physics of the ladder compounds correctly. Usually, we neglect a trivial scaling $\tilde{J}$ and regard an angle θ with

$$J = \tilde{J}\cos\theta \quad \text{and} \quad J_{\text{cyc}} = \tilde{J}\sin\theta \tag{1.6}$$

as the relevant parameter of the model.

The zero-temperature behavior for the spin ladder with cyclic exchange was studied in several works[1] [52, 53, 1, 54]. The ground-state phase diagram of the spin ladder with cyclic exchange was provided for the whole parameter space in [1]. In Fig. 1.7, the phase diagram is depicted along with sketches of the proposed order.

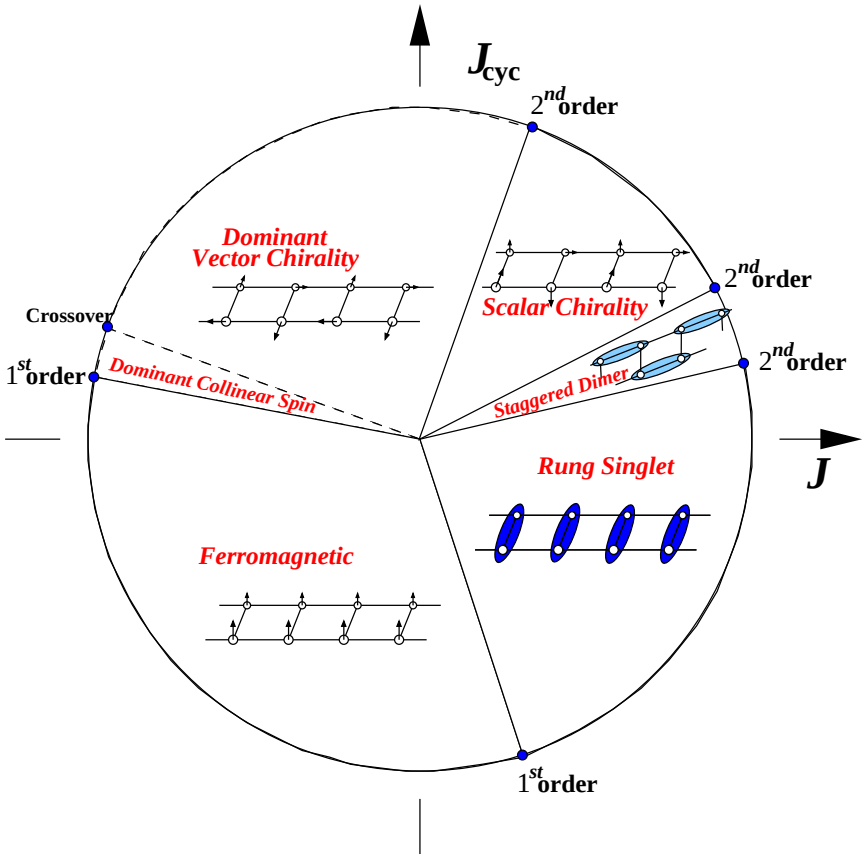

Figure 1.7: Phase diagram of the spin ladder following [1, 55].

For small positive and down to large negative values of ring exchange the ladder stays in the **rung-singlet phase** where we have a unique singlet ground state with a finite excitation gap to triplet excitations. The ground state can be represented by a product state of singlets on the rungs with momentum $k = 0$.

The second order quantum phase transition to a dimerized phase at $\theta \approx 0.06\pi$ is a transition of the Takhtajan-Babujian-type[56, 57] which is characterized by a spontaneous breaking of discrete Z_2-symmetry. In the **staggered-dimer phase** the ground state can be pictured

[1] A second Hamiltonian derived from Eq. 1.3 with $J_d = 0, \tilde{J}_{cyc} := J_{ll} = J_{rr} = -J_{dd}$ leaves three free parameters J_l, J_r and $\tilde{J}_{cyc}$. It has been considered in [50, 51]. Both Hamiltonians differ only by (usually small) two-spin interactions along the diagonals of the ladder.

as a staggered arrangement of dimers on the ladder's legs. Thus, it is two-fold degenerate with momenta $(0,0)$ and (π,π) breaking a discrete symmetry. The lowest lying excitation is a triplet with a small gap to the ground state energy.

The exact point $\theta = \arctan(1/2) \approx 0.1476\pi$ is invariant under the duality transformation described in Section 1.5.1. Here, the system is critical and a quantum phase transition takes place. Beyond this phase transition, the dimerization vanishes rapidly and we find a gapped phase with long-ranged order in the **staggered scalar chirality**. The order parameter is linked to the stagger-dimer order by the duality transformation (Section 1.5.1).

Another second-order quantum phase transition of Takhtajan-Babujian-type is located at $\theta \approx 0.38\pi$. For $\theta > 0.38\pi$, we find a short range ordered **vector-chirality phase** with a unique ground state and a fully gapped excitation spectrum similar to the rung-singlet phase. In contrast to the rung-singlet phase the dominant ground state correlations are not the spin-spin correlations, but correlations of the vector chirality order parameters. A smooth crossover at $\theta \approx 0.85$ leads over to the **collinear-spin phase**, a short range ordered region, where spins on the same leg (on different legs) exhibit ferromagnetic (antiferromagnetic) correlations. The system has a unique ground state and a fully gapped spectrum.

The last phase is the fully polarized **ferromagnetic phase**. It is located between two first order transitions at $\theta = 0.94\pi$ and $\theta = 0.40$.

In Chapter 5, the thermodynamic properties of Hamiltonian (1.5) will be considered in detail.

1.5.1 Duality transformation

The introduction of the duality transformation contributed significantly to the understanding of the phases of the spin ladder with cyclic exchange. In [54], a duality transformation corresponding to a gauge transformation of the singlet rung state [42] was proposed. The unitary operator is given by

$$U_\varphi = \prod_j e^{i\varphi(\mathrm{S}_{1,j}\cdot\mathrm{S}_{2,j}-\frac{1}{4})} \tag{1.7}$$

with $\varphi = \pi/2$. It maps the two spins of a rung to the following objects (we omit the rung index j):

$$\tilde{\mathbf{S}}_1 = \frac{1}{2}(\mathbf{S}_1+\mathbf{S}_2) - \mathbf{S}_1\times\mathbf{S}_2 \tag{1.8}$$

$$\tilde{\mathbf{S}}_2 = \frac{1}{2}(\mathbf{S}_1+\mathbf{S}_2) + \mathbf{S}_1\times\mathbf{S}_2 \tag{1.9}$$

It is easily shown that $\tilde{\mathbf{S}}_1$ and $\tilde{\mathbf{S}}_2$ satisfy the spin commutation relations and represent two spins of size $S = 1/2$. Application of the duality transformation on the new spin variables restore the original spin variables. In the language of group theory, it is a canonical transformation for the lowest representation of SU(2)×SU(2), and conserves the value of the Casimir operators in this representation [55].

Another general Hamiltonian covering the same models as (1.3) was introduced within the context of the duality transformation [42]:

$$\begin{aligned} H_{\mathrm{WXYZ}} &= J_r \sum_j \left(\mathbf{S}_{1,j}\cdot\mathbf{S}_{2,j}\right) + J_{rr}\sum_j \left(\mathbf{S}_{1,j}\cdot\mathbf{S}_{2,j}\right)\left(\mathbf{S}_{1,j+1}\cdot\mathbf{S}_{2,j+1}\right) \\ &+W\sum_j \left(\mathbf{S}_{1,j}+\mathbf{S}_{2,j}\right)\cdot\left(\mathbf{S}_{1,j+1}+\mathbf{S}_{2,j+1}\right) \\ &+X\sum_j \left\{\left(\mathbf{S}_{1,j}\cdot\mathbf{S}_{1,j+1}\right)\left(\mathbf{S}_{2,j}\cdot\mathbf{S}_{2,j+1}\right)+\left(\mathbf{S}_{1,j}\cdot\mathbf{S}_{2,j+1}\right)\left(\mathbf{S}_{1,j+1}\cdot\mathbf{S}_{2,j+1}\right)\right\} \\ &+Y\sum_j \left\{\left(\mathbf{S}_{1,j}-\mathbf{S}_{2,j}\right)\cdot\left(\mathbf{S}_{1,j+1}-\mathbf{S}_{2,j+1}\right)+4\left(\mathbf{S}_{1,j}\times\mathbf{S}_{2,j}\right)\cdot\left(\mathbf{S}_{1,j+1}\times\mathbf{S}_{2,j+1}\right)\right\} \\ &+Z\sum_j \left\{\left(\mathbf{S}_{1,j}-\mathbf{S}_{2,j}\right)\cdot\left(\mathbf{S}_{1,j+1}-\mathbf{S}_{2,j+1}\right)-4\left(\mathbf{S}_{1,j}\times\mathbf{S}_{2,j}\right)\cdot\left(\mathbf{S}_{1,j+1}\times\mathbf{S}_{2,j+1}\right)\right\} \end{aligned} \tag{1.10}$$

The relation to (1.3) is given by

$$W = \frac{1}{2}(J_{\perp}+J_{\mathrm{d}}), \quad X=\frac{1}{2}(J_{\parallel}+J_{\mathrm{dd}}), \tag{1.11}$$

$$Y = \frac{1}{16}(J_{\parallel}-J_{\mathrm{dd}})+\frac{1}{4}(J_{\perp}-J_{\mathrm{d}}), \quad Z=-\frac{1}{16}(J_{\parallel}-J_{\mathrm{dd}})+\frac{1}{4}(J_{\perp}-J_{\mathrm{d}}). \tag{1.12}$$

The duality transformation maps the parameters $(J_r, J_{rr}, W, X, Y, Z)$ to $(J_r, J_{rr}, W, X, Y, -Z)$, i.e.,it only affects the coupling Z. For $Z=0$ the model is self-dual and shows a U(1) symmetry because it is invariant under a transformation (1.7) with arbitrary φ [42].

Thus, the Hamiltonian (1.3) is form-invariant under the duality transformation and contains a self-dual sub-class of models for $(J_{\parallel}-J_{\mathrm{dd}})=4(J_{\perp}-J_{\mathrm{d}})$.

2 Exact results on spin ladders

This chapter illustrates the character of the ground states of the spin ladder with cyclic four-spin exchange in its different phases.

We start with introducing a reasonable basis for the Hilbert space of a four-spin plaquette. Hereby, we take advantage of the symmetries of the model. A lower bound to the ground state energy is given by an exact diagonalization of the spin ladder Hamiltonian on a plaquette. Upper bounds are calculated analytically by variational states making use of the matrix product ansatz.

2.1 Basis states of a four-spin plaquette

The spin ladder model is composed of interactions on four-spin plaquettes which, put on a chain, form the ladder. Choosing a reasonable basis of a four-spin plaquette will simplify and clarify analytical and numerical calculations.

It is essential to regard the system's symmetries for this purpose. In the class of interaction terms under consideration, see Hamiltonian (1.3), the following quantities are conserved in the plaquette:

- The SU(2) symmetry of the isotropic interaction leads to a conservation of the total spin S, defined by
$$S(S+1) = (\mathbf{S}_{1,j} + \mathbf{S}_{2,j} + \mathbf{S}_{1,j+1} + \mathbf{S}_{2,j+1})^2.$$
- The weaker assumption of a rotational invariance within the XY-plane leads to the conservation of the z-component S^z of the total spin. (Due to spin-flip (time-reversal) symmetry it is sufficient to consider positive S^z-values, only.)
- The reflection symmetry in rung direction leads to a parity P conservation under leg exchange.
- The reflection symmetry in leg direction leads to a parity conservation which is related to the momentum k conservation regarding ladders with more than two rungs.

By exploiting the various symmetries of the ladder, the corresponding Hilbert space can be separated into distinct subspaces, so the effort of analytical and numerical calculations is lowered.

For a convenient description of the states, we start by symmetrizing the two spins 1/2 linked by a common rung and obtain three triplet states

$$|t_+\rangle = \left|\begin{smallmatrix}\uparrow\\\uparrow\end{smallmatrix}\right\rangle, \quad |t_0\rangle = \frac{1}{\sqrt{2}}\left(\left|\begin{smallmatrix}\uparrow\\\downarrow\end{smallmatrix}\right\rangle + \left|\begin{smallmatrix}\downarrow\\\uparrow\end{smallmatrix}\right\rangle\right), \quad \text{and} \quad |t_-\rangle = \left|\begin{smallmatrix}\downarrow\\\downarrow\end{smallmatrix}\right\rangle \tag{2.1}$$

with parity $P = +1$ as well as one singlet state

$$|s_0\rangle = \frac{1}{\sqrt{2}}\left(\left|\begin{smallmatrix}\uparrow\\\downarrow\end{smallmatrix}\right\rangle - \left|\begin{smallmatrix}\downarrow\\\uparrow\end{smallmatrix}\right\rangle\right) \tag{2.2}$$

having parity $P = -1$. It is natural to symmetrize the rung spins in this context since the leg exchange symmetry plays a special role: It survives when the plaquette is extended to a ladder.

In order to classify the 16 plaquette states, we arrange them by total spin $S = 0, 1, 2$. The five $S = 2$-states

$$(S = 2, P = 1, k = 0)$$

$$\begin{array}{rcl:rcl} S^z = \pm 2 & : & |\phi_{2_{\pm 2}}\rangle & = & |t_\pm t_\pm\rangle \\ S^z = \pm 1 & : & |\phi_{2_{\pm 1}}\rangle & = & \frac{1}{\sqrt{2}}\left(|t_\pm t_0\rangle + |t_0 t_\pm\rangle\right) \\ S^z = 0 & : & |\phi_{2_0}\rangle & = & \frac{1}{\sqrt{6}}\left(2|t_0 t_0\rangle + |t_+ t_-\rangle + |t_- t_+\rangle\right) \end{array} \tag{2.3}$$

are symmetric under spin reflection along rungs, legs and diagonals. The nine $S = 1$-states are grouped into three triplets each of which is symmetric under spin reflection along either rungs, legs or diagonals and anti-symmetric under spin reflection along the other two directions. For example, the $S = 1$-state which is symmetric regarding reflection along rungs can be expressed as two $S = 1$-triplets which have been formed by symmetrized $S = \frac{1}{2}$-spins on rungs and coupled to a new $S = 1$-triplet:

$$(S = 1, P = 1, k = \pi)$$

$$\begin{array}{rcl:rcl} S^z = \pm 1 & : & |\phi^{\perp}_{1_{\pm 1}}\rangle & = & \pm\frac{1}{\sqrt{2}}\left(|t_\pm t_0\rangle - |t_0 t_\pm\rangle\right) \\ S^z = 0 & : & |\phi^{\perp}_{1_0}\rangle & = & \frac{1}{\sqrt{2}}\left(|t_+ t_-\rangle - |t_- t_+\rangle\right) \end{array}$$

$$(S = 1, P = -1, k = 0)$$

$$\begin{array}{rcl:rcl} S^z = \pm 1 & : & |\phi^{\parallel}_{1_{\pm 1}}\rangle & = & \frac{1}{\sqrt{2}}\left(|t_\pm s_0\rangle + |s_0 t_\pm\rangle\right) \\ S^z = 0 & : & |\phi^{\parallel}_{1_0}\rangle & = & \frac{1}{\sqrt{2}}\left(|t_0 s_0\rangle + |s_0 t_0\rangle\right) \end{array} \tag{2.4}$$

$$(S = 1, P = -1, k = \pi)$$

$$\begin{array}{rcl:rcl} S^z = \pm 1 & : & |\phi^{\times}_{1_{\pm 1}}\rangle & = & \frac{1}{\sqrt{2}}\left(|t_\pm s_0\rangle - |s_0 t_\pm\rangle\right) \\ S^z = 0 & : & |\phi^{\times}_{1_0}\rangle & = & \frac{1}{\sqrt{2}}\left(|t_0 s_0\rangle - |s_0 t_0\rangle\right) \end{array}$$

According to this procedure, one can construct three $S = 0$-states consisting of a tensor product of two singlets, formed by anti-symmetrized $S = \frac{1}{2}$-spins on rungs, legs or diagonals. These three states, however, are not linearly independent since they only span a Hilbert space of dimension two. Therefore, we have to select two suitable states for an appropriate basis. Because of the particular role of the leg exchange symmetry, we choose a basis

$$(S = 0, P = 1, k = 0)$$

$$\begin{array}{rcl:rcl} S^z = 0 & : & |\phi^{\perp}_0\rangle & = & |s_0 s_0\rangle \\ S^z = 0 & : & |\phi^{\parallel,\times}_0\rangle & = & \frac{1}{\sqrt{3}}\left(|t_0 t_0\rangle - |t_+ t_-\rangle - |t_- t_+\rangle\right) \end{array} \tag{2.5}$$

built by the state consisting of a product of rung singlets and the state orthogonal to it. The latter is, indeed, the difference between the state constructed by leg singlets and the state constructed by diagonal singlets. For completeness, we provide the representation of the $S = 0$-states with singlets on legs and diagonals:

$$\begin{aligned} |\phi_0^{\parallel}\rangle &= \tfrac{1}{2}\left(|s_0 s_0\rangle - |t_0 t_0\rangle + |t_+ t_-\rangle + |t_- t_+\rangle\right) &&= \tfrac{1}{2}\left(|\phi_0^{\perp}\rangle - \sqrt{3}|\phi_0^{\parallel,\times}\rangle\right) \\ |\phi_0^{\times}\rangle &= \tfrac{1}{2}\left(-|s_0 s_0\rangle - |t_0 t_0\rangle + |t_+ t_-\rangle + |t_- t_+\rangle\right) &&= -\tfrac{1}{2}\left(|\phi_0^{\perp}\rangle + \sqrt{3}|\phi_0^{\parallel,\times}\rangle\right) \end{aligned} \tag{2.6}$$

2.2 Plaquette operators

In the spin ladder with four-spin exchange, the most general Hamiltonian (1.3) consists of various interaction terms on the plaquette (Here, the rung index j is omitted in the operator names.):

$$\begin{aligned} \mathcal{O}_l &= (\mathbf{S}_{1,j}\cdot\mathbf{S}_{1,j+1} + \mathbf{S}_{2,j}\cdot\mathbf{S}_{2,j+1}) \\ &= \tfrac{1}{2}\left(\mathcal{P}_2 - \mathcal{P}_1^{\perp} + \mathcal{P}_1^{\parallel} - \mathcal{P}_1^{\times} - 2\mathcal{P}_0^{\parallel,\times}\right) + \tfrac{\sqrt{3}}{2}\left(|\phi_0^{\perp}\rangle\langle\phi_0^{\parallel,\times}| + |\phi_0^{\parallel,\times}\rangle\langle\phi_0^{\perp}|\right) && (2.7) \\ \mathcal{O}_r &= (\mathbf{S}_{1,j}\cdot\mathbf{S}_{2,j} + \mathbf{S}_{1,j+1}\cdot\mathbf{S}_{2,j+1}) \\ &= \tfrac{1}{2}\left(\mathcal{P}_2 + \mathcal{P}_1^{\perp} - \mathcal{P}_1^{\parallel} - \mathcal{P}_1^{\times} - 3\mathcal{P}_0^{\perp} + \mathcal{P}_0^{\parallel,\times}\right) && (2.8) \\ \mathcal{O}_d &= (\mathbf{S}_{1,j}\cdot\mathbf{S}_{2,j+1} + \mathbf{S}_{2,j}\cdot\mathbf{S}_{1,j+1}) \\ &= \tfrac{1}{2}\left(\mathcal{P}_2 - \mathcal{P}_1^{\perp} - \mathcal{P}_1^{\parallel} + \mathcal{P}_1^{\times} - 2\mathcal{P}_0^{\parallel,\times}\right) - \tfrac{\sqrt{3}}{2}\left(|\phi_0^{\perp}\rangle\langle\phi_0^{\parallel,\times}| + |\phi_0^{\parallel,\times}\rangle\langle\phi_0^{\perp}|\right) && (2.9) \\ \mathcal{O}_{ll} &= (\mathbf{S}_{1,j}\cdot\mathbf{S}_{1,j+1})\,(\mathbf{S}_{2,j}\cdot\mathbf{S}_{2,j+1}) \\ &= \tfrac{1}{16}\left(\mathcal{P}_2 - 3\mathcal{P}_1^{\perp} + \mathcal{P}_1^{\parallel} - 3\mathcal{P}_1^{\times} + 7\mathcal{P}_0^{\perp} + 3\mathcal{P}_0^{\parallel,\times}\right) - \tfrac{\sqrt{3}}{8}\left(|\phi_0^{\perp}\rangle\langle\phi_0^{\parallel,\times}| + |\phi_0^{\parallel,\times}\rangle\langle\phi_0^{\perp}|\right) && (2.10) \\ \mathcal{O}_{rr} &= (\mathbf{S}_{1,j}\cdot\mathbf{S}_{2,j})\,(\mathbf{S}_{1,j+1}\cdot\mathbf{S}_{2,j+1}) \\ &= \tfrac{1}{16}\left(\mathcal{P}_2 + \mathcal{P}_1^{\perp} - 3\mathcal{P}_1^{\parallel} - 3\mathcal{P}_1^{\times} + 9\mathcal{P}_0^{\perp} + \mathcal{P}_0^{\parallel,\times}\right) && (2.11) \\ \mathcal{O}_{dd} &= (\mathbf{S}_{1,j}\cdot\mathbf{S}_{2,j+1})\,(\mathbf{S}_{2,j}\cdot\mathbf{S}_{1,j+1}) \\ &= \tfrac{1}{16}\left(\mathcal{P}_2 - 3\mathcal{P}_1^{\perp} - 3\mathcal{P}_1^{\parallel} + \mathcal{P}_1^{\times} + 7\mathcal{P}_0^{\perp} + 3\mathcal{P}_0^{\parallel,\times}\right) + \tfrac{\sqrt{3}}{8}\left(|\phi_0^{\perp}\rangle\langle\phi_0^{\parallel,\times}| + |\phi_0^{\parallel,\times}\rangle\langle\phi_0^{\perp}|\right) && (2.12) \\ P_{\square} + P_{\square}^{-1} &= 2\mathcal{P}_2 - 2\mathcal{P}_1^{\times} + \mathcal{P}_0^{\perp} - \mathcal{P}_0^{\parallel,\times} - \sqrt{3}\left(|\phi_0^{\perp}\rangle\langle\phi_0^{\parallel,\times}| + |\phi_0^{\parallel,\times}\rangle\langle\phi_0^{\perp}|\right) && (2.13) \end{aligned}$$

For a basis representation we have chosen the plaquette states listed in Section 2.1. The projection operator $\mathcal{P}^Q$ denotes the projection $|\phi^Q\rangle\langle\phi^Q|$ on a certain sub-state characterized by quantum numbers Q, *e.g.*

$$\mathcal{P}_1^{\perp} = \mathcal{P}_{1_{+1}}^{\perp} + \mathcal{P}_{1_0}^{\perp} + \mathcal{P}_{1_{-1}}^{\perp} = |\phi_{1_{+1}}^{\perp}\rangle\langle\phi_{1_{+1}}^{\perp}| + \ldots \tag{2.14}$$

The Hamiltonian of the spin ladder with cyclic four-spin exchange (1.5) confined to a

plaquette is described as

$$\begin{aligned} H &= J\left(\mathcal{O}_l + \frac{1}{2}\mathcal{O}_r\right) + J_{\text{cyc}}(P_\square + P_\square^{-1}) \\ &= \tfrac{1}{4}\left[(3J+8J_{\text{cyc}})\mathcal{P}_2 - J\mathcal{P}_1^{\perp} + J\mathcal{P}_1^{\parallel} + (-3J-8J_{\text{cyc}})\mathcal{P}_1^{\times}\right] \\ &\quad + \tfrac{1}{4}\left[(-3J+4J_{\text{cyc}})\mathcal{P}_0^{\perp} + (-3J-4J_{\text{cyc}})\mathcal{P}_0^{\parallel,\times}\right] + \tfrac{\sqrt{3}}{2}(J-2J_{\text{cyc}})\left(\left|\phi_0^{\perp}\right\rangle\left\langle\phi_0^{\parallel,\times}\right| + \left|\phi_0^{\parallel,\times}\right\rangle\left\langle\phi_0^{\perp}\right|\right) \end{aligned} \tag{2.15}$$

in this basis representation. It's easy to see that all basis states in the $S = 2$ and $S = 1$ subspaces are eigenstates of the Hamiltonian. Their eigenenergies are the coefficients of the projectors. All eigenenergies of the plaquette including the $S = 0$-sector will be discussed in Section 2.3.

The impact of the duality transformation (1.7) on the rung symmetrized states

$$U_{\frac{\pi}{2}} = \left|t_{+,0,-}\right\rangle\left\langle t_{+,0,-}\right| - i\left|s_0\right\rangle\left\langle s_0\right| \tag{2.16}$$

provides the singlet state with an imaginary coefficient. The representation of the duality transformation extended to the plaquette reads

$$U_{\frac{\pi}{2}} = \mathcal{P}_2 + \mathcal{P}_1^{\perp} - i\mathcal{P}_1^{\parallel} - i\mathcal{P}_1^{\times} - \mathcal{P}_0^{\perp} + \mathcal{P}_0^{\parallel,\times} \tag{2.17}$$

adding imaginary phases to certain eigenstates.

As introduced in Section 1.5, different order parameters arise in the various phases of the spin ladder with cyclic exchange (1.5):

- The rung-singlet phase is described by $\mathcal{O}_r$. The commutator with the system's Hamiltonian $[H, \mathcal{O}_r]$ vanishes only at the point $J_{\text{cyc}}/J = 1/2$ which is a fixed point of the duality transformation. The number of singlets and triplets on the rungs is conserved in this case.

- The staggered-dimer phase has dimers sitting on alternating legs locally described by the staggered-dimer order parameter

$$\begin{aligned} \mathcal{O}_{\text{SD}} &= \mathbf{S}_{1,j}\cdot\mathbf{S}_{1,j+1} - \mathbf{S}_{2,j}\cdot\mathbf{S}_{2,j+1} \\ &= \left|\phi_1^{\perp}\right\rangle\left\langle\phi_1^{\times}\right| + \left|\phi_1^{\times}\right\rangle\left\langle\phi_1^{\perp}\right| \end{aligned} \tag{2.18}$$

  which breaks the translational symmetry and connects sub-spaces with $k = 0$ and $k = \pi$.

- The scalar-chirality phase is believed to have staggered long range order in the scalar chirality. The local order parameter $\mathbf{S}_{1,j}\cdot\left(\mathbf{S}_{2,j}\times\mathbf{S}_{1,j+1}\right)$ has a spatial modulation with wave vector (π,π) leading to

$$\begin{aligned} \mathcal{O}_{\text{SC}} &= \left(\mathbf{S}_{1,j}+\mathbf{S}_{2,j}\right)\cdot\left(\mathbf{S}_{1,j+1}\times\mathbf{S}_{2,j+1}\right) + \left(\mathbf{S}_{1,j+1}+\mathbf{S}_{2,j+1}\right)\cdot\left(\mathbf{S}_{1,j}\times\mathbf{S}_{2,j}\right) \\ &= -\mathrm{i}\left|\phi_1^{\perp}\right\rangle\left\langle\phi_1^{\times}\right| + \mathrm{i}\left|\phi_1^{\times}\right\rangle\left\langle\phi_1^{\perp}\right| \end{aligned} \tag{2.19}$$

  which is the duality-transformed staggered-dimer order parameter (2.18).

- The vector chirality is a second chirality which is discussed in the context of frustrated spin systems. For the spin ladder, correlations in the vector-chirality of rungs becomes dominant in the so called vector-chirality phase [54, 1]. The vector chirality on a rung is defined by $\mathbf{S}_{1,j} \times \mathbf{S}_{2,j}$ which is the dual operator to the Néel spin $(\mathbf{S}_{1,j} - \mathbf{S}_{2,j})/2$. In the case of a dominant vector-chirality ordering the scalar product of two rung vector-chiralities

$$\begin{aligned} \mathcal{O}_{\mathrm{VC}} &= (\mathbf{S}_{1,j} \times \mathbf{S}_{2,j}) \cdot (\mathbf{S}_{1,j+1} \times \mathbf{S}_{2,j+1}) \\ &= \frac{1}{4}\left[\mathcal{P}_1^{\parallel} - \mathcal{P}_1^{\times} - \sqrt{3}\left(|\phi_0^{\perp}\rangle\langle\phi_0^{\parallel,\times}| + |\phi_0^{\parallel,\times}\rangle\langle\phi_0^{\perp}|\right)\right] \end{aligned} \tag{2.20}$$

  is the relevant plaquette operator.

- Within the dominant-collinear spin region, spins on the same leg (on different legs) exhibit ferromagnetic (antiferromagnetic) correlations. The order parameter on a single plaquette

$$\begin{aligned} \mathcal{O}_{\mathrm{Col}} &= \frac{1}{4}\left(\mathbf{S}_{1,j} + \mathbf{S}_{1,j+1} - \mathbf{S}_{2,j} - \mathbf{S}_{2,j+1}\right)^2 \\ &= \mathcal{P}_1^{\parallel} + \mathcal{P}_0^{\perp} + \frac{\sqrt{3}}{2}\left(|\phi_0^{\perp}\rangle\langle\phi_0^{\parallel,\times}| + |\phi_0^{\parallel,\times}\rangle\langle\phi_0^{\perp}|\right) + \frac{1}{2} \end{aligned} \tag{2.21}$$

  keeps track of this behavior.

2.3 Eigenenergies of a single plaquette

In this section, the Hamiltonian of the spin ladder with cyclic exchange is diagonalized on a single plaquette. Its eigenvalues provide a lower bound for the exact ground-state energy of the ladder. The nature of the lowest-energy eigenstate—together with an upper bound provided by a variational state— will help us to characterize the nature of the ground-state.

We already chose a reasonable set of basis states in Section 2.1. Out of the 16 plaquette states, 14 states are fixed consistently with the symmetry without any free parameters. A two-dimensional subspace remains for the case of vanishing total spin. As the model Hamiltonian is given in the language of projection operators onto those quantum-number conserving states (2.15), we simply read off the eigenenergies

$$\begin{aligned} E_2 &= \tfrac{1}{4}(3\cos\theta + 8\sin\theta), & E_1^{\perp} &= -\tfrac{1}{4}\cos\theta \\ E_1^{\parallel} &= \tfrac{1}{4}\cos\theta & E_1^{\times} &= \tfrac{1}{4}(-3\cos\theta - 8\sin\theta) \end{aligned} \tag{2.22}$$

of the single-plaquette system in the $S = 2$ and $S = 1$ subspaces where we neglected the trivial rescaling $\tilde{J}$. Five degenerate $S = 2$ states show ferromagnetic ordering. Each of the three $S = 1$ energies belongs to a plaquette-triplet composed of triplets on either rungs, legs, or diagonals.

The eigenenergies

$$E_0^{\mathrm{hi,lo}} = -\frac{3}{4}\cos\theta \pm \frac{1}{2}x \tag{2.23}$$

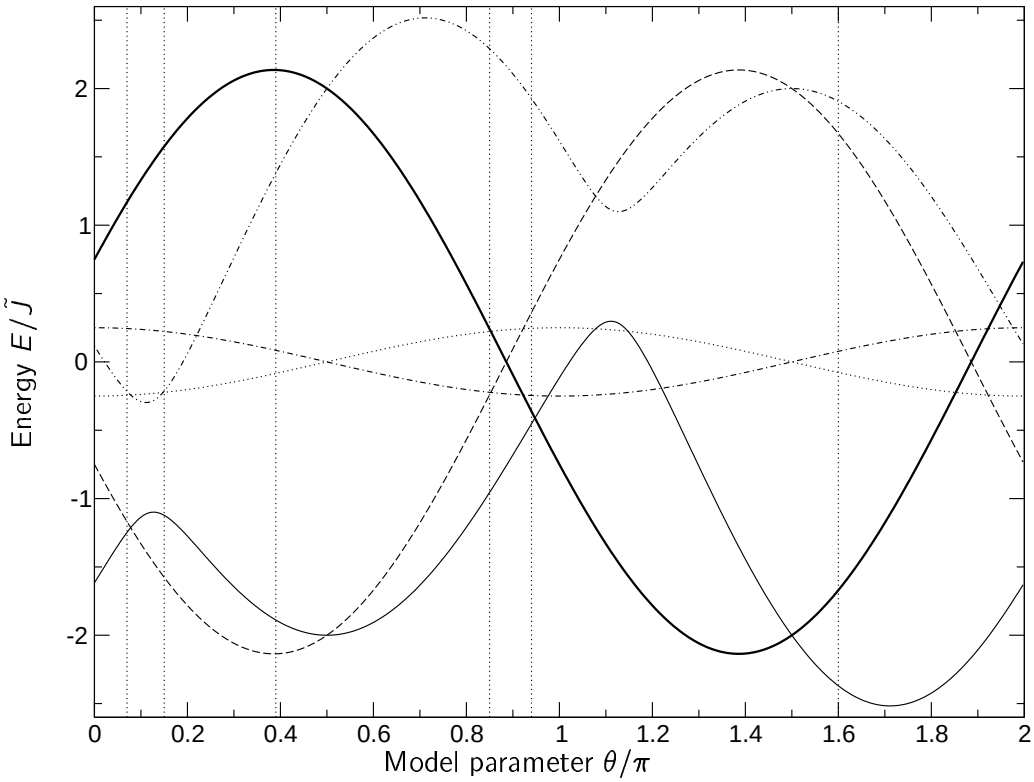

Figure 2.1: Plaquette energies of the spin ladder with cyclic exchange versus system parameter θ. The fat black line represents the ferromagnetic state with $S = 2$. The states with triplets on rungs (dotted), legs (dot-dashed), and diagonals (dashed) have a total spin $S = 1$. The upper (double-dot-dashed) and lower (thin straight) lines represent eigenenergies of the $S = 0$ subspace. The phase boundaries proposed in [1] have been included as vertical, dotted lines.

with

$$x := \sqrt{16 - 12\,\cos\theta \sin\theta - 13\,\cos^2\theta} \tag{2.24}$$

can be calculated by diagonalization within the $S = 0$ subspace. All plaquette-eigenenergies are plotted versus the model parameter θ in Fig. 2.1.

As we have three interesting, but non-orthogonal, plaquette-states in the $S = 0$-subspace, it is worth to mention that at $\theta = \arctan(1/4) \simeq 0.078\pi$ ($\theta = \pi/2$) the lowest energy eigenstate is the state with singlets on the legs $\left|\phi_0^{\parallel}\right\rangle$ (on the diagonals $\left|\phi_0^{\times}\right\rangle$). The state $\left|\phi_0^{\perp}\right\rangle$ is the lowest energy state for $\theta = \pi + \arctan(1/2) \simeq -0.85\pi$. The contributions to the lowest-energy $S = 0$ eigenstate are plotted in Fig. 2.2.

In general, plaquette ground states cannot be extended to a state of the whole chain in a straightforward fashion. Only the state with singlets on rungs and the $S = 2$ ferromagnetic states can be written as a simple product state on the whole ladder. In all other cases,

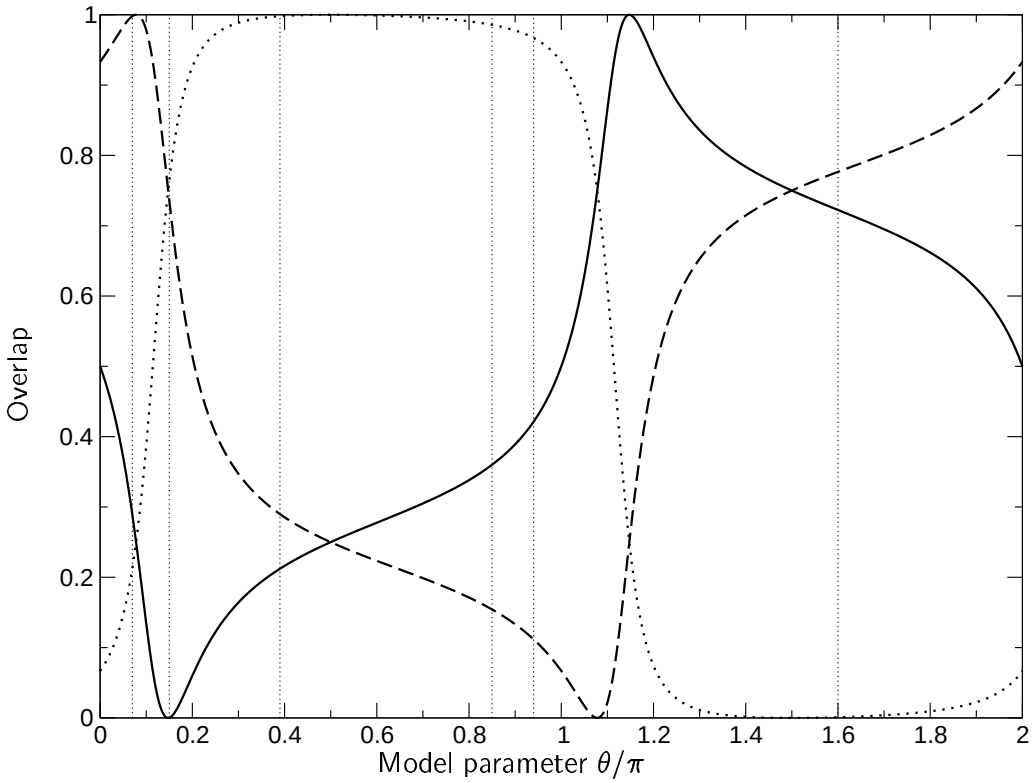

Figure 2.2: Overlap of $|\phi_0^{\perp}\rangle$ (straight line), $|\phi_0^{\parallel}\rangle$ (dashed), and $|\phi_0^{\times}\rangle$ (dotted) with the lowest plaquette-energy eigenstate in the $S = 0$ subspace versus system parameter θ. The phase boundaries proposed in [1] have been included as vertical, dotted lines.

we have an admixture of energetically higher lying local plaquette states when we consider states on the full ladder. The eigenstate of the plaquette which is lowest in energy thus provides a lower bound to the full ladder ground state energy.

Exact upper bounds of the ground state energy can be obtained with variational states of matrix product type. These matrix product states are states defined on the whole ladder, but no eigenstates of the ladder Hamiltonian in general.

2.4 Matrix product states as variational states

Upper bounds for the ground state energy will be derived by a variational approach based on matrix product states in this section. Similar calculations have been done for the bilinear-biquadratic spin-1 chain in [58]. If the upper bound agrees with the lower bound derived in Section 2.3 the corresponding state is an optimal ground state. We expect the matrix

product variational states to give us a good physical picture of the ground state in different parameter regimes.

Matrix product states were introduced as a convenient representation of the valence bond states (VBS) for integer-spin chains [59, 60]. Similar considerations have been done in [61]. In terms of the original spin states, VBS wavefunctions factorize in terms of matrix states which considerably simplifies all calculations. Matrix product states have also proven to be a useful tool for constructing new classes of spin Hamiltonians with exactly known ground states [59, 60, 62, 63, 64, 65], for variational study of the ground state properties of one and quasi-one dimensional spin chains systems [58, 66, 67], and also for the study of elementary excitations [68, 69, 70, 71]. Matrix product states can be generalized to vertex state models in two and higher dimensions [72, 73, 63, 74, 75].

In the framework of ladders, the matrix product ansatz has been applied both for variational states and for constructing models with optimum ground state. Optimum ground states are global ground states constructed of only those local states which are ground states of the local Hamiltonian as well. The matrix product ansatz was adopted to the spin-1/2 two-leg ladder with two-spin rung, leg, and additional diagonal interaction in [66]. Variational ground state energies as well as spin and string correlation functions were computed. In [64], a model class with four-spin interaction was introduced which possesses unique or twofold degenerate ground states of matrix product type. Within these ground states, the state with staggered dimers on the ladder's legs was given as a matrix product state in addition to AKLT-type states. Based on this work, a model with exact scalar chiral ground state was constructed by consideration of the duality transformation [42].

In this section, we extend the previous approaches. A set of matrix product states shall now be considered as variational states for the spin ladder with cyclic four-spin exchange including the states proposed earlier. We work out the character of the ground state in the different phases of the model. Since we deal with variational states which give upper bounds to the ground state energy we do not expect to find the exact phase boundaries, but expedient approximations.

The matrix product state considered here

$$\left|\Psi(u)\right\rangle = \mathrm{tr}\left(\prod_{j=1}^{L} g_j(u)\right) \tag{2.25}$$

can be written as a trace of the product of matrices

$$g_j(u) = \begin{pmatrix} u\left|s_0\right\rangle_j + \left|t_0\right\rangle_j & -\sqrt{2}\left|t_+\right\rangle_j \\ \sqrt{2}\left|t_-\right\rangle_j & u\left|s_0\right\rangle_j - \left|t_0\right\rangle_j \end{pmatrix} \tag{2.26}$$

containing the local rung-symmetrized states from Eqs. (2.1) and (2.2) as elements. In general, the parameter u is complex.

The ansatz is chosen to be isotropic with respect to SU(2) rotational symmetry which is the symmetry of the ladder Hamiltonian under study. An anisotropic ansatz would

replace the $\sqrt{2}$-factor in Eq. (2.26) by another variational parameter [66]. The following calculations have also been carried out with this additional anisotropy parameter. However, no improvement of the variational energies could be found. Therefore, the results are not shown and we only discuss the isotropic states explicitely.

The total spin of (2.25) vanishes (see [67]) making it an appropriate trial state for the interesting antiferromagnetic regime. For the ferromagnetic part of the phase diagram, the variational state of choice is the ferromagnetic product state with maximal spin alignment and an energy (2.22) ($S = 2$ plaquette state).

The ansatz (2.25) has two limiting cases: For $u = 0$, all rung-singlet contributions are eliminated. Thus, we get the AKLT-state of the spin-1 chain [76, 77]. The simple product-state with only singlets on the rungs emerges in the case of infinite u.

Since we expect phases with spontaneously broken translational symmetry, an additional degree of freedom is appropriate. Hence, we allow an alternation of the parameter u by every second site. So, our variational state

$$\left|\Psi(u,\sigma)\right\rangle = \mathrm{tr}\left(\prod_{j=1}^{L/2} g_{2j}(u)\, g_{2j+1}(\sigma u)\right) \tag{2.27}$$

gains another parameter σ which we allow to be complex. Later, we will show that $\sigma = \pm 1$ holds for the lowest energy variational states. This ansatz comprises further states with well known physical interpretation. For $u = 1$ and $\sigma = -1$, we obtain a state with singlets on the legs arranged in a staggered order [64]. Applying the duality transformation to exactly this state, a state with perfect scalar-chiral order is obtained. It is written with a purely imaginary parameter $u = i$ and $\sigma = -1$ in the matrix-product form [42].

2.4.1 Energy of the variational state

The transfer matrix method[59] for matrix product states allows us to calculate the expectation values of certain operators explicitely. The technique makes use of the structure of the matrix product ansatz. In our case, it essentially involves a diagonalization of a product of 4×4 (number) matrices.

We choose the Hamiltonian H of the spin ladder with cyclic exchange, see Eq. (1.5), as the operator whose expectation values are to be determined in this case. If we proceed like this, we find the local expectation value of H given by

$$\begin{aligned} w(u,\sigma) :=& \frac{1}{N}\left\langle\Psi(u,\sigma)\middle|H\middle|\Psi(u,\sigma)\right\rangle \\ =& -\frac{3}{2}J + \frac{3}{4}\left(-3J - 4J_{\mathrm{cyc}}\right) + \frac{3|u|^2}{8}\left(|\sigma+1|^2 J + |\sigma-1|^2\left(-3J - 8J_{\mathrm{cyc}}\right)\right) \\ &+ \sqrt{3}\left(\sigma u^2 + \sigma^* u^{*2}\right)\frac{\sqrt{3}}{2}\left(J - 2J_{\mathrm{cyc}}\right) + \frac{1}{4}|\sigma|^2|u|^4\left(-3J + 4J_{\mathrm{cyc}}\right) \end{aligned} \tag{2.28}$$

where N is the number of rungs of the ladder. The detailed calculations can be found in Appendix A. This expectation value $w(u,\sigma)$ still has to be divided by the norm

$$Z(u,\sigma) := \langle \Psi(u,\sigma) | \Psi(u,\sigma) \rangle = \left(|u|^2 + 3\right)\left(|\sigma u|^2 + 3\right) \tag{2.29}$$

of the matrix product state to get the correct expectation value $e(u,\sigma) = w(u,\sigma)/Z(u,\sigma)$. We want to find a variational state $|\Psi_{\text{var}}\rangle$ of type (2.27) with a minimal local energy e_{var} regarding the matrix product state's parameters u and σ as variational parameters.

It will turn out to be useful to write the complex state parameters

$$u = re^{i\phi} \text{ and } \sigma = se^{i\alpha} \tag{2.30}$$

in terms of norm and phase, for our purpose. With this definition, we rewrite Eq. (2.28) as

$$\begin{aligned} w(u,\sigma) = \frac{3}{4}\Big[&(-5J - 4J_{\text{cyc}}) + r^2(s^2+1)(-J - 4J_{\text{cyc}}) + 4sr^2(J + 2J_{\text{cyc}})\cos\alpha \\ &+ 4sr^2(J - 2J_{\text{cyc}})\cos(2\phi + \alpha) + s^2r^4\left(-J + \frac{4}{3}J_{\text{cyc}}\right)\Big] \end{aligned} \tag{2.31}$$

which allows to us to consider two positive real numbers r and s as well as two angles $0 \le \phi, \alpha \le 2\pi$ instead of complex numbers. The third term in Eq. (2.31) is minimal for $\alpha = \pi$ (if $J + 2J_{\text{cyc}} > 0$) and $\alpha = 0$ (if $J + 2J_{\text{cyc}} < 0$). With α fixed, we can determine the optimal value of ϕ. By consideration of the fourth term we find that, for $J - 2J_{\text{cyc}} > 0$, it is best to choose $\phi = (\alpha - \pi)/2$ while $\phi = \alpha/2$ is best for $J - 2J_{\text{cyc}} < 0$. We conclude from these conditions that an appropriate u is either real oder purely imaginary and that σ is a real number.

In sectors with fixed ϕ and α, the variational energy e takes the form

$$e(s,r) \quad = \quad \frac{3}{4}\,\frac{a_1 s^2 r^4 + 2a_2 s r^2 + a_3(s^2+1)r^2 + a_4}{s^2 r^4 + 3(s^2+1)r^2 + 9} \tag{2.32}$$

with the constants $a_{1,2,3,4}$ depending on the system variables J and J_{cyc}. It has a local extremum[1] at

$$s = 1, \quad r^2 = \frac{3(a_2 + a_3) - a_4}{(a_2 + a_3) - 3a_1} \tag{2.33}$$

with an energy

$$e_{\text{var}} = \frac{3}{4}\,\frac{a_1 a_4 - (a_2 + a_3)^2}{9a_1 - 6(a_2 + a_3) + a_4}\,. \tag{2.34}$$

Besides the local extrema we have to consider the boundaries. Here we find

$$r^2 \to 0, 0 < s < \infty \quad : \quad E_{\text{var}} = \frac{a_4}{12}, \quad r^2 \to \infty, 0 < s < \infty : E_{\text{var}} = \frac{3a_1}{4} \tag{2.35}$$

$$r^2 \to \infty, s \to 0 \quad : \quad E_{\text{var}} = \frac{a_3}{4}, \quad r^2 \to 0, s \to \infty : E_{\text{var}} = \frac{a_3}{4}. \tag{2.36}$$

With these preceding calculations, we continue to find lowest-energy variational states for spin ladders with different amounts of ring-exchange.

[1] For a calculation, set $x := sr^2, y := (s^2+1)r^2$ and calculate derivatives.

2.4.2 Calculation of variational energies in different regimes

We now have to consider different pairs of the variables α and ϕ for different regimes of the Hamiltonian' s coupling parameters as mentioned above. For obtaining a local extremum (2.33), we set $s = 1$ in the following. The other limits of infinite and vanishing s have been found to be unimportant in the examined cases. Further, we again eliminate the trivial rescaling degree of freedom and set $J = \cos\theta$ and $J_{\mathrm{cyc}} = \sin\theta$.

Starting with $2\pi - \arctan(1/2) < \theta < \arctan(1/2)$ and, thus, $\alpha = \pi, \phi = 0$, we look at the model class including the Heisenberg ladder for $\theta = 0$. The adequate variational energy

$$e^{\pi,0}(r) = \tfrac{3}{4}\frac{(-5\cos\theta-4\sin\theta)-r^2(10\cos\theta+8\sin\theta)+r^4\left(-\cos\theta+\frac{4}{3}\sin\theta\right)}{(r^2+3)^2} \tag{2.37}$$

has a local minimum

$$e^{\pi,0}_{\mathrm{var}} = \frac{\cos^2\theta - 32\cos\theta\sin\theta - 16}{16\,(\cos\theta + 2\sin\theta)} \quad \text{at} \quad r^2 = \frac{5\cos\theta + 4\sin\theta}{\cos\theta + 4\sin\theta} \tag{2.38}$$

for $\theta > -\arctan(1/4)$ which is also global minimum in this area. For $\theta < -\arctan\frac{1}{4}$ the global minimum

$$e^{\infty}_{\mathrm{var}} = -\frac{3}{4}\cos\theta + \sin\theta \tag{2.39}$$

is found for $r \to \infty$. The variational states takes the simple form of a product of rung-singlet states in this case.

Turning to the next phase, $\arctan(1/2) < \theta < \pi - \arctan(1/2)$, we have to set $\alpha = \pi, \phi = \pi/2$. The energy

$$e^{\pi,\pi/2}(r) = \tfrac{3}{4}\frac{(-5\cos\theta-4\sin\theta)+r^2(-2\cos\theta-24\sin\theta)+r^4\left(-\cos\theta+\frac{4}{3}\sin\theta\right)}{(r^2+3)^2} \tag{2.40}$$

has a global minimum

$$e^{\pi,\pi/2}_{\mathrm{var}} = \frac{-115\cos^2\theta + 20\cos\theta\sin\theta + 112}{8\,(\cos\theta - 10\sin\theta)} \quad \text{at} \quad r^2 = \frac{\cos\theta - 16\sin\theta}{\cos\theta - 8\sin\theta} \tag{2.41}$$

within the whole region.

Setting $\alpha = 0, \phi = 0$ in the regime $\pi - \arctan(1/2) < \theta < \pi + \arctan(1/2)$, we find an energy

$$e^{0,0}(r) = \tfrac{3}{4}\frac{(-5\cos\theta-4\sin\theta)+r^2(6\cos\theta-8\sin\theta)+r^4\left(-\cos\theta+\frac{4}{3}\sin\theta\right)}{(r^2+3)^2} \tag{2.42}$$

for the variational state. In the whole range, there is a global minimum

$$e^{0,0}_{\mathrm{var}} = \frac{13\cos^2\theta + 16\cos\theta\sin\theta - 16}{32\,(-\cos\theta + \sin\theta)} \quad \text{at} \quad r^2 = \frac{7\cos\theta - 4\sin\theta}{3\cos\theta - 4\sin\theta}. \tag{2.43}$$

Finally, for $\alpha = 0, \phi = \pi/2$ when $\pi + \arctan(1/2) < \theta < 2\pi - \arctan(1/2)$, the variational energy is

$$e^{0,\pi/2}(r) = \tfrac{3}{4}\frac{(-5\cos\theta-4\sin\theta)+r^2(-2\cos\theta+8\sin\theta)+r^4\left(-\cos\theta+\frac{4}{3}\sin\theta\right)}{(r^2+3)^2}. \tag{2.44}$$

with a global minimum

$$e_{\mathrm{var}}^{0,\pi/2} = \frac{-19\cos^2\theta - 4\cos\theta\sin\theta + 16}{8\,(\cos\theta + 2\sin\theta)} \quad \text{at} \quad r^2 = 8\tan\theta + 1, \tag{2.45}$$

if $\theta < 3\pi/2$. For $\theta > 3\pi/2$ the global minimum is found in the rung-singlet state which has the energy (2.39).

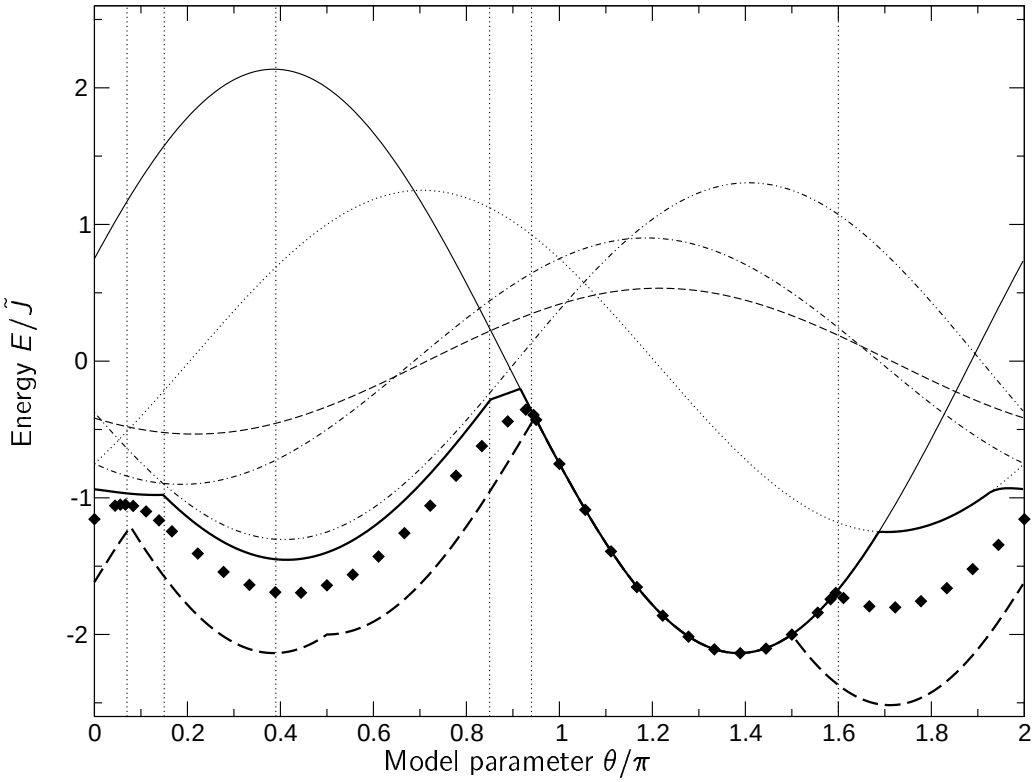

Figure 2.3: Variational energies of matrix product states (2.25)–(2.27) for the spin ladder with cyclic exchange. The fat black line is the lowest variational energy e_{var} calculated by the matrix product ansatz versus system parameter θ. The fat dashed line gives the lower bound of the local energy provided by diagonalization of the local Hamiltonian. The thin lines are energies of selected (matrix) product states: Ferromagnetic (straight), rung-singlet (dotted), ALKT-type (dashed), staggered dimers on leg (dot-dashed), and scalar-chirality (double-dot-dashed) state. The diamonds denote the approximated ground-state energy extrapolated from TMRG data. The phase boundaries proposed in [1] have been included as vertical dotted lines.

Between $\theta = \pi - \arctan((\sqrt{154} - 7)/20) = 0.916\pi$ and $\theta = -\arctan(3/2) \approx -0.31\pi$ the ferromagnetic energy gets favorable. Here, we have to consider a ferromagnetic state as best variational state.

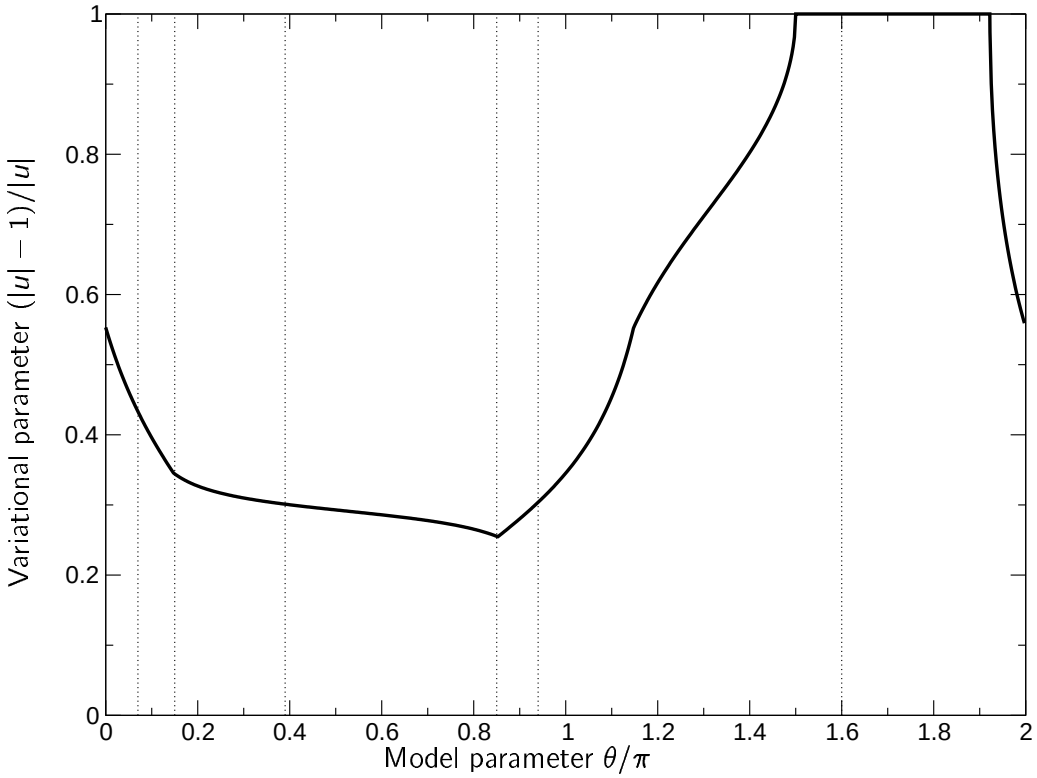

Figure 2.4: Variational parameter within different regimes. The ratio $(|u|-1)/|u|$ is plotted versus the system parameter θ. If $(|u|-1)/|u| = 0$ (and $\sigma = -1$) the system is in a pure staggered-dimer or scalar-chirality state which is not fulfilled for the variational states in any regime. If $(|u|-1)/|u| = 1$, a rung-singlet state is the favorable state.

In summary, we identified the variational states following ansatz (2.27) with lowest energy within the whole parameter range of the spin ladder (1.5). The corresponding variational energies are plotted in Fig. 2.3 along with several prominent matrix-product-type states. Note that we included the ferromagnetic state as well. The variational parameter $r = |u|$ minimizing the variational energy is plotted in Fig. 2.4 as additional information.

2.5 Discussion of ground-state properties

In this section, we discuss our analytical results of the ground state properties of the spin ladder with cyclic four-spin exchange. We include a comparison to the scenario presented in Chapter 1.5.

We start the discussion of our variational studies from the well-studied point $\theta = 0$ where no ring-exchange is present and the model reduces to the Heisenberg ladder, see Section 1.3.

Here, we usually picture the ground-state as a product state of rung spins coupled to singlets. This rung-singlet character extends when ring-exchange is turned on. However, the phase extension to negative values of ring-exchange ranges further than the phase extension to positive values of ring-exchange. Indeed, within $-\arctan(3/2) < \theta < -\arctan(1/4)$ the pure rung-singlet state is the variational matrix product state which is lowest in energy. The lower bound provided by exact diagonalization lies about an energy unit below the upper bound, so the model has no optimum ground-state in this region. Yet, this will not significantly change the picture of a rung-singlet state because the lower-bound state has a zero total plaquette spin as well and the rung-singlets give a major contribution, see Fig. 2.2. The larger overlap with a plaquette state with singlets on the legs plays a minor role because the latter cannot be extended to the full chain in the sense of a product state. Lastly, upper bound and lower bound energy are well separated from the higher energies of other plaquette and variational states. From our analytical calculations, we come to the conclusion that the rung-singlet picture of the ground state is valid within the region $-\arctan(3/2) < \theta < -\arctan(1/4)$.

Our starting point, the Heisenberg ladder, lies in the transition range to the staggered-dimer phase. We identify three potentially relevant points for the location of the phase transition from the rung-singlet to the staggered-dimer phase: At $\theta = -\arctan(1/4)$, a variational state with staggering crosses the pure rung-singlet state and gets minimal in energy. At $\theta = 0$, the state with staggered dimers on legs crosses the rung-singlet state. At $\theta = \arctan(1/4)$, an $S = 1$-state crosses an $S = 0$-state in the plaquette-energies. The favored plaquette state now consists of triplets on diagonals coupled to a local $S = 1$ state. We conclude from these considerations that the transition happens within the relatively broad range $-\arctan(1/4) \leq \theta \leq \arctan(1/4)$.

Arguments shall be presented, though, that the true transition point lies near the upper limit of this range: The variational matrix product state has the character of a rung singlet state with only a small staggered contribution near the center of the rung-singlet phase because the variational parameter u is still big, see Fig. 2.4. At $\theta = -\arctan(1/4)$, upper (variational energy) and lower bound (plaquette energy) differ by more than one unit of energy while, at $\theta = \arctan(1/4)$, the difference is less than one fourth of an energy unit. Because of this, we expect the ground state for bigger θ to be closer to an optimal ground state which is a staggered state with dimers on legs. Indeed, we see from Fig. 2.3 that a numerical calculation of the ground state energy follows the form of rung-singlet energy up to almost $\theta = \arctan(1/4)$ rather than approaching the variational state. In [66, 70], a variational approach with different matrix product states was done for the Heisenberg ladder. Two spins were coupled along the diagonal of a plaquette to triplet states. They found that an AKLT-state of these diagonal-triplets provided a variational energy $-e = 1.102$ which is lower in energy than the staggered-dimer state energy.

Within the staggered phase, the lower bound is the $S = 1$-plaquette state with a small gap to the $S = 0$-state on the plaquette which is next in energy. Both plaquette states cannot be extended to product states of the whole chain. The upper bound is given by a slightly modulated staggered-dimer matrix product state. All other antiferromagnetic variational

states are close by in energy. We notice that the ground state energy from Fig. 2.3 is close to the matrix product ansatz variational energy. From this we conclude that the ground state can indeed be pictured as two degenerate states with dimers on the legs arranged in a staggered order. An existing energy gap is supposed to be small and the spectrum will be dense because the variational and plaquette energies lie so close together.

The only phase transition point which is known exactly is located at $\theta = \arctan(1/2)$. The transition from the staggered-dimer phase to the scalar-chirality phase is a fixed point of the duality transformation (1.7). We see the duality in the energy level crossing of the staggered-dimer matrix product state ($u = 1$) and the scalar-chirality matrix product state ($u = i$). At the same time, the lowest lying variational state changes to a state with scalar-chiral ordering. In contrast to this apparent behavior in the matrix product state, no signature in the calculated ground state energy (Fig. 2.3) or in the energetically lowest plaquette state can be seen.

Within the whole predicted scalar-chirality phase, the low-energy variational state has a scalar-chiral ordering and, thus, is two-fold degenerate. It lies energetically very close to the pure scalar-chirality state. The plaquette's low-energy state is still the $S = 1$ state with triplets on the diagonals. It lies well below the variational energy, but does not have an extension to the whole ladder. The spectrum of energies broadens again after the energies lay close together in the preceeding phase. We find the ground state energy from Fig. 2.3 close to the variational energy.

There is no indication in the matrix product states for the transition to the vector-chirality phase which was predicted for $\theta \approx 0.39\pi$. There is, however, a level-crossing from an $S = 1$-state to an $S = 0$-state in the lowest plaquette-energy at $\theta = \pi/2$. The favored plaquette state has singlets on the diagonals of a plaquette. We find no evidence for a phase transition in the ground state energy from Fig. 2.3.

In the vector-chirality phase the lowest variational energy is still found in the scalar-chirality matrix product state. Complementary to the scalar-chirality phase, the plaquette's lowest energy state for the bulk of the vector-chirality phase is found in the $S = 0$ sector. This plaquette state, again, cannot be extended to the whole chain. There is a good agreement between ground state energy from Fig. 2.3 and the variational energy. We cannot argue from our calculations that the ground state is unique as it is claimed [1]. The spectrum of matrix-product states gains a broad width, so there is evidence for a gap.

At $\theta = \pi - \arctan(1/2) = 0.852\pi$, an interesting region sets in which is characterized by a number of level-crossings in the matrix product states: At $\theta = \pi - \arctan(1/2)$, the variational state looses staggering and the weight of the rung-singlet contribution grows rapidly. This is the so called "smooth crossover" to the dominant-collinear-spin phase where the spins on a common leg (rung) are orientated parallel (antiparallel). At $\theta = \pi - \arctan((\sqrt{154} - 7)/20) = 0.916\pi$, the variational state crosses the ferromagnetic state which is an optimum grund state. This is a lower bound for the point where ferromagnetism is allowed to set in. An upper bound for the ferromagnetic regime to start is at $\theta = \pi - \arctan(1/6) = 0.947\pi$ where the lowest $S = 0$-plaquette state crosses the ferromagnetic state.

Within the ferromagnetic phase, the ground state is clearly separated from the matrix product states. The ground state is a product state ($S = 2$ on each plaquette) representing a fully polarized ferromagnet. In Fig. 2.3 the optimum ground-state properties of the ferromagnet are clearly visible. Here, plaquette state energy, ground-state energy and variational energy are identical. At both boundaries, we see a kink in the ground-state energy which is a signature of a first-order phase transition.

At $\theta = -\pi/2$, the $S = 0$-plaquette state with a high rung-singlet contribution crosses the ferromagnetic state. The pure rung-singlet state, however, gets lower in energy than the ferromagnetic state at $\theta = -\arctan(3/2) \approx -0.31\pi$. We expect the phase transition to happen somewhere in between those two points. Indeed, the predicted value of $\theta = -0.40\pi$ is located almost exactly in the middle.

As a conclusion, we obtained upper and lower bounds to the ground state energy in the whole parameter range of the spin ladder with cyclic four-spin exchange. We found physically representative (matrix) product states for the rung-singlet phase, the staggered-dimer phase, the scalar-chirality phase, and the ferromagnetic states. Limiting points for the location of the phase transitions were given. In this way, we supported the ground state phase diagram of [1] by exact calculations.

3 Quantum TMRG

The quantum Transfer Matrix Density Matrix Renormalization Group (QTMRG or shorter: TMRG) is a powerful numerical algorithm for the calculation of the thermodynamics of one dimensional quantum systems. In the framework of this thesis, I developed a high-performance implementation of the TMRG method which provided the thermodynamical properties presented in Chapter 5. The TMRG method succeeds in combining three refined approaches: Trotter-Suzuki decomposition, transfer-matrix formalism and density-matrix renormalization group (DMRG).

In this chapter, we start with a description of the classical decomposition of quantum chains (Section 3.1) which is the basis of many numerical finite-temperature approaches. The decomposition yields a classical system on a two-dimensional infinite lattice. The calculation of its partition function can be reduced to finding only the lowest eigenvalues of an infinite-sized transfer matrix (Section 3.2). We can force the transfer matrix to a fixed size when we iteratively expand in a way that unimportant degrees of freedom are omitted in each step by DMRG (Section 3.3). Finally, we present the iteration procedure for the quantum TMRG method (Section 3.4).

3.1 Classical decomposition of quantum chains

The statistical properties of a given quantum system with Hamiltonian H in thermodynamic equilibrium are encoded by the partition function

$$Z = \operatorname{tr} \mathrm{e}^{-\beta H}. \tag{3.1}$$

Its calculation demands knowledge about the whole spectrum of H. In only a small number of cases Z can be calculated analytically [78]. For both analytical and numerical purposes it is often useful to map a d-dimensional quantum system onto a $(d+1)$-dimensional classical system. After elimination of the quantum mechanical fluctuations, the corresponding two-dimensional classical system can be subject to existing exact and approximation techniques like the transfer-matrix method introduced by Kramers and Wannier [79] and Monte Carlo simulations [80].

3.1.1 Trotter-Suzuki-decomposition

The most prominent $d+1$-dimensional classical decomposition of the partition function for a d-dimensional quantum system has been established by Suzuki [81, 82, 83, 84]. One-dimensional chains with only nearest-neighbor interaction are considered in the following. Note that the quasi one-dimensional two-leg spin ladder can be mapped onto a quantum chain. [1] The decomposition itself, however, works as well in higher dimensions and with

[1] The most natural mapping of a spin ladder merges both legs to a single $S = 1/2$ chain of twice the length of the ladder. This induces up to third-nearest-neighbor interaction when cyclic four-spin exchange for the ladder is considered. If, however, the sites of the quantum chain consist of rung-triplet states (2.1) and rung-singlet states (2.2) of the ladder, the chain Hamiltonian (2.15) will only have nearest-neighbor terms even if there is cyclic four-spin exchange in the corresponding ladder model.

further interactions.

In an arbitrarily chosen basis, the chain Hamitonian H as well as the thermodynamically relevant density operator $e^{-\beta H}$ are represented by $n^L \times n^L$-matrices, with n being the number of local states. Thus, the matrices of both quantities grow exponentially with the chain length L preventing an exact diagonalization of systems with reasonable sizes.

In the case where the Hamiltonian

$$\tilde{H} = \sum_{j=1}^{L} \tilde{h}_{j,j+1}; \quad \text{with } \left[\tilde{h}_{j,j+1}, \tilde{h}_{k,k+1}\right] = 0 \text{ if } j \neq k \tag{3.2}$$

consists of commuting nearest-neighbor interaction only i.e., in classical systems, the imaginary time quantum-mechanical propagator $e^{-\beta \tilde{H}}$ reduces to a product of locally acting propagators which leads to

$$Z = tr e^{-\beta \sum \tilde{h}} = tr \left(e^{-\beta \tilde{h}}\right)^L. \tag{3.3}$$

This tremendously diminishes calculational effort because only the small $n \times n$-matrix $\tilde{h}$ has to be diagonalized for a calculation of Z. For real quantum systems, however, a different strategy has to be chosen.

In a considerable number of quantum systems only interaction between nearest neighbors predominates. So, one succeeds in splitting the Hamiltonian

$$H = \sum_{j=1}^{L} h_{j,j+1} = H_{\text{odd}} + H_{\text{even}} \quad \text{with} \quad H_{\text{odd/even}} := \sum_{j=\text{odd/even}} h_{j,j+1} \tag{3.4}$$

into just two sums H_{odd} and H_{even} of pairwise commuting local terms. We aim at a decoupling of both sums so that each part can be treated in a fashion similar to the non-commuting case sketched above. Applying the so called Trotter formula [85], we can describe the partition function

$$\begin{aligned} Z = \operatorname{tr} e^{-\beta(H_{\text{odd}} + H_{\text{even}})} &= \lim_{M \to \infty} \operatorname{tr} \left(e^{-\epsilon H_{\text{odd}}} e^{-\epsilon H_{\text{even}}}\right)^M \\ &= \lim_{M \to \infty} \operatorname{tr} \left(\left[\prod_{j=\text{odd}} e^{-\epsilon h_{j,j+1}} \right] \left[\prod_{j=\text{even}} e^{-\epsilon h_{j,j+1}} \right] \right)^M \end{aligned} \tag{3.5}$$

(with $\epsilon := \beta/M$) as a trace over a product of alternating operators which exactly holds in the case of infinite M (Trotter limit). It can be shown that the error for finite M is of order $\mathcal{O}(\epsilon^2)$ [86]. As a benefit from this factorization, we are able to insert $2M$ identities of the form

$$\sum \left| s_1 \ldots s_L \right\rangle \left\langle s_1 \ldots s_L \right| = 1 \tag{3.6}$$

pictured as slices of discrete temperature or imaginary time, where the chain state $\left| s_1 \ldots s_L \right\rangle$ is the tensor product of local quantum states $\left| s_j \right\rangle$ at site j. Thus, we achieve a classical two

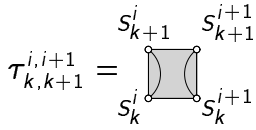

Figure 3.1: Graphical representation of 4-spin transfer-matrix τ. The bended curves illustrate the symmetries of the object.

dimensional model, spanned by the real space or chain direction and the auxiliary introduced imaginary time or so called Trotter direction.

The local transfer matrix (see Fig. 3.1)

$$\tau^{i,i+1}_{k,k+1} := \left\langle s^i_k s^{i+1}_k \middle| \mathrm{e}^{-\epsilon h_{i,i+1}} \middle| s^i_{k+1} s^{i+1}_{k+1} \right\rangle \tag{3.7}$$

coupling imaginary-time slides k with $k+1$ at real space sites i and $i+1$ is a fourth order tensor of dimension $n \times n \times n \times n = n^4$. With this definition, the partition function of the quantum chain (3.5) now reads as a partition function

$$Z = \sum_{\substack{\{s^\nu_\mu\} \\ \nu = 1 \ldots L, \\ \mu = 1 \ldots 2M}} \prod_{k=1}^{M} \prod_{i=1}^{L/2} \tau^{2i-1,2i}_{2k-1,2k} \tau^{2i,2i+1}_{2k,2k+1} \tag{3.8}$$

of a two-dimensional chequerboard-type classical model (see Fig. 3.2). Note that real space

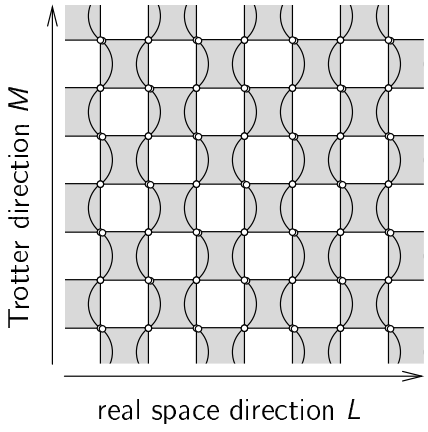

Figure 3.2: Graphical representation of Trotter decomposition (3.8). The four-spin transfer matrices have been composed in a chequerboard-like fashion which has its cause in the even/odd distinction. The small circles represent classical spin variables to be summed over. Periodic boundary conditions in both directions are assumed (not depicted here).

and Trotter direction appear in a symmetric fashion. Nevertheless, general Hamiltonians introduce a reduced symmetry into the local transfer matrix τ leading to a net anisotropy of the chequerboard model.

Thermal expectation values of local operators can be calculated by a modified partition function. We recall the statistical definition of the thermodynamical expectation value

$$< \mathcal{O}_i >= \frac{Z(\mathcal{O}_i)}{Z}, \qquad Z(\mathcal{O}_i) = \mathrm{tr}\, \mathcal{O}_i \mathrm{e}^{-\beta H} \tag{3.9}$$

of an operator $\mathcal{O}$ living at a site i. It is now an easy task to write down the non-normalized expectation value $Z(\hat{O}_i)$ in terms of the two-dimensional classical model similar to (3.8). We introduce the modified local transfer-matrix

$$\tilde{\tau}^{i,i+1}_{k,k+1} := \left\langle s^i_k s^{i+1}_k \middle| \mathcal{O}_i \mathrm{e}^{-\epsilon h_{i,i+1}} \middle| s^i_{k+1} s^{i+1}_{k+1} \right\rangle \tag{3.10}$$

and replace one standard transfer-matrix within the product (3.8) by it in order to get

$$Z(\hat{O}_i) = \sum_{\substack{\{s^\nu_\mu\} \\ \nu = 1 \ldots L, \\ \mu = 1 \ldots 2M}} \left(\tau^{1,2}_{1,2} \tau^{2,3}_{2,3} \ldots \tilde{\tau}^{j,j+1}_{1,2} \tau^{j+1,j+2}_{2,3} \ldots \tau^{L-1,L}_{1,2} \tau^{L,L+1}_{2,3} \prod_{k=2}^{M} \prod_{i=1}^{L/2} \tau^{2i-1,2i}_{2k-1,2k} \tau^{2i,2i+1}_{2k,2k+1} \right) \tag{3.11}$$

Periodic boundary conditions are imposed by the trace in (3.9), so without loss of generality we place $\tilde{\tau}$ in row $k = 1$ of the Trotter direction at an odd site j.

Equations (3.7) and (3.8) contain the whole thermodynamics of the underlying quantum system in the limit $M \to \infty$ with $\beta = \epsilon M$. There are, however, quantum-classical decompositions differing from the chequerboard approach presented in this section.

3.1.2 Alternative decomposition

In addition to the well-established chequerboard-like decomposition of a quantum chain, other Trotter decompositions have already been proposed by Suzuki [81]. In [87], Sirker and Klümper introduced a decomposition which reduces the periodicity of the classical plane along the Trotter direction to one column while the chequerboard model leads to a two-column-wide period. The advantages of this method shall be discussed in the framework of Quantum TMRG (see sect. 3.4). Here, we want to sketch the basic idea.

In this different approach, again, the partition function

$$Z = \lim_{M \to \infty} \mathrm{tr} \left\{ [T_1(\epsilon) T_2(\epsilon)]^{M/2} \right\} \quad \text{with} \quad T_{1,2}(\epsilon) = T_{\mathrm{R,L}} \mathrm{e}^{-\epsilon H + \mathcal{O}(\epsilon^2)} \tag{3.12}$$

is composed of a trace over a field of two distinct transfer matrices $T_{1,2}$ propagating along the Trotter direction. In contrast to (3.5) the chain Hamiltonian is no longer split into mutually commuting parts $H_{\mathrm{odd,even}}$ but the rows are now build up of infinitesimal evolution operators of the whole Hamiltonian adopting left and right shift operators $T_{\mathrm{R,L}}$. Note that because of translational invariance, $[T_{\mathrm{R,L}}, H] = 0$. Graphically (see Fig. 3.3), the decomposition is represented as rows of alternately rotated local transfer matrices τ. It can be shown that as in the chequerboard decomposition the corrections to the approximated partitions functions and free energies are no larger than $\mathcal{O}(\epsilon^2)$ [88].

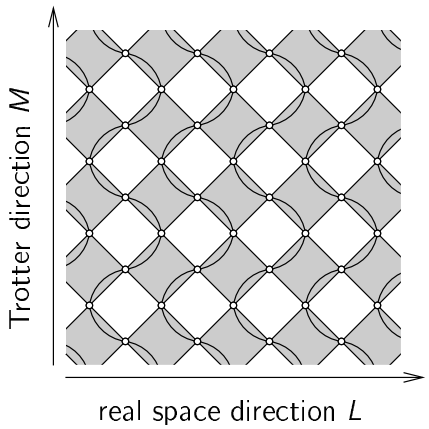

Figure 3.3: Graphical representation of the alternative Trotter decomposition (3.12).

3.2 Transfer-matrix approach

The two-dimensional lattice emerging from the Trotter-Suzuki decomposition of quantum chains consists of equal rows and columns with width of three sites in real space or Trotter direction, respectively. Consider again the partition function of the chequerboard decomposition (3.8) which we repeat for convenience

$$Z = \sum_{\substack{\{s_\mu^\nu\} \\ \nu=1\ldots L, \\ \mu=1\ldots 2M}} \prod_{k=1}^{M} \prod_{i=1}^{L/2} \tau_{2k-1,2k}^{2i-1,2i} \tau_{2k,2k+1}^{2i,2i+1}. \tag{3.13}$$

We obtained this two-dimensional model when we extended the density operator $e^{-\beta H}$ into the imaginary-time direction. The other way round, we can split the system into slices of imaginary-time for two fixed neighboring spins. A product of these vertical transfer matrices will make up the system. We, thus, combine one column of local transfer matrices into a $n^{2M} \times n^{2M}$-matrix

$$\mathcal{T}(s_{(\mu=1..2M)}^{2i-1}, s_{(\mu=1..2M)}^{2i+1}) := \sum_{\substack{\{s_\mu^{2i}\} \\ \mu=1\ldots 2M}} \prod_{k=1}^{M} \tau_{2k-1,2k}^{2i-1,2i} \tau_{2k,2k+1}^{2i,2i+1} \tag{3.14}$$

which we call vertical transfer matrix. Is is depicted in Fig. 3.4. This could as well be done with a row of transfer matrices, but this would lead us back to (3.5) and, finally, to finding

the spectrum of H.[2] With vertical transfer matrices, Eq. (3.8) becomes

$$Z = \sum_{\substack{\{s_\mu^{2\nu-1}\} \\ \nu=1\ldots L/2, \\ \mu=1\ldots 2M}} \prod_{i=1}^{L/2} \mathcal{T}(s^{2i-1}_{(\mu=1..2M)}, s^{2i+1}_{(\mu=1..2M)}) = \mathrm{tr}\, \mathcal{T}^{\frac{L}{2}} \tag{3.15}$$

a product of matrices [79]. The latter equality holds because in a translationally invariant chain the real space index of the vertical transfer matrix $\mathcal{T}$ can be omitted.

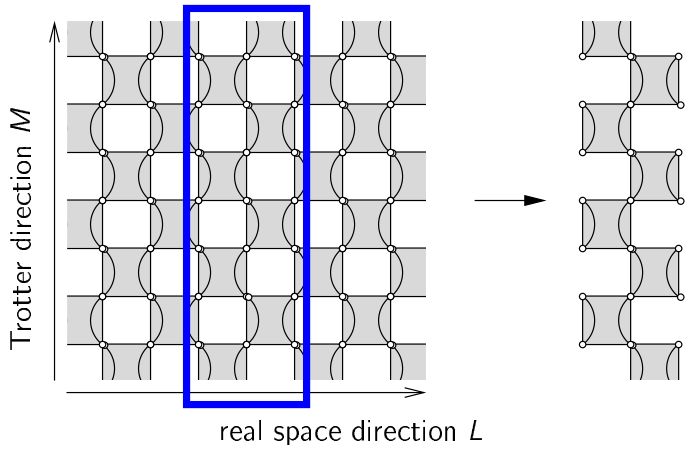

Figure 3.4: Graphical representation of the vertical transfer matrix (3.14). Periodic boundary conditions in the Trotter direction are assumed (not depicted here).

Unfortunately, except for models with an expecially well-condition structure, the infinite-sized vertical transfer-matrix $\mathcal{T}$ from (3.14) cannot be calculated analytically. An important simplification, however, in the calculation of physically relevant quantities such as free energy density or thermodynamical expectation values lies in the fact that they depend only on the largest eigenvalues of the transfer matrix $\mathcal{T}$.

With the complete set of eigenvalues λ_i and eigenvectors $|\Psi_i\rangle$ of $\mathcal{T}$ and Eq. (3.15), we find that the free energy density at temperature T

$$f = -\lim_{L\to\infty} \frac{1}{\beta L} \ln Z = -\lim_{L\to\infty} \frac{1}{\beta L} \ln \left(\sum_l \lambda_l^{L/2} \right) = -\frac{\ln \lambda_{\max}}{2\beta} \tag{3.16}$$

as fundamental thermodynamic quantity is determined by only the largest eigenvalue $\lambda_{\max}$ of $\mathcal{T}$ in the thermodynamic limit. In Section 3.2.1, we provide arguments that $\lambda_{\max}$ is always unique.

[2] Both choices, though, lead in their limits to the same result. So, Trotter and thermodynamic limit can be exchanged [82].

The calculation of the expectation value of a local operator $\mathcal{O}$ requires the definition of a modified transfer matrix

$$\mathcal{T}_{\mathcal{O}}(s^{2i-1}_{(\mu=1..2M)}, s^{2i+1}_{(\mu=1..2M)}) := \tilde{\tau}^{2i-1,2i}_{1,2}\tau^{2i,2i+1}_{2,3} \sum_{\substack{\{s^{2i}_{\mu}\}\\ \mu=1\ldots 2M}} \prod_{k=2}^{M} \tau^{2i-1,2i}_{2k-1,2k}\tau^{2i,2i+1}_{2k,2k+1} \tag{3.17}$$

with the local modified transfer matrix $\tilde{\tau}^{2i-1,2i}_{1,2}$ from Eq. (3.10) for arbitrary sites $2i-1$ and i. This leads to an expectation value

$$\begin{aligned}\langle \mathcal{O}_l \rangle &= \frac{Z(\mathcal{O}_l)}{Z} = \lim_{L\to\infty} \frac{\operatorname{tr} \mathcal{T}^{(L/2-1)}\mathcal{T}_{\mathcal{O}}}{\operatorname{tr} \mathcal{T}^{L/2}} \\ &= \lim_{L\to\infty} \underbrace{\sum_i \frac{\lambda_i^{M-1}}{\sum_{i'} \lambda_{i'}^{M}}}_{\neq 0,\ \text{only if } \lambda_i=\lambda_{\max}} \langle \Psi_i | \mathcal{T}_{\mathcal{O}} | \Psi_i \rangle = \frac{\langle \Psi_{\max} | \mathcal{T}_{\mathcal{O}} | \Psi_{\max} \rangle}{\lambda_{\max}}\end{aligned} \tag{3.18}$$

involving again only the largest eigenvalue and eigenvector.

3.2.1 Spectrum of the quantum transfer matrix

An analysis of the transfer-matrix spectrum can give an argument why the largest eigenvalue is non-degenerate.

For the limiting case $T \to \infty$, the local transfer-matrix of the Trotter decomposition (3.7) reduces to

$$\tau^{i,i+1}_{k,k+1} := \langle s^i_k s^{i+1}_k | e^{-\epsilon h_{i,i+1}} | s^i_{k+1} s^{i+1}_{k+1} \rangle = \delta_{s^i_k, s^i_{k+1}} \delta_{s^{i+1}_k, s^{i+1}_{k+1}} \tag{3.19}$$

which means that the initial spin configuration will not be changed by the transfer-matrix. This simple form can be made plausible if we remember that each state of the Hilbert space of the system has the same Boltzmann weight in the $T \to \infty$ limit because it has an equal energy. From this, it is easy to prove that the the largest eigenvalue of $\mathcal{T}$ is given by $\lambda_1 = n^2$, with the number of local states n, and all other eigenvalues are zero.

The gap between the leading and next-leading eigenvalues of the the transfer matrix becomes smaller with decreasing temperature. However, we expect that the gap vanishes only at zero temperature because a vanishing gap indicates a diverging correlation length [89], i.e., a critical point or a certain kind of long range order. They are expected to be present in a one-dimensional quantum system only at zero temperature. This has been proven by Mermin and Wagner [90] for ferro- or antiferromagnetic order in 1D Heisenberg models. Although a rigorous statement has not been formulated yet, the absence of phase transitions at finite temperature is believed to be correct for all one-dimensional equilibrium systems [91, 92]. Therefore the free energy at non-zero temperature with fixed Trotter number M is determined solely by the largest eigenvalue of the transfer matrix in the thermodynamic limit.

3.3 Density Matrix Renormalization Group (DMRG)

The numerical algorithms in this work base on the density matrix renormalization group (DMRG) introduced by White [93, 94]. We will briefly review the concepts of DMRG in this section.

The DMRG was originally developed to compute the ground state and low-energy spectrum of a quantum system with short-range interactions. It allows to treat large systems at high precision and does not suffer from the negative sign problem which makes quantum Monte-Carlo methods of limited use for frustrated or fermionic systems.

In the DMRG, we consider large-sized systems by iteratively building them up from smaller systems. At each iteration step, irrelevant states are projected out to keep the space of states at a fixed size.

3.3.1 Density-matrix projection

The key idea behind DMRG is the density-matrix projection which gives the prescription how to truncate the Hilbert space

We consider a large system, commonly named superblock, composed of two interacting subsystems, the system block and the environment block. An arbitrary state $|\psi\rangle$ of the superblock can be represented in a basis formed by tensor product of basis states from the system and the environment block

$$|\psi\rangle = \sum_{i=1}^{N_{\mathrm{SB}}} \sum_{j=1}^{N_{\mathrm{EB}}} \psi_{i,j} |\alpha_i\rangle_{\mathrm{SB}} |\beta_j\rangle_{\mathrm{EB}} \tag{3.20}$$

where $\{|\alpha_i\rangle\}$ is the basis of the system block with size N_{SB} and $\{|\beta_i\rangle\}$ is the basis of the environment block with size N_{EB}. The aim is to find a minimal set of new basis states for the system block that reproduce the given state of the superblock optimally. Then, we can truncate the basis of the system block without changing the state (and the properties) of the superblock. Generally, the superblock state cannot be written as a simple product of one system and one environment state. A fact which is referred to as entanglement, a concept which has become an active field of research within the past few years in the context of quantum information theory [95, 96, 97, 98, 99].

The density-matrix projection provides a new basis for the system block that represents the superblock state and is optimal in the above meaning by density-matrix diagonalization. The reduced density matrix of the system block

$$\langle \alpha_i' | \rho | \alpha_i \rangle = \sum_{j=1}^{N_{\mathrm{EB}}} \psi_{i,j}^* \psi_{i',j} \tag{3.21}$$

contains all information about the entanglement between system and environment block [99, 95]. The relevant states of the system block are then given by those eigenvectors of

the reduced density matrix which have the largest eigenvalues. The number $N_{\mathrm{SB}'} < N_{\mathrm{SB}}$ of these eigenvectors which have the largest eigenvalues make up the new basis of the system block.

This truncation prescription has been derived by three argumentation lines: 1. The statistical physics approach which concentrates on the expectation value of operators [100]. 2. The quantum mechanics approach which aims at the error minimization of an approximative wavefunction [93, 94]. 3. The quantum information approach [101, 95, 99, 97, 98, 96] which shows that the density-matrix projection preserves a maximum of system-environment entanglement.

3.3.2 Algorithm

The iteration procedure may vary depending on the system and its properties we are interested in. In this chapter, we present the iteration procedure describing the original $T = 0$ DMRG introduced by White [93]. In Section 3.4 and Chapter 4, the appropriate algorithms will be given for some DMRG variants. It useful to start with a sketch of infinite size algorithm (The notation follows [102].):

i. We start from a lattice of small size ℓ. The system block S of Hilbert space size m^S consists of a basis $\{|m_\ell^S\rangle\}$, the Hamiltonian $\hat{H}_\ell^S$ and operators known in this basis. At initialization, this is maybe still an exact basis of the block ($N_{\mathrm{site}}^\ell \leq m^S$)

ii. The new system block S' is built from S and one additional site. Its Hilbert space has a size $N^S = m^S N_{\mathrm{site}}$ and its basis consists of product states $\{|m_\ell^S \sigma\rangle\} \equiv \{|m_\ell^S\rangle|\sigma\rangle\}$. The Hamiltonian $\hat{H}_{\ell+1}^S$ on S' can be expressed in this basis, but this is usually not done explicitely in order to save storage.

iii. We form the superblock of length $2\ell+2$ from system S' and environment which is S' reflected, if symmetries allow. The Hilbert space has a size $(N^S)^2$. The superblock Hamiltonian $\hat{H}_{2\ell+2}$ could be constructed explicitely.

iv. The ground state $|\Psi\rangle$ of $\hat{H}_{2\ell+2}$ is determined by large sparse matrix diagonalization. This is by far the most time consuming part!

v. The desired ground state properties (energies and correlators) from $|\Psi\rangle$ are calculated. This step might be left out at some intermediate lengths.

vi. The reduced density matrix is constructed $\hat{\rho} = \mathrm{tr}_E |\Psi\rangle\langle\Psi|$ and the eigenbasis $|w_\alpha\rangle$ ordered by descending eigenvalues w_α calculated. The new basis for S' is formed by taking the m^S eigenstates with largest weights. We build a $N^S \times m^S$ rectangular matrix T with elements $\langle m_\ell^S \sigma | m_{\ell+1}^S \rangle$.

vii. We perform the reduced basis transformation $\hat{H}_{\ell+1}^{\mathrm{tr}} = T^\dagger \hat{H}_{\ell+1} T$ onto the new m^S-state basis. We rename $\hat{H}_{\ell+1}^{\mathrm{tr}} \to \hat{H}_{\ell+1}$ and restart with the new block size $\ell+1$ at

step (ii.) until the final length is reached. The operator representations are updated in this step as well.

In Fig. 3.5, we present a schematic plot of the infinite-size algorithm.

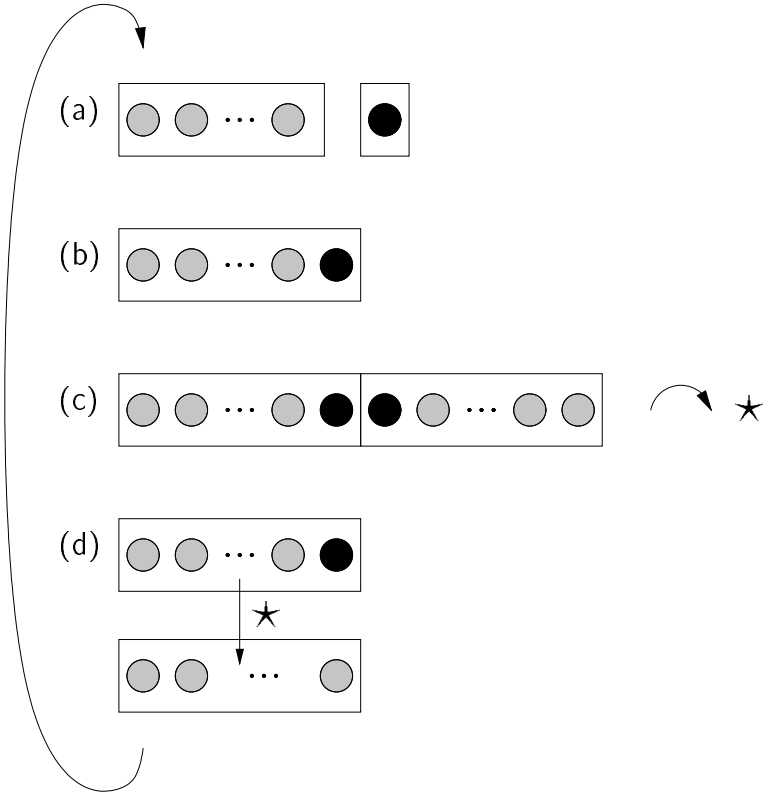

Figure 3.5: Schematic plot of the infinite-size algorithm: From a system block and a single-site block (a), we construct a new system block (b) by simple tensor product. The system block and its mirror image form the superblock (c). The reduced density matrix is formed from its ground state. Finally the system block (d) is projected to the new basis.

The DMRG has been successfully applies to systems of sizes up to $L \sim 1000$. However, it is important to perform an extrapolation first in $m \to \infty$ then in $L \to \infty$.

Finite-size algorithm

The infinite-system algorithm does not give satisfactory results in all cases of interest. Problems arise if the environment in the early growing of the chain does not resemble the system of final length closely enough, for example, if the system is inhomogeneous. Then the states retained in the early stage do not have to be important for the desired final

state. Here the finite-system algorithm helps out. The idea is to optimize the chosen basis for a system of fixed length by shifting the 'free' sites through the system. To do this the system is built to a desired length with the infinite-system algorithm, but in subsequent steps one of the blocks grows at the cost of the other block shrinking. In each step the reduced basis transformation is only performed for the growing block.

The largest eigenvalues of the quantum transfer matrix are targeted by TMRG-calculations. The spectrum of transfer matrices is considered to be well-behaved in the sense that there is a finite gap between the largest and second largest eigenvalue, see Section 3.2.1. This is why the finite-size algorithm is generally not implemented for TMRG studies.

Errors

The errors from the DMRG can be estimated in several ways. Roughly speaking, the eigenvalues of the reduced density matrix measure the importance of the corresponding eigenstates for representing the target state. Therefore, the truncation error which is defined as the sum of all the eigenvalues of the states not kept as basis states is often proportional to the errors of physical quantities calculated within the DMRG. However, there are other sources of error which are not captured in the truncation error which come from the fact that the chain is built up and long-range interaction are cut off. A careful convergence analysis in the number of kept states m usually provides a more reliable estimation of the full error. The DMRG is exact when $m \to \infty$. However, convergence up to tiny errors of, say, 10^{-7} is usually achieved even for moderate values of $m \approx 50 - 300$, at least for ground state properties of one-dimensional systems with local interactions. This is related to the fact that for these states the reduced density matrices can be shown to have an eigenvalue spectrum that is exponentially decaying. Therefore, the truncation error is exponentially suppressed as the number of kept states m is increased. Although it cannot be ruled out that an ill-behaved system may be trapped in a metastable state for intermediate values of m, this phenomenon seems to be exceedingly rare in practice.

In some cases, the errors of different quantities that are calculated during the same DMRG run can significantly differ in size. As an example, the precision in the ground state energy in the Spin-1 Heisenberg model could be calculated to decent precision with very little states. Looking at the ground-state entanglement entropy of the same calculations, one could observe a very strong dependence on the number of states [103].

3.3.3 Further DMRG-applications

Since the introduction of DMRG a large family of DMRG methods evolved to aim at different kinds of model classes. A recent and exhaustive review was given in [102]. Here, we mention only same recent extensions.

A different perspective on the DMRG algorithm was recently provided from quantum information theory. It has been known for some time that the truncated DMRG states always belong to the class matrix product states [104, 105, 106]. In fact, the DMRG can be recast

as a variational method that uses matrix product states as ansatz wave functions, and finds the optimal state among them [104]. This alternative formulation recently opened up a new perspective on extensions of the DMRG that overcome many of its original limitations: For example, the original DMRG was improved drastically with respect to the description of time-dependent systems [107, 108, 109] and of periodic boundary conditions [110]; and efficient algorithms for two-dimensional models and finite temperature seem to be within reach [111, 110].

3.4 Transfer Matrix DMRG

The correspondence of d-dimensional quantum systems and $d+1$-dimensional classical models inspired Nishino to apply a modified DMRG algorithm to two-dimensional classical models. In 1995, he introduced the Transfer Matrix DMRG (TMRG) [112] yielding the computation of the highest eigenvalue of the transfer matrix. Only one year later, Nishino and Okunishi presented a numerical variant of Baxter's Corner Transfer Matrix method [113, 114, 78] based on the DMRG [115] connecting the system's corner transfer matrices to the renormalized density matrix of DMRG. This method will be reviewed in Chapter 4 where it will be extended to quantum systems.

The problem of finding the extreme eigenstates of the one-dimensional transfer matrix strongly resembles the search for the lowest-lying excitations of a chain Hamiltonian as in conventional DMRG. While, however, only the small eigenvalues (low energies) of the Hamiltonian matrix are of special interest in the latter case, we yield for the highest eigenvalues of the transfer matrix in the two-dimensional classical model. Application of the DMRG in order to find the highest eigenvalues of a transfer matrix establishes the Transfer Matrix DMRG or shorter the TMRG. The abbreviation TMRG can also stand for temperature DMRG which aims more at the underlying physical system.

The TMRG for quantum systems combines Trotter-Suzuki decomposition, the transfer-method and DMRG. It has been proposed by Bursill et al.[116] and significantly improved by Wang, Xiang [117] and Shibata [118].

3.4.1 Algorithm

In principle, the TMRG algorithm is nothing else but the application of the DMRG method (see Section 3.3) onto the quantum transfer matrix $\mathcal{T}$. Whereas the DMRG is basically designed for computing the ground state and low excitations, respectively, the TMRG computes the leading part of the spectrum. Even if the basics of the TMRG are closely related to its DMRG predecessor, the rich structure of the transfer-matrices turns the algorithm to be slightly more sophisticated. One of the basic differences to DMRG is the discrimination between odd and even iteration step resulting from the chequerboard decomposition.

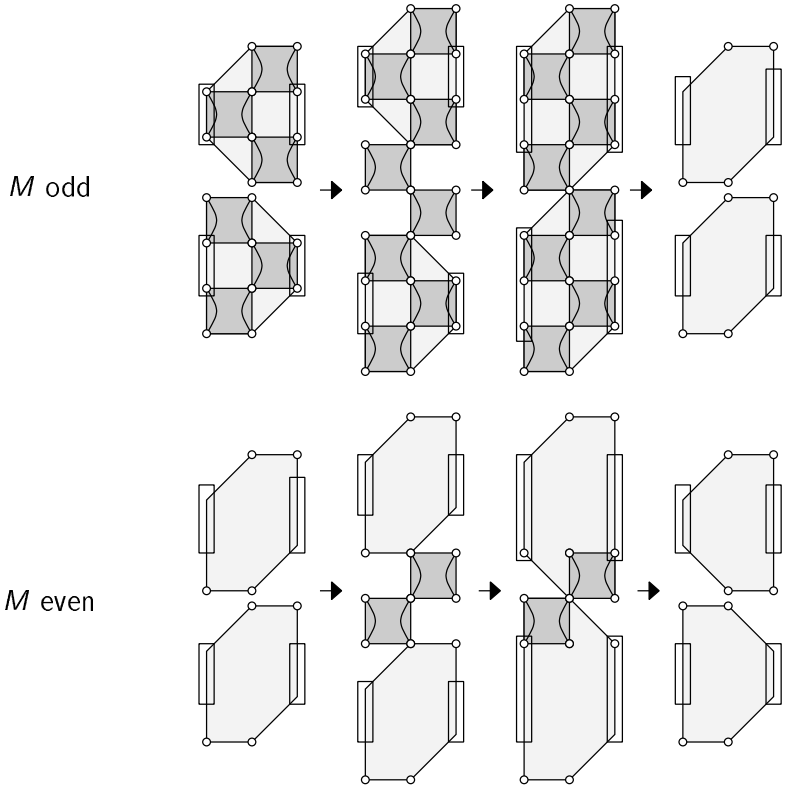

Figure 3.6: Sketch of the TMRG algorithm. The enlargement procedure is illustrated for the two cases of M odd and M even. In each iteration step the system and environment block are increased by one plaquette and reduced to a fixed size by density matrix projection. Within this procedure the shape of the block tensors changes from step to step. Further illustration can be found in [119].

We start by constructing the system block

$$S = \begin{cases} (\tau_{1,2}\tau_{3,4}\cdots\tau_{M,M+1})(\tau_{2,3}\tau_{4,5}\cdots\tau_{M-1,M}) & \text{if } M \text{ odd} \\ (\tau_{1,2}\tau_{3,4}\cdots\tau_{M-1,M})(\tau_{2,3}\tau_{4,5}\cdots\tau_{M,M+1}) & \text{if } M \text{ even} \end{cases} \tag{3.22}$$

and the environment block

$$E = \begin{cases} (\tau_{M+2,M+3}\cdots\tau_{2M-1,2M})(\tau_{M+1,M+2}\cdots\tau_{2M,1}) & \text{if } M \text{ odd} \\ (\tau_{M+1,M+2}\cdots\tau_{2M-1,2M})(\tau_{M+2,M+3}\cdots\tau_{2M,1}) & \text{if } M \text{ even} \end{cases} \tag{3.23}$$

from the local transfer matrices. Both blocks are tensors which can be written in a basis representation

$$\left(S^{s_1' n_S' s_2'}_{s_1 n_S s_2}\right) \quad \text{and} \quad \left(E^{s_1' n_E' s_2'}_{s_1 n_E s_2}\right) \tag{3.24}$$

where the s-indices label spin sites and the n-indices join $M-1$ spins to a block spin. Thus, the dimension of S and E is $n^4\tilde{m}^2$ with $\tilde{m} = n^{2(M-1)}$. In this notation, n is the number of states of a single site.

i. The transfer matrix $\mathcal{T}$ can now be assembled by

$$\mathcal{T}_M{}^{s_1' n_S' s_2' n_E'}_{s_1 n_S s_2 n_E} = \begin{cases} S^{\tilde{s}_1 n_S' \tilde{s}_2}_{s_1 n_S s_2} \cdot E^{s_2' n_E' s_1'}_{\tilde{s}_2 n_E \tilde{s}_1} & \text{if } M \text{ odd} \\ S^{\tilde{s}_1 n_S' \tilde{s}_2}_{s_1 n_S s_2} \cdot E^{\tilde{s}_2 n_E' s_1'}_{\tilde{s}_2 n_E \tilde{s}_1} & \text{if } M \text{ even} \end{cases} \tag{3.25}$$

where we used the convention that equal upper and lower indices are summed out. The dimension of $\mathcal{T}_M$ is then given by $n^4 \cdot \tilde{m}^4$. To save computer storage, the environment has not to stored explicitely if the system is translationally invariant.

Now, the leading left and right eigenvectors

$$\left|\Lambda_0^{L/R}\right\rangle = \left(\Lambda^{L/R}_{s_1 n_S s_2 n_E}\right) \tag{3.26}$$

of the quantum transfer matrix $\mathcal{T}_M$ are computed. With these results, we can calculate the required thermodynamic properties. For the calculation of local expectation values, we have to multiply the operator to the system block and build the modified quantum transfer matrix. If correlation lengths are of interest, not only the leading, but also the next leading eigenvalues have to be computed.

ii. We use the right and left eigenstates to construct the reduced density matrix

$$\rho^{\tilde{n}_S'}_{\tilde{n}_S} = \sum_{s_1' n_S' s_2 n_E} \Lambda^R_{s_1' n_S' s_2 n_E} \Lambda^L_{s_1 n_S s_2 n_E} \tag{3.27}$$

where $\tilde{n}_S = n_S \otimes s$ and $\tilde{n}_S' = n_S' \otimes s'$. The reduced transfer matrix ρ has the dimension $n^2 \cdot \tilde{m}^2$. Note, that in contrast to the standard DMRG algorithm, the density matrix is not symmetric.

iii. Diagonalize ρ. Use the m leading eigenvectors of the spectrum to construct left and right projectors V and U, respectively. The variable $m < \tilde{m} \cdot n$ labels the number of retained states of the DMRG algorithms. The leading right eigenvectors of ρ appear as columns of U and the left eigenvectors make up the rows of V. U and V have the dimension $m \cdot \tilde{m} \cdot n$.

iv. This system is enlarged by one local transfer matrix:

$$\tilde{S}^{s_1' \tilde{n}_S' s_2'}_{s_1 \tilde{n}_S s_2} = \begin{cases} S^{s_1' n_S' \tilde{s}}_{s_1 n_S s} \, \tau^{s' s_2'}_{\tilde{s} s_2} & \text{if } M \text{ odd} \\ S^{s_1' n_S' s'}_{s_1 n_S \tilde{s}} \, \tau^{s' s_2'}_{\tilde{s} s_2} & \text{if } M \text{ even} \end{cases} \tag{3.28}$$

The tensor $\tilde{S}$ has large dimension $n^6 \cdot \tilde{m}^2$. The projectors U and V are used to truncate $\tilde{S}$:

$$S^{s_1' n_S s_2'}_{s_1 n_S' s_2} = U^{n_S'}_{\tilde{n}_S'} \cdot \tilde{S}^{s_1' \tilde{n}_S' s_2'}_{s_1 \tilde{n}_S s_2} \cdot V^{\tilde{n}_S}_{n_S} \tag{3.29}$$

With this, the dimension of S is reduced to $n^4 \cdot m^2$.

v. We replace $\tilde{m}$ by m and restarted the iteration at step ii.

The presentation of the algorithm follows closing the corresponding section in [119] where illustrative additional pictorial representations were provided. For further details on the method, see the detailed review of Shibata[120].

3.5 Technical annotations

In the framework of this thesis, a new TMRG implementation was developed. The code was written in the programming language C++ and the underlying mathematical objects were implemented in classes. Thus, different levels of hierarchy can be screened from one another and protected against undesired access. This allows clear and complex programming at the same time. The enlargement of the system block can be expressed as a function of two objects without dealing with confusing indices on a higher level. On a lower level, all routines which the main running time is spent on, have been optimized. The most time-consuming part in TMRG programs are matrix-multiplications. These routines have been implemented from some refined high-performance libraries (Sun Performance Library, ARPACK) to save system resources. The maximal number of preserved states m could be increased from $m \approx 120$ of an older TMRG program to $m \approx 300$ which made our study of frustrated systems feasible.

The program code was developed and tested on the institute's local computer network, mainly on a Sun, UltraSPARC-II, 502MHz, 512 MB. The final calculations have been carried out on a compute server, Sun Fire 15K containing 72 processors of type UltraSPARC-III with a clock speed of 900 MHz and 144 Giga-Byte RAM. On both systems the code was compiled by the Sun WorkShop 6 update 2 C++ compiler.

4 Quantum CTMRG

The Quantum Corner Transfer Matrix DMRG (QCTMRG) for the calculation of thermodynamic properties of finite one-dimensional quantum systems will be introduced in this chapter. This new method is based on Nishino's Corner Transfer Matrix DMRG (CTMRG) for classical systems. In the CTMRG method calculating the partition sum and obtaining the reduced density is one step and does not involve finding eigenvectors of large matrices. Thus, CTMRG performs drastically better than the TMRG method for classical systems. Can we benefit from the ideas of the CTMRG in the quantum case?

We implemented the QCTMRG method within the framework of this PhD-thesis. The algorithm and its essential features are presented in this chapter. We close with first results and a discussion of the method's performance.

4.1 Corner TMRG for classical models

An improved algorithm for two-dimensional classical models was introduced by Nishino and Okunishi [115] using the idea of DMRG for a numerical algorithm in terms of Baxter's Corner Transfer matrix method [113, 114, 78]. We shall briefly sketch the outline of the algorithm. A nice introduction can be found in original works [115, 121] and in the framework of a general DMRG review [102]. For our extension of the CTMRG, similar iteration steps will be presented in more detail in Section 4.2.

Figure 4.1: Representation of a four-spin plaquette W. The symmetries of the cartoon represent the isotropic interaction of the interaction-round-a-face (IRF) model studied by Nishino [115, 121].

Consider again a two-dimensional system of $L \times L$ sites connected through classical nearest-neighbor interactions. Now the two-dimensional lattice can be split into four quadrants $C_{1,2,3,4}$, each of size $L/2 \times L/2$. Under the assumption of open boundary conditions each quadrant can be interpreted as corner transfer matrix of size $n^{L/2} \times n^{L/2}$ with two open edges and two edges which are summed out. For simplicity we assume that symmetries are such that each corner transfer matrix can be described by the same symmetric matrix $C(a, b)$. This is, indeed, not an unusual feature and allows us to identify the matrix C with its transpose. Now the partition function of the two-dimensional system takes the form

$$Z = \operatorname{tr} C^4 = \lambda_1^4 + \lambda_2^4 + \dots \tag{4.1}$$

which is the sum over the fourth power of the eigenvalues of the corner transfer matrix $\lambda_1, \lambda_2, \dots$.

A systematic enlargement of an exactly solvable small initial system is required to obtain the infinite size properties of the two-dimensional system. For a renormalization procedure

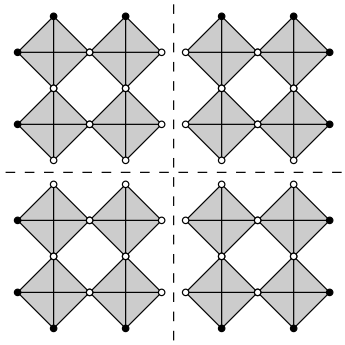

Figure 4.2: Decomposition of a 4×4 system into four corner transfer matrices. A square-shaped classical system with 40 sites emerging from the bond variables of the IRF model is divided into four equally sized sub-squares. Each sub-square has two open edges which will be summed out in the partition function. The remaining two free edges are left as degrees of freedom. Thus, each sub-square can mathematically be represented by a matrix.

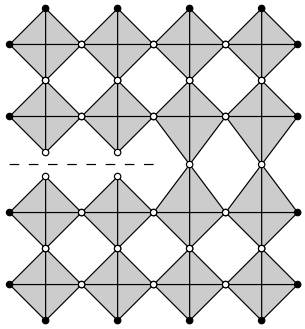

Figure 4.3: Reduced density matrix formed by four corner transfer matrices corresponds to a cut of the system.

in the sense of DMRG consider the quantity

$$\rho_{i,j} = \frac{1}{Z} \sum_{i,j} C(i,a)C(a,b)C(b,c)C(c,j), \tag{4.2}$$

which meets the requirements of a density matrix as can be checked easily. In a picture introduced by Nishino [115, 121] one can imagine $\rho_{i,j}$ as a "cut" of the the system, see Fig. 4.3. The density matrix $\rho_{i,j}$ can be considered as a reduced density matrix since it covers only half of the systems length while the other half is traced out. Note that we have obtained a reduced density matrix without finding eigenvalues of some large sparse matrix like in conventional DMRG.

Yet, complete diagonalization of the corner transfer matrix $C = \sum_j \lambda_j |v_j\rangle\langle v_j|$ is still needed, but this step has to be done in TMRG as well. It uses considerably less resources than

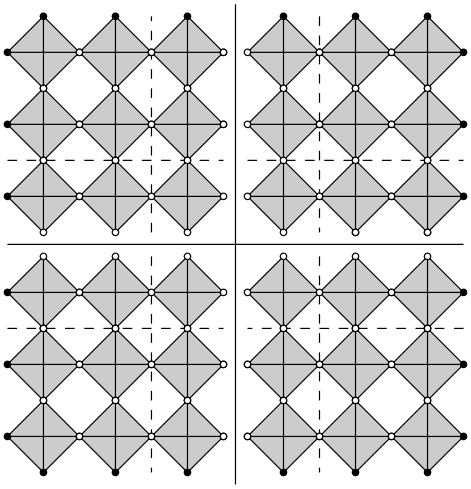

Figure 4.4: Enlargement of the corner transfer matrices.

finding eigenvalues of the vertical transfer matrix from TMRG. The diagonalized corner transfer matrix gives the diagonalized form of the reduced density matrix:

$$\rho_{i,j} = \frac{1}{Z} \sum_j \lambda_j^4 |v_j\rangle\langle v_j| \tag{4.3}$$

Like in the DMRG method, we can adopt the eigenvectors belonging to a certain number of m highest eigenvalues in order to find a truncated form

$$\tilde{C} = \sum_{j=1}^{m} \lambda_j |v_j\rangle\langle v_j|, \quad \lambda_1 > \lambda_2 > \dots \tag{4.4}$$

of the corner transfer matrix. With the help of the small four-spin plaquette W and a half-row transfer matrix P, we enlarge the truncated corner transfer matrix (Fig. 4.4). Iteratively we continue by diagonalization of the enlarged corner matrix.

The CTMRG has been applied to Ising models with spin-1/2 [121] and spin-3/2[122]. A vertex model with 7 vertex configurations [123] and self-avoiding walk models in two dimensions [124, 125] have been considered.

In [126], a powerful variant of the CTMRG has been introduced for one-dimensional stochastic system like the diffusion-annihilation process or the branch-fusion process. Here the decomposition includes a real space and real time direction. The light-cone TMRG (LCTMRG) is a modification of the corner-transfer-matrix DMRG, adjusted by an additional causality argument. The conservation of probabilities which is an essential feature of real-time stochastic systems leads to a triangle-shaped Trotter decomposition. This "light cone" leads to a significant reduction of resources. The causality argument used by the LCTMRG method is not applicable for quantum systems since the Trotter-Suzuki decomposition works with the imaginary time direction.

4.2 CTMRG for quantum systems

The application of the CTMRG-algorithm on the two-dimensional system emerging from the Trotter-Suzuki decomposition of a quantum chain (figs. 3.2 and 3.3) leads to the idea of a Corner Transfer Matrix DMRG for one-dimensional quantum models (QCTMRG). In contrast to the generically classical models treated with CTMRG so far, two substantial differences arise in dealing with a Trotter decomposition:

- A significant anisotropy evolving from existence of a well-distinguished real space and a Trotter direction.
- Calculation of the trace in order to obtain the partition function demands periodic boundary conditions in the two-dimensional plane.

Both aspects will be considered in our implementation.

We consider a two-dimensional rectangular lattice decomposed by a Trotter decomposition. Starting with an initial system small enough to be treated analytically, our aim is to iteratively expand this system in both directions to large enough sizes.

Periodic boundary conditions correspond to the trace in the calculation of the partition function. They are physically essential in Trotter direction. We are, however, free to choose open boundary conditions in real space direction. This choice significantly reduces computational effort because the tensor-dimensionality of the corner tiles is now three rather than four in the case of real-space periodic boundary conditions. Thus, free sites at both real space edges will be integrated out, whereas the edge states regarding Trotter direction are left as degrees of freedom in order to permit periodical closing.

4.3 Renormalization algorithm

At an arbitrary renormalization step, we consider a lattice of fixed size in both directions divided into four parts as in the corner transfer matrix method (see Fig. 4.5). Assuming free edges in Trotter direction, we no longer deal with two-dimensional matrices as in conventional CTMRG, but with three-dimensional tensors. So the pieces of the system are third and fourth order tensors and, thus, shall rather be called tiles than–somewhat misleadingly–matrices in this context. Here, a composition of left resp. right corner tiles C_L, C_R makes up the whole system.

Now we introduce some additional tiles which are required for enlarging the system in the renormalization step (Fig. 4.6). The unit cell of the two-dimensional Trotter decomposition forms the smallest basic tile W with four free edges. Arising from the spatial symmetries, three more tiles play the role of the row-to-row transfer matrix of CTMRG. Here, we have for both left and right side the row-to-row tiles P_L and P_R and a single column-to-column tile P_V, which are tensors of third resp. fourth order[1].

[1] Depending of the symmetries of the spin chain and the Trotter decomposition, C_L and C_R as well as P_L

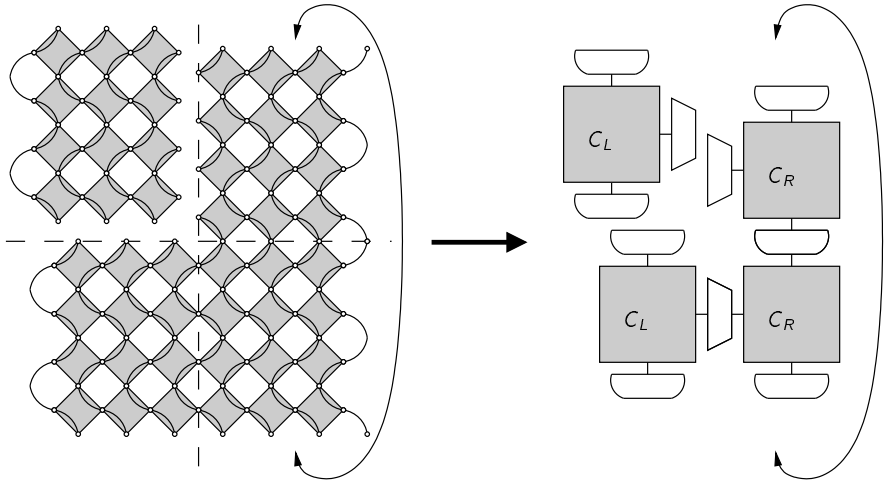

Figure 4.5: Trotter decomposition segmented into four corner tiles. The periodical boundary conditions are illustrated by the double-headed arrow. The corner tiles C_L, C_R have been depicted by special symbols reflecting the underlying symmetry. We adopted the quantum-classical decomposition introduced by Sirker [see (3.12)] in our approach.

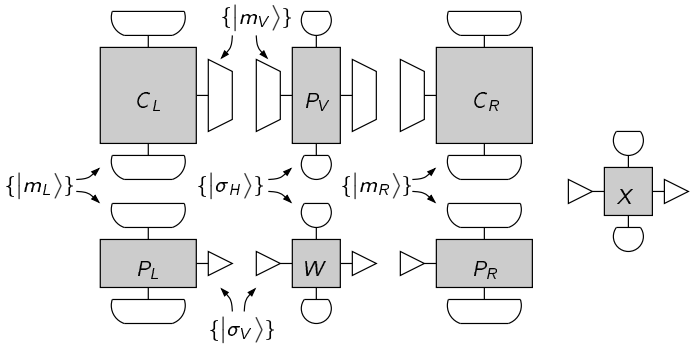

Figure 4.6: Graphical representation of left and right corner tiles C_L, C_R, row-to-row tiles P_L, P_R, column-to-column tile P_V and basic tile W. An additional tile X is used for the measurement of expectation values.

Together with these tiles, we have to keep account of the different bases associated with their edges. The basic tile W demands a vertical basis $\{|\sigma_V\rangle\}$ at the left and right edge and a horizontal basis $\{|\sigma_H\rangle\}$ at the upper and lower edge, both consisting of one- or two-site states depending on the size of the unit cell of the Trotter decomposition. These bases will be unaffected by changes within the renormalization procedure. The edge bases

and P_R can be represented by a single tile in special cases. Here, we assume the general case with no vertical reflection symmetry.

of the corner tiles, however, are iteratively renormalized during the CTMRG-iterations representing states of an increasing spin chain. Still, they are chosen to keep a fixed maximum size. The maximum size of the vertical-edge basis $\{|m_V\rangle\}$ of the corner tiles is m_V. The horizontal edges of the corner tiles are different for the left/right corner tile. Their bases $\{|m_L\rangle\}, \{|m_R\rangle\}$ have a maximum size of m_L resp. m_R. Tiles P_L, P_R and P_V include bases which stay unaltered as well as renormalized bases corresponding to their different edges.

With the concept of the constituting tiles, we sketch the outline of the QCTMRG algorithm:

i. **Construction of initial tiles**
In the special case of the Sirker-like decomposition (see Section 3.1.2), the basic tile W (Fig. 4.7) as well as the column-to-column tile P_V are built by addition of two mutually rotated transfer matrices τ. The left row-to-row tile P_L and the left corner tile C_L arise by summing out the left free sites of W. For the right row-to-row tile P_R and the right corner tile C_R the right free sites of W are bent into the horizontal edges in order to aim a summation with the neighboring site on the lower/upper tile when composing tiles. In Fig. 4.8 the construction of all initial tiles is depicted. These initial tiles demand the construction of the initial bases. The vertical basis of corner and column-to-column tile is $\{|m_V\rangle\} = \{|\sigma_V\rangle\} = \{|\sigma\rangle \otimes |\sigma\rangle\}$, while the horizontal basis of left corner and row-to-row tile is $\{|m_L\rangle\} = \{|\sigma_H\rangle\} = \{|\sigma\rangle\}$, and the horizontal basis of right corner and row-to-row tile is $\{|m_R\rangle\} = \{|\sigma\rangle \otimes |\sigma\rangle\}$ in the first iteration.

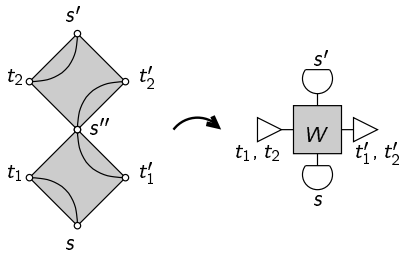

Figure 4.7: Graphical representation of the basic tile W in the Sirker-decomposition. A composition of two transfer matrices can be depicted as a tile with four arms at the edges. The shape of the arms symbolizes the symmetries of the tile and the bases of the underlying tensor operator.

ii. **Calculation of expectation values**

All tiles are combined to form a periodically closed two-dimensional lattice in order to determine the partition function of the system. Summing out the states on the inner edges, we obtain the desired partition function Z of the system. The partition function $Z(O)$ of the modified system with a certain operator O situated in the middle of the lattice (see Fig. 4.9) can be realized similarly. Thus, the thermodynamical expectation value $\langle O \rangle = Z(O)/Z$ of the system can be computed.

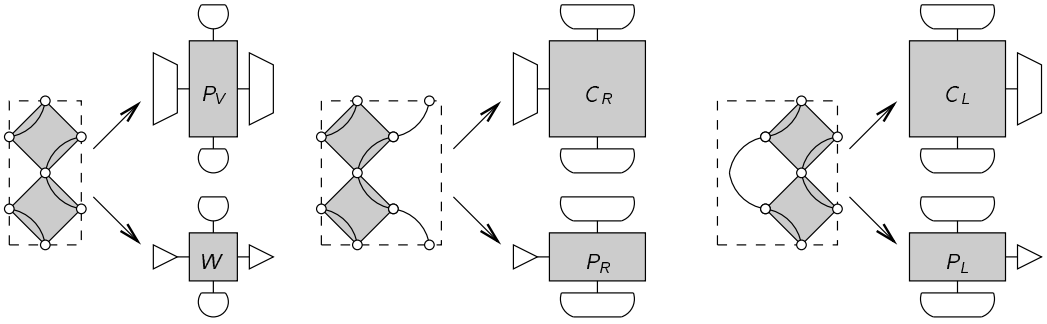

Figure 4.8: Graphical representation of the initial tiles.

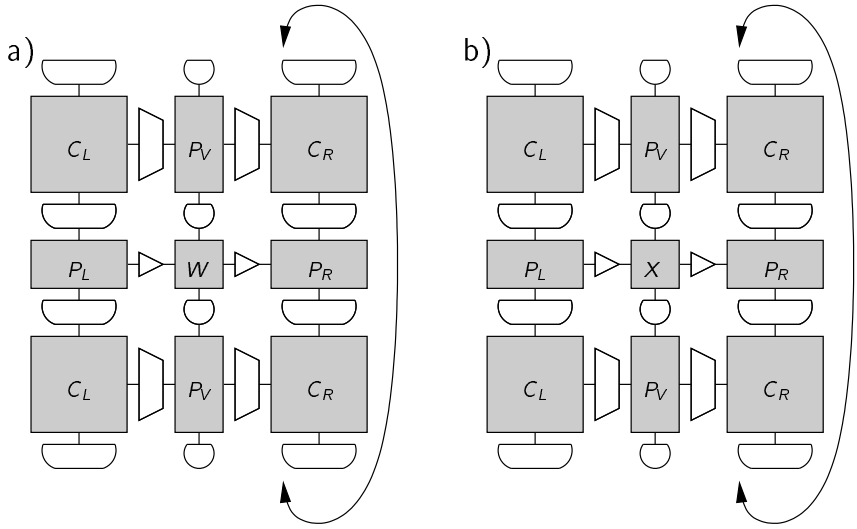

Figure 4.9: (a) Calculation of the partition function Z and (b) of the partition function of the system containing a certain operator $Z(O)$.

iii. **Enlargement of system tiles**

In the next step of the renormalization process, the system is expanded by enlargement of the corner tiles in applying a row-to-row, a column-to-colum tile and the basic tile. Correspondingly, the row-to-row and column-to-column tiles have to be expanded by addition of the basic tile. These enlargement steps, which technically correspond to matrix-multiplication, are illustrated in Fig. 4.10. Enlargement of the tiles implies enlargement of the bases, which is done by simple tensor products $\{|\tilde{m}_V\rangle\} = \{|m_V\rangle \otimes |\sigma_V\rangle\}$, $\{|\tilde{m}_L\rangle\} = \{|m_L\rangle \otimes |\sigma_H\rangle\}$ and $\{|\tilde{m}_R\rangle\} = \{|m_R\rangle \otimes |\sigma_H\rangle\}$. Note that the sizes of the bases grow by a factor of 4 to 16 depending on the underlying spin system, which correspondingly increases the size of the tiles.

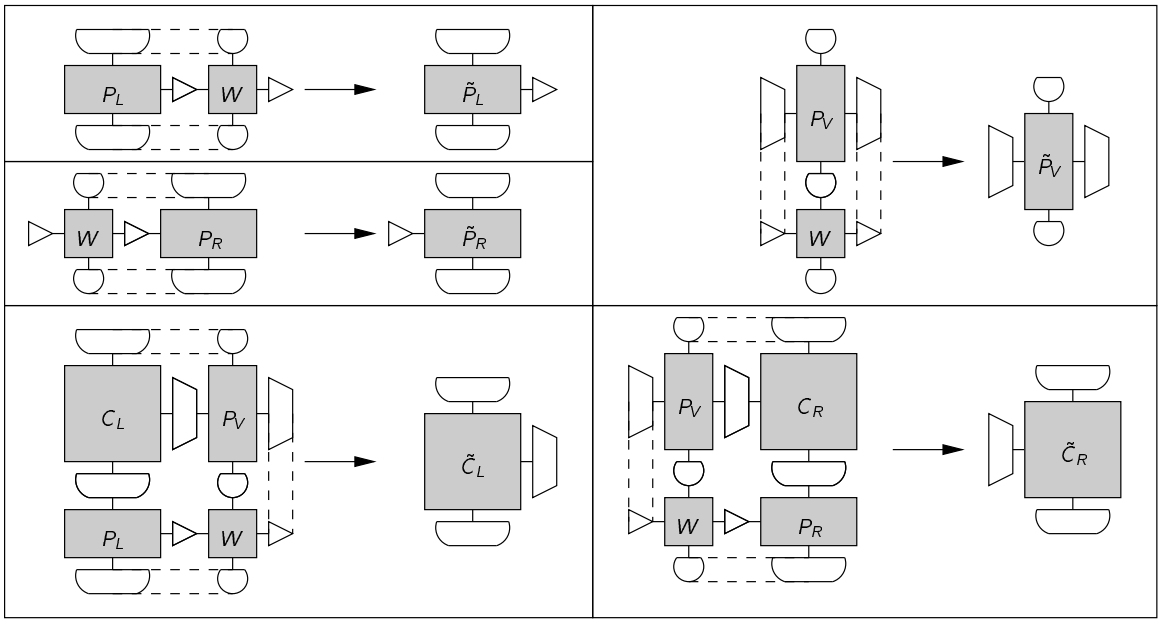

Figure 4.10: Enlargement of system tiles.

iv. **Construction of reduced density matrices**

The crucial step in the DMRG-like renormalization procedure is the construction of the reduced density matrix. In the Trotter decomposed lattice, three density matrices ρ_V, ρ_L and ρ_R are required in order to renormalize the three different types of bases appearing in the system. Aiming at the partition function, we have to put four corner matrices together and to sum out all common edges. The concept of the reduced density matrix, however, is to compose the corner matrices and to sum out all but one edge. The picture of the reduced density matrices then corresponds to cuts of the system (see Fig. 4.11).

v. **Truncation of bases**

The idea behind renormalization group procedures is to iteratively integrate out insignificant degrees of freedom. In the context of DMRG-type algorithms, measuring the contribution of states for calculating the partition function is carried out by diagonalization of the reduced density matrix. Since the partition function is nothing but the trace over the reduced density matrix, eigenstates with large eigenvalues will dominate the sum. Conservation of the bases' sizes demands truncation of the eigenstates with lowest weight. So, we establish a projection onto the m states with largest eigenvalues as renormalization prescription. Since a projection is obtained for each of the three bases, all edges of the system tiles are now reduced to a fixed size keeping only the most relevant states for calculation of the partition function.

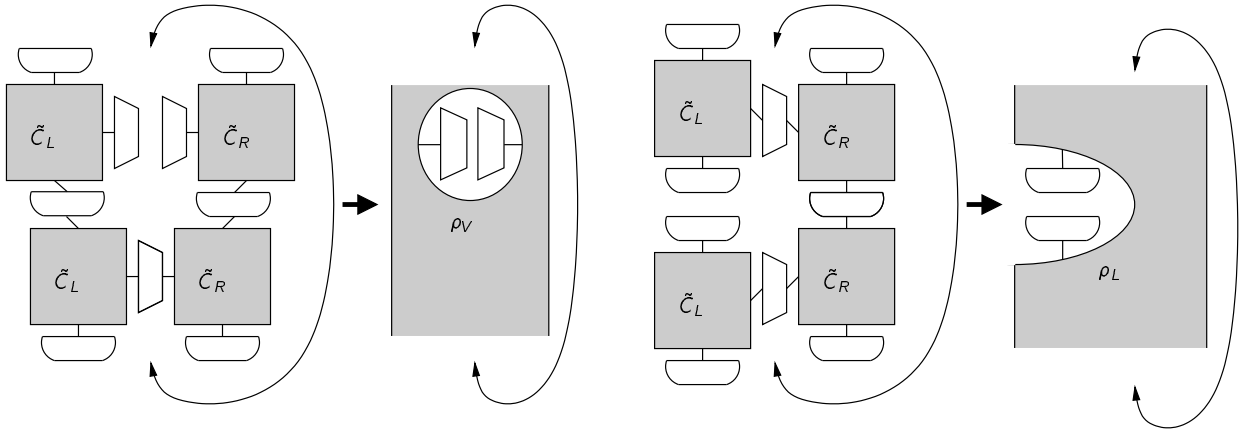

Figure 4.11: QCTMRG cuts.

vi. **Iteration**

Go to step (ii) until desired system size is reached.

4.3.1 Normalization of growing tiles

While our interest lies in the calculation of (local) expectation values of a certain quantum mechanical system, we have to deal with the partition functions of an iteratively increased classical system in the QCTMRG-algorithm. Thus, the partition function is a rapidly growing entity leading to several huge matrix entries in the tiles' numerical representation in each renormalization step. So, the program runs the risk of exceeding the numerical capacity of the variables of the system. To avoid this problem, a constant prefactor is extracted in each renormalization step. For details, see Appendix B.

4.4 Results

We computed the energy and the free energy of the Ising model[127] for a first comparison. The antiferromagnetic Ising chain ($J > 0$) with the classical Hamiltonian

$$H = J \sum_j \sigma_j \sigma_{j+1} \tag{4.5}$$

is exactly solvable by a transfer matrix method [79]. The classical Ising spin σ can take the values $+1, -1$. We first like to review some analytical results obtained by transfer matrix calculations.

In the QCTMRG method, open boundary conditions are preferable. Thus, our analytical

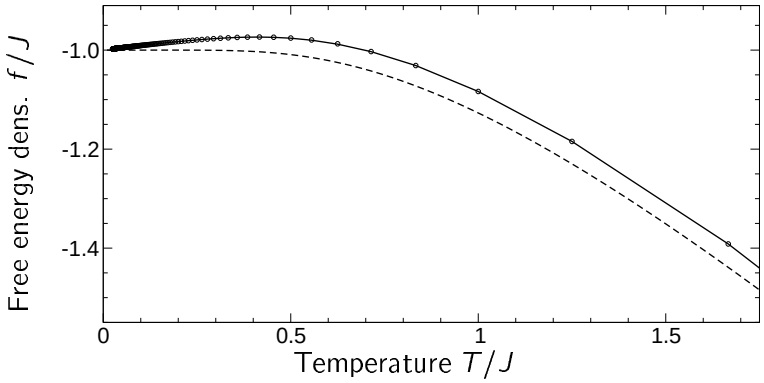

Figure 4.12: Free energy per site vs. temperature for the antiferromagnetic Ising chain of varying chain length. The free energy (circles) from QCTMRG with $m = 32$ and $\epsilon = 0.05$ agrees to high precision with the exact value (4.7)(straight line). Note that the chain length is $L = 10/T$. The free energy of the infinite chain is plotted (dashed line) for comparison.

calculations focus on this case as well. By transfer matrix, we get the partition function

$$Z(L,T) = 2^L \cosh^{L-1}\left(\frac{J}{T}\right) \tag{4.6}$$

for open boundary conditions. This leads to a free energy per site of

$$f(L,T) = -\frac{T}{L}\ln Z = -T\left[\frac{L-1}{L}\cosh\left(\frac{J}{T}\right) + \ln 2\right]. \tag{4.7}$$

The average energy per site

$$e_{\text{avg}}(L,T) = -\frac{1}{L}\frac{T^2\partial}{\partial T}\ln Z = -\frac{L-1}{L}J\tanh\left(\frac{J}{T}\right) \tag{4.8}$$

is calculated with respect to the whole chain. However, apart from the boundaries we get a local energy expectation value

$$\left\langle J\sigma_j\sigma_{j+1}\right\rangle_{(L,T)} = -J\tanh\left(\frac{J}{T}\right) \tag{4.9}$$

for a chain of length L at temperature T which does not show finite size effects.

The thermodynamics of the Ising chain has been computed by the QCTMRG algorithm. We kept $m = 32$ states within the renormalization procedure and chose the inverse factor of temperature T and number of imaginary time steps M to be $\epsilon = (TM)^{-1} = 0.05$. We expect an excellent agreement with the analytical results because the Trotter decomposition becomes exact for the classical Ising model. In Figures 4.12 and 4.13 the numerical results are plotted and, indeed, both data show the expected agreement.

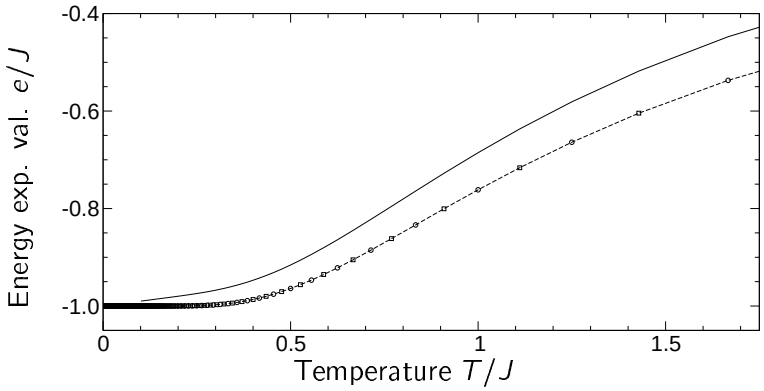

Figure 4.13: Expected local energy in the center of the chain vs. temperature for the antiferromagnetic Ising chain of varying chain length. The local energy expectation value in the center of the chain (circles and squares denote odd and even chain lengths) from QCTMRG with $m = 32$ and $\epsilon = 0.05$ agrees to high precision to the thermal average local energy (4.9) of the infinite chain (dashed line). The average local energy (4.8) for a chain of length L (straight line) differs because of the fluctuating edge spins from open boundary conditions. Note that the chain length is $L = 10/T$.

We face a different situation in considering the antiferromagnetic spin-1/2 Heisenberg model

$$H = J \sum_j \mathbf{S}_j \cdot \mathbf{S}_{j+1} \tag{4.10}$$

on the chain. The model is exactly solvable [128] but quantum fluctuations are no longer suppressed. Thus, the Heisenberg chain can serve as a trial system for the QCTMRG algorithm.

We calculated the free energy and the expectation value of the energy operator in the middle of the chain, see figs. (4.14) and (4.16). The calculations have been done with fixed ratio $\epsilon = 0.05$ while the preserved number of states m from the renormalization was varied from $m = 50$ to $m = 400$.

In Fig. (4.14), the free energy density is plotted against temperature. Note that the chain length is related to temperature by $L = 10/T$. With increasing m the free energy tends to converge. Interestingly, the convergence is faster for lower values of T and correspondingly larger system sizes. We account for that point later in Section 4.5.2. For a comparison, we added the well-converged data for an infinite chain calculated by conventional TMRG. We see the deviation of the QCTMRG data from this curve more pronounced at higher temperatures which are related to smaller system sizes. Thus, we can interpret the deviation as a finite-size effect.

For three points of fixed temperature and chain lengths the free energy density f was extrapolated, see Fig. 4.15. We find f growing with $1/m$ for each point. This results from

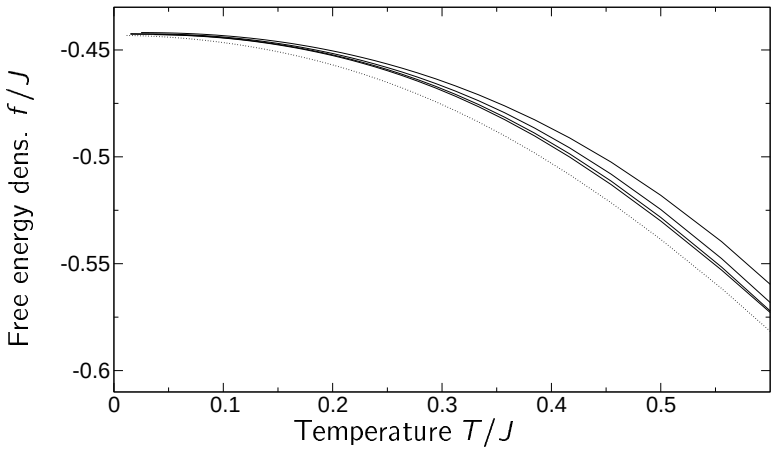

Figure 4.14: Free energy density vs. temperature for the Heisenberg chain of varying chain length. The free energy density is plotted for different QCTMRG calculations (straight lines) with a preserved number of states $m = 50, 100, 200, 400$ (from top to bottom). Note that the chain length is $L = 10/T$. The free energy density (data from TMRG, $m = 200$) of the infinite chain is plotted (dotted) for comparison.

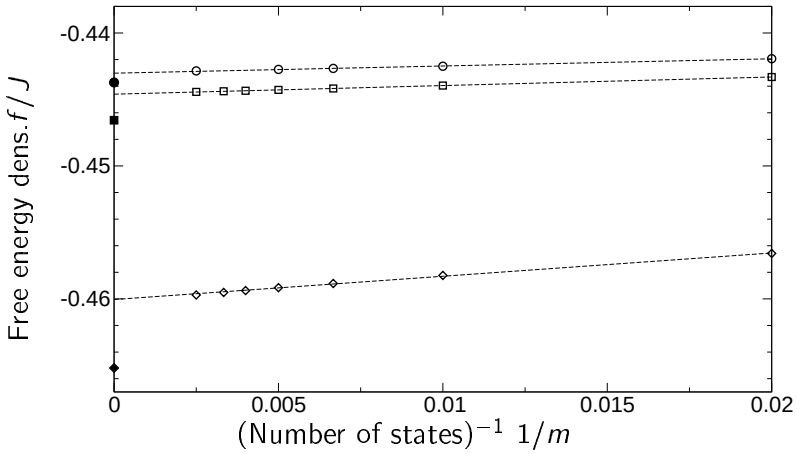

Figure 4.15: Free energy density vs. inverse number of states for the Heisenberg chain of various lengths at various temperatures. The free energy density of chains with $T = 0.25J$ and $L = 40$ (diamonds), $T = 0.1J$ and $L = 100$ (squares), and $T = 0.04J$ and $L = 250$ (circles) has been calculated by QCTMRG (open symbols) with a varying number of states kept during the renormalization. The dashed lines are linear fits. The filled symbols denote the free energy of an infinite system calculated by TMRG.

the fact that the partition sum is underestimated for smaller number of states kept m. This leads to a monotonically increasing free energy for growing $1/m$. As already noticed earlier, the convergence is better for smaller temperature and larger system sizes.

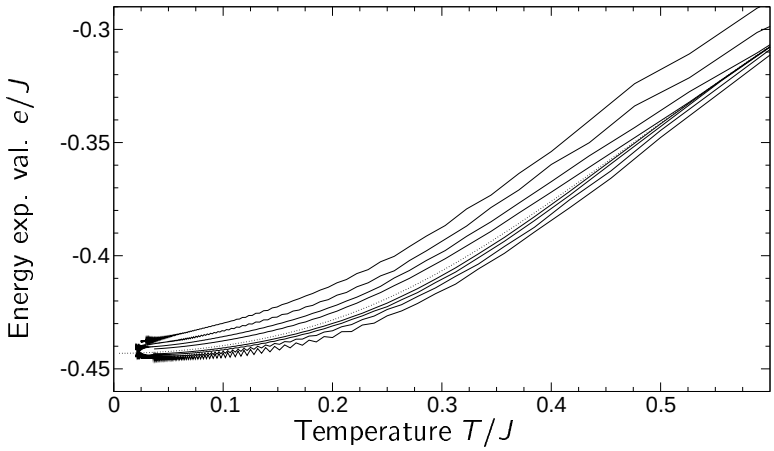

Figure 4.16: Energy per site vs. temperature for the Heisenberg chain of varying chain length. The energy expectation value at the chain center is plotted for different QCTMRG calculations with a preserved number of states $m = 50, 100, 200, 400$ (from outside to inside). The upper curves belong to systems with an odd number of sites, the lower curve belong to systems with an even number of sites. Note that the chain length is $L = 10/T$. The exact energy density of the infinite chain is plotted (dotted) for comparison.

The energy expectation value in the center of the chain has been calculated for various system sizes and temperatures in Fig. 4.16. Again we have $\epsilon = 0.05$ which leads to a fixed relation $LT = 10$ for the QCTMRG data. Odd and even chain lengths are included in this calculation, in contrast to the free energy data which has only been given for even chains. For odd chains, the expectation value was taken from a plaquette at the exact center of the decomposition. For even chains, we considered one of the two central plaquettes.

Even chain lengths appear as the natural choice in the renormalization procedure. Chains with an odd number of sites have a well-defined central site which might give better results.

We find the even system energy expectation values lying below the infinite system value and the odd system lying above the infinite system value. The low-energy spectrum of the antiferromagnetic Heisenberg chain involves spin-1/2 spinons which can be identified with quantum domain walls. The ground state is a total spin singlet on chains with an even number of spins. In odd chains there is no spin singlet ground state and so always a spinon "excitation" is present. In the domain wall picture, there is always a kink present. For this reason, we expect the chains with an even number of sites to possess a lower local energy than chains with an odd number of sites. However, we expect that the expectation values for even and odd chains converge to the same limit in an infinite chain. This description

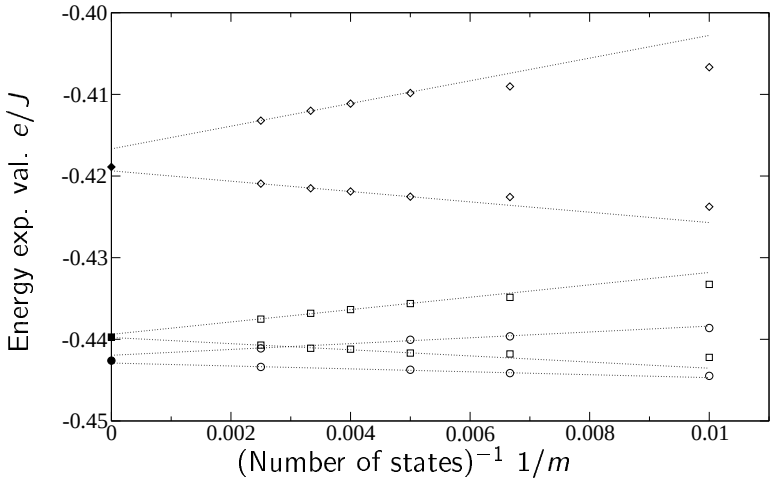

Figure 4.17: Energy per site vs. inverse number of states for the Heisenberg chain of various lengths at various temperatures. The energy expectation values at the center of even chains (lower symbols) with $T = 0.25J$ and $L = 40$ (diamonds), $T = 0.1J$ and $L = 100$ (squares), and $T = 0.04J$ and $L = 250$ (circles) and of odd chains (upper symbols) with $T = 0.256J$ and $L = 39$ (diamonds), $T = 0.101J$ and $L = 99$ (squares), and $T = 0.0402J$ and $L = 249$ (circles). have been calculated. We denote the exact energy density of the infinite chain by full symbols. The dashed lines are linear fits.

agrees well with our observed behavior.

In either case, we have a strong dependence of the expectation value on the number of preserved states m in the renormalization group. For both even and odd number of sites, we can still distinguish the data curves up to low temperatures even for high values of m. Yet, the convergence for even system sizes is faster than for odd sizes.

To get a more quantitative picture we plotted the convergence of several points of fixed temperature and system size, see Fig. 4.17. Like in the free energy data, the low-T and larger sized systems show a better convergence. We included linear fits for a better understanding. The expectation values for even/odd sized system at finite temperatures seem to differ even in an $1/m$ extrapolation. The infinite-chain expectation value lies well-between those boundaries. For larger system sizes and lower temperatures we obtain a better convergence in $1/m$. However, we recommend a careful analysis beyond linear approximation if high-precision data is needed.

The results from this section shall serve as an illustrating background for a discussion of the scope of application and the limits of the QCTMRG technique.

4.5 Discussion of the QCTMRG method

The QCTMRG method combines the corner-transfer-matrix technique and the DMRG to obtain thermodynamic data for one-dimensional quantum systems of finite size. A crucial attribute for the QCTMRG algorithm is the fixed relation between system size and temperature during the renormalization loops. This condition sets the focus of the method to finite size systems, in contrast to the TMRG. Yet, a significant advantage in computational resources would make the QCTMRG an interesting choice for low-temperature studies of very large systems where finite-size effects play a marginal role.

4.5.1 Running time and storage use

For a view on the algorithm's running time and storage use, we studied the scaling behavior with the number of states kept m of the different steps in the algorithm. See Sec. B.1 in the appendix. We find the algorithm to take asymptotically $\mathcal{O}(m^4)$ elementary floating point operations (FLOPS) and a storage use of order $\mathcal{O}(m^3)$ floating point numbers for large m. However, the most time is spend in matrix-multiplications operations where a naive approach would give a running time of $\mathcal{O}(N^3)$ FLOPS for multiplication of two $N \times N$ matrices. In contrast to this, the fastest algorithm currently known has an asymptotic running-time of $\mathcal{O}(N^{2.376})$ FLOPS. So we expect the running-time to scale asymptotically with well-below fourth order in m in a clever implementation.

In case of the transfer-matrix DMRG algorithm, the by-far most time consuming part is the Implicitly Restarted Arnoldi Method (IRAM) employed to find the largest eigenvalues of the transfer-matrix. We, thus, expect the asymptotic scaling behavior to be dominated by this routine from the ARPACK-library. The running-time of the IRAM routine depends sensitively on the problem. Thus, it performs with between $\mathcal{O}(1)$ and $\mathcal{O}(N)$ $\times$ the cost of a certain matrix-vector product when $N \times N$ is the size of the matrix. In our case, the demanded matrix-vector product has a cost of $\mathcal{O}(m^3)$ flops and the total matrix has a basis of size $N \propto m^2$. We thus expect the total running-time to vary between $\mathcal{O}(m^5)$ worst case and $\mathcal{O}(m^3)$ best case. Further reduction might be achieved when clever algorithms for matrix multiplications are implemented.

The storage scales with the size of of the system-block-transfer-matrix ($\mathcal{O}(m^2)$ numbers), while the storage usage is determined by the size of the corner tile ($\mathcal{O}(m^3)$ numbers) in the QCTMRG method.

From the theoretical point of view, the QCTMRG and the TMRG algorithms have similar running-times in the large-m limit. The TMRG algorithm will be favorable in some special cases where the IRAM routine reaches a fast convergence. For some ill-posed problems, however, the QCTMRG algorithm might have an advantage. The TMRG algorithm is the clear winner when storage usage is a sensible quantity.

In our implementation, we observed a roughly similar running time of both algorithms for different number of preserved states m. The storage use was, indeed, higher in the QCTMRG algorithm.

4.5.2 Fundamental challenges

Yet, we still face some fundamental challenges of the QCTMRG algorithm in addition to the advantages of TMRG concerning the use of system resources. As already mentioned above, the quantum character of our system enforces periodical boundary conditions in Trotter direction which makes the two-dimensional corner transfer-matrix from Nishino's CTMRG a three-dimensional tensor in the case of QCTMRG. This is the reason behind an increase in running-time and storage which is crucial and destroys the advantages from the development of CTMRG over TMRG.

Another more subtle point involves the spectra of the reduced density matrices from the renormalization procedure. Consider the limit $T \to \infty$ which is close to the starting system of TMRG and QCTMRG where $\beta = 1/T = \epsilon M$ is small. As shown in Section 3.2.1, the local transfer-matrix of the Trotter decomposition (3.7) reduces to

$$\tau^{i,i+1}_{k,k+1} := \left\langle s^i_k s^{i+1}_k \middle| \mathrm{e}^{-\epsilon h_{i,i+1}} \middle| s^i_{k+1} s^{i+1}_{k+1} \right\rangle = \delta_{s^i_k, s^i_{k+1}} \delta_{s^{i+1}_k, s^{i+1}_{k+1}} \tag{4.11}$$

which means that the initial spin configuration will not be changed by the transfer-matrix.

Now, we consider a Trotter decomposition like Fig. 3.2 for infinite temperature or vanishing ϵ. The chosen graphical representation depicts the Kronecker symbols as lines passing through the transfer-matrix plaquettes. If the system is periodically closed in Trotter direction and has open boundaries in space direction, we can imagine the paths as non-interacting lines around a cylinder. This depicts the trace from the partition sum.

Building a reduced density matrix introduces a vertical or horizontal cut into the system. Consider the case of a cut in Trotter direction which corresponds to the cut in TMRG. One "spin path" has been cut through while all the others stay intact, *i.e.* they still are summed out in the reduced density matrix. Only the intersected thread determines the eigenspectrum of the reduced density matrix. With a straightforward calculation (see appendix C for a similar calculation on the Ising model), we find one or two degenerate eigenvalues depending on whether we intersect an odd or even number of sites. All other eigenvalues remain zero in this case. This turns our renormalization step, which is a truncation of basis states, to be highly effective. In a system with small ϵ we still find a small number of dominating eigenvalues which lead a DMRG renormalization to success.

The opposite situation is faced when the cut is made in space direction. If the underlying spin chain has a number of $2L$ spins, the density matrix will "cut" as much as L paths. All L spins act separately and, thus, all spin configurations have the same contribution to the partition function. Merely the remaining degrees of freedom will be summed out. Consequently, we are left with a reduced density matrix which has S^L degenerate eigenstates when S is the spin size. No effective truncation can be found. The situation in cases with high, but finite temperature is certainly less ill-posed. Though, still we expect a slow decay of the spectrum of the reduced transfer matrix.

This scenario explains why our calculated QCTMRG data show a most significant deviation from the expected values at higher temperatures. Starting with a small system size the algorithm can still handle the system with high precision. For larger system sizes, a

truncation has to be done during the renormalization step which cannot be optimal since the reduced density matrix will still have a flat spectrum. At even larger system sizes and lower temperatures the spectrum of horizontal density matrix will become acceptably well-behaved again.

4.5.3 Conclusion

We developed a new method for finite-temperature studies of one-dimensional quantum systems based on the CTMRG of Nishino. The free energy densities and a thermal energy expectation values at the chain centers have been successfully calculated for the classical Ising chain and the antiferromagnetic spin-1/2 Heisenberg chain by the Quantum Corner-Transfer Matrix DMRG. Reliable results were given for finite temperatures and system sizes. Yet, the algorithm faces two difficulties:

- Periodic boundary conditions reduce the efficiency.
- The reduced density matrix in space direction has a slowly decaying eigenspectrum.

If finite-temperature data in the thermodynamic limit is aimed at, the quantum TMRG method is certainly still the method of choice. At least one of the mentioned problems should be solved to make the QCTMRG technique an attractive option.

5 Thermodynamics of spin ladders with cyclic exchange

Thermodynamic properties of spin ladder systems have been discussed in a number of papers [37, 129, 130, 18, 131, 132, 133]. However, the focus was mainly on models not containing four-spin interaction. The first providing specific heat and magnetic susceptibility data for a ladder model with four-spin exchange were Bühler et al. [50, 134]. They obtained results from exact complete diagonalization and a high-temperature series expansion method incorporating $T = 0$ information (ground state energy, dispersion) from a continuous unitary transformation method [51]. Yet, they focused on only small positive values of four-spin exchange and did not calculate generalized susceptibilities.

In this chapter, we will present various thermodynamical quantities for the complete phase diagram of the spin ladder with cyclic exchange. This includes the specific heat and magnetic susceptibility as experimentally accessible system properties of particular interest. Unknown microscopic couplings can be revealed when experimental data are compared to thermodynamic properties of effective models. We illustrate the special characteristics of the phases by providing thermal expectation values of local operators. We identify phases with spontaneously broken Z_2-symmetry by calculating generalized susceptibilities.

All calculations were performed by the numerical Transfer Matrix DMRG introduced in Chapter 3. The convergence in the DMRG parameter m was checked for all calculations. While convergence was often already reached at $m = 100$, in general, $m = 300$ was found to be a good choice. In some samples, we also checked the influence of the choice ϵ. Here, we confirmed that the well-establish value $\epsilon = 0.05$ gives most appropriate results. All calculation were performed on a compute server of type Sun Fire 15K at the Zentrum für angewandte Informatik, Universität zu Köln. Each calculation took up to a week of computational time.

Along with the results we give a discussion of the interesting properties for finite temperature and sketch the impact of the quantum phase transitions in this model on $T > 0$ data.

In the following, we set $k_B = 1$ and $g\mu_B = 1$ for simplicity.

5.1 Local expectation values

The TMRG method gives us the possibility to calculate the thermal expectation values of operators on a single plaquette. A huge number of potential operators can be thought of for the plaquette has a number of sixteen states. However, the conservation laws helps us to concentrate on the essential non-trivial plaquette-operators and to get, by this, a good understanding of the physics.

The Hamiltonian shows a number of symmetries, see Section 2.1, which lead to conserved quantities and allow us to choose a well-justified set of basis states. Thus, no operator connecting two subspaces with a different configuration of such quantum numbers (S, S^z, P, k) will have a non-vanishing expectation value.

A basis set of operators which can form each possible plaquette operator with non-trivial expectation value is given by projectors onto the basis states, (2.3), (2.4), and (2.5). Since

the $S = 0$-subspace is twofold degenerate, we will consider the thermal expectation value of the overlap between both $S = 0$-states

$$\mathcal{O}_0 = |\phi_0^{\perp}\rangle\langle\phi_0^{\parallel,\times}| + |\phi_0^{\parallel,\times}\rangle\langle\phi_0^{\perp}| \tag{5.1}$$

as well. For states with non-zero total spin, all operators within a spin multiplet have the same expectation value because of the $SU(2)$ symmetry. For this reason, it suffices to calculate seven thermal expectation values

$$\langle\mathcal{P}_2\rangle,\ \langle\mathcal{P}_1^{\perp}\rangle,\ \langle\mathcal{P}_1^{\parallel}\rangle,\ \langle\mathcal{P}_1^{\times}\rangle,\ \langle\mathcal{P}_0^{\perp}\rangle,\ \langle\mathcal{P}_0^{\parallel,\times}\rangle,\ \langle\mathcal{O}_0\rangle \tag{5.2}$$

in order to restore the expectation values of all non-trivial plaquette-operators. The expectation values of the projectors $\langle\mathcal{P}_0^{\perp}\rangle$ and $\langle\mathcal{P}_0^{\parallel,\times}\rangle$ together with the expectation value of the overlap $\langle\mathcal{O}_0\rangle$ give us the expectation values of every operator in the $S = 0$ subspace of the plaquette. A diagonalization of this subspace helps us to find the operator $|\phi_0^{\mathrm{hi}}\rangle$ with highest expectation value and the operator $|\phi_0^{\mathrm{lo}}\rangle$ with lowest expectation value with $S = 0$ on the plaquette.

In figs. 5.1 and 5.2, the thermal expectation values of the plaquette-projectors are plotted. In the insets, we present the overlap of the highest contributing $S = 0$ state with the plaquette states with singlets on rungs, legs, and diagonals, in order to identify the character of the state.

An interpretation of these expectation values can be given as a reduced density matrix: All degrees of freedom except the spin alignment on a single plaquette are traced out of the thermodynamic ensemble of states by the projection operators. We succeeded in obtaining a diagonal representation of this 16×16-matrix. In [135], such a reduced density matrix of a degenerate ground-state was diagonalized in order to identify the relevant order parameters of the spin ladder in the spontaneously-broken symmetry phase.

For a comparison with the numerical TMRG data, we give the $T = 0$ expectation values of the matrix-product ground-state introduced in Eq. (2.27):

$$\langle\mathcal{P}_2\rangle = 0, \qquad \langle\mathcal{P}_1^{\perp}\rangle = \frac{6}{\left(|u|^2+3\right)^2}, \tag{5.3}$$

$$\langle\mathcal{P}_1^{\parallel}\rangle = \frac{\frac{3}{2}|u|^2\left(\sigma+1\right)^2}{\left(|u|^2+3\right)^2}, \qquad \langle\mathcal{P}_1^{\times}\rangle = \frac{\frac{3}{2}|u|^2\left(\sigma-1\right)^2}{\left(|u|^2+3\right)^2}, \tag{5.4}$$

$$\langle\mathcal{P}_0^{\mathrm{hi}}\rangle = \frac{|u|^4+3}{\left(|u|^2+3\right)^2}, \qquad \langle\mathcal{P}_0^{\mathrm{lo}}\rangle = 0 \tag{5.5}$$

with

$$|\phi_0^{\mathrm{hi}}\rangle = \frac{1}{\sqrt{|u|^4+3}}\left(\sigma u^2|\phi_0^{\perp}\rangle + \sqrt{3}|\phi_0^{\parallel,\times}\rangle\right) \tag{5.6}$$

The expectation values with respect to the variational parameter u are depicted in Fig. 5.3.

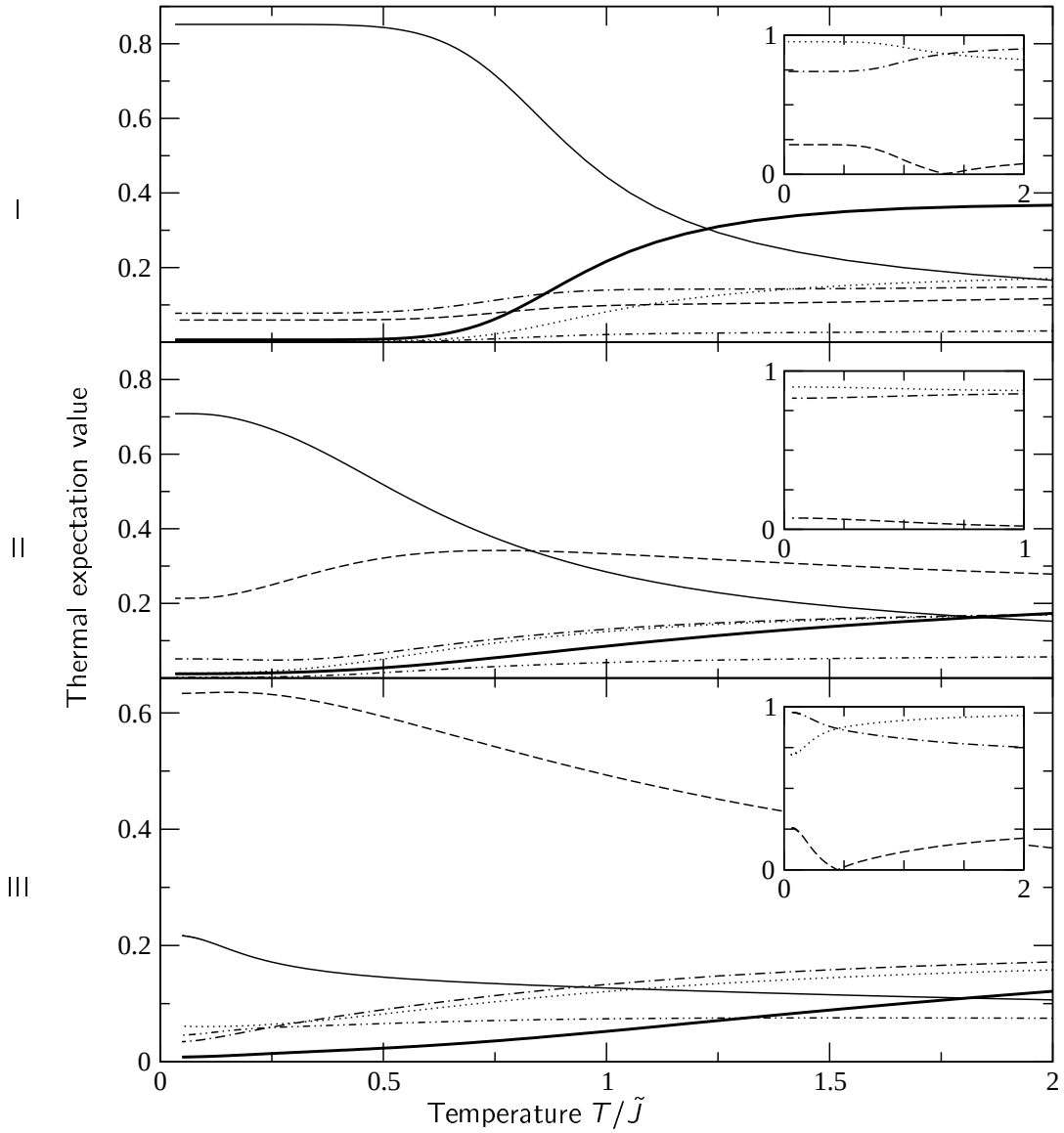

Figure 5.1: Expectation values of projectors onto plaquette states versus temperature for representative systems in the various phases. The expectation value of the projectors $\langle \mathcal{P}_2 \rangle$ (fat solid), $\langle \mathcal{P}_1^{\perp} \rangle$ (dotted), $\langle \mathcal{P}_1^{\parallel} \rangle$ (dot-dashed), $\langle \mathcal{P}_1^{\times} \rangle$ (dashed), $\langle \mathcal{P}_0^{\mathrm{hi}} \rangle$ (thin solid), and $\langle \mathcal{P}_0^{\mathrm{lo}} \rangle$ (double-dot-dashed line) are plotted from TMRG calculations. In the insets, we show the overlap of $|\phi_0^{\mathrm{hi}}\rangle$ with $|\phi_0^{\perp}\rangle$ (dotted), $|\phi_0^{\parallel}\rangle$ (dot-dashed), and $|\phi_0^{\times}\rangle$ (dashed line). These data are given for two ladder systems in the rung-singlet phase at $\theta = -2/9\pi$ (I) and $\theta = 0$ (II) and for one system in the staggered-dimer phase at $\theta = 1/9\pi$ (III).

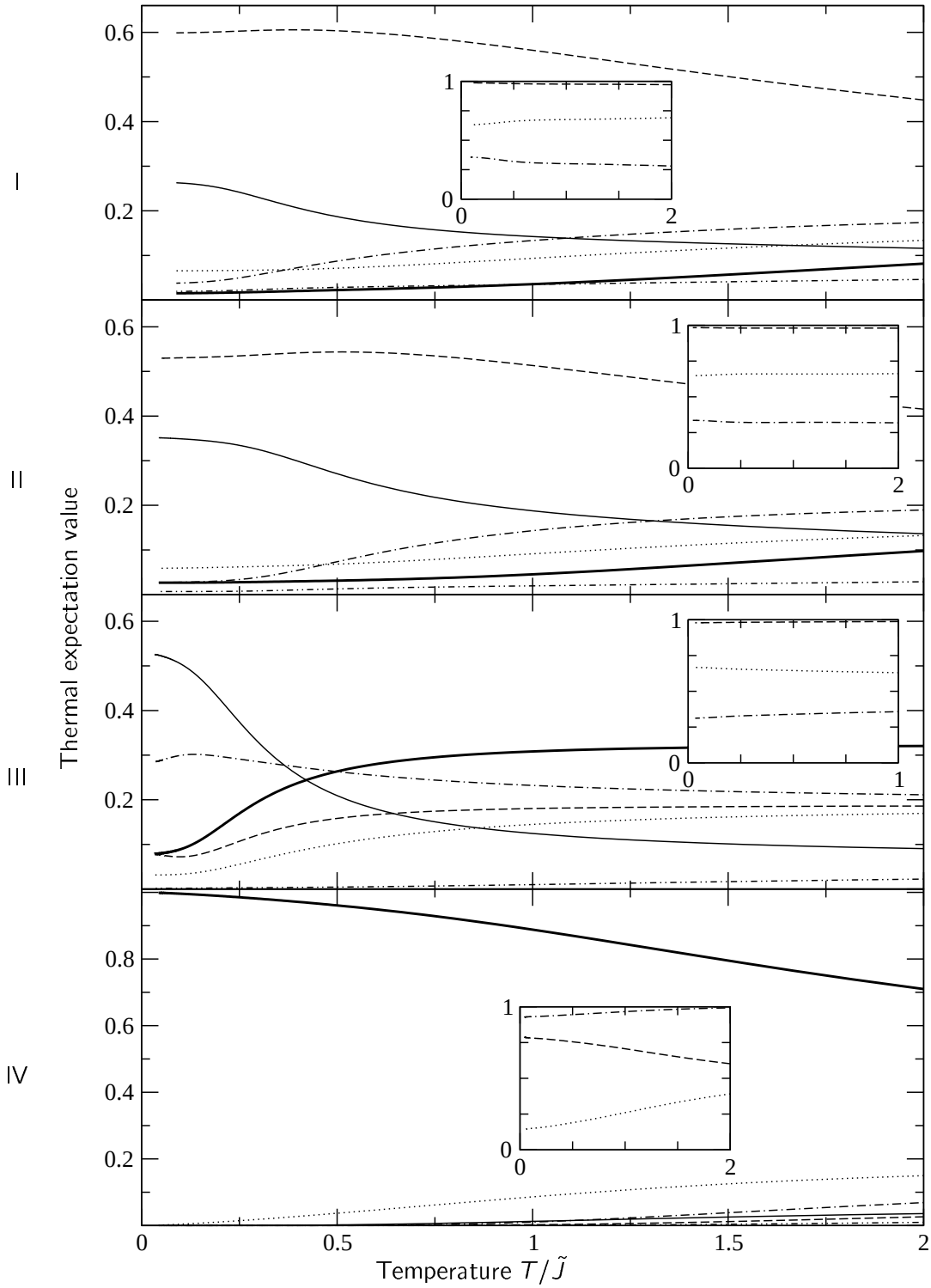

Figure 5.2: Expectation values of projectors onto plaquette states versus temperature for representative systems in the various phases. (Legend see Fig. 5.1). I: scalar-chirality phase at $\theta = 1/3\pi$, II: vector-chirality phase at $\theta = 5/9\pi$, III: dominant-collinear-spin phase at $\theta = 8/9\pi$, IV: ferromagnetic phase at $\theta = -2/3\pi$.

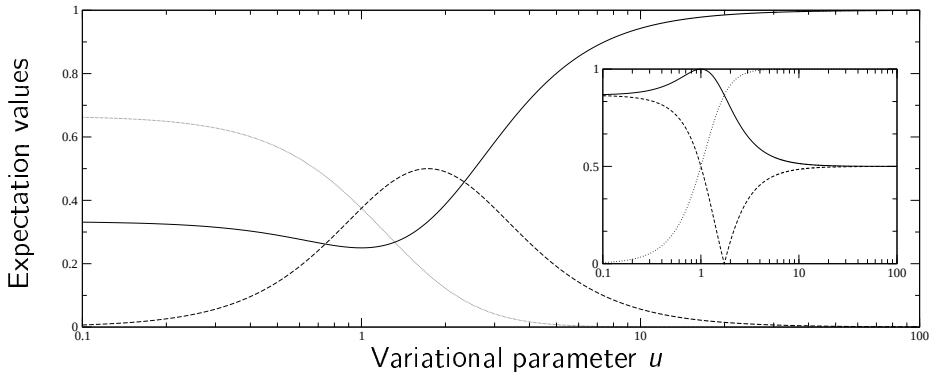

Figure 5.3: Expectation values of projectors onto plaquette states vs. variational parameter of Eq. (2.27): $\langle \mathcal{P}_1^{\perp} \rangle$ (dotted), $\langle \mathcal{P}_1^{\parallel} \rangle$ for $\sigma = 1$ or $\langle \mathcal{P}_1^{\times} \rangle$ for $\sigma = -1$ (dashed), and $\langle \mathcal{P}_0^{\mathrm{hi}} \rangle$ (solid line). In the insets, we show the overlap (absolute value) of $|\phi_0^{\mathrm{hi}}\rangle$ with: $|\phi_0^{\perp}\rangle$ (dotted), $|\phi_0^{\parallel}\rangle$ (dashed), and $|\phi_0^{\times}\rangle$ (solid line). for $\sigma\,\mathrm{sgn}(u^2) = 1$. For $\sigma\,\mathrm{sgn}(u^2) = -1$, the solid and dashed curves must be interchanged. Note the logarithmic scale of u.

5.1.1 Rung-singlet order parameter

The rung-singlet state is one of the possible product states. All neighboring spins on a rung are coupled to a singlet state on the ladder, see Section 2.4. It is the exact ground state of the ladder in the limit of decoupled rungs which can be deformed into the Heisenberg ladder without crossing a phase transition [2]. This fact leads to the successful application of the continuous unitary transformations method for the rung-singlet phase of the ladder with cyclic exchange [51].

We calculated two quantities in order to detect the presence of rung-singlet ordering. In Fig. 5.4, we calculated the possibility to find a singlet state on a rung. The expectation value of the projector can vary between 0 and 1. The average value for infinite temperature is 1/4. In Fig. 5.5 (thick lines), we calculated the possibility to find singlets on both rungs of a plaquette, *i.e.* on neighboring rungs. This can be understood as a two-point correlation function. Here, the expectation value can vary between 0 and 1 as well, but the average of uncorrelated spins is only 1/16. We will now discuss the basic features of the phases with respect to these parameters.

Within the rung-singlet phase, we find a clear dominance of the rung-singlet states for low temperatures. As discussed in Chapter 2, the rung-singlet character of the ground state is strong in the lower part of the phase diagram (for example $\theta = -2/9\pi$) while it is in stronger competition with other phases around the Heisenberg ladder ($\theta = 0$). This is exactly what we see at the two reference points from that phase. Further, a plateau for the order parameters at $\theta = -2/9\pi$ emerges for low temperatures. We conclude that the rung-singlet ordering stays stable up to temperatures $T \approx 0.6\tilde{J}$ when states with

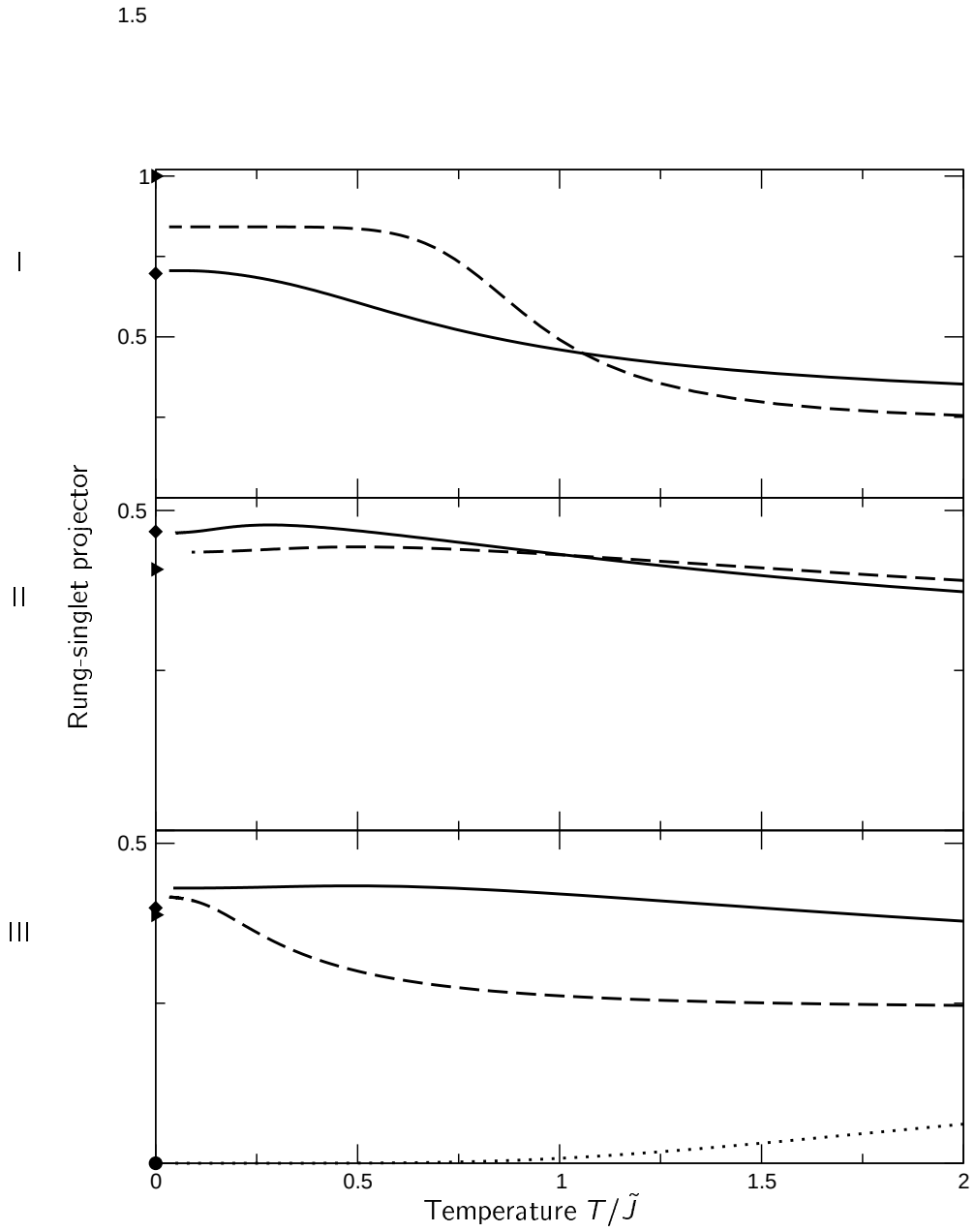

Figure 5.4: Projector $|s_0\rangle\langle s_0|$ onto a singlet state on a single rung versus temperature for representative systems in the various phases. I: rung-singlet phase at $\theta = -2/9\pi$ (dashed line) and $\theta = 0$ (solid), II: staggered-dimer phase at $\theta = 1/9\pi$ (solid), and scalar-chirality phase at $\theta = 1/3\pi$ (dashed), III: vector-chirality phase at $\theta = 5/9\pi$ (solid), dominant-collinear-spin phase at $\theta = 8/9\pi$ (dashed), and ferromagnetic phase at $\theta = -2/3\pi$ (dotted). Data from TMRG-calculation. At $T = 0$, the ground-state expectation value of the variational matrix product state (Chapter 2) is depicted (diamond for solid, triangle for dashed, circle for dotted line).

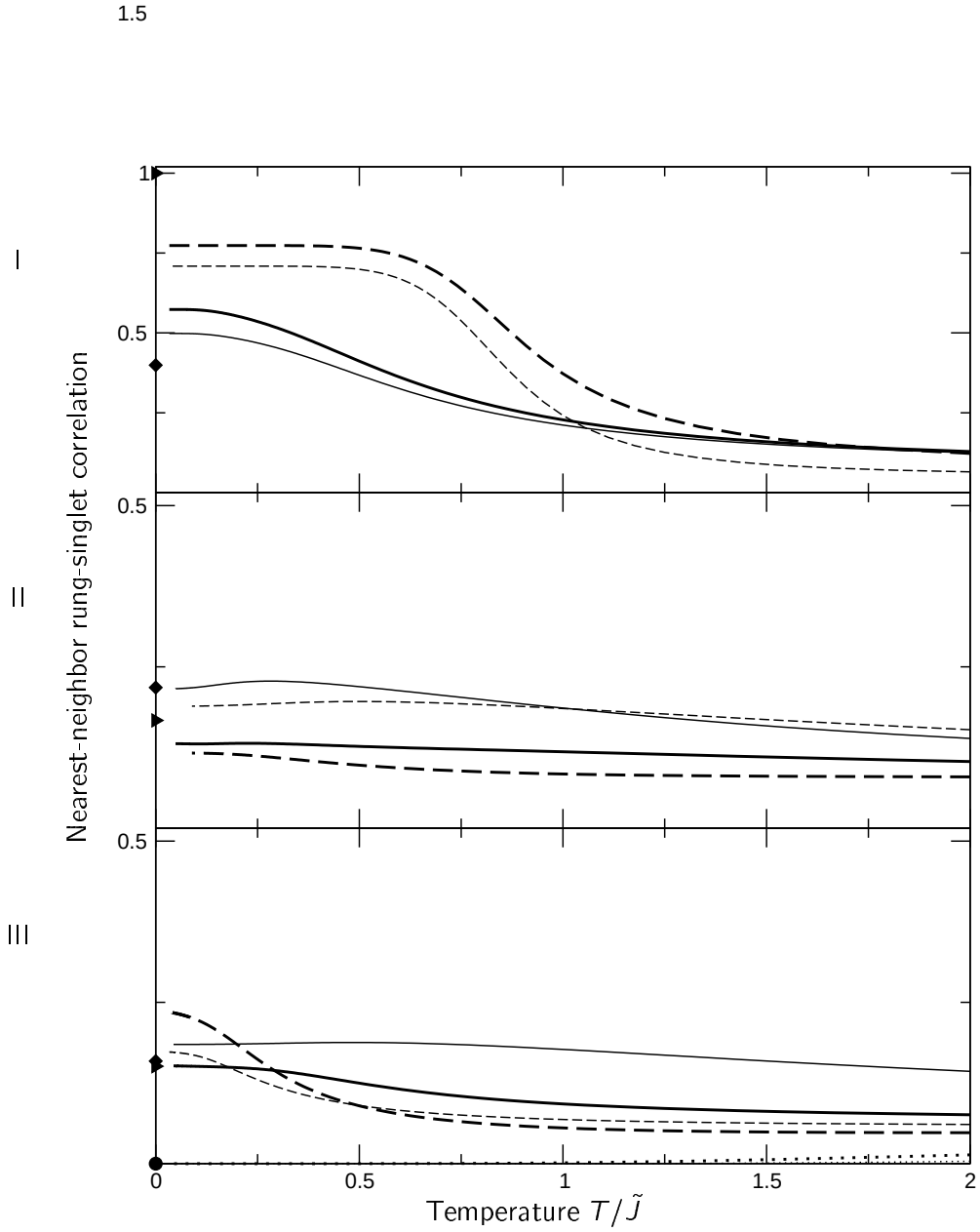

Figure 5.5: Two-point correlation for singlets on nearest-neighbor rungs $\langle \mathcal{P}_0^{\perp} \rangle$ (thick lines) versus temperature for representative systems in the various phases. I: rung-singlet phase at $\theta = -2/9\pi$ (dashed line) and $\theta = 0$ (solid), II: staggered-dimer phase at $\theta = 1/9\pi$ (solid), and scalar-chirality phase at $\theta = 1/3\pi$ (dashed), III: vector-chirality phase at $\theta = 5/9\pi$ (solid), dominant-collinear-spin phase at $\theta = 8/9\pi$ (dashed), and ferromagnetic phase at $\theta = -2/3\pi$ (dotted). Data from TMRG-calculation. At $T = 0$, the ground-state expectation value of the variational matrix product state (Chapter 2) is depicted (diamond for solid, triangle for dashed, circle for dotted line). Thin lines: squared curves of Fig. 5.4.

small rung-singlet contributions can be excited. At $\theta = 0$ no such pronounced behavior is observed. Here, the stable temperature range is smaller.

In the phases with symmetry-breaking in the ground states as well as in the vector-chirality phase, the rung-singlet contribution is still larger than the average value, but especially the two-point correlation drops well-below the rung-singlet phase expectation values.

For the dominant-collinear-spin phase, we find significantly smaller expectation values than in the rung singlet-phase. However, for low temperatures the two-point correlation is above average. There is, however, a rapid decrease with increasing temperature. This decrease is caused by ferromagnetic states which are low in energy in the vicinity of the ferromagnetic phase. As expected, rung singlets are suppressed in the ferromagnetic phase.

In Chapter 2, we found variational matrix product states with staggered ordering. The variational states give the expectation values

$$\left\langle \Psi(u,\sigma)\right| \left(\left|s_0\right\rangle_j \left\langle s_0\right|_j \right) \left|\Psi(u,\sigma)\right\rangle = \frac{|u|^2}{|u|^2+3} \quad \text{and} \tag{5.7}$$

$$\left\langle \Psi(u,\sigma)\right| \left(\mathcal{P}_0^{\perp}\right)_j \left|\Psi(u,\sigma)\right\rangle = \frac{|u|^4}{(|u|^2+3)^2} \tag{5.8}$$

for our local parameters on a rung j. Considering the adequate variational parameters, we plotted their ground state expectation values as small symbols at $T = 0$ in figs. 5.4 and 5.5.

Asides from the model with $\theta = -2/9\pi$, all thermal expectation values show good convergence towards the corresponding variational value in Fig. 5.4. In Fig. 5.5, the thermal expectation values show the expected convergence only in the vector-chirality and in the ferromagnetic phase. An explanation of this behavior can be found in the expectation values of the variational states (5.7) and (5.8). Note that the probability of finding two singlets on neighboring rungs is just the square of the possibility of finding a singlet on one rung. This is just the random statistical distribution of the rung-singlets. Hence, the rung-singlets are uncorrelated in the variational state.

For a comparison, we plotted the squared single rung-singlet expectation value into Fig. 5.5 (thin lines) which corresponds to a statistical distribution. In the rung-singlet phase, we see that singlets attract each other. We have a probability to find another singlet next to a singlet which is enhanced. In the staggered phases and in the vector-chirality phase, it is vice versa: Singlets repel each other slightly. In the dominant-collinear-spin phase, we find attracting singlets again. Note that the deviation of the statistical behavior sets in at low temperatures in this case. Lacking singlets, we find none of this interesting behavior in the ferromagnetic phase.

5.1.2 Vector-chirality order parameter

In Fig. 5.6, the expectation value for the vector-chirality (2.20) is plotted for representative systems from the various phases. We included the $T = 0$ expectation value of the corre-

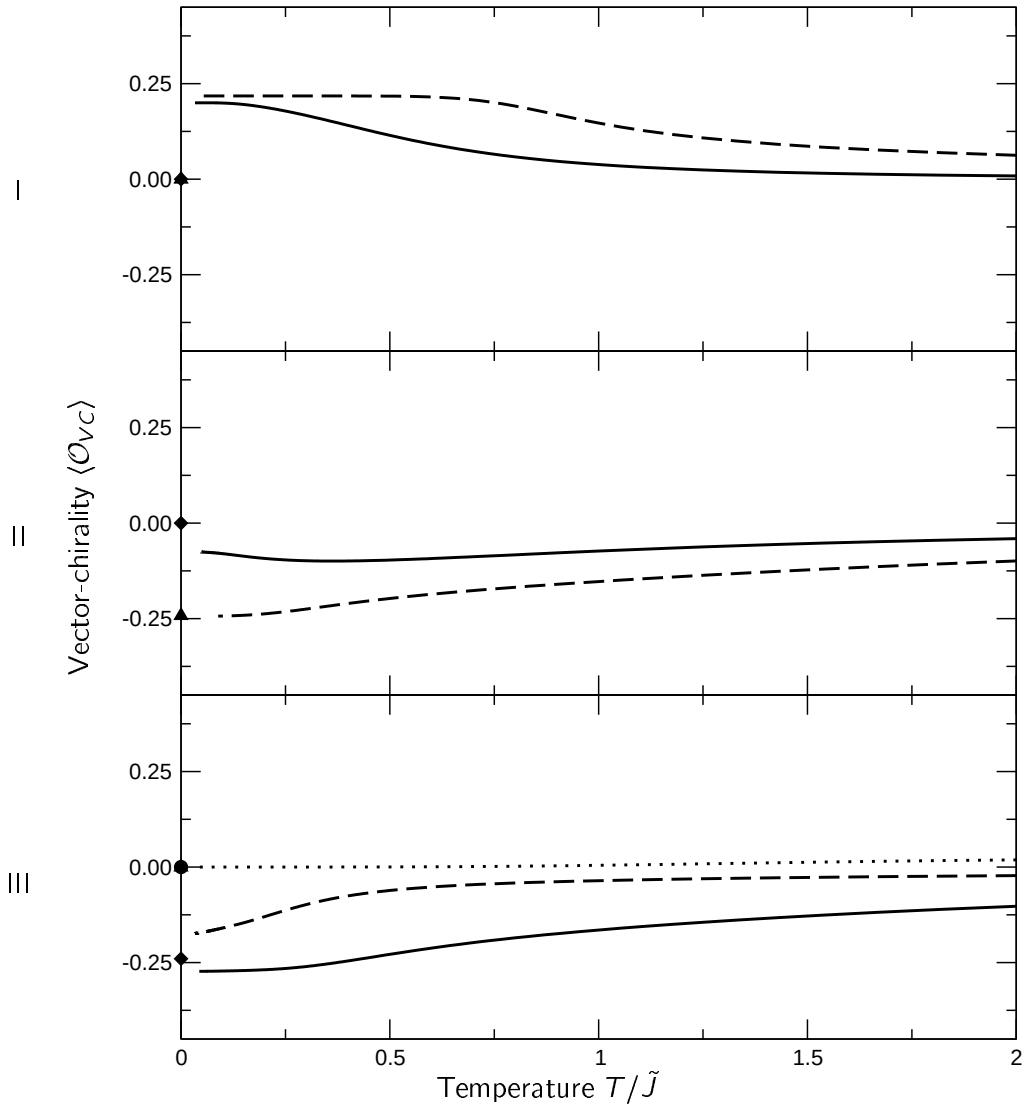

Figure 5.6: Vector-chirality $\langle \mathcal{O}_{VC} \rangle$ versus temperature for representative systems in the various phases. I: rung-singlet phase at $\theta = -2/9\pi$ (dashed line) and $\theta = 0$ (solid), II: staggered-dimer phase at $\theta = 1/9\pi$ (solid), and scalar-chirality phase at $\theta = 1/3\pi$ (dashed), III: vector-chirality phase at $\theta = 5/9\pi$ (solid), dominant-collinear-spin phase at $\theta = 8/9\pi$ (dashed), and ferromagnetic phase at $\theta = -2/3\pi$ (dotted). Data from TMRG-calculation. At $T = 0$, the ground-state expectation value of the variational matrix product state (Chapter 2) is depicted (diamond for solid, triangle for dashed, circle for dotted line).

sponding variational matrix product states for a comparison. The expectation vanishes in the infinite temperature limit which is satisfied for each curve.

In the rung-singlet phase, both expectation values rise to positive values near 1/4 in the low temperature limit where a plateau emerges. However, the variational state expectation value differs significantly from these plateau values: Neither of these variational states gives any vector-chirality contribution.

The staggered-dimer phase has a only a small negative vector-chirality expectation value. The reference variational state gives a value of zero. In the scalar-chirality phase, the vector-chirality and its variational state take a value of $-1/4$ for very low temperatures. The dominant vector-chirality phase even falls below this value. The variational state has a slightly lower expectation value. In the dominant-collinear-spin system, the vector-chirality expectation value tends to $-1/5$ for small temperatures. The ferromagnetic phase has no contribution to the vector-chirality for $T \to 0$.

5.1.3 Collinear-spin order parameter

The local order parameter for the dominant-collinear-spin phase (2.21) has a $T \to \infty$ expectation value of 5/8. Its behavior with respect to temperature is plotted in Fig. 5.7 together with the $T = 0$ expectation values from the variational states.

In the rung-singlet phase, the representative curves lie slightly above the average of uncorrelated spins. While the Heisenberg system converges to its variational expectation value, the system at $\theta = -2/9\pi$ does not reach the value 3/2 of its corresponding variational state for $T \to 0$. The phases with symmetry breaking in the ground state deviate weakly from the average of uncorrelated spins. The staggered-dimer system falls off while the scalar-chirality system increases when $T = 0$ is approached. Both curves agree with the variational states' zero-temperature behavior.

The vector-chirality representative system shows essentially the same graph as the scalar-chirality system. For $T \to 0$, the expectation value approaches a finite value close to the variational state's expectation value, The model at $\theta = 5/9\pi$, however, leads to an expectation value of nearly 3/2 at $T \to 0$ which is maximum for the plotted curves from all phases. Here, we find a drastic deviation of the corresponding variational state's expectation value because in the variational state the contribution of $\langle \mathcal{P}_1^{\perp} \rangle$ is overestimated. The ferromagnetic state follows a smooth curve towards its $T = 0$ expectation value 1/2.

The collinear-spin order parameter gives, though restricted to a single plaquette, a good indication for the dominance of the collinear-spin correlations predicted for $T \to 0$ by [1]. In the discussion of the phase transition to the ferromagnetic phase (Section 5.5.4), we will use the collinear-spin operator to explain the influence of the level-crossing associated with the first order quantum phase transition on thermal properties.

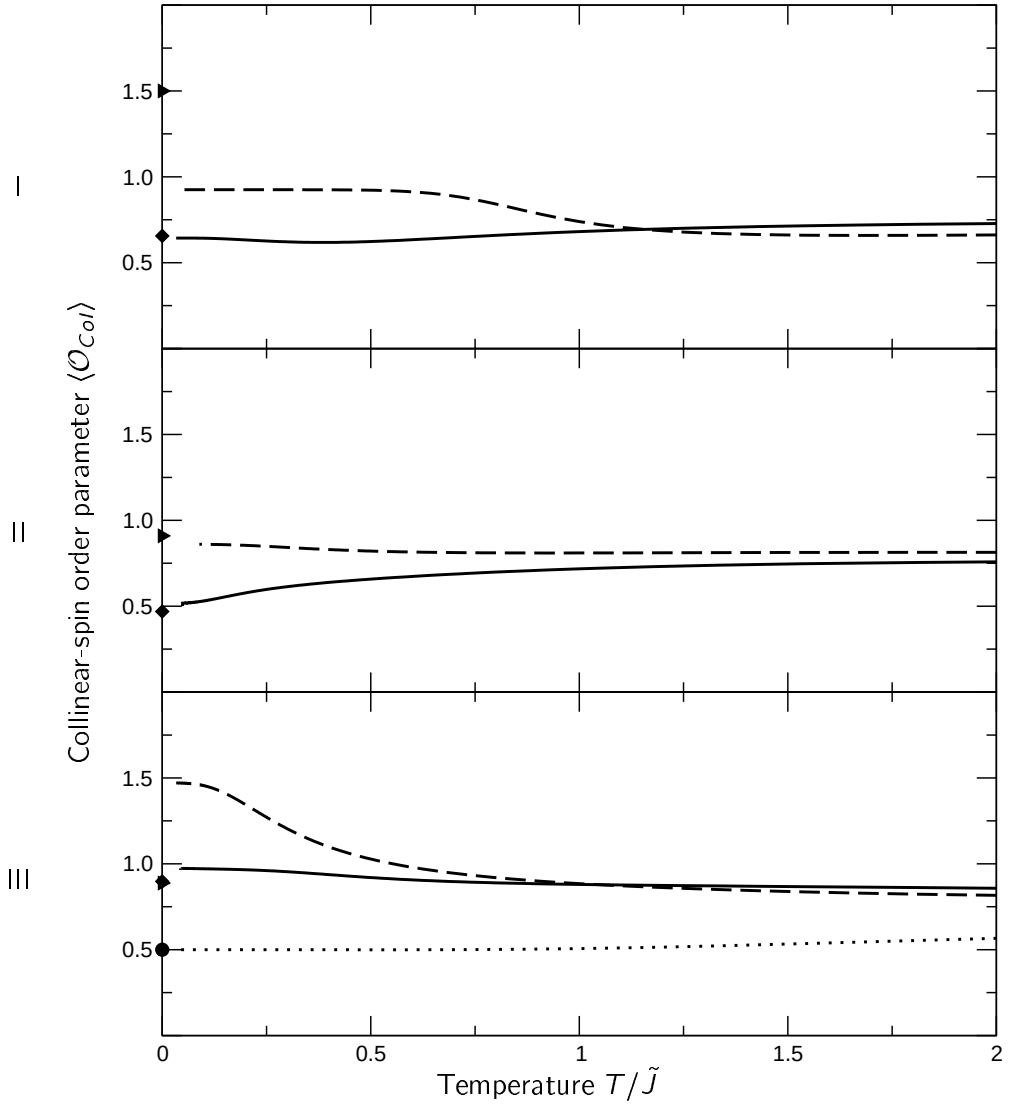

Figure 5.7: Collinear-spin order parameter $\langle \mathcal{O}_{Col} \rangle$ versus temperature for representative systems in the various phases. I: rung-singlet phase at $\theta = -2/9\pi$ (dashed line) and $\theta = 0$ (solid), II: staggered-dimer phase at $\theta = 1/9\pi$ (solid), and scalar-chirality phase at $\theta = 1/3\pi$ (dashed), III: vector-chirality phase at $\theta = 5/9\pi$ (solid), dominant-collinear-spin phase at $\theta = 8/9\pi$ (dashed), and ferromagnetic phase at $\theta = -2/3\pi$ (dotted). Data from TMRG-calculation.

5.2 Specific heat

The specific heat capacity (or shorter: specific heat) is the amount of energy required to raise the temperature of one lattice site by one energy unit. Specific heat measurements can provide very rich quantitative information on the distribution of electronic states and their interactions and is experimentally accessible easily. Therefore, it can be considered as a fingerprint of the spectral characteristics of a physical system. It keeps track of critical behavior and phase transitions. Specific heat measurements of spin ladder materials have been conducted down to very low temperatures.

5.2.1 General properties

The specific heat c is defined by the first derivative of the specific entropy $s = S/N$ (system size N) with respect to temperature multiplied by the temperature T:

$$c = \frac{1}{N} T \frac{\partial S}{\partial T} \tag{5.9}$$

By making use of the equivalence of thermodynamic potentials, the specific heat can be calculated in two distinct ways, namely as the first derivative of the local energy $u(T)$ or the second derivative of the free energy $f(T)$:

$$c = \frac{\partial u}{\partial T} = -T \frac{\partial^2 f}{\partial T^2} \tag{5.10}$$

This relationship becomes important for numerical calculations where second derivatives lose precision compared to first derivatives. We calculated the specific heat from the first derivative of the expectation value of the local Hamiltonian.

Note that the specific heat

$$c = \frac{1}{N} \frac{\Delta E^2}{T^2} = \frac{1}{N} \frac{\langle H^2 \rangle - \langle H \rangle^2}{T^2} > 0 \tag{5.11}$$

is a measure for energy fluctuations at a certain temperature T. From this, we see that C is always non-negative and that c cannot be expressed in terms of an expectation value of a local operator since $\langle H^2 \rangle$ contains long-range interactions.

From a high temperature expansion of the partition function we find

$$c \propto 1/T^2 \text{ for } T \to \infty. \tag{5.12}$$

No such general form is given for low temperatures. In many cases, however, the low-lying energy spectrum of a system is known and low-temperature approximation for the specific heat can be derived analytically. In systems with some ferro- or antiferromagnetic long-range order at zero temperature, for example, the low-lying excitations are spin waves.

These gapless modes lead to a power-law behavior of the specific heat at low temperatures. A ferromagnet has

$$c \propto T^{d/2} \tag{5.13}$$

and an antiferromagnet has

$$c \propto T^{d} \tag{5.14}$$

with space dimension d [136]. On the other hand, if there is a gap Δ in the system, the specific heat decays exponentially

$$c \propto e^{-\Delta/T} \tag{5.15}$$

for very low temperatures. Additionally, if the elementary excitations are weakly interacting massive bosons the specific heat reads

$$c \propto T^{d/2-2} e^{-\Delta/T} \tag{5.16}$$

with space dimension d [137, 136]. The spin ladder with two spin interaction can be considered as a system with magnon-type excitations (dispersion $\epsilon_k = \Delta + a|\ |k|\ - \pi|^n + \sigma h$). Its low-temperature approximation ($T \to 0, n = 2$)

$$c \ \propto \ \left(\frac{\Delta}{a}\right)^{1/2} \left(\frac{\Delta}{T}\right)^{3/2} \left[1 + \frac{T}{\Delta} + \frac{3}{4}\left(\frac{T}{\Delta}\right)^{2}\right] \mathrm{e}^{-\Delta/T} \tag{5.17}$$

($T \to 0, n = 2$) was given by [37]. We note that the temperature dependence of c involves only on the ratio Δ/T in this case.

One-dimensional quantum systems at a critical point are conformally invariant [138]. In this case, the specific heat shows a linear low-temperature behavior

$$c = \frac{\pi \tilde{c}}{3 v_{\mathrm{F}}} T \tag{5.18}$$

where $\tilde{c}$ is the conformal anomaly (or central charge) and v_{F} the velocity of elementary excitations (and k_{B} have been set to unity.) [139, 140].

5.2.2 Specific heat of the spin ladder

The spin ladder with cyclic exchange exhibits a rich phase diagram which includes critical points, quantum phase transitions and spontaneously broken symmetries (see Section 1.5). From this, we expect the specific heat to show significantly different shapes in the various phases reflecting their different properties.

With TMRG, we calculated the specific heat for the complete parameter space of Hamiltonian (1.5). In Fig. 5.8, the specific heat of special points from distinct phases is plotted. These show structures which are representative for their phases. We identify three types of curves reflecting the underlying physics: Specific heat for the gapped phases with unique ground state, for the ferromagnet and for the phases with doubly-degenerate ground state. We close this section with a discussion of the behavior at the phase boundaries.

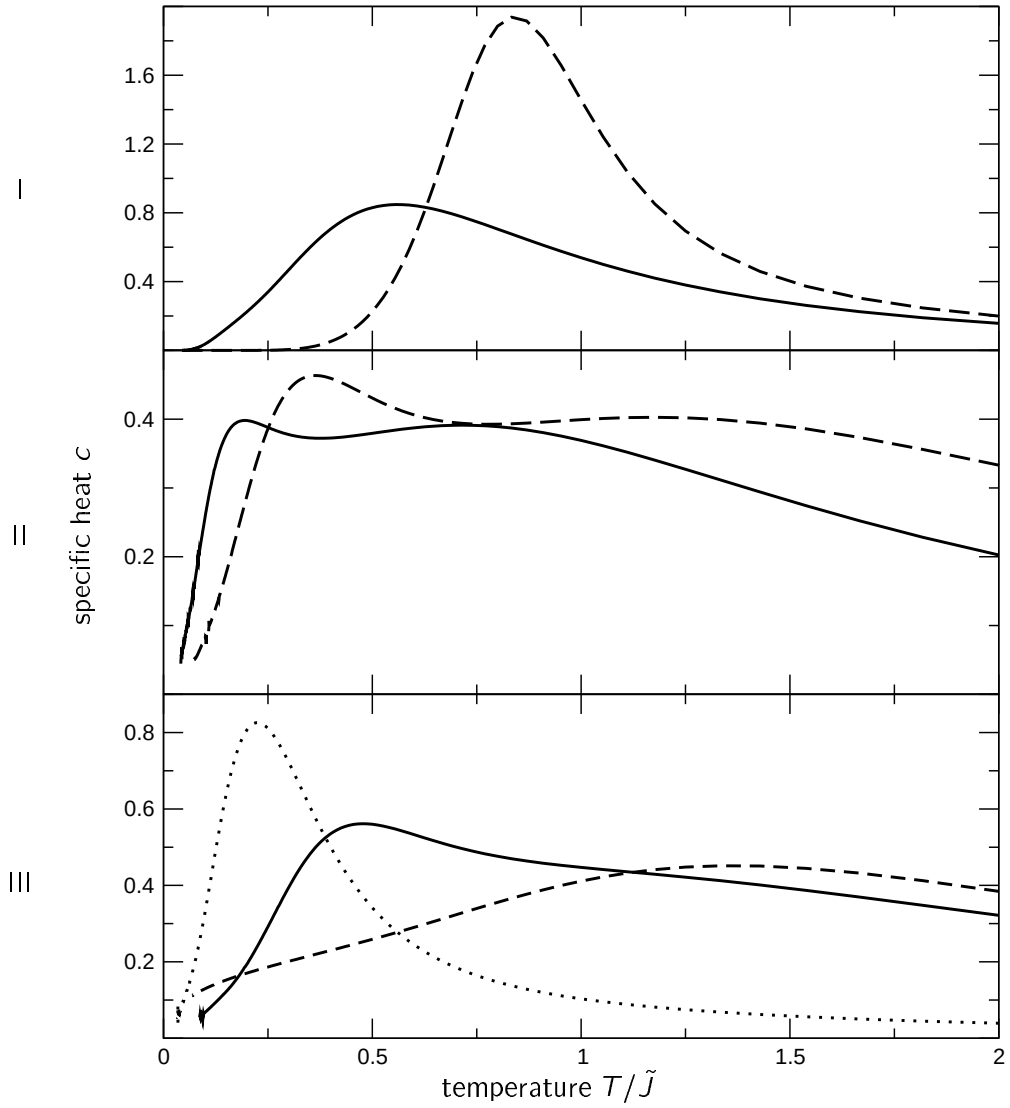

Figure 5.8: Specific heat versus temperature for representative points in the various phases. I: rung-singlet phase at $\theta = -2/9\pi$ (dashed line) and $\theta = 0$ (solid), II: staggered-dimer phase at $\theta = 1/9\pi$ (solid), and scalar-chirality phase at $\theta = 1/3\pi$ (dashed), III: vector-chirality phase at $\theta = 5/9\pi$ (solid), dominant-collinear-spin phase at $\theta = 8/9\pi$ (dashed), and ferromagnetic phase at $\theta = -2/3\pi$ (dotted). Data from TMRG-calculation.

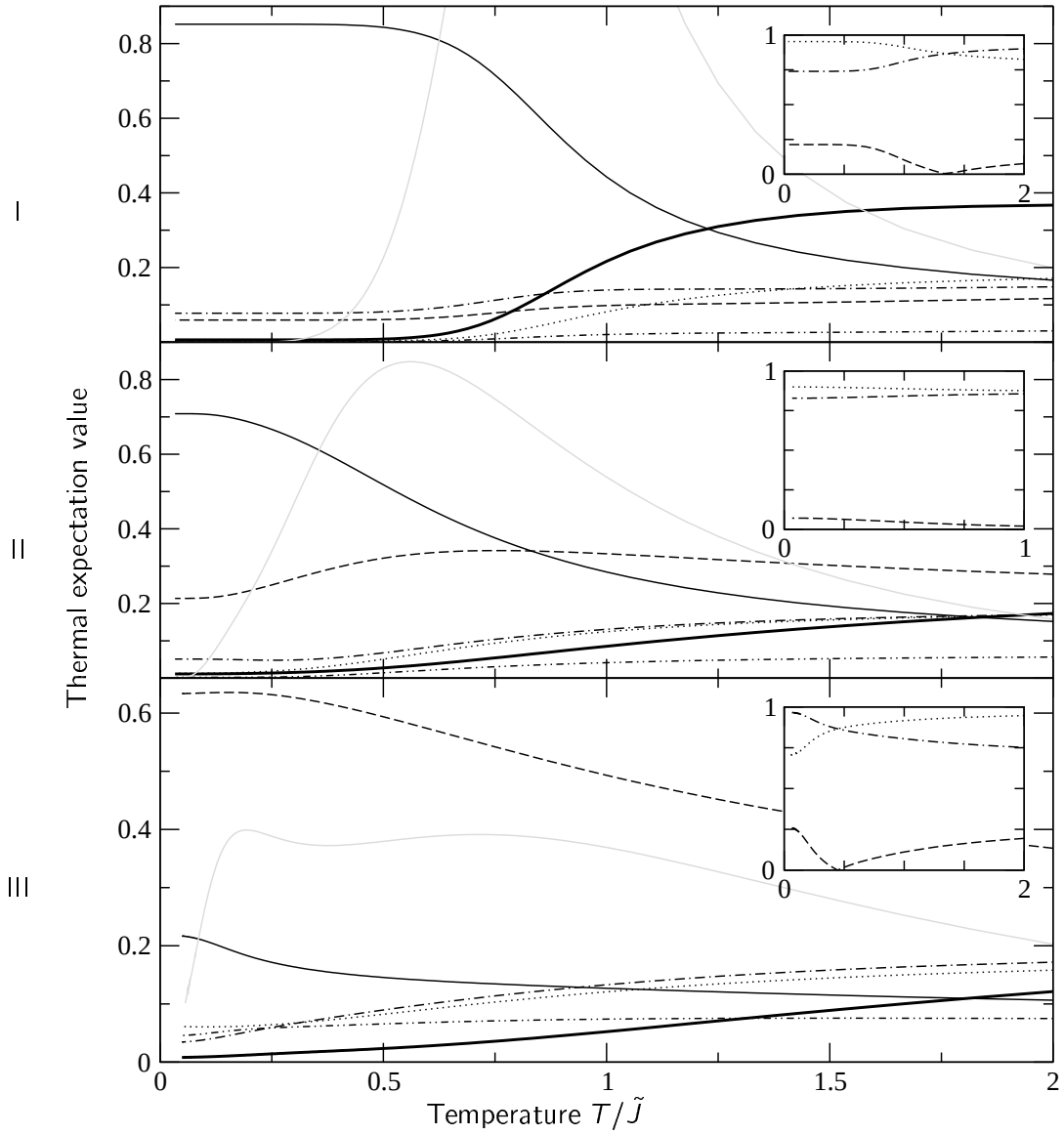

Figure 5.9: Same plots as in Fig. 5.1 with specific heat data represented as solid grey line.

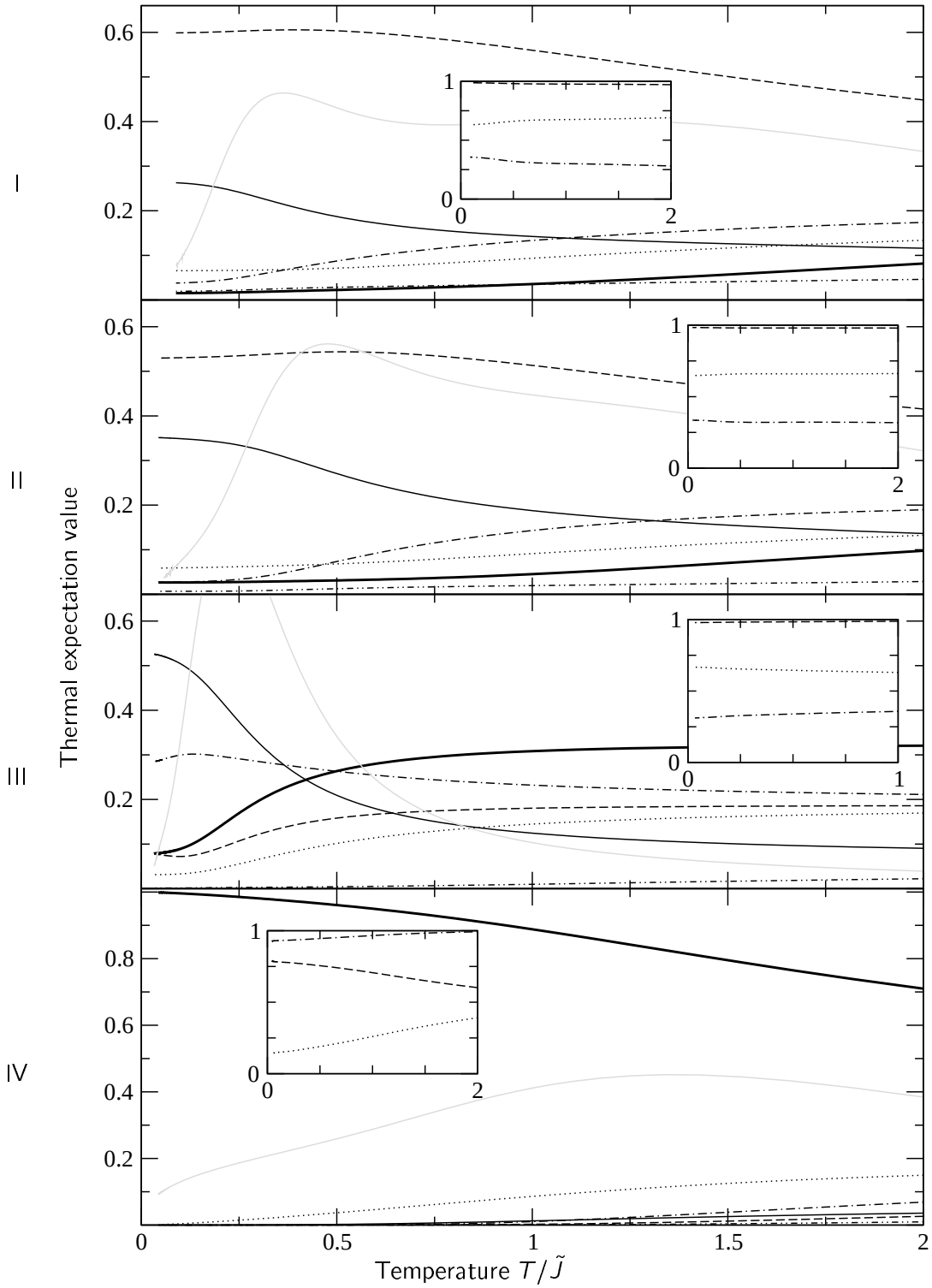

Figure 5.10: Same plots as in Fig. 5.2 with specific heat data represented as solid grey line.

5.2.3 Specific heat in the gapped phases with unique ground state

The antiferromagnetic rung-singlet phase and the dominant vector-chirality/collinear-spin phase possess a unique ground state and finite excitation gap thus meeting the scenario proposed by Haldane [3, 4, 141]. In the reference points pictured in Fig. 5.8, the exponential decay can clearly be seen for the Haldane phases. It is, however, generally not an easy task to deduce the correct value of the energy gap if the correct asymptotics is not known precisely to the first few orders because of the dominance of the exponential function. For the whole temperature range, the temperature dependence of the specific heat is roughly of Schottky-type

$$c_{\text{Schottky}} = n\left(\frac{\Delta}{T}\right)^2 \frac{\mathrm{e}^{-\frac{\Delta}{T}}}{\left(1+n\mathrm{e}^{-\frac{\Delta}{T}}\right)^2}. \tag{5.19}$$

which is the specific heat of a $(n+1)$-level system (unique ground state and n degenerate states at an energy Δ) in the gapped systems without long-range ordering. This fact has also been observed in the spin-1 chain [142]. For the high-temperature regime, we observe the T^{-2}-law (5.12) which is the high-temperature limit for the Schottky-peak approximation as well.

However, the excitation gap is generally not fitted correctly by a Schottky peak. Gapped systems show an exponential increase for low temperatures. The precise $T \to 0$ asymptotics can be described if the dispersion of the low-lying excitation is known. In [37], the low-lying excitation were found to be magnons arising from the picture that the system is essentially a ground state consisting of singlets and excitations are produced by breaking up singlets. Based on this, a low-temperature approximation (5.17) for the Heisenberg ladder was given. This picture was adopted in [143, 51, 40]. Starting from the isolated rung-dimer limit suitably chosen continuous unitary transformations (CUT) were used to map the ladder to an effective system with conservation of singlets and triplets. In this way, spectral densities of the spin ladder within the rung-singlet phase were calculated successfully.

The first to provide specific heat and magnetic susceptibility data for a ladder model with four-spin exchange, defined by (1.3) with $J_d = 0$ and $\frac{1}{2}J_{rr} = \frac{1}{2}J_{ll} = -\frac{1}{2}J_{dd} := J^B_{\text{cyc}}$ were Bühler et al.[50, 134]. They obtained results from exact complete diagonalization and a high-temperature series expansion (HTSE) method incorporating $T = 0$ information (ground state energy, dispersion) from a CUT method, see [51]. Discussing the models arising from the two parameter $0 < x = J_l/J_r \quad 1$ and $0 < x_{\text{cyc}} = J^B_{\text{cyc}}/J_r \ll 1$ subspace a competition was found between the leg coupling x and cyclic exchange x_{cyc}. The leg ordering stabilizes antiferromagnetic ordering against magnetic perturbations and shifts the peak to higher temperatures while decreasing its height. The frustrating cyclic exchange x_{cyc} leads to a decrease of the overall dispersion [52, 51]. It shifts the specific heat and susceptibility peaks to lower temperature with increasing x_{cyc}. The results of [50] were compared with our results and a good agreement was found [144]. The HTSE method used involves knowledge about the ground state energy and the low-temperature asymptotics. When this behavior is not precisely known the HTSE becomes unstable at low temperatures.

In the reference points (Fig. 5.8) of the rung-singlet phase, we see that the specific heat peak of the point at $\theta = -2/9\pi$ is higher and located at higher temperatures than the peak in the Heisenberg model. This behavior can be explained in the context of the results from the previous section: At $\theta = -2/9\pi$ the system shows the rung-singlet character more clearly than at $\theta = 0$ where stronger admixtures of triplets play a role. A more detailed discussion for the interesting region in the vicinity to the transition to the ferromagnetic regime will be given in Section 5.5.5.

The vector-chirality phase shows a clear maximum but has a pronounced shoulder at higher temperatures which is a remnant of the double-peak structure observed in the neighboring scalar-chirality phase. In the dominant-collinear-spin phase a strong peak appears at low temperatures which can be interpreted as a consequence of a flat dispersion in the low-lying excitation spectrum.

5.2.4 Specific heat of the ferromagnet

The excitation spectrum of a ferromagnet is described by spin waves which are magnons with a quadratic dispersion in the long wave-length limit. There is no excitation gap above the highly degenerate ground state. These properties cause a rapid increase of the entropy for temperatures close to $T = 0$ resulting in a specific heat $c \propto T^{1/2}$ without the exponential factor.

The specific heat features a broad peak with a maximum at high temperatures at the ferromagnetic reference system in Fig. 5.8. This behavior is owed to the fact that ferromagnetic excitations lie well below other excitation energies which set in at a higher temperature, compare Figs. 2.1 and 5.2. These properties including the low-temperature behavior can be seen in the reference model at $\theta = -2/3\pi$.

5.2.5 Specific heat in the phases with doubly-degenerate ground state

Double peaks in the specific heat have been theoretically and experimentally observed in a number of spin systems. The double-peak structure is a signature of two different kinds of excitations on well-separated energy scales.

In [145], a double peak structure appeared in the thermodynamics of layered Ising models. Ordering of finite regions and global ordering of infinite range, in different temperature ranges leads to the structure of the specific heat curves in this three dimensional model. Several models show a specific-heat double peak when an external magnetic field is applied. This helps with the interpretation of the underlying type of excitation. The $(1, \frac{1}{2})$ ferrimagnet $H = \sum_{j=1}^{N} \left(\mathbf{S}_j \cdot \mathbf{s}_j + \delta \mathbf{s}_j \cdot \mathbf{S}_{j+1}\right)$, with two kinds of spin $S = 1$, $s = \frac{1}{2}$ and an optional dimerization δ, is an example for a system in which application of a magnetic field leads to a separation of energy scales [146, 147, 148, 149]. As a result, the specific heat shows two pronounced peaks each of which can be associated with one out of two dominant excitations. The low-energy spectrum can be described in terms of spin wave theory [150]. The spin-wave-theory approach starts from a Néel state with a macroscopic

magnetization $M = (S - s)N$. The resulting energy dispersion gives both a ferromagnetic, gapless excitation branch (Goldstone modes) and antiferromagnetic gapped excitations. The antiferromagnetic zig-zag spin chain in magnetic fields was studied by TMRG in [151]. They found a double peak structure at fields above h_{c2} which gives the onset of saturation. Here, a down spin in the otherwise fully polarized state can be regarded as a spinless fermion. The additional low-temperature peak moves to lower temperatures when h approaches h_{c2} from above. From this it was concluded that the peak could be interpreted as divergence of the density of states at the bottom of the dispersion curve.[151]

In an $S = 1/2$ alternating Heisenberg chain system F_5PNN a second low energy peak was measured [152] for a field strength $h_{c1} < h < h_{c2}$ which moves to lower temperatures with increasing field. Thermodynamical properties of magnetic field effects on the ladder compound $Cu_2(C_5H_{12}N_2)_2Cl_4$ were measured by NMR in [153, 154]. Theoretical studies of two-leg Heisenberg ladders without four-spin interaction were performed by TMRG in [131] and the magnetization and specific-heat properties were essentially confirmed. The low-energy spectrum of the ladder in a strong magnetic field model can be described in terms of an effective XXZ Heisenberg model. It shows soft modes at field strengths right above the critical fields which marks the onset of zero magnetization. This is exactly the region where a double peak occurs in the specific heat [131].

The so-called delta chain or saw-tooth chain was studied in [155, 156, 157]. It shows a double peak in the specific heat which is a result of the presence of topological excitations called kinks and anti-kinks which always appear in pairs in a frustrated quantum chain with a doubly degenerate ground state. There is a mass associated with the quasi-particle anti-kink. The low-temperature peak position was shown to depend on the creation energy of an anti-kink while the kinetic energy of the anti-kink gives the broadening of this peak. A high anti-kink mass, thus, gives localization of the quasi-particles leading to a large divergence in the density of states and to a sharp peak. Having a doubly degenerate ground state and including frustration, the delta chain might give the correct scenario for the excitations in the spontaneously broken symmetry phases of the spin ladder.

We conclude that there are two well-separated energy scales for the excitation spectrum of systems which show a double peak in the specific heat. Additionally, the dispersion of the lower excitations is supposed to be flat to give a sharp shape of the low-temperature peak.

For a discussion of the staggered-dimer phase and the scalar-chirality phase of the spin ladder, we have to review the ground state properties. We concentrate on the staggered-dimer phase because the scalar-chirality phase is described by the duality transformation of the former phase. The sketch of the ground state of the staggered-dimer phase exhibits dimers on the legs arranged in a staggered order. A discussion of a model with this ground-state structure has been given in terms of a matrix product ground state in [158]. This approach started from a matrix product state of the form (2.27) which was considered to be a ground state of a special ladder class which includes four-spin exchange but has no common point with our model. In this setting, they managed to calculate the low-lying spectrum by constructing variational states. Two types of excitations were considered: A

singlet-triplet excitation where a dimer breaks up, and a topological excitation in terms of solitons where the staggered order is shifted by one site. The excitation gaps of the different excitations depend on some model parameters. There is also a dispersionless magnon mode present which is usually high in energy.

Since the doubly degenerate ground state is a feature of the staggered-dimer phase in the spin ladder with cyclic exchange and the staggered-dimer configuration is a good sketch of its properties, we suggest that the picture of the low-lying excitations can be transferred to our case as well. In this case, the low-temperature peak reflects low-lying elementary excitations as described above while the rest of the spectrum sets in at higher temperatures.

As a support for this picture, we consider the matrix-product state with staggering, given in Eq. (A.23) with $\sigma = -1$ and u real. The state is formed by the plaquette operators $|\phi_{1_0}^{\times}\rangle$, $|\phi_{1_0}^{\perp}\rangle$, and $|\phi_0^{\parallel}\rangle$ (for $u = 1$) only. In Fig. 5.9, we see that, indeed, these plaquette operators have the highest expectation values in the low-temperature regime. Their decrease marks the low-temperature peak. The high-temperature peak is located at a temperature where the plaquette-singlet state loses weight compared to a state with triplets on legs.

Since the scalar-chirality phase is dual to the staggered-dimer phase, we can extend the above argumentation via the duality transformation (1.8) to this phase. Here, the same plaquette states are expected to dominate the ground state with $|\phi_0^{\times}\rangle$ (for $u = \mathrm{i}$) being now the relevant $S = 0$ plaquette state.

5.2.6 Specific heat for the whole parameter space

In order to see how the specific heat evolves within the whole parameter space, we calculated it at several further points. The local maxima of the specific heat were determined numerically. They are plotted in Fig. 5.11 and their heights are shown.

This specific heat peak of the rung-singlet phase persists within the whole phase. The highest temperature associated with this peak takes the value $T = 0.88\tilde{J}$ and is located at $\theta = -0.193\pi$. At the staggered-dimer-phase boundary, the peak temperature decreases continuously to $T \approx 0.2\tilde{J}$. In the close vicinity of the phase transition to the ferromagnetic phase the specific heat shows two local maxima. We will comment on that in detail in Section 5.5.5.

The staggered-dimer phase is characterized by a double peak-structure (5.8). There is a steep slope at lower temperatures and very slow decay for $T \to \infty$. The low-temperature peak is located at $T = (0.2 - 0.4)\tilde{J}$. It emerges continuously from the rung-singlet-phase peak. The high-temperature peak is not yet present at the phase transition to the rung-singlet phase, but evolves from a shoulder. It is located at $T = (0.5 - 0.8)\tilde{J}$. The scalar-chirality phase shows the same double-peak structure as the preceding phase. The lower temperature peak lies again in the range $T = (0.2 - 0.4)\tilde{J}$. The high-temperature peaks is located between $T = 0.9\tilde{J}$ and $T = 1.2\tilde{J}$. Both peaks get shifted to higher temperatures with increasing θ.

In the vector-chirality phase the high-T peak degenerates to a shoulder again. The low-

a.

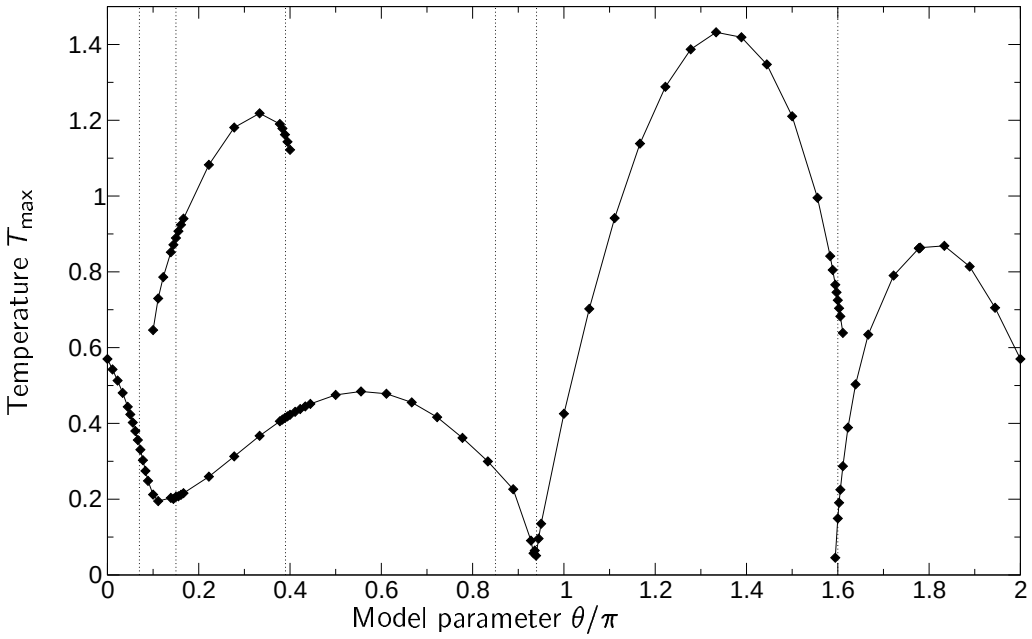

b.

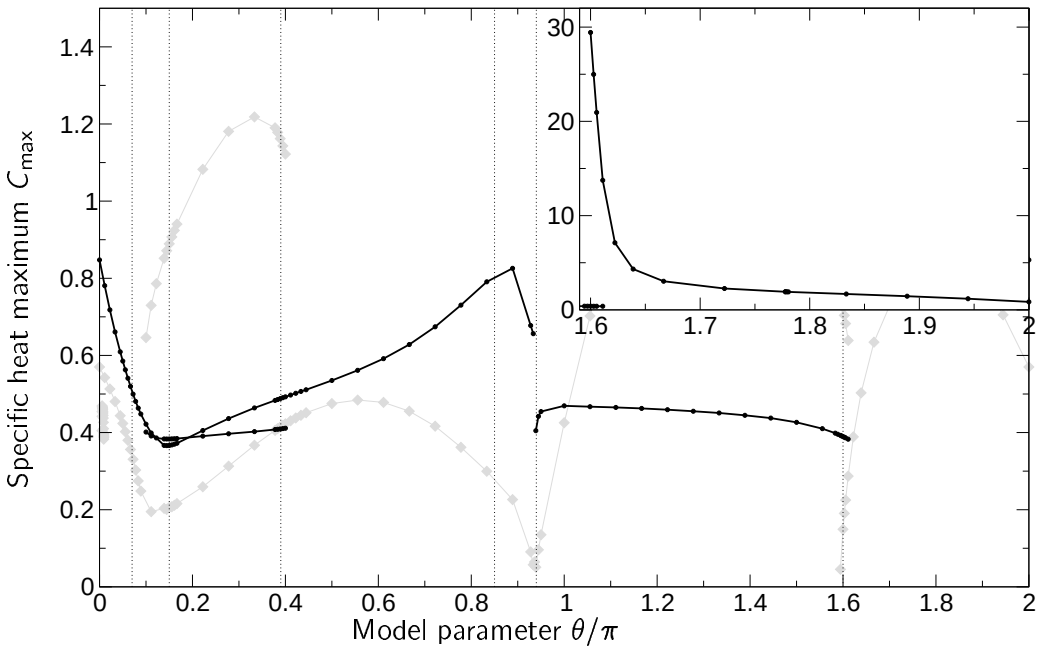

Figure 5.11: Local maxima of specific heat curves versus model parameter θ. a. Temperature of peak b. Maximal specific heat at peak (Inset: Zoom for rung-singlet region, gray shaded: Temperature from a.). Diamonds/circles are data from TMRG ($m = 300$). The solid lines serve only as a guide to the eye. The phase boundaries proposed in [1] have been included as vertical dotted lines.

temperature peak increases constantly with the system parameter θ. The peak reaches a highest temperature $T = 0.48\tilde{J}$ at $\theta = 0.58\pi$. No distinct feature is found in the dominant-collinear-spin phase which is connected to the vector-chirality phase by a smooth crossover. We have a pronounced peak at low temperatures which shifts to zero temperature in approaching the transition to the ferromagnetic phase. The ferromagnetic phase has a single broad peak. It is located at infinitely small temperature at the phase transition from the dominant-collinear-spin spin phase and shifts to maximum temperature $T = 1.44\tilde{J}$ at $\theta = -0.651\pi$. The peak decreases to a temperature of $T \approx 0.73\tilde{J}$ at the boundary to the rung-singlet phase.

In the discussion of the phase transition in the model (Section 5.5), we will refocus on the specific heat. There, we will explain the special properties of the specific heat in the vicinity of the first order quantum phase transitions.

5.3 Magnetic susceptibility

The magnetic susceptibility describes the response of a system to a magnetic field. More formally, it is the derivative of the expectation value of the magnetization for a specific magnetic field h_0:

$$\chi_M(h_0) = \frac{\partial \langle m(h) \rangle)}{\partial h}\Big|_{h_0} \tag{5.20}$$

The zero field susceptibility $\chi_\mathrm{M} = \chi_\mathrm{M}(h = 0)$ contains information about the magnetic excitations of a model. Since, in numerics, applied fields always have a finite size, we have to replace the derivative from (5.20) by a difference quotient:

$$\chi_\mathrm{M} \approx \frac{\langle m(h) \rangle - \langle m(-h) \rangle}{2h} = \frac{\langle m(h) \rangle}{h}, \quad \text{if } \langle m(\Delta h) \rangle = -\langle m(-h) \rangle \tag{5.21}$$

with a small field h. Thus, we first have to consider the magnetization curve before we numerically calculate zero temperature susceptibilities. The difference quotient is generally stable for different small field sizes in the antiferromagnetic regime and a field size of $h \approx 0.05$ is often appropriate.

In Fig. (5.12), we present the magnetic susceptibilities of some reference points in different phases. As for the specific heat some general forms of temperature dependence related to the properties of the studied model can be found.

In the rung-singlet phase, the susceptibility shows a pronounced peak with an exponential decay to $T \to 0$. The exponential decay results from a finite excitation gap in this phase. In [50], the susceptibility of the spin ladder with cyclic exchange was calculated by HTSE and showed to be consistent with our data. In the dominant-collinear-spin phase, the same behavior is observed as in the rung-singlet phase, but the peak is moved to lower temperatures. Here, ferromagnetic excitations lie low in energy and, thus, give a high contribution to the entropy at low temperatures. In the representative model of the vector-chirality phase, we see a flat, very broad peak. The susceptibility seems to turn to finite

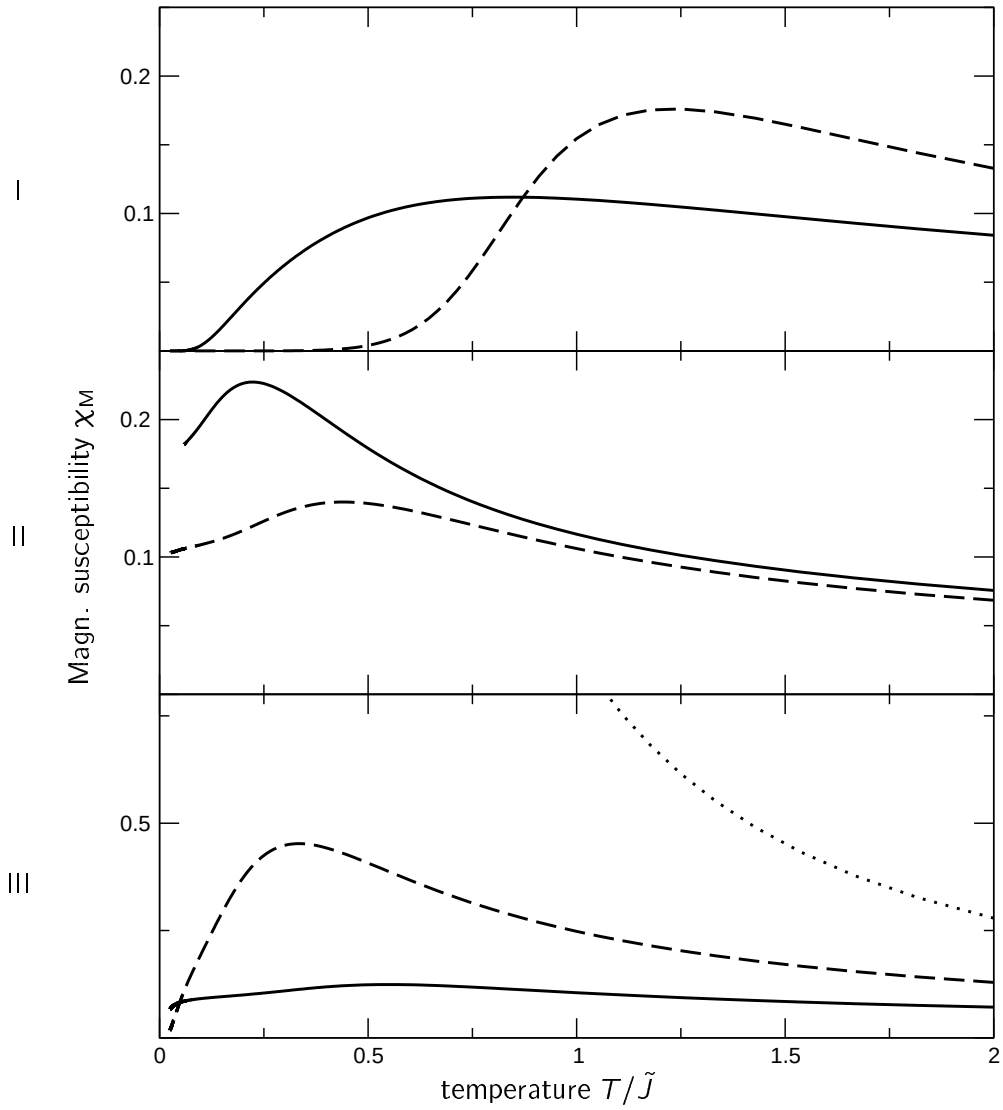

Figure 5.12: Magnetic susceptibility versus temperature for representative systems in the various phases. I: rung-singlet phase at $\theta = -2/9\pi$ (dashed line) and $\theta = 0$ (solid), II: staggered-dimer phase at $\theta = 1/9\pi$ (solid), and scalar-chirality phase at $\theta = 1/3\pi$ (dashed), III: vector-chirality phase at $\theta = 5/9\pi$ (solid), dominant-collinear-spin phase at $\theta = 8/9\pi$ (dashed), and ferromagnetic phase at $\theta = -2/3\pi$ (dotted). The susceptibility diverges for the ferromagnetic phase. The low-temperature regime is plotted in Fig. 5.14. Data from TMRG-calculation.

values for $T \to 0$. Calculations for different magnetic field sizes showed no essential difference in the curvature. However, in a closer zoom, we found a sudden decay for

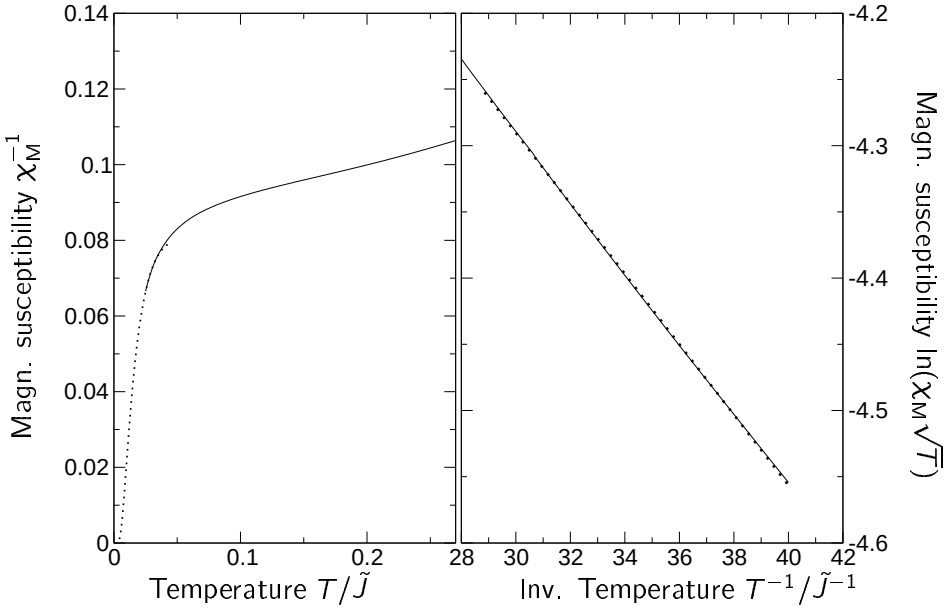

Figure 5.13: Low-temperature behavior of magnetic susceptibility for $\theta = 5/9\pi$ (vector-chirality phase). The solid curve in both plots is the susceptibility data from TMRG ($h = 0.05, m = 200$). On the right hand side we plotted $\ln(\chi_M\sqrt{T})$ against inverse temperature and applied a linear fit (dotted). This fitted curve was added to the left plot which is a zoom of the lower curve of Fig. 5.12 II.

$T \to 0$ at $T \approx 0.05$ (Fig. 5.13, left plot). In [37], a low temperature approximation was given for the magnetic susceptibility of the Heisenberg ladder

$$\chi_M \propto \frac{1}{\sqrt{T}} e^{-\frac{\Delta}{T}} \tag{5.22}$$

based on the same assumptions that lead to (5.17). Referring to this low-temperature approximation, we plotted $\ln(\chi_M\sqrt{T})$ against T^{-1}(Fig. 5.13, right plot). The expected linear behavior is apparent. A linear regression gives a slope of $\Delta = 0.0267$. No precise estimate for the excitation gap can be given since the finite field of $h = 0.05$ is of the same order of magnitude as Δ. However, for the model with $\theta = \pi/2$ a lower bound $\Delta \geq 0.016 J_{cyc}$ to the system gap of the same order of magnitude was given [159] which is consistent with our data.

The magnetic low-temperature properties of a ferromagnet can be described properly by spin-wave theory. For the spontaneous magnetization in the limit of $h \to 0$ one obtains Bloch's $T^{3/2}$ law [160, 161] for low temperatures:

$$m(T) \approx m(0)\left[1 - \alpha T^{3/2}\right] \tag{5.23}$$

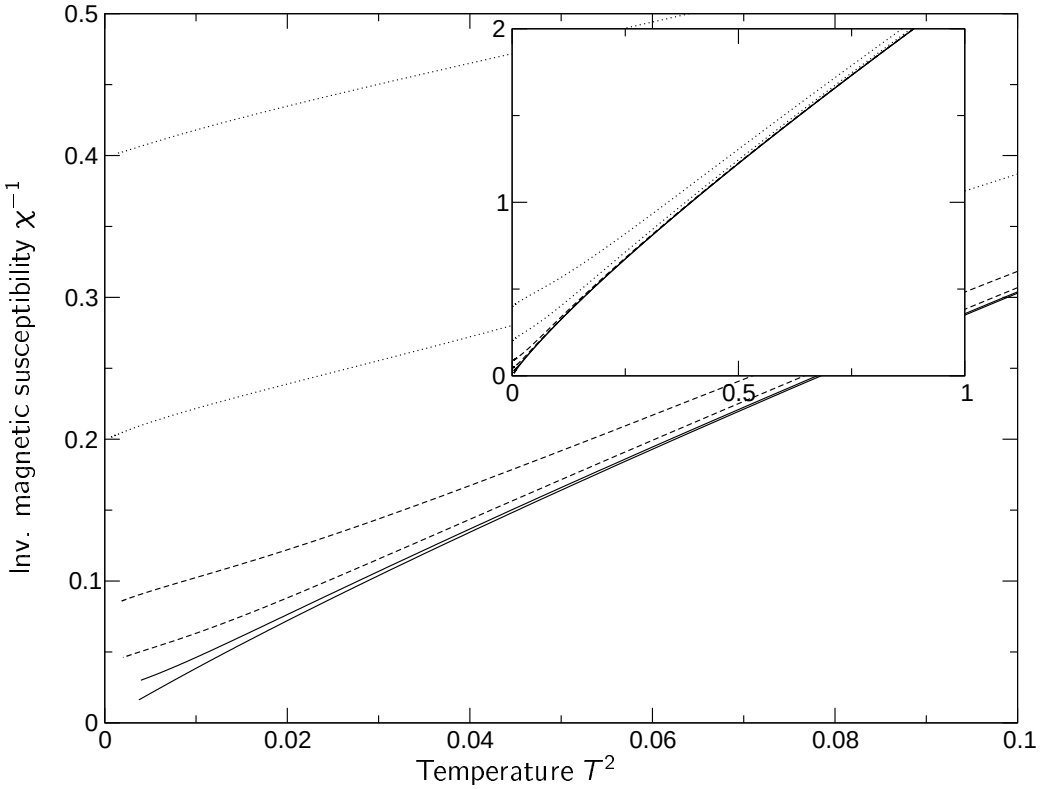

Figure 5.14: Inverse magnetic susceptibility versus squared temperature for the ferromagnetic model at $\theta = -6/9\pi$ calculated for magnetic fields of various strength. The curves (from bottom to top) belong to fields of strength $h = 0.001, 0.005$ (solid lines), $h = 0.01, 0.02$ (dashed lines), $h = 0.05, 0.1$ (dotted lines). In the inset, the same curves for a broader temperature range are shown. We see an excellent agreement with the expected $\chi \propto T^{-2}$ behavior in the limit for vanishing magnetic field. Data from TMRG with $m = 300$.

This approximation contains the saturated magnetization $m(0) = SN$ (for a number N of spins S) and a constant α. The zero-field susceptibility diverges in the limit $T \to 0$ like

$$\chi_{\text{ferro}} \propto \frac{1}{T^2} \tag{5.24}$$

as was shown for isotropic ferromagnetic Heisenberg chains with arbitrary spin by thermodynamic Bethe ansatz [162]. We expect this behavior for the ferromagnetic spin ladder as well because it can be mapped to the ferromagnetic spin-1 Heisenberg chain. We calculated the susceptibility according to (5.20) and present a plot of the inverse susceptibility in Fig. 5.14. Our results show clearly the predicted asymptotics. Note that the calculation were performed down to very low temperatures $T \approx 0.005$.

The phases with doubly-degenerate ground states and very small excitation gap both show

a flat susceptibility curve. The susceptibility exhibits a peak located at the position of the low-temperature peak of the specific heat data which is a signature of the spectrum of low-lying soliton and magnon excitations of the staggered ground states. The susceptibility stays finite down to low temperatures. However, the TMRG data ($m = 200$, $\epsilon = 0.05$) is reliable down to $T \approx 0.02 - 0.05$ only. Due to the small excitation gap [159] in these phases the correct low-temperature cannot be determined from the magnetic susceptibility calculated by TMRG.

5.4 Generalized susceptibilities

Within its phase diagram the spin ladder with cyclic exchange exhibits two phases with a spontaneously broken discrete symmetry including a two-fold degenerate ground-state and an excitation gap. An adequate way to study a system with a degenerate ground state is to apply a small external symmetry-breaking field and to measure the response of the system. The sensitivity of system for small perturbation is captured by a (generalized) susceptibility.

This approach was applied to n-leg spin ladders with third-nearest-neighbor two-spin interaction [163]. The spontaneous dimerization of the ground state of odd-leg ladders was revealed for a considerable amount of frustrating third-nearest-neighbor coupling from a $T = 0$ DMRG study.

In our case, the phases with spontaneously broken symmetry are the staggered-dimer and the scalar-chirality phase. In the case of the staggered-dimer phase, the order parameter is

$$\mathcal{O}_{\mathrm{SD}} = \sum_j \mathrm{e}^{i\pi j} \left(\mathbf{S}_{1,j} \cdot \mathbf{S}_{1,j+1} - \mathbf{S}_{2,j} \cdot \mathbf{S}_{2,j+1} \right). \tag{5.25}$$

Its ground state expectation values should be equal in size, but of opposite sign for either of the two ground-states. However, without external symmetry-breaking the two degenerate ground-states are inextricably entangled, thus no finite expectation value of the order parameter can be measured. In order to reveal the degeneracy by TMRG we apply a small but finite field α which couples the order parameter to the Hamiltonian of the system:

$$H_{\mathrm{eff}} = H + \alpha \, \mathcal{O}_{\mathrm{SD}} \tag{5.26}$$

Regarding this effective system, the TMRG method allows us to calculate the thermal expectation value

$$O_{\mathrm{SD}} = \left\langle \mathcal{O}_{\mathrm{SD}} \right\rangle_{H_{\mathrm{eff}}} \tag{5.27}$$

of the staggered-dimer operator [1] which we call "staggered-leg dimerization". With these quantities, we define the corresponding susceptibility

$$\chi_{\mathrm{SD}} = \left. \frac{\partial O_{\mathrm{SD}}}{\partial \alpha} \right|_{\alpha=0} \tag{5.28}$$

[1] Technically, it suffices to calculate the expectation value of the order parameter confined to a single plaquette.

for zero field $\alpha = 0$. If the system possesses a spontaneously broken symmetry, O_{SD} will stay finite as the external field α goes to zero or, in other words, the susceptibility will diverge for $T \to 0$. Note that this relation holds exactly only in the thermodynamic limit.

In the TMRG method, ladders of infinite size are studied. However, we have to deal with small, but finite fields in any numerical calculation and we calculate at finite temperatures by TMRG. Statements about the $T = 0$ behavior demand a careful extrapolation. For this reason it is instructive to consider a simple system meeting the proposed scenario in the low-energy regime.

The ferromagnetic Ising chain [127] in a longitudinal magnetic field

$$H = \sum_{j}^{N} -J\sigma_j\sigma_{j+1} - \sum_{j}^{N} h\sigma_{j+1} \tag{5.29}$$

($\sigma = \pm 1$ are classical spin variables, $J > 0$ the coupling constant, and h the applied magnetic field) possesses two fully polarized ground states and an excitation gap. Its Z_2-symmetry can be broken spontaneously. These properties are shared by the proposed character of the staggered-dimer and scalar-chirality phase. The thermodynamic properties can be calculated quite easily by a transfer matrix method making it an ideal test case.

We reinterpret the magnetization as the thermal expectation value of the order parameter

$$O_{\mathrm{SD}}(\alpha, T) = -\frac{1}{\beta}\frac{\partial}{\partial\alpha}\ln Z(\alpha, T) = \frac{\mathrm{e}^{\beta J}\sinh(\beta h)}{\sqrt{\mathrm{e}^{2\beta J}\sinh^2(\beta h) + \mathrm{e}^{-2\beta J}}}. \tag{5.30}$$

For the limit $T \to 0$, the expectation value converges to saturation

$$O_{\mathrm{SD}}(\alpha, T \to 0) = 1 \tag{5.31}$$

which has to be adjusted to the appropriate value. The susceptibility becomes

$$\chi_{\mathrm{SD}}(0, T) = \frac{\mathrm{e}^{J/T}}{T} \tag{5.32}$$

for the zero field limit.

5.4.1 Staggered-dimer susceptibility

As a representative system, we discuss the staggered-dimer susceptibility of the model with $\theta = \pi/9$ in detail. First, we determine the expectation value of (5.30) in various fields (see Fig. 5.15 a.). We get approximately the correct line shapes predicted by (5.30) and a $J \approx 0.05$ by an estimate two-parameter fit which is of the order of magnitude of the energy gap [159]. In contrast to the magnetization in the Ising chain, the staggered-leg dimerization (5.31) of the ladder system does not approach a common saturation value O_{sat} in the $T \to 0$ limit for all field strengths. These differences show the limitations of the Ising approximation. Although we believe that the plots show the correct low-temperature data,

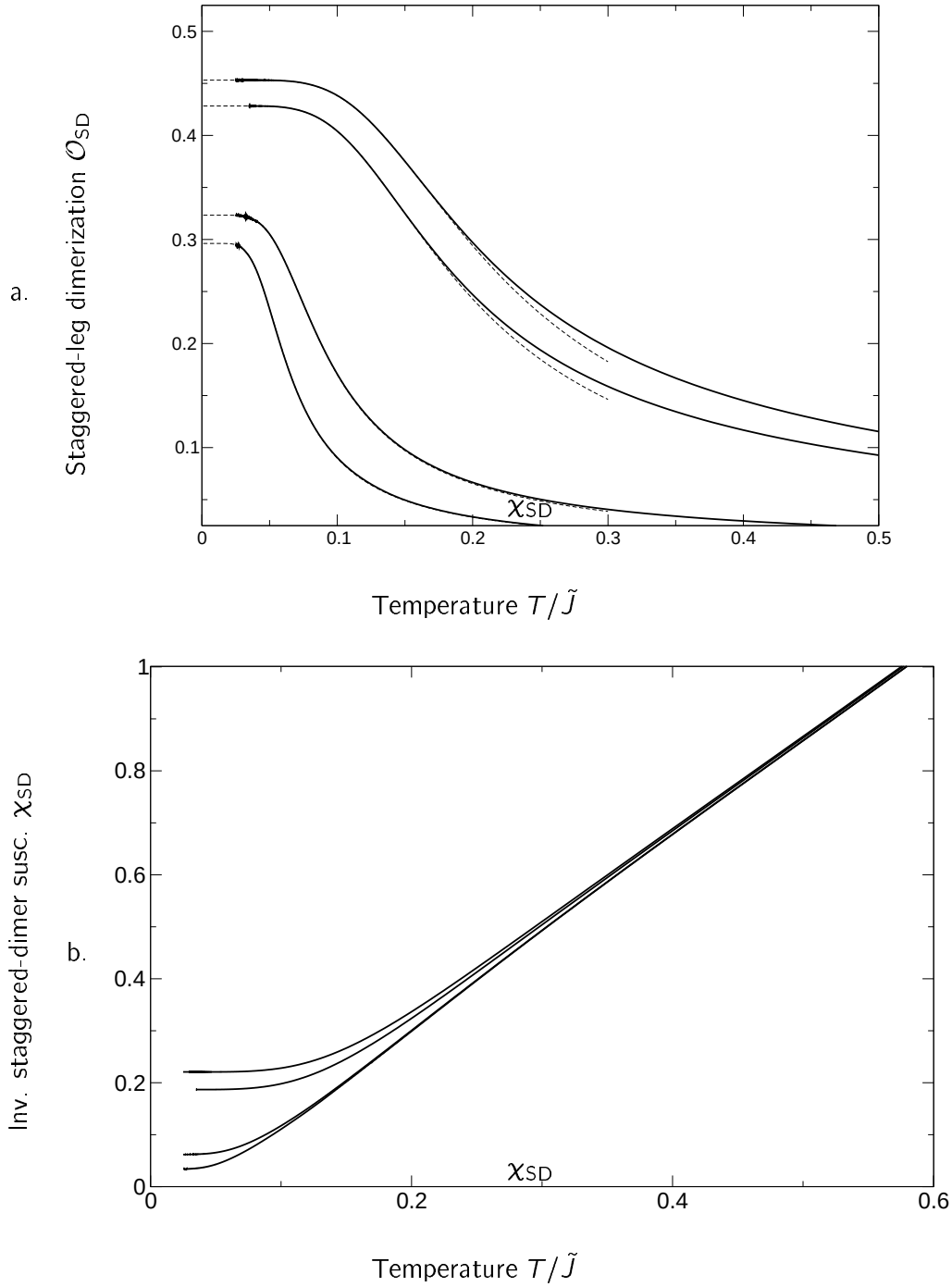

Figure 5.15: a. Expectation value of staggered-leg dimerization versus temperature for the fields $\alpha = 0.1, 0.08, 0.02, 0.01$ (from top to bottom). The black solid lines are TMRG data ($m = 100$)), the dotted curves are separate fits of the Ising susceptibility (5.30) with a the $T \to 0$ value as an additional degree of freedom.
b. Inverse staggered-dimer susceptibility versus temperature calculated by the fields $\alpha = 0.1, 0.08, 0.02, 0.01$ (from top to bottom).

a small deviation to lower values of staggered-leg dimerization still seems likely[2]. From the dimerization data, we calculate the staggered-dimer susceptibility. In Fig. 5.15 b., the inverse value is plotted against temperature. The linear increase at higher temperatures can be motivated by Eq. (5.32) which is an analog of the Curie law for ferromagnets. At low temperatures the curves separate. All curves still tend to finite susceptibilities for $T \to 0$, but this value decreases for smaller fields.

In Fig. 5.16, we plotted the staggered-dimer susceptibility for the reference points from different phases. The staggered-dimer susceptibility is very flat in the ferromagnetic phase. For the other phases, the susceptibility approaches finite values for $T \to 0$ except for the staggered-dimer phase where it diverges. An interesting behavior can be observed in the rung-singlet phase. Here, the staggered-dimer susceptibility has a pronounced peak which increases in size and moves to lower temperatures as it approaches the staggered-dimer phase. It can be interpreted as an indication of the vicinity to the phase transition. In the phases with chirality, the susceptibility has a flat structure and an estimated finite value at $T \to 0$. The dominant-collinear-spin phase exhibits a susceptibility nearly identical to the susceptibility of the Heisenberg ladder.

5.4.2 Scalar-chirality susceptibility

The scalar-chirality phase is related to the staggered-dimer phase via the duality transformation (1.7). The appropriate order parameter is the scalar-chirality operator (2.19)

$$\mathcal{O}_{\mathrm{SC}} = \left(\mathbf{S}_{1,j}+\mathbf{S}_{2,j}\right) \cdot \left(\mathbf{S}_{1,j+1}\times\mathbf{S}_{2,j+1}\right) + \left(\mathbf{S}_{1,j+1}+\mathbf{S}_{2,j+1}\right) \cdot \left(\mathbf{S}_{1,j}\times\mathbf{S}_{2,j}\right). \tag{5.33}$$

The scalar-chirality susceptibility χ_{SC} shall be introduced in analogy to the staggered-dimer susceptibility. The associated field shall be denoted by η.

We expect a divergence of the scalar-chirality susceptibility for the scalar-chirality phase in the $T \to 0$ asymptotics and finite or vanishing susceptibilities in the other phases. The susceptibilities of the reference points are presented in Fig. 5.17. The models in the rung-singlet phase have a single peak at $T \approx \tilde{J}$ and finite susceptibility at $T \to 0$. The curves have the same form as for the staggered-dimer susceptibility but the peaks shifted to higher temperatures and the susceptibility is weaker in the whole temperature range. This difference is caused by the larger distance to the scalar-chirality phase compared to the neighboring staggered-dimer phase. The vicinity of the scalar-chirality is sensed by the model in the staggered-dimer phase: It has a pronounced peak at low temperatures. The representative model of the dominant-collinear-spin phase has a peak at low temperatures and a finite susceptibility for $T \to 0$. The ferromagnetic model shows no significant response.

[2] It was not possible to calculate properties of models with a TMRG parameter larger than $m = 100$ down to very low temperatures because of numerical instabilities for $m > 100$. This phenomenon seems to be connected to the staggering which might carry the risk of over-estimating irrelevant states during the renormalization procedure. Further research on this matter would be desirable.

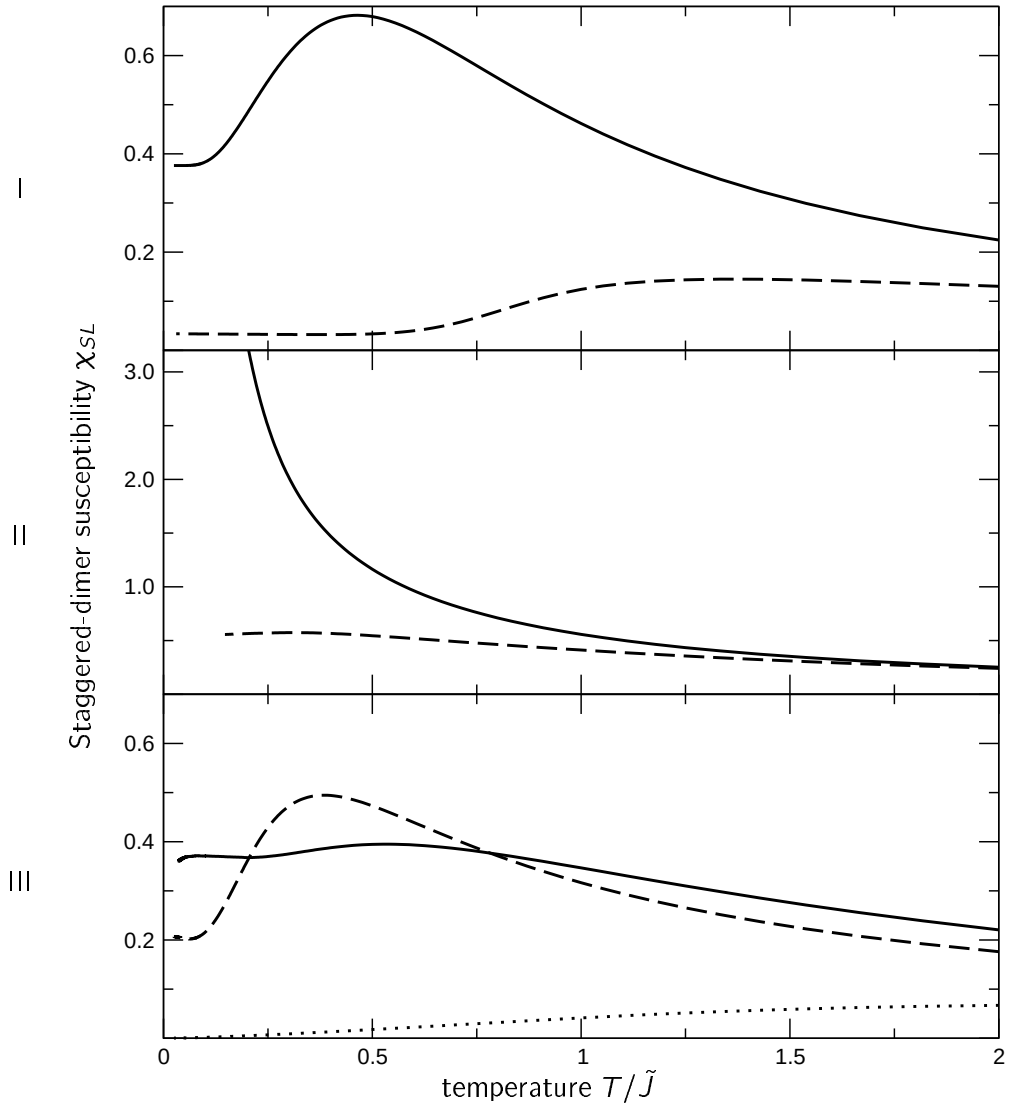

Figure 5.16: Staggered-dimer susceptibility versus temperature for representative systems in the various phases. I: rung-singlet phase at $\theta = -2/9\pi$ (dashed line) and $\theta = 0$ (solid), II: staggered-dimer phase at $\theta = 1/9\pi$ (solid), and scalar-chirality phase at $\theta = 1/3\pi$ (dashed), III: vector-chirality phase at $\theta = 5/9\pi$ (solid), dominant-collinear-spin phase at $\theta = 8/9\pi$ (dashed), and ferromagnetic phase at $\theta = -2/3\pi$ (dotted). Data from TMRG-calculation.

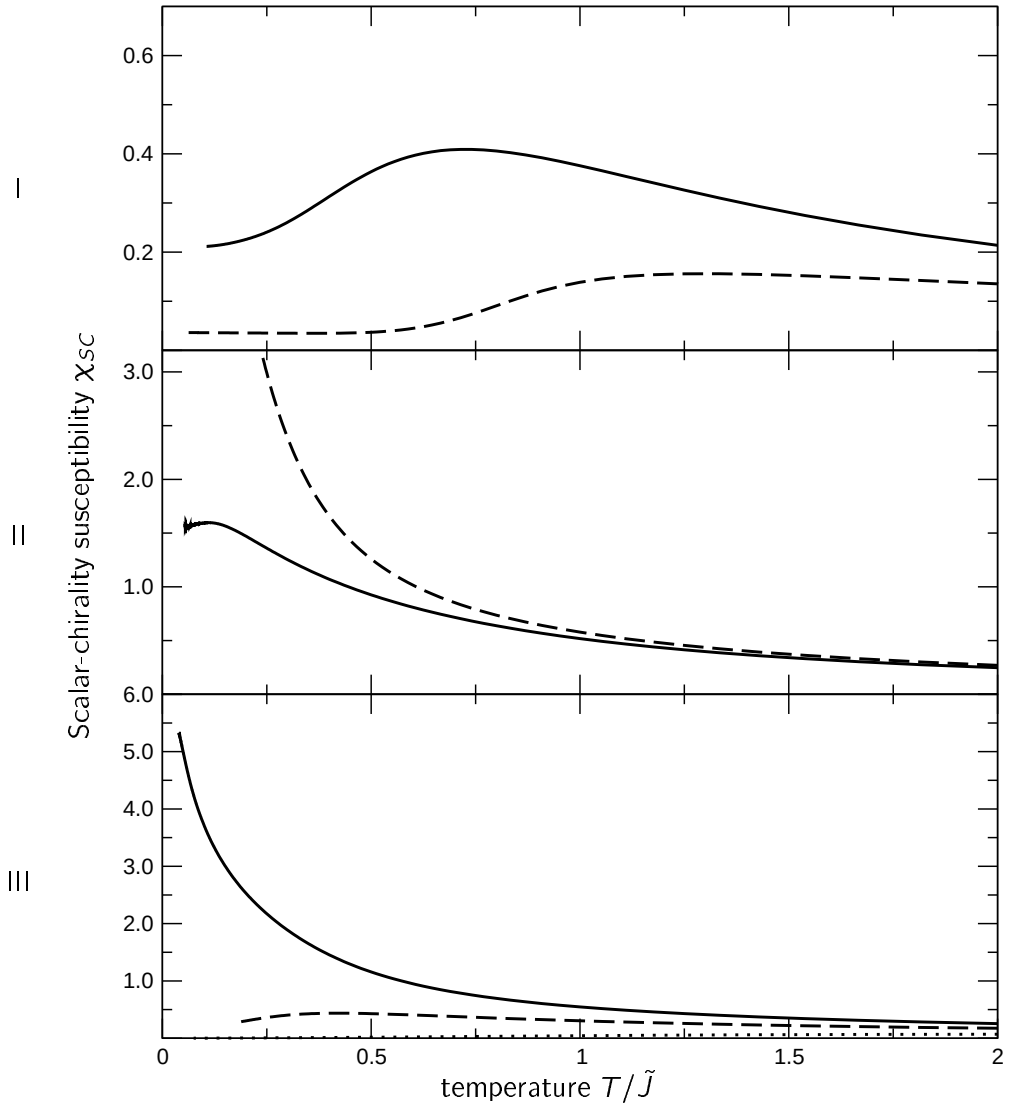

Figure 5.17: Scalar-chirality susceptibility versus temperature for representative systems in the various phases. I: rung-singlet phase at $\theta = -2/9\pi$ (dashed line) and $\theta = 0$ (solid), II: staggered-dimer phase at $\theta = 1/9\pi$ (solid), and scalar-chirality phase at $\theta = 1/3\pi$ (dashed), III: vector-chirality phase at $\theta = 5/9\pi$ (solid), dominant-collinear-spin phase at $\theta = 8/9\pi$ (dashed), and ferromagnetic phase at $\theta = -2/3\pi$ (dotted). Data from TMRG-calculation.

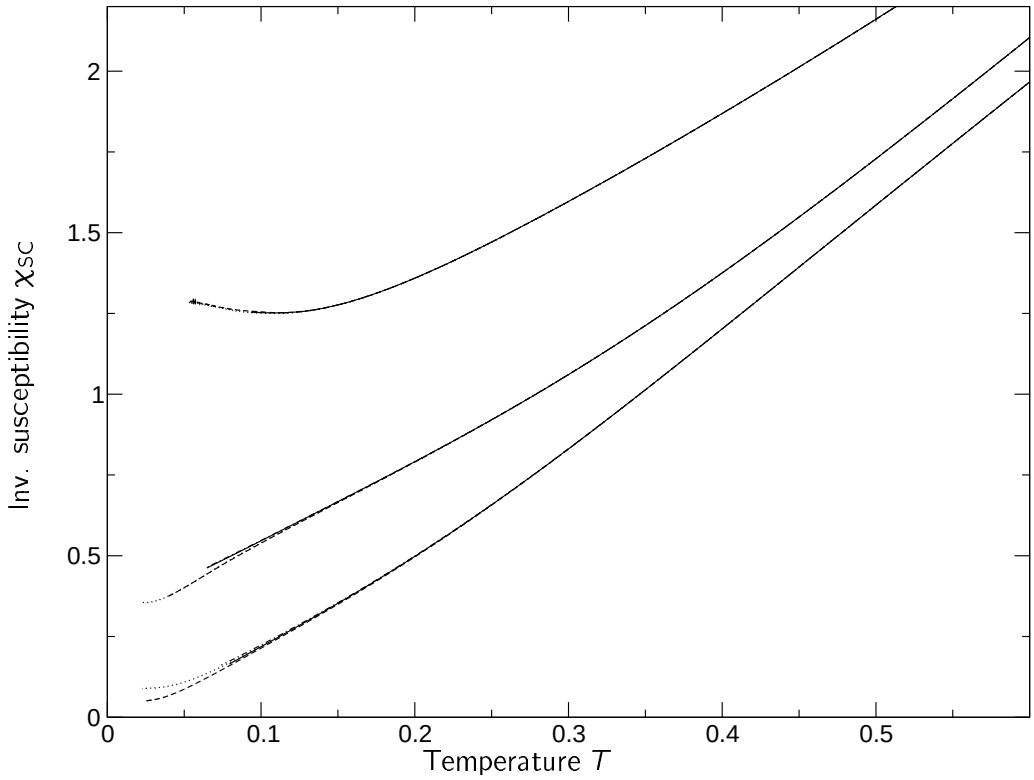

Figure 5.18: Inverse scalar-chirality susceptibility versus temperature for representative systems in the scalar-chirality phase (lower curves) at $\theta = 1/3\pi$ and neighboring phases (upper curves: staggered-dimer phase at $\theta = 1/9\pi$, central curves: vector-chirality phase at $\theta = 5/9\pi$). We calculated the susceptibility as the numerical derivative of the scalar-chirality with symmetry breaking fields η from TMRG with m conserved states (dotted: $\eta = 0.01$, $m = 200$; dashed: $\eta = 0.005$, $m = 200$; dot-dashed: $\eta = 0.01$, $m = 300$; solid: $\eta = 0.005$, $m = 300$).

Two candidates for a diverging scalar-chirality susceptibility can be identified from Fig. 5.17. The models in the phases with dominating chiral correlations both give a strong response to the scalar-chirality field. For a closer look, we plotted the inverse susceptibilities of these systems along with the reference point from the staggered-dimer phase in Fig. 5.18. As can be seen, the numerics is significantly better behaved in this case. DMRG parameter values up to $m = 300$ were reached and small fields $\eta \leq 0.01$ could be considered. We conclude from this data that the scalar-chirality susceptibility indeed only diverges in the scalar-chirality phase as expected. The vector-chirality phase still has a strong response at $T \to 0$ but has no spontaneously broken symmetry. In the staggered-dimer phase, the susceptibility reaches a strong maximum a low temperatures but decreases for $T \to 0$.

The generalized susceptibilities proved to be a useful tool to analyze the excitation spectrum

of the models. We provided evidence for a broken symmetry of the ground state in two phases from thermodynamical data. The vicinity of phase transitions was seen in the susceptibilities belonging to the ordering involved. While the divergence of the scalar-chirality susceptibility in the corresponding phase could be clearly confirmed, the staggered-dimer susceptibility suffered from numerical instabilities. This could be a point to concentrate on in further studies.

5.5 Phase transitions

In this section, the focus will be on the phase transitions between the phases of the spin ladder with cyclic exchange. We will discuss the influence of phase transitions on thermodynamical quantities in the framework introduced above. Estimates for the location of the phase transitions as well as a comparison to results from other studies will be provided.

5.5.1 Rung-singlet phase to staggered-dimer phase

The second order quantum phase transition from the rung-singlet phase to the staggered dimer phase has been subject to discussions since the model class had been established. The existence of dimerized phases on a ladder with four-spin interaction has been shown in [164, 158, 165]. In [52, 166, 53], a dimerized phase was conjectured. Its existence was confirmed by a subsequent study [1] where the Lieb-Schultz-Mattis twist operator [167, 168] which signals the transition by a sign change, was applied. This critical point was also focused on in [166] where a central charge of $c = 3/2$ for the underlying conformal field theory was obtained from numerical calculations. It was claimed that the universality class it belongs to is described by the $k = 2$ SU(2) Wess-Zumino-Witten type in the continuum limit. Thus, it is a transition of the Takhtajan-Babujian-type[56, 57] which is characterized by a spontaneous breaking of discrete Z_2-symmetry.

Although agreement about the character of the phase transition has been reached, the precise point of the phase transition is still unknown. Earlier works based on DMRG proposed $\theta_c \approx 0.0889\pi$ [169] and exact diagonalization plus conformal field theory 0.060π[166]. In the year 2003, the transition points 0.09π [54], $(0.07 \pm 0.01)\pi$ [1], and $(0.0597 \pm 0.0003)\pi$ [170] have been obtained by DMRG studies. In the same year, with the CUT method the transition point was found at $(0.051 \pm 0.009)\pi$ [51].

The dense spectrum of the Hamiltonian (see Fig. 2.1, where the plaquette states lie close together in energy) and the small gap are the cause why it is so hard to get a precise numerical estimate of the phase transition. From the considerations of plaquette states and matrix-product variational states we identified three points of interest in the context of the phase transition: At $\theta = -\arctan(1/4) \approx -0.078\pi$, the variational state with lowest energy includes staggering. At $\theta = 0$, the staggered-dimer state crosses rung-singlet state in the matrix-product states and, at $\arctan(1/4) \approx 0.078\pi$, there is a level crossing in the plaquette states.

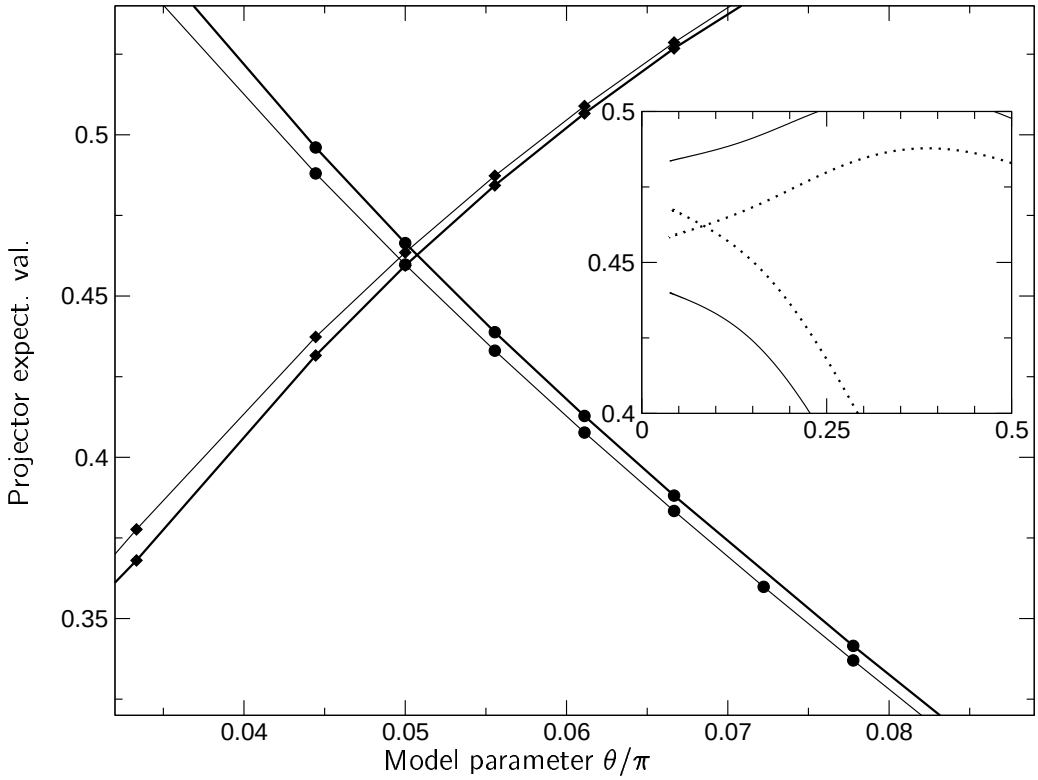

Figure 5.19: Plaquette projector expectation values versus model parameter. Level-crossing between plaquette states with highest contribution $S = 0$-state $\mathcal{P}_0^{\text{hi}}$ (circles) and $S = 1$-state $\mathcal{P}_1^{\times}$ (diamonds) at $T = 0.1$ (thin line) and $T = 0.05$ (thick line). In the inset: Expectation values of $\mathcal{P}_1^{\times}$ (upper lines) and $\mathcal{P}_0^{\text{hi}}$ (lower lines) for $\theta = 0.0500\pi$ (dashed) and $\theta = 0.0556\pi$ (solid).

From conformal field theory, we expect a linear low-temperature behavior (5.18) of the specific heat at the precise point of the second order phase transition. Indeed, our numerical data is consistent with a linear low-temperature behavior around $\theta = 0.05\pi$. No precise estimate for the location of the phase transition can be given, though, because small data fluctuations owed to the iterated truncation procedure defeat a trustworthy analysis at very low temperatures. We face the same situation in the numerics at the staggered-dimer to scalar-chirality phase transition and the scalar-chirality phase to vector-chirality phase transition.

In Fig. 5.19, we consider again the dominant plaquette projectors in both regimes. Indeed, at $\theta \approx 0.053\pi$ we observe a level-crossing from the plaquette singlet $\mathcal{P}_0^{\text{hi}}$ to the plaquette triplet $\mathcal{P}_1^{\times}$. Although this is not a proof for a phase transition it strongly indicates a change in the character of the ground state. The smooth crossover is consistent with the picture of a second order quantum phase transition. At the same point, we see a change

in the two-point rung-singlet correlation (see Section 5.1.1). In the rung-singlet phase, the probability to find two singlets on neighboring rungs is enhanced while it is suppressed in the staggered-leg phase. From both observations, we expect the precise location of the phase transition between $\theta = 0.0500\pi$ and $\theta = 0.0556\pi$.

5.5.2 Staggered-dimer phase to scalar-chirality phase

At $\theta = \arctan(1/2) \approx 0.1476\pi$, the model is self-dual and shows a U(1) symmetry because it is invariant under a transformation (1.7) with arbitrary φ [42]. The overlap between $\left|\phi_0^{\perp}\right\rangle$ and $\left|\phi_0^{\parallel,\times}\right\rangle$ vanishes at this point, see Fig. 2.2. The energetically lowest $S = 0$ state is $\left|\phi_0^{\parallel,\times}\right\rangle$, a superposition between the state with singlets on the legs and the state with singlets on the diagonals. This behavior can as well be observed in the thermal expectation values.

In the vicinity of the phase transition, the low-temperature specific-heat peak becomes smaller in size than the second peak. A minimum is reached exactly at the transition point. This can be explained by the fact that low-lying excitations close the gap at the phase transition and weight in the density of states is shifted from the peak maximum towards lower temperatures. In [131], a similar observation was made for a spin ladder under magnetic field.

5.5.3 Scalar-chirality phase to vector-chirality phase

The phase transition from the scalar-chirality phase to the vector-chirality phase was claimed to be in the same universality class as the rung-singlet to staggered-dimer transition [55]. Two DMRG studies references give its possible position $\theta_c \approx 0.38\pi$ [54] and $(0.39 \pm 0.01)\pi$ [1]. This the position near the parameter $\theta \approx 0.4\pi$ where the high-temperature peak in the specific heat becomes a shoulder of the other peak. This behavior could be related to the phase transition.

5.5.4 Vector-chirality/collinear-spin phase to ferromagnetic phase

For the first order quantum phase transition from the dominant-collinear-spin phase to the ferromagnetic phase, we have two exact boundaries. The parameter $\theta \approx 0.916\pi$ is a lower bound for phase transition from the variational states, and $\theta \approx 0.947\pi$ is an upper bound for phase transition from the plaquette states, see Section 2.5. The predicted value $\theta_c = 0.94\pi$ lies near the upper bound.

For the first order transition to the ferromagnetic phase, we expect a jump in the zero-temperature magnetic susceptibility. While the singlet ground state of the dominant-collinear-spin phase gives no response to an infinitely small magnetic field, the spontaneous magnetization leads to a divergence of the magnetic susceptibility in the ferromagnetic phase. We plotted the susceptibility of several points around the expected phase transition

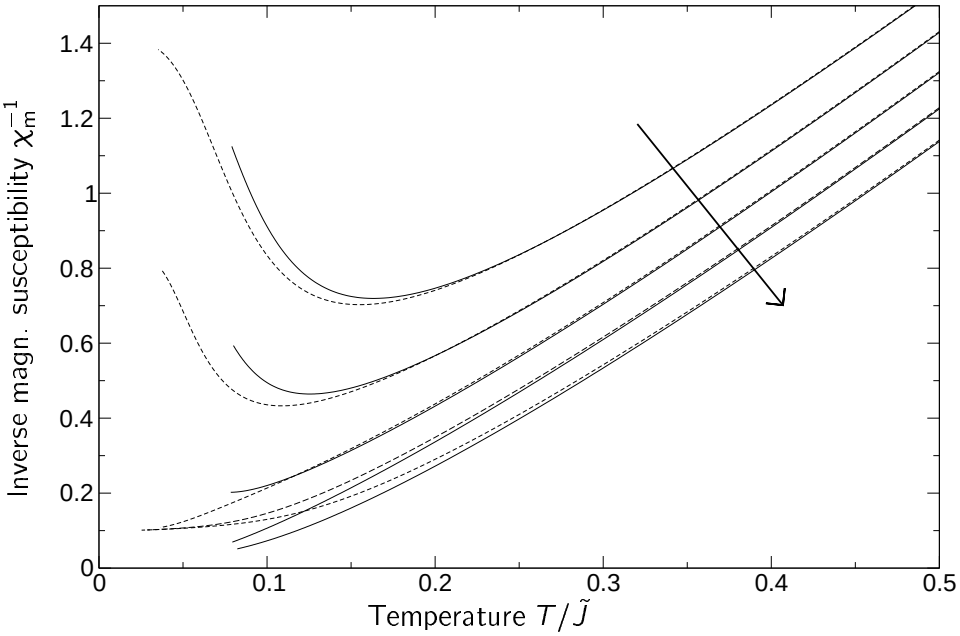

Figure 5.20: Inverse magnetic susceptibility versus temperature in the vicinity of the dominant-collinear-spin/ferromagnetic phase transition. For each model the susceptibility was calculated at a small magnetic field $h = 0.05$ (dashed lines) and $h = 0.01$ (solid lines). The susceptibility for the models $\theta/\pi = 0.922, 0.928, 0.933, 0.939, 0.944$ (in the sense of the arrow) is depicted. Data from TMRG ($m = 200$).

in Fig. 5.20. All curves show the expected linear Curie-law behavior for higher temperatures. For $\theta \leq 0.933\pi$, the inverse susceptibility changes curvature and increases again for $T \to 0$. This effect is strengthened for smaller magnetic fields. For $\theta \geq 0.939\pi$, the inverse susceptibilities tend to a finite value $\chi_m \approx 0.1$ for a field $h = 0.05$ and tend to a very small finite value $\chi_m \approx 0.02$ for a field $h = 0.01$. Note, at this point, that we need a small field to numerically calculate the zero-field magnetic susceptibility. This has two consequences: 1. The applied field itself can generally drive the phase transition which leads to an overestimation of the susceptibility which scales with the field strength in the phase with singlet ground state. 2. The zero-field susceptibility will never show a divergence for the estimate by difference quotient because the denominator is always finite due to the finite field in our calculations. Thus, the susceptibility will be underestimated for larger applied fields. Both effects can clearly be seen in Fig. 5.20. These observations suggest a phase transition at $0.933\pi < \theta < 0.939\pi$.

At the estimated point of the phase transition, the position of the specific heat is minimal with respect to temperature (see Fig. 5.11 a.). This behavior can be motivated by considering the plaquette states. At a first order phase transition we expect a level-crossing

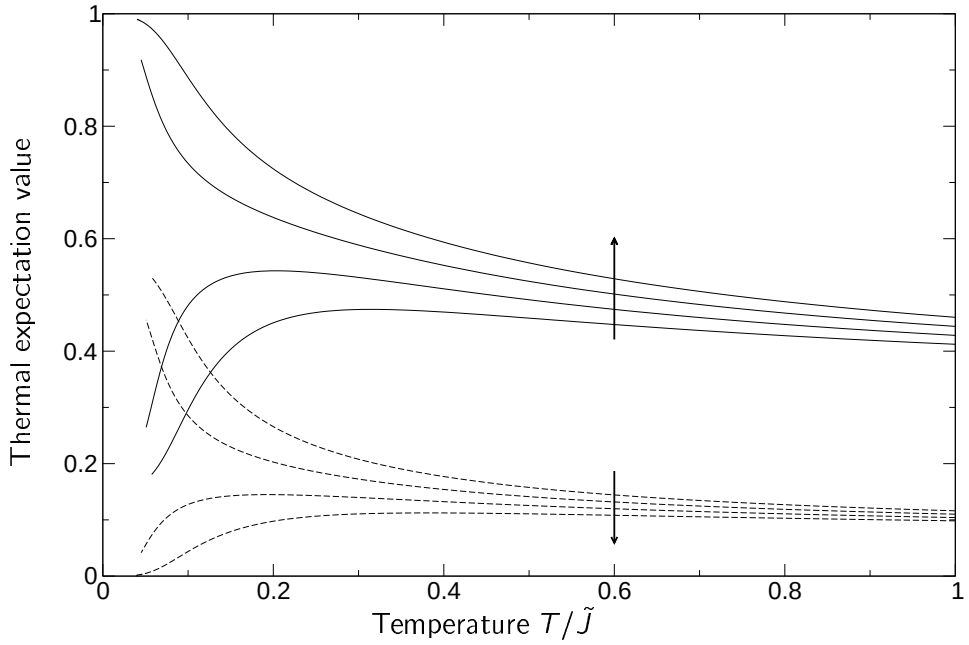

Figure 5.21: Thermal expectation value of plaquette operators $\langle \mathcal{P}_2 \rangle$ (solid line) and $\left\langle \mathcal{P}_0^{\times,\perp} \right\rangle$ (dashed line) versus temperature in the vicinity of the dominant-collinear-spin/ferromagnetic phase transition. The expectation values for the models $\theta/\pi = 0.928, 0.933, 0.939, 0.944$ (in the sense of the arrows) is depicted. Data from TMRG ($m = 200$).

of two phases with different characters. The ferromagnetic phase will give the maximum weight for the operator $\mathcal{P}_2$ which projects on the $S = 2$ subspace. The dominating, but not long-ranged order is locally described by the collinear-spin order parameter $\mathcal{O}_{\mathrm{Col}}$ (2.21) in the dominant-collinear-spin phase. Its expectation value can vary between $-\frac{1}{2}$ and $\frac{3}{2}$ and is close to maximum in the dominant-collinear-spin phase. In order to compare the influence of this competing orders, we consider the plaquette projector on the eigenstate

$$|\phi_0^{\times,\perp}\rangle = \frac{1}{2}\left(\sqrt{3}|\phi_0^{\perp}\rangle + |\phi_0^{\parallel,\times}\rangle\right) \tag{5.34}$$

of $\mathcal{O}_{\mathrm{Col}}$ which has maximal energy. Both projectors are plotted in Fig. 5.21. The thermal expectation values of the different models develop a significant distinction for low temperatures. The ferromagnetic systems ($\theta/\pi = 0.939, 0.944$) gain a high contribution of the $S = 2$ state as expected and suppress the thermal expectation value which is sensitive to collinear-ordering. The systems from the gapped phase ($\theta/\pi = 0.928, 0.933$) have low weight for the ferromagnetic states and a high contribution from $\left\langle |\phi_0^{\times,\perp}\rangle \right\rangle$. Assuming that these local expectation values give a correct estimate for the type of order present in the ladder, the phase transition is located at point θ where the dominating projector

weight changes in Fig.5.21. This is in the range $0.933\pi < \theta < 0.939\pi$ as suggested by the magnetic susceptibility data.

The specific heat has a peak at temperatures where states with a significant spectral weight become relevant weight in the thermodynamic ensemble indicated by a steep slope of the entropy. We can identify the relevant temperatures with the regions where the dominant plaquette states rapidly win weight. These regions move to $T = 0$ when the phase transition is approached.

The reason why the peaks are located at small temperatures comes from the fact that, in the vicinity of the phase transition, we have a flat dispersion spectrum. This can be seen in Fig. 2.1 The ferromagnetic plaquette state lies close in energy to the the rest of the plaquette spectrum at the phase transition we consider here. In the middle of the phase, the distance in energy of the plaquette excitations is maximal which is reflected in a maximum temperature of the specific heat peak.

5.5.5 Ferromagnetic phase to rung-singlet phase

The first-order quantum phase transition [1] from the ferromagnetic to the rung-singlet phase shows interesting behavior in the thermodynamics. In Fig. 5.22 we present the specific heat data of four representative points near that transition. For the points in the ferromagnetic phase, the specific heat scales like $\sqrt{T}$ (5.13) in the low-temperature regime. There is a broad peak at a temperature $T \approx 0.6\tilde{J}$. When we cross the transition to the rung-singlet phase we find that a very sharp and high peak at low temperatures arises. The broad peak from the ferromagnetic phase is, however, still present almost at the same position. For higher values of θ the sharp peak broadens and loses height and shifts to higher temperatures until it merges with the peak from the ferromagnetic phase at a value of $\theta \approx -0.380$. A similar pronounced behavior can be seen in the entropy (Fig. 5.23). Here, a steep increase at finite temperature corresponds to the peak which is found in the specific heat.

We will give a description of this phase transition by considering a possible scenario. In a second step, we will confirm the essential properties of this scenario and show the difference between the assumptions and the situation faced in the ladder in detail by a comparison with the numerical data.

Assume that the ladder rungs can carry either only singlets or triplets. No admixtures between rung-singlets and rung-triplets are allowed by a high energy barrier. In that case, the Hilbert space reduces to the product space of a singlet ladder state with only singlets on the rungs and the complete Hilbert space of a spin-1 chain. The spin-1 chain is considered to be in a ferromagnetic regime with a highly degenerate ground state and soft modes in the spectrum.

We introduce a parameter θ which varies the singlet and ferromagnetic energies such that a first-order phase transition indicated by the level-crossing of singlet and ferromagnet at $\theta = \theta_c$ and $T = 0$ is induced. At a point close to the phase transition the free energy of

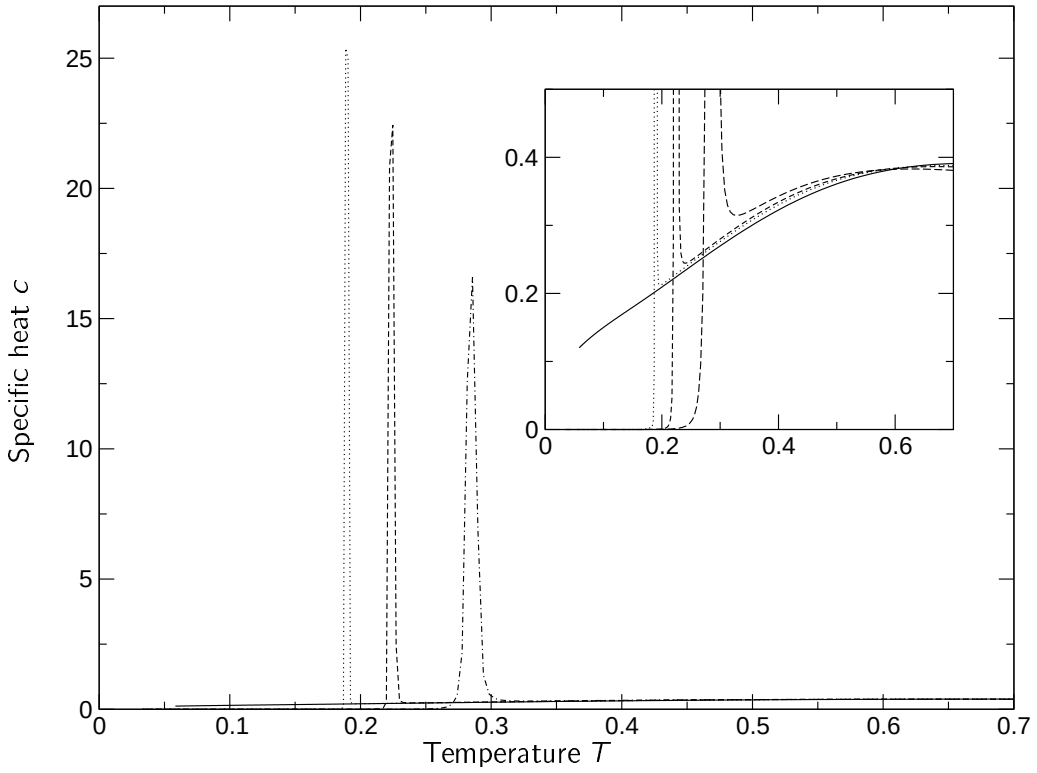

Figure 5.22: Specific heat near the ferromagnetic to rung-singlet phase transition. Plotted is data for $\theta = -0.403\pi$ (solid), $\theta = -0.397\pi$ (dotted), $\theta = -0.394\pi$ (dashed), and $\theta = -0.389\pi$ (dot-dashed line). The inset shows the same curves for a different scaling ratio. The peak of the ferromagnetic phase (solid line) survives at the inset of the rung-singlet phase. Here, we observe an additional very sharp peak at low-temperatures. Moving further into the rung-singlet phase the peak broadens, flattens and shifts to higher temperatures.

the singlet and the ferromagnet will read

$$F_{\mathrm{FM}} = E_{\mathrm{FM}} + \alpha T^{\frac{3}{2}}, \tag{5.35}$$

$$F_{\mathrm{RS}} = E_{\mathrm{RS}}. \tag{5.36}$$

at low temperatures. E_{FM} and E_{RS} are the ground state energies of the ferromagnet and the singlet state and α is a constant. The entropy of the ferromagnet is determined by spin wave excitation modes with a quadratic dispersion and thus gives a contribution proportional to $T^{\frac{3}{2}}$. If the system approaches the transition point from the ferromagnetic site, we will hardly see consequences in the thermodynamics because the singlet excitation has a vanishing contribution compared to the ferromagnetic spin wave excitation spectrum. More interesting features are expected in the singlet phase close to the transition point. Here, we get a sudden high contribution to the density of states at the gap energy. This

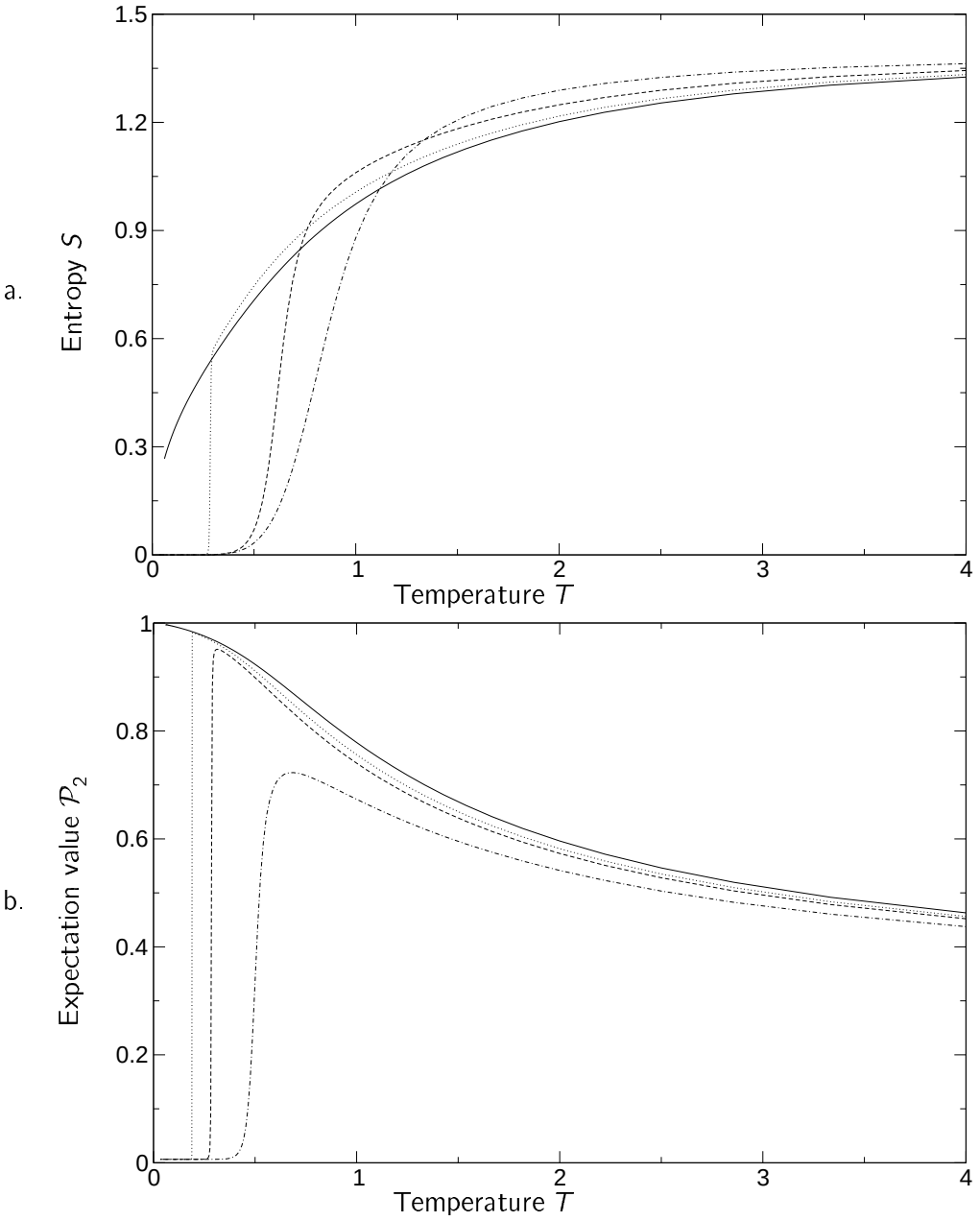

Figure 5.23: a. Entropy near the ferromagnetic to rung-singlet phase transition. Data is plotted for $\theta = -0.411\pi$ (solid), $\theta = -0.389\pi$ (dotted), $\theta = -3/9\pi$ (dashed), and $\theta = -2/9\pi$ (dot-dashed line).
b. Expectation value of the projector on ferromagnetic plaquette states (2.3) near the ferromagnetic to rung-singlet phase transition. Plotted is data for $\theta = -0.411\pi$ (solid), $\theta = -0.397\pi$ (dotted), $\theta = -0.389\pi$ (dashed), and $\theta = -0.361\pi$ (dot-dashed line).

results in a steep increase of the entropy and, thus, a sharp peak in the specific heat at a characteristic temperature T_{ch}. We identify T_{ch} as the point where the ferromagnet wins enough entropy to have the same free energy as the singlet which is energetically favored. With this, it follows:

$$F_{\mathrm{FM}}(T_{\mathrm{ch}}) = F_{\mathrm{RS}}(T_{\mathrm{ch}}) \quad \Rightarrow \quad T_{\mathrm{ch}} = \left(\frac{E_{\mathrm{RS}} - E_{\mathrm{FM}}}{\alpha}\right)^{\frac{2}{3}} \tag{5.37}$$

From the predicted level-crossing we further assume that the energy difference scales linearly close to the critical point

$$E_{\mathrm{RS}} - E_{\mathrm{FM}} \propto \theta - \theta_c \tag{5.38}$$

leading to a scaling law for the characteristic temperature

$$T_{\mathrm{ch}} = c\,(\theta - \theta_c)^{2/3} \tag{5.39}$$

with a constant c. At this point, one should remember that there is no phase transition for finite temperatures in one-dimensional systems. So, we expect no phase transition at T_{ch} but a transition which becomes a smooth crossover-region with increasing temperature. Still, the quite sharp low-temperature increase in the entropy of models near the phase transition give a remnant of a true first-order phase transition at finite temperatures. In this case, the steep increase would become a non-analyticity which gives the latent heat at a finite-temperature phase transition.

Further consequences arise from the fact that the ferromagnetic states with a macroscopic magnetization form the only excitations in the singlet phase. From this, we expect a jump in the zero-field susceptibility at T_{ch} and, if a field is applied, a discontinuity from zero to saturation in the zero-temperature magnetization. This is in contrast to the usual behavior where after overcoming a singlet-triplet gap the magnetization continuously increases from zero when a magnetic field is applied. It results from a common picture where the low-lying excitations are formed by sparse rung-triplets within a bulk of rung-singlets. Yet, in our simplified model these kind of excitations are suppressed and won't contribute to the low-temperature behavior. This argumentation follows [171] where a spin ladder model class differing from ours was considered for a phase transition driven by magnetic field. There, it was claimed that such a phase behavior is only possible when a certain amount of frustration is present.

To check this scenario we recall the results from the exact calculations in Chapter 2. We found an exact upper bound ($\theta_{\mathrm{u}} \approx -0.31\pi$) and an exact lower bound ($\theta_{\mathrm{u}} = -\pi/2$) for the phase transition. In this region, the lowest-energy plaquette states are the ferromagnetic state and a state in the $S = 0$ subspace (see Fig. 2.1). The $S = 1$ plaquette states (2.4) which mix rung-singlets and rung-triplets are sufficiently higher in energy. This could be enough to keep the rung-singlet and rung-triplet spaces separated like in the suggested model. However, the low-energy $S = 0$ state is not the pure rung-singlet state but contains some admixture of rung-triplet states to be minimal in energy.

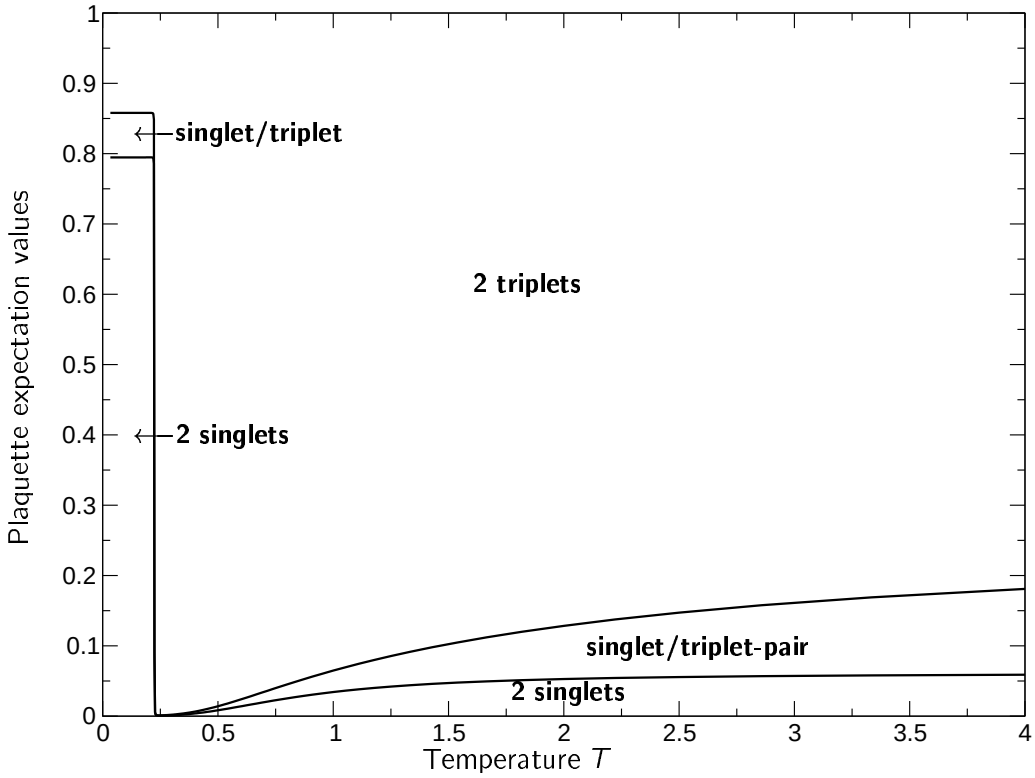

Figure 5.24: Expectation value of plaquette projectors versus temperature near the ferromagnetic phase transition at $\theta = -0.394\pi$ (solid). We plotted the probability to find pairs of singlets, triplets, or a singlet/triplet-pair on a plaquette. The curves are the thermal expectation values of $\langle s_0 s_0 \rangle$ (lower line) and $(\langle s_0 \cdot \rangle + \langle \cdot s_0 \rangle)$ (upper line). TMRG-data ($m = 300$).

We checked the contributions of rung-singlets and -triplets for a representative point by TMRG data (see Fig.5.24). Both expectation values stay constant in the low-temperature regime up to $T_{\mathrm{ch}} \approx 0.02$. More than 80% of the rungs contain singlets. There is only a small admixture of rung-triplets each of which has a rung-singlet neighbor with a probability of 40%. At temperature T_{ch} the expectation values change almost abruptly. Above T_{ch}, the thermodynamics is dominated by the ferromagnetic states.

In Fig. 5.25, we give a zoom of Fig. 5.11. In this parameter region the specific heat has a very sharp peak at low temperatures which can be identified with the characteristic temperature T_{ch} where ferromagnetic excitations set in. The location of the peaks is given for different parameters θ. The curve $T_{\mathrm{ch}}(\theta)$ is highly consistent with an estimate of the form (5.39) where we determined $c = 4.20 \pm 0.04$. The location of the phase transition $\theta_{\mathrm{c}} = (-0.4067 \pm 0.004)\pi$ can even be given with a higher accuracy. This result is well consistent with the result $\theta_c = -0.40\pi$ from exact diagonalization and DMRG published

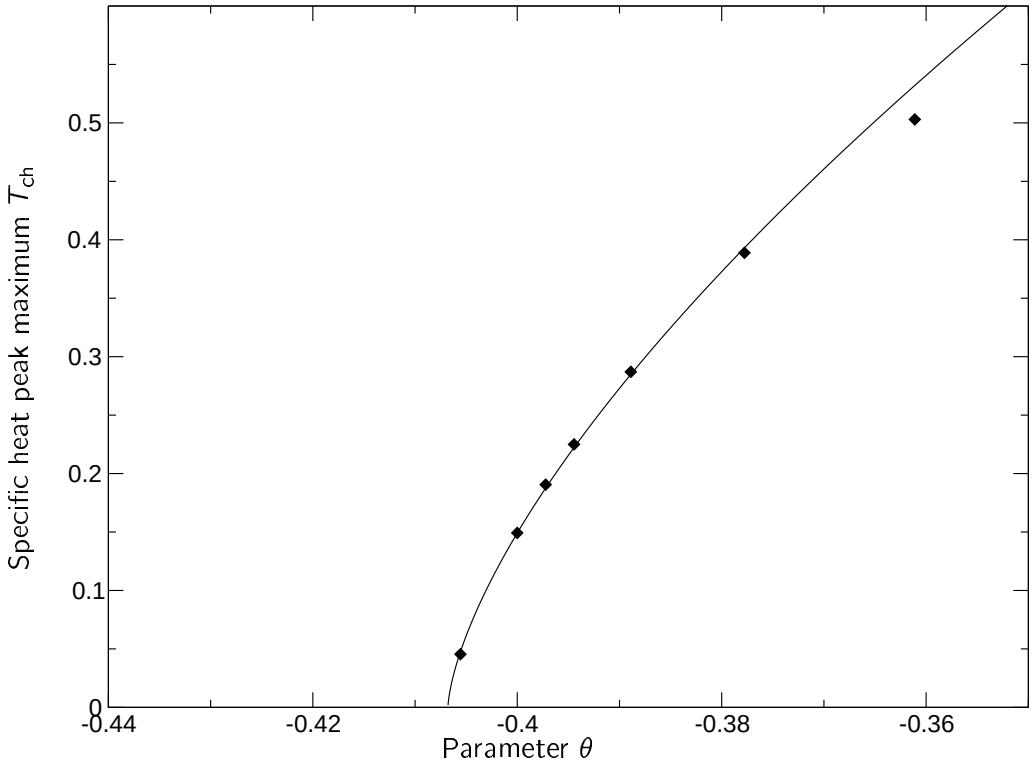

Figure 5.25: Zoom of Fig. 5.11. Temperature T_{ch} for the sharp peaks of the specific heat versus system parameter θ (diamonds). The solid line is an estimate of the form $c\,|\theta - \theta_c|^{2/3}$.

in [1].

To check the influence of an external magnetic field, we considered a system in the rung-singlet phase near the phase transition under a magnetic field h. In the inset of Fig. 5.26 the magnetization m is plotted against the temperature for various magnetic fields. Coming from high temperatures, the magnetization increases with raising field. For values $h \leq 0.05$ the magnetization falls off abruptly at a certain low temperature. For higher fields the system reaches saturation $m_{sat} = 0.5$ for $T \to 0$. At the point of the magnetization change, the specific heat has the characteristic sharp peak which survives from the zero-field case. For higher magnetic fields, the peak moves to lower temperatures. We expect a phase transition at some critical field $0.05 < h_c < 0.1$ where the ferromagnetic excitation spectrum is gapless. For higher fields, we observe an exponential low-temperature decay in the specific heat which is the fingerprint of a phase with energy gap. The gap results from the energy that is needed to break up a fully polarized state and to create a magnon excitation. This gap grows with h as can be seen in the weaker increase of the specific heat for higher magnetic field. Yet, in the plot for $h = 0.1$ still a visible small shoulder is present which comes from the low lying ferromagnetic spectrum. A closer look at the low-

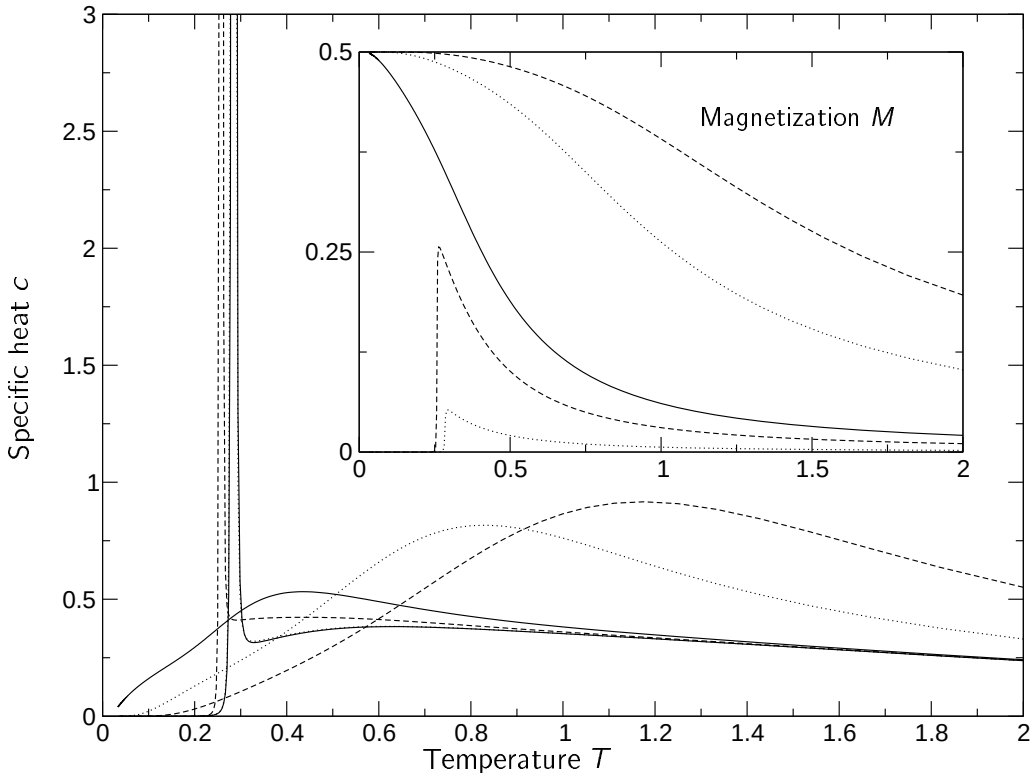

Figure 5.26: Specific heat (inset: magnetization) versus temperature for model at $\theta = -0.389\pi$ with magnetic field of various strength. Three models have zero magnetization for $T = 0$: $h = 0$ (solid line),$h = 0.01$ (dotted), and $h = 0.05$ (dashed). Three models saturate for $T = 0$: $h = 0.1$ (solid), $h = 0.5$ (dotted), and $h = 1.0$ (dashed). Models with $h \leq 0.05$ show the characteristic sharp peak for low temperatures ($h = 0$ and $h = 0.01$ are almost indistinguishable). The magnetization for zero field $h = 0$ vanishes.

temperature behavior, though, gives an exponential behavior. Thus, the system is already in the fully polarized phase with a gap at $h = 0.1$.

We conclude that the above-presented scenario of a first order quantum phase transition between a ferromagnetic and a singlet phase agrees perfectly with the numerical data. A stable ground state with strong rung-singlet character exists on one site of the spectrum and a ferromagnetic state exists on the other side. We also confirm a mechanism that suppresses the mixture of rungs and triplets which is essential for the character and sharpness of the transition. The scaling behavior of the specific-heat maxima was reproduced correctly and on this basis the position of the quantum phase transition was estimated with high precision. Finally, we found the expected behavior in the rung-singlet phase close to the ferromagnetic phase when a magnetic field is applied. A similar phase transition

to a fully polarized phase appears. This leads to similar signatures in the thermodynamic quantities.

6 Conclusions

In this thesis, we determined the finite temperature behavior of the spin ladder with arbitrary cyclic exchange. The calculated properties include specific heat, magnetic and generalized susceptibilities, and thermal expectation values of a complete basis set of plaquette operators. The proposed $T = 0$ behavior was confirmed and the picture of different competing interactions was extended to finite temperatures. In this context, we were also able to explain some unusual features of the specific heat at special points in the model. The results were obtained by Transfer Matrix DMRG (TMRG) and a supporting variational calculation with a set of matrix-product states was done for $T = 0$. We developed a new numerical technique QCTMRG and provided a thorough analysis of its performance. In the following, we give a concluding summary along with an outlook for the different aspects of this thesis.

QCTMRG

Based on Nishino's Corner Transfer Matrix DMRG (CTMRG) method, we developed a new numerical approach for the calculation of thermodynamic properties of one-dimensional quantum systems. The so-called quantum CTMRG (QCTRMG) is based on the Trotter-Suzuki decomposition of quantum chains. The QCTMRG method separates the arising classical model into four quadrants and expands them iteratively while the basis of the edge states is kept at a fixed size by truncation via density-matrix projection. In contrast to the classical CTMRG a significant anisotropy evolved from the existence of a well-distinguished real space and a Trotter direction and the calculation of the trace in order to obtain the partition function demanded periodic boundary conditions of the two-dimensional plane.

We implemented the algorithm in object-oriented design in the C++ programming language. For the resource-consuming matrix-multiplications, routines from a specially optimized high-performance library were adopted. The free energy densities and thermal energy expectation values at the chain centers have been successfully calculated for the classical Ising chain and the antiferromagnetic spin-1/2 Heisenberg chain by the Quantum Corner-Transfer Matrix DMRG. Reliable results were given for finite temperatures and system sizes.

QCTMRG and the TMRG have the same asymptotics for the running time in the large-m limit. TMRG has less storage use though. The periodic boundary conditions implied by the trace in the partition function destroys the advantages from the development of CTMRG over TMRG. Additionally, the flat eigenspectrum of the horizontal density matrix gives bad estimates at high temperatures.

Outlook: If finite-temperature data in the thermodynamic limit is aimed at, the quantum TMRG method is certainly still the method of choice. At least one of the mentioned problems should be solved to make the QCTMRG technique an attractive option.

TMRG

The Quantum Transfer Matrix DMRG (QTMRG or shorter: TMRG) is a powerful numerical algorithm for the calculation of the thermodynamics of one dimensional quantum

systems. In the framework of this thesis, a high-performance implementation of the TMRG method was developed which provided the thermodynamical properties of the spin ladder with cyclic exchange.

The TMRG method bases on the DMRG which can be interpreted as a variational method in the space of matrix-product states [104, 110]. As invented by S. R. White in 1992[93] the fundamental idea is the density-matrix projection in order to truncate the Hilbert space at each step of an iterative enlargement procedure. This concept was extended successfully to the application at finite temperatures [117, 118]. Principally, the one-dimensional quantum chain is mapped onto a classical two-dimensional chequerboard model by a Trotter-Suzuki decomposition. The thermodynamics is captured in the largest eigenvalues of the quantum transfer matrix which is determined by DMRG. We conclude that the TMRG algorithm is indeed an optimal choice for our purposes. Alternatively, quantum Monte-Carlo simulations are often chosen to study thermodynamic properties, but the TMRG has some fundamental advantages: The thermodynamics are treated in the exact thermodynamic limit of the quantum chain. This is guaranteed by the underlying transfer-matrix approach. Thus no finite size corrections affect the TMRG data. More importantly, the TMRG does not suffer from the "sign problem" known from quantum Monte-Carlo simulations of frustrated models.

Outlook: Generally, the family of DMRG methods is rapidly growing. Much progress has been made within the last few years. A short overview about the recent work has already been given in Section 3.3.3. The recent developments in DMRG theory [102] lead to a better understanding of the method and the connection between the quality of the density matrix projection and the entanglement of the underlying states. Detailed studies of this behavior are still missing in the TMRG case. Major differences to the DMRG method have to be faced: Both transfer matrix and reduced density-matrix are asymmetric and there is still no rigorous proof in which way to choose an optimal density matrix [116, 117, 118, 157, 172, 173]. Further, no agreement has been reached about the definition of an entanglement measure for finite temperatures, see [103] for a review. These challenges span an interesting field of research.

Plaquette operators

Spin models usually possess some symmetries which often include translational invariance and conservation of the total spin S and its z-component. On the spin ladder, we have an additional parity symmetry which divides the Hilbert space into two parts represented by the number of rung-singlets modulo 2. Regarding these symmetries on the ladder, we provided a complete set of 16 basis states that conserve the quantum numbers associated with the symmetries. Except for a two-fold degenerate $S = 0$ subspace, each of the remaining 14 plaquette states can be uniquely determined by its quantum numbers. It is now an illuminating task to write down the Hamiltonian and relevant operators in terms of these plaquette eigenstate. Thus, a representation by plaquette-state projection operators is achieved. This approach is frequently used in the context of matrix-product ground states

[63, 65, 71]. By this representation, we already obtain all eigenvalues of the plaquette Hamiltonian which can give already a rough sketch of the expected phase. At the same time, these plaquette energies provide a lower bound to the local ground-state energy. If the ground-state energy has the same local energy as the plaquette state it is to be considered an optimal ground state. An exact upper bound to the ground-state energy is given by variational states. We provided variational states of the matrix-product type [59, 60] which were essentially able to capture the proposed ground-state characteristics.

Two positive aspects emerged in the consideration of thermal quantities:

1. Different types of dominating order were proposed for the various phases of the model. Assuming the local operator associated with this order keeps the symmetries of the model, there exists an operator representation in terms of plaquette projectors. Reversely, if all thermal expectation values of the 16 plaquette projectors plus one overlap expectation value for the $S = 0$ subspace are known, the thermal expectation value of an arbitrary operator can be constructed without further numerical TMRG calculations. In fact, the number of projector expectation values to be considered reduces to five plus one overlap when SU(2) symmetry is fulfilled.

2. The analysis of the thermal expectation values of the projectors provided valuable information about the specific heat peaks. Level crossings in the projector expectation value often indicate a sudden rise of entropy and, thus, a peak in the specific heat. If the types of order which are present in the model are known, the expectation values can give important information where certain states become important. Yet, no information about true long-range order can be provided, but this is not supposed to exist in one-dimensional system at finite-temperature anyway. For a quick and informative analysis of specific heat data especially in the vicinity of phase transitions it turned out to be a useful tool.

Outlook: The consideration of thermal expectation values of local eigenstates can easily be extended to other systems when thermodynamical data is considered. They are feasible by almost no extra cost in the TMRG algorithm and provide important evidence for proposed spectral behavior.

Thermodynamics of the spin ladder with cyclic exchange

In this work, a picture of the thermodynamical behavior of the whole parameter range of the spin ladder model with cyclic exchange

$$H = \cos\theta \sum_{\tau\in\{1,2\},j} \mathbf{S}_{\tau,j}\cdot\mathbf{S}_{\tau,j+1} + \cos\theta \sum_{j} \mathbf{S}_{1,j}\cdot\mathbf{S}_{2,j} + \sin\theta \sum_{j} \left(P_{\square} + P_{\square}^{-1}\right) \tag{6.1}$$

has been given, see Fig. 6.1. At this point, we will summarize the essential features of the phase diagram.

Rung-singlet phase. At $\theta = 0$ the ladder is a an gapped phase with a unique ground state and exponentially decaying correlation. The ground state can be sketched as singlets sitting on the rungs of the ladders. The rung-singlet phase extends when a finite value of ring-exchange is turned on. We showed that the singlet expectation value is indeed

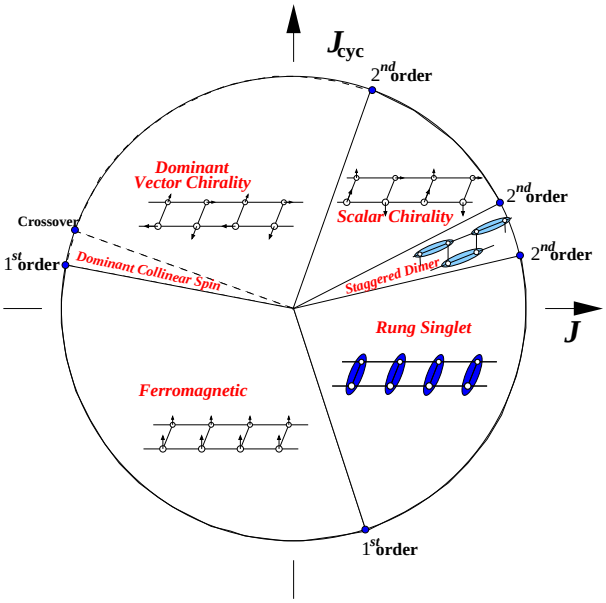

Figure 6.1: Phase diagram of the spin ladder following [1, 55].

dominant in this phase. The specific heat shows a single Schottky-like peak and a clear exponential decay for $T \to 0$. A similar behavior is seen in the magnetic susceptibility. The specific heat and magnetic susceptibility curves in this phase were found to be consistent with previous results [50]. The peak of the specific heat moves to lower temperatures when a positive amount of cyclic exchange is switched on. This is caused by the flat dispersion spectrum of the solitonic and magnon-excitations of the staggered-dimer phase which get lower in energy in vicinity of the phase transition.

The position of the second order quantum phase transition is still under discussion [169, 166, 54, 1, 170, 51]. We observed a level crossing in the thermal expectation values of the relevant operator between $\theta = 0.0500\pi$ and 0.0556π. This is no proof, but may be considered as a strong indication for a phase transition to the staggered-dimer phase at this point. The result is consistent with some of the more recent data $\theta = (0.0597 \pm 0.0003)\pi$ [170] and $\theta = (0.051 \pm 0.009)\pi$ [51].

Staggered-dimer phase. The picture of the ground state in the staggered-dimer phase is characterized by the arrangement of dimers on the legs in a staggered order. This order is long-ranged and leads to a doubly degenerate ground state. The phase was shown to possess a very small excitation gap [1]. An adequate way to study a system with a degenerate ground state is to apply a small external symmetry-breaking field and to measure the response of the system. The sensitivity of system for small perturbation is then captured by a generalized susceptibility. In the staggered-dimer phase, we were able to show that the susceptibility which is associated with the staggered-dimer order diverges at a representative point $\theta = \pi/9$ from the staggered-dimer phase for $T \to 0$ while it goes

to zero or to finite values in the other phase. This is a signature of the long-range order present in the ground state. The specific heat in this phase has a characteristic double peak structure. In [158], a set of possible low-lying excitations above a matrix-product ground-state was given exactly in terms of magnons and solitonic excitations. For the staggered-dimer phase, we propose similar excitations which lie low in energy and have a flat dispersion. The rest of the spectrum sets in at a higher energy scale. This scenario leading to the double-peak in the specific heat can be supported by thermal expectation values of plaquette operators.

At $\theta = \arctan(1/2) \approx 0.1476\pi$, the model is self-dual and shows a U(1) symmetry because it is invariant under a transformation (1.7) with arbitrary φ [42]. In the vicinity of the phase transition, the low-temperature specific-heat peak becomes smaller in size than the second peak. A minimum is reached exactly at the transition point. In [131], a similar observation was made for a spin ladder under magnetic field.

Scalar-chirality phase. The system enters a state with scalar-chiral long-range order which corresponds to the staggered-dimer order under the duality transformation at $\theta = \arctan(1/2)$ [1, 54]. The associated susceptibility for this phase diverges at a representative point $\theta = \pi/3$ for $T \to 0$. For representative points from other phases the scalar-chirality susceptibility converges to finite values for $T \to 0$. The specific heat maxima move to higher temperatures for higher values of θ which indicates that the dispersion of excitations inclines again.

The phase transition from the scalar-chirality phase to the vector-chirality phase ($\theta \approx 0.38\pi$ [54] and $(0.39 \pm 0.01)\pi$ [1]) was claimed to be in the same universality class as the rung-singlet to staggered-dimer transition [55]. At $\theta \approx 0.4\pi$, we observe a point where the high-temperature peak in the specific heat becomes a shoulder of the other peak. This behavior could be related to the phase transition.

Dominant vector-chirality/collinear-spin phase. In [1], the dominant vector-chirality phase was introduced as a short range ordered phase with a unique ground state and a fully gapped excitation spectrum similar to the rung-singlet phase. The vector-chirality phase shows a clear maximum in the specific heat but it has a pronounced shoulder at higher temperatures which is a remnant of the double-peak structure observed in the neighboring scalar-chirality phase. The shoulder vanishes for increasing cyclic-exchange.

At $\theta = \pi - \arctan(1/2)$ there is a crossover region to dominant-collinear-spin correlations. In [1], it was found that the correlation lengths are very small in that region. This behavior leads to a strong peak in the specific heat data which corresponds to the short range-ordering.

At $\theta = 0.94\pi$, a first-order quantum phase transition to the ferromagnetic phase was proposed in [1]. While the singlet ground state of the dominant-collinear-spin phase gives no response to an infinitely small magnetic field, the spontaneous magnetization of the ferromagnet leads to a divergence of the magnetic susceptibility at $T = 0$. We calculated the magnetic susceptibility in the vicinity of the predicted phase transition and found that the divergence sets in between $0.933\pi < \theta < 0.939\pi$. At the estimated point of the phase transition, the position of the specific heat was found to be minimal with respect

to temperature because there is a flat dispersion spectrum for the low-lying states in the vicinity of the phase transition motivated by a dense spectrum of plaquette eigenenergies.

Ferromagnetic phase:

The specific heat of the ferromagnet has a single peak that moves to higher temperatures as θ is increased. It declines again in temperature when the phase transition to the rung-singlet phase is approached. This can be motivated by the distance of the ferromagnetic ground state, which is an optimum ground state, to the other states in the energy spectrum of the plaquette.

At $\theta = (-0.4067 \pm 0.004)\pi$, we observe a rather unusual first-order quantum phase transition from the ferromagnetic phase to the rung-singlet phase. States that contain both singlets and triplets on a plaquette are higher in energy than the ferromagnet and the plaquette singlet state as can be seen from the plaquette energies. Thus we can consider a situation where a singlet ladder state (rung-singlet phase) and the ladder ferromagnet perform a level-crossing at the phase transition. All other states are high in energy can be neglected—to a first approximation. This level-crossing leads to a sharp peak in the specific heat of models close to the phase transition in the rung-singlet phase. This peak corresponds to a sudden jump in the entropy caused by the emerging ferromagnetic spectrum. We predicted a scaling law $T_{\mathrm{ch}} = c\,(\theta - \theta_c)^{2/3}$ for the peak position which is highly consistent with an observation from the TMRG specific heat data. Additionally, we showed that a similar phase transition can be driven by an external magnetic field.

As a conclusion, we summarize the most important results of our study:

- The proposed $T = 0$ phase diagram of the spin ladder with cyclic exchange is consistent with our results from thermodynamic studies. Although no phase transition for finite temperatures is expected in one dimension, a rich $T > 0$ behavior was found.
- We observed a double peak in the specific heat of the broken symmetry phases.
- A caricature of a first order phase transition for $T > 0$ was found in a quasi one-dimensional spin system.

Outlook:

- In order to clarify the exact position of the second order quantum phase transitions, further studies with the generalized susceptibilities could be helpful.
- It seems to be a promising task to study the thermal behavior under magnetic fields at different points in the phase diagram. Mila [174] predicted the emergence of magnetization plateaus if frustration is present in the model.
- The thermal studies could be extended to other points in a general spin ladder system [55] or to include anisotropies. It might be fruitful, for example, to find a connecting line from the dimerized phases to a model with matrix-product ground state [158, 42] in order to clarify the details of the excitation spectrum.

- In principal, the TMRG method allows the calculation of correlation lengths as well. However, it is a sophisticated task to deduce the order parameter associated to the correlation lengths from the numerical data. In the case of the spin ladder with its rich phase diagram, it appears to be worthwhile to start an attempt.

A Matrix product states as variational states

Upper bounds for the ground state energy will be derived by a variational approach adopting matrix product states. Similar calculations have been done in [58] for the bilinear-biquadratic spin-1 chain. Lower bounds are given by the lowest eigenvalue of the local interaction as derived earlier. Note that the lower bound is only reached if the ground state is an optimal state, like the ferromagnetic ground state or the VBS state.

We expect the matrix product variational states to give us a picture of the ground state in different parameter regimes.

The general form of the transfer matrix of a given operator A is

$$T(u) = \begin{pmatrix} \langle g_{11}|A|g_{11}\rangle & \langle g_{12}|A|g_{12}\rangle & \langle g_{11}|A|g_{12}\rangle & \langle g_{12}|A|g_{11}\rangle \\ \langle g_{21}|A|g_{21}\rangle & \langle g_{22}|A|g_{22}\rangle & \langle g_{21}|A|g_{22}\rangle & \langle g_{22}|A|g_{21}\rangle \\ \langle g_{11}|A|g_{21}\rangle & \langle g_{12}|A|g_{22}\rangle & \langle g_{11}|A|g_{22}\rangle & \langle g_{12}|A|g_{21}\rangle \\ \langle g_{21}|A|g_{11}\rangle & \langle g_{22}|A|g_{12}\rangle & \langle g_{21}|A|g_{12}\rangle & \langle g_{22}|A|g_{11}\rangle \end{pmatrix}. \tag{A.1}$$

From

$$g_l(u) = \begin{pmatrix} u|s_0\rangle_l + |t_0\rangle_l & -\sqrt{2}|t_+\rangle_l \\ \sqrt{2}|t_-\rangle_l & u|s_0\rangle_l - |t_0\rangle_l \end{pmatrix} \tag{A.2}$$

follows the corresponding transfer matrix (site indices are omitted)

$$T(u) = \begin{pmatrix} a_1 + a_2 + a_3 + a_4 & a_{13} & -a_5 - a_6 & -a_9 - a_{10} \\ a_{14} & a_1 + a_2 - a_3 - a_4 & a_{11} - a_{12} & a_7 - a_8 \\ a_7 + a_8 & -a_9 + a_{10} & a_1 - a_2 - a_3 + a_4 & a_{15} \\ a_{11} + a_{12} & -a_5 + a_6 & a_{16} & a_1 - a_2 + a_3 - a_4 \end{pmatrix} \tag{A.3}$$

with

$$\begin{aligned} a_1 &:= u^* u\langle s_0|A|s_0\rangle & a_2 &:= \langle t_0|A|t_0\rangle \\ a_3 &:= u^*\langle s_0|A|t_0\rangle & a_4 &:= u\langle t_0|A|s_0\rangle \\ a_5 &:= \sqrt{2}u^*\langle s_0|A|t_+\rangle & a_6 &:= \sqrt{2}\langle t_0|A|t_+\rangle \\ a_7 &:= \sqrt{2}u^*\langle s_0|A|t_-\rangle & a_8 &:= \sqrt{2}\langle t_0|A|t_-\rangle \\ a_9 &:= \sqrt{2}u\langle t_+|A|s_0\rangle & a_{10} &:= \sqrt{2}\langle t_+|A|t_0\rangle \\ a_{11} &:= \sqrt{2}u\langle t_-|A|s_0\rangle & a_{12} &:= \sqrt{2}\langle t_-|A|t_0\rangle \\ a_{13} &:= 2\langle t_+|A|t_+\rangle & a_{14} &:= 2\langle t_-|A|t_-\rangle \\ a_{15} &:= -2\langle t_+|A|t_-\rangle & a_{16} &:= -2\langle t_-|A|t_+\rangle. \end{aligned} \tag{A.4}$$

For a reduction of the matrix, we assume $A = A^\dagger$ hermitian. This leads to the transfer matrix

$$T_l(u) = \begin{pmatrix} a_1 + a_2 + b + b^* & d_1 & -c_1 - c_2 & (-c_1 - c_2)^* \\ d_2 & a_1 + a_2 - b - b^* & (c_3 - c_4)^* & c_3 - c_4 \\ c_3 + c_4 & (-c_1 + c_2)^* & a_1 - a_2 - b + b^* & e \\ (c_3 + c_4)^* & -c_1 + c_2 & e & a_1 - a_2 + b - b^* \end{pmatrix} \tag{A.5}$$

with

$$\begin{array}{llllllll} a_1 & := & u^*u\langle s_0|A|s_0\rangle & a_2 & := & \langle t_0|A|t_0\rangle & b & := & u^*\langle s_0|A|t_0\rangle \\ c_1 & := & \sqrt{2}u^*\langle s_0|A|t_+\rangle & c_2 & := & \sqrt{2}\langle t_0|A|t_+\rangle & & & \\ c_3 & := & \sqrt{2}u^*\langle s_0|A|t_-\rangle & c_4 & := & \sqrt{2}\langle t_0|A|t_-\rangle & & & \\ d_1 & := & 2\langle t_+|A|t_+\rangle & d_2 & := & 2\langle t_-|A|t_-\rangle & e & := & -2\langle t_+|A|t_-\rangle. \end{array} \tag{A.6}$$

If A conserves S^z-value and is symmetric under spin-flip we find the transfer matrix

$$T(u) = \begin{pmatrix} a_1+a_2+b+b^* & d & 0 & 0 \\ d & a_1+a_2-b-b^* & 0 & 0 \\ 0 & 0 & a_1-a_2-b+b^* & 0 \\ 0 & 0 & 0 & a_1-a_2+b-b^* \end{pmatrix} \tag{A.7}$$

with

$$\begin{array}{rcrcl} a_1 & := & u^*u\langle s_0|A|s_0\rangle, & a_2 & := & \langle t_0|A|t_0\rangle \\ b & := & u^*\langle s_0|A|t_0\rangle, & d & := & 2\langle t_\pm|A|t_\pm\rangle. \end{array} \tag{A.8}$$

The most important transfer matrix is the transfer matrix of the identity operator. Here, we calculate

$$a_1 = |u|,\ a_2 = 1,\ b = 0,\ d = 2 \tag{A.9}$$

which gives

$$T_{\mathbb{1}}(u) = \begin{pmatrix} |u|^2+1 & 2 & 0 & 0 \\ 2 & |u|^2+1 & 0 & 0 \\ 0 & 0 & |u|^2-1 & 0 \\ 0 & 0 & 0 & |u|^2-1 \end{pmatrix}. \tag{A.10}$$

for arbitrary complex u. The transfer matrices eigenvalues and -vectors are:

$$\begin{array}{rcrcl} \chi_1 & = & |u|^2+3, & |u_1\rangle & = & \frac{1}{\sqrt{2}}(1,1,0,0)^t \\ \chi_2 & = & |u|^2-1, & |u_2\rangle & = & \frac{1}{\sqrt{2}}(1,-1,0,0)^t \\ \chi_3 & = & |u|^2-1, & |u_3\rangle & = & (0,0,1,0)^t \\ \chi_4 & = & |u|^2-1, & |u_4\rangle & = & (0,0,0,1)^t \end{array} \tag{A.11}$$

In order to obtain the energy of the variational state, we have to calculate the expectation value of the local Hamiltonian which affects two sites. Thus, we consider the state matrix of two sites i.e.,a plaquette of the ladder:

$$\tilde{g}(u,\sigma) = g_l(u) \times g_{l+1}(\sigma u) = \begin{pmatrix} |\tilde{g}_{11}\rangle & |\tilde{g}_{12}\rangle \\ |\tilde{g}_{21}\rangle & |\tilde{g}_{22}\rangle \end{pmatrix} \tag{A.12}$$

with

$$|\tilde{g}_{11}\rangle = \sigma u^2|s_0 s_0\rangle + u\left(|s_0 t_0\rangle + \sigma|t_0 s_0\rangle\right) + |t_0 t_0\rangle - 2|t_+ t_-\rangle \tag{A.13}$$

$$|\tilde{g}_{12}\rangle = -\sqrt{2}\left(u\left[|s_0 t_+\rangle + \sigma|t_+ s_0\rangle\right] + \left[|t_0 t_+\rangle - |t_+ t_0\rangle\right]\right) \tag{A.14}$$

$$|\tilde{g}_{21}\rangle = \sqrt{2}\left(u\left[|s_0 t_-\rangle + \sigma|t_- s_0\rangle\right] - \left[|t_0 t_-\rangle - |t_- t_0\rangle\right]\right) \tag{A.15}$$

$$|\tilde{g}_{22}\rangle = \sigma u^2|s_0 s_0\rangle - u\left(|s_0 t_0\rangle + \sigma|t_0 s_0\rangle\right) + |t_0 t_0\rangle - 2|t_- t_+\rangle. \tag{A.16}$$

We can represent the entries of the state matrix in the basis from Section 2.1:

$$\begin{aligned}
\left|\tilde{g}_{11}\right\rangle &= -\sqrt{2}\left|\phi^{\perp}_{1_0}\right\rangle + \tfrac{u}{\sqrt{2}}\Big([\sigma+1]\left|\phi^{\parallel}_{1_0}\right\rangle + [\sigma-1]\left|\phi^{\times}_{1_0}\right\rangle\Big) + \sqrt{3}\left|\phi^{\parallel,\times}_{0}\right\rangle + \sigma u^2\left|\phi^{\perp}_{0}\right\rangle && \text{(A.17)}\\
\left|\tilde{g}_{12}\right\rangle &= 2\left|\phi^{\perp}_{1_{+1}}\right\rangle - u\Big([\sigma+1]\left|\phi^{\parallel}_{1_{+1}}\right\rangle + [\sigma-1]\left|\phi^{\times}_{1_{+1}}\right\rangle\Big) && \text{(A.18)}\\
\left|\tilde{g}_{21}\right\rangle &= -2\left|\phi^{\perp}_{1_{-1}}\right\rangle + u\Big([\sigma+1]\left|\phi^{\parallel}_{1_{-1}}\right\rangle + [\sigma-1]\left|\phi^{\times}_{1_{-1}}\right\rangle\Big) && \text{(A.19)}\\
\left|\tilde{g}_{22}\right\rangle &= \sqrt{2}\left|\phi^{\perp}_{1_0}\right\rangle - \tfrac{u}{\sqrt{2}}\Big([\sigma+1]\left|\phi^{\parallel}_{1_0}\right\rangle + [\sigma-1]\left|\phi^{\times}_{1_0}\right\rangle\Big) + \sqrt{3}\left|\phi^{\parallel,\times}_{0}\right\rangle + \sigma u^2\left|\phi^{\perp}_{0}\right\rangle && \text{(A.20)}
\end{aligned}$$

With the auxiliary state matrices

$$\begin{aligned}
g_1^{\perp} &= \begin{pmatrix} |\phi^{\perp}_{1_0}\rangle & -\sqrt{2}|\phi^{\perp}_{1_{+1}}\rangle \\ \sqrt{2}|\phi^{\perp}_{1_{-1}}\rangle & -|\phi^{\perp}_{1_0}\rangle \end{pmatrix}, \quad g_1^{\parallel} = \begin{pmatrix} |\phi^{\parallel}_{1_0}\rangle & -\sqrt{2}|\phi^{\parallel}_{1_{+1}}\rangle \\ \sqrt{2}|\phi^{\parallel}_{1_{-1}}\rangle & -|\phi^{\parallel}_{1_0}\rangle \end{pmatrix} && \text{(A.21)}\\
g_1^{\times} &= \begin{pmatrix} |\phi^{\times}_{1_0}\rangle & -\sqrt{2}|\phi^{\times}_{1_{+1}}\rangle \\ \sqrt{2}|\phi^{\times}_{1_{-1}}\rangle & -|\phi^{\times}_{1_0}\rangle \end{pmatrix}, && \text{(A.22)}
\end{aligned}$$

the state matrix (A.12) takes the form

$$\begin{aligned}
\tilde{g}(u,\sigma) &= -\sqrt{2}g_1^{\perp} + \frac{u}{\sqrt{2}}[\sigma+1]g_1^{\parallel} + \frac{u}{\sqrt{2}}[\sigma-1]g_1^{\times} \\
&\quad + \Big(\sigma u^2\left|\phi^{\perp}_0\right\rangle + \sqrt{3}\left|\phi^{\parallel,\times}_0\right\rangle\Big) \quad . && \text{(A.23)}
\end{aligned}$$

Special cases:

$$\begin{aligned}
\tilde{g}(u=0) &= -\sqrt{2}g_1^{\perp} + \sqrt{3}\left|\phi^{\parallel,\times}_0\right\rangle && \text{(A.26)}\\
\tilde{g}(u\to\infty) &= \sigma u^2\left|\phi^{\perp}_0\right\rangle && \text{(A.27)}\\
\tilde{g}(u=1,\sigma=-1) &= -\sqrt{2}\left(g_1^{\perp}+g_1^{\times}\right) - \underbrace{\Big(\left|\phi^{\perp}_0\right\rangle - \sqrt{3}\left|\phi^{\parallel,\times}_0\right\rangle\Big)}_{2\left|\phi^{\parallel}_0\right\rangle} \\
&= -2\begin{pmatrix} \left|\begin{smallmatrix} t_0 \\ s_0 \end{smallmatrix}\right\rangle - \left|\begin{smallmatrix} s_0 \\ s_0 \end{smallmatrix}\right\rangle & -\sqrt{2}\left|\begin{smallmatrix} t_+ \\ s_0 \end{smallmatrix}\right\rangle \\ \sqrt{2}\left|\begin{smallmatrix} t_- \\ s_0 \end{smallmatrix}\right\rangle & -\left|\begin{smallmatrix} t_0 \\ s_0 \end{smallmatrix}\right\rangle - \left|\begin{smallmatrix} s_0 \\ s_0 \end{smallmatrix}\right\rangle \end{pmatrix} && \text{(A.28)}\\
\tilde{g}(u=i,\sigma=-1) &= -\sqrt{2}\left(g_1^{\perp}+ig_1^{\times}\right) + \underbrace{\Big(\left|\phi^{\perp}_0\right\rangle + \sqrt{3}\left|\phi^{\parallel,\times}_0\right\rangle\Big)}_{-2\left|\phi^{\times}_0\right\rangle} && \text{(A.29)}
\end{aligned}$$

The transfer matrix for hermitian and parity as well as S^z-conserving two-site operator A has the form

$$T(u) = \begin{pmatrix} a & c & 0 & 0 \\ c & a & 0 & 0 \\ 0 & 0 & e & 0 \\ 0 & 0 & 0 & e \end{pmatrix} \qquad \text{(A.30)}$$

with

$$\begin{aligned}
a &= \langle \tilde{g}_{11}|A|\tilde{g}_{11}\rangle \\
&= 2\langle \phi_{1_0}^{\perp}|A|\phi_{1_0}^{\perp}\rangle + 3\langle \phi_0^{\parallel,\times}|A|\phi_0^{\parallel,\times}\rangle + \frac{|u|^2}{2}\left(|\sigma+1|^2\langle \phi_{1_0}^{\parallel}|A|\phi_{1_0}^{\parallel}\rangle + |\sigma-1|^2\langle \phi_{1_0}^{\times}|A|\phi_{1_0}^{\times}\rangle\right) \\
&\quad +\sqrt{3}\left(\sigma u^2\langle \phi_0^{\parallel,\times}|A|\phi_0^{\perp}\rangle + \sigma^* u^{*2}\langle \phi_0^{\perp}|A|\phi_0^{\parallel,\times}\rangle\right) + |\sigma|^2|u|^4\langle \phi_0^{\perp}|A|\phi_0^{\perp}\rangle \\
c &= \langle \tilde{g}_{12}|A|\tilde{g}_{12}\rangle \\
&= 4\langle \phi_{1_{\pm1}}^{\perp}|A|\phi_{1_{\pm1}}^{\perp}\rangle + |u|^2\left(|\sigma+1|^2\langle \phi_{1_{\pm1}}^{\parallel}|A|\phi_{1_{\pm1}}^{\parallel}\rangle + |\sigma-1|^2\langle \phi_{1_{\pm1}}^{\times}|A|\phi_{1_{\pm1}}^{\times}\rangle\right) \\
e &= \langle \tilde{g}_{11}|A|\tilde{g}_{22}\rangle \\
&= -2\langle \phi_{1_0}^{\perp}|A|\phi_{1_0}^{\perp}\rangle + 3\langle \phi_0^{\parallel,\times}|A|\phi_0^{\parallel,\times}\rangle - \frac{|u|^2}{2}\left(|\sigma+1|^2\langle \phi_{1_0}^{\parallel}|A|\phi_{1_0}^{\parallel}\rangle + |\sigma-1|^2\langle \phi_{1_0}^{\times}|A|\phi_{1_0}^{\times}\rangle\right) \\
&\quad +\sqrt{3}\left(\sigma u^2\langle \phi_0^{\parallel,\times}|A|\phi_0^{\perp}\rangle + \sigma^* u^{*2}\langle \phi_0^{\perp}|A|\phi_0^{\parallel,\times}\rangle\right) + |\sigma|^2|u|^4\langle \phi_0^{\perp}|A|\phi_0^{\perp}\rangle
\end{aligned}$$

The transfer matrices eigenvalues and -vectors are:

$$\begin{array}{lllll}
\chi_1 = a+c, & |u_1\rangle = \frac{1}{\sqrt{2}}(1,1,0,0)^t \\
\chi_2 = a-c, & |u_2\rangle = \frac{1}{\sqrt{2}}(1,-1,0,0)^t \\
\chi_3 = e, & |u_3\rangle = (0,0,1,0)^t \\
\chi_4 = e, & |u_4\rangle = (0,0,0,1)^t
\end{array} \tag{A.31}$$

For SU(2)-symmetric operators the eigenvalues are

$$\chi_1 = 6\langle \phi_1^{\perp}|A|\phi_1^{\perp}\rangle + 3\langle \phi_0^{\parallel,\times}|A|\phi_0^{\parallel,\times}\rangle + \tfrac{3|u|^2}{2}\left(|\sigma+1|^2\langle \phi_1^{\parallel}|A|\phi_1^{\parallel}\rangle + |\sigma-1|^2\langle \phi_1^{\times}|A|\phi_1^{\times}\rangle\right) \tag{A.32}$$

$$+\sqrt{3}\left(\sigma u^2\langle \phi_0^{\parallel,\times}|A|\phi_0^{\perp}\rangle + \sigma^* u^{*2}\langle \phi_0^{\perp}|A|\phi_0^{\parallel,\times}\rangle\right) + |\sigma|^2|u|^4\langle \phi_0^{\perp}|A|\phi_0^{\perp}\rangle \tag{A.33}$$

$$\chi_{2,3,4} = -2\langle \phi_1^{\perp}|A|\phi_1^{\perp}\rangle + 3\langle \phi_0^{\parallel,\times}|A|\phi_0^{\parallel,\times}\rangle - \tfrac{|u|^2}{2}\left(|\sigma+1|^2\langle \phi_1^{\parallel}|A|\phi_1^{\parallel}\rangle + |\sigma-1|^2\langle \phi_1^{\times}|A|\phi_1^{\times}\rangle\right) \tag{A.34}$$

$$+\sqrt{3}\left(\sigma u^2\langle \phi_0^{\parallel,\times}|A|\phi_0^{\perp}\rangle + \sigma^* u^{*2}\langle \phi_0^{\perp}|A|\phi_0^{\parallel,\times}\rangle\right) + |\sigma|^2|u|^4\langle \phi_0^{\perp}|A|\phi_0^{\perp}\rangle \tag{A.35}$$

Regard $A = \mathrm{id}$:

$$a = 5 + |u|^2\left(|\sigma|^2+1\right) + |\sigma|^2|u|^4 \tag{A.36}$$

$$c = 4 + 2|u|^2\left(|\sigma|^2+1\right) \tag{A.37}$$

$$e = 1 - |u|^2\left(|\sigma|^2+1\right) + |\sigma|^2|u|^4 \tag{A.38}$$

with this: (A.39)

$$\kappa_1 = \left(|u|^2+3\right)\left(|\sigma u|^2+3\right) \tag{A.40}$$

$$\kappa_{2,3,4} = \left(|u|^2-1\right)\left(|\sigma u|^2-1\right) \tag{A.41}$$

Regard $A = H$:

$$
\begin{aligned}
\eta_1 &= -\frac{3}{2}J + \frac{3}{4}\left(-3J - 4J_{\mathrm{cyc}}\right) + \frac{3|u|^2}{8}\left(|\sigma+1|^2 J + |\sigma-1|^2\left(-3J - 8J_{\mathrm{cyc}}\right)\right) \\
&\quad + \sqrt{3}\left(\sigma u^2 + \sigma^* u^{*2}\right)\frac{\sqrt{3}}{2}\left(J - 2J_{\mathrm{cyc}}\right) + \frac{1}{4}|\sigma|^2|u|^4\left(-3J + 4J_{\mathrm{cyc}}\right) \\
\eta_{2,3,4} &= \frac{1}{2}J + \frac{3}{4}\left(-3J - 4J_{\mathrm{cyc}}\right) - \frac{|u|^2}{8}\left(|\sigma+1|^2 J + |\sigma-1|^2\left(-3J - 8J_{\mathrm{cyc}}\right)\right) \\
&\quad + \sqrt{3}\left(\sigma u^2 + \sigma^* u^{*2}\right)\frac{\sqrt{3}}{2}\left(J - 2J_{\mathrm{cyc}}\right) + \frac{1}{4}|\sigma|^2|u|^4\left(-3J + 4J_{\mathrm{cyc}}\right)
\end{aligned}
$$

Use the representation $u = re^{i\phi}$ and $\sigma = re^{i\alpha}$:

$$
\begin{aligned}
\eta_1 &= \frac{3}{4}\left(-5J - 4J_{\mathrm{cyc}}\right) + \frac{3r^2}{8}\left(\left(s^2 + 1 + 2s\cos\alpha\right)J + \left(s^2 + 1 - 2s\cos\alpha\right)\left(-3J - 8J_{\mathrm{cyc}}\right)\right) \\
&\quad + 3sr^2\cos\left(2\phi + \alpha\right)\left(J - 2J_{\mathrm{cyc}}\right) + \frac{1}{4}s^2 r^4\left(-3J + 4J_{\mathrm{cyc}}\right) \\
&= \frac{3}{4}\Big[\left(-5J - 4J_{\mathrm{cyc}}\right) + r^2(s^2+1)\left(-J - 4J_{\mathrm{cyc}}\right) + 4sr^2\cos\alpha\left(J + 2J_{\mathrm{cyc}}\right) \\
&\quad + 4sr^2\cos\left(2\phi + \alpha\right)\left(J - 2J_{\mathrm{cyc}}\right) + s^2 r^4\left(-J + \frac{4}{3}J_{\mathrm{cyc}}\right)\Big]
\end{aligned}
$$

With these calculations, we easily obtain the energies of a class of variational states of the matrix product type for the spin ladder with cyclic exchange.

$$(S=2, P=1, k=0)$$

$$\begin{aligned}
S^z &= \pm 2 : |\phi_{2_{\pm 2}}\rangle = \left| \begin{smallmatrix} t_\pm \\ t_\pm \end{smallmatrix} \right\rangle \\
S^z &= \pm 1 : |\phi_{2_{\pm 1}}\rangle = \frac{1}{\sqrt{2}} \left(\left| \begin{smallmatrix} t_\pm \\ t_0 \end{smallmatrix} \right\rangle + \left| \begin{smallmatrix} t_0 \\ t_\pm \end{smallmatrix} \right\rangle \right) \\
S^z &= 0 : |\phi_{2_0}\rangle = \frac{1}{\sqrt{6}} \left(2 \left| \begin{smallmatrix} t_0 \\ t_0 \end{smallmatrix} \right\rangle + \left| \begin{smallmatrix} t_+ \\ t_- \end{smallmatrix} \right\rangle + \left| \begin{smallmatrix} t_- \\ t_+ \end{smallmatrix} \right\rangle \right)
\end{aligned}$$

$$(S=1, P=-1, k=0)$$

$$\begin{aligned}
S^z &= \pm 1 : |\phi^{\parallel}_{1_{\pm 1}}\rangle = \pm \frac{1}{\sqrt{2}} \left(\left| \begin{smallmatrix} t_\pm \\ t_0 \end{smallmatrix} \right\rangle - \left| \begin{smallmatrix} t_0 \\ t_\pm \end{smallmatrix} \right\rangle \right) \\
S^z &= 0 : |\phi^{\parallel}_{1_0}\rangle = \frac{1}{\sqrt{2}} \left(\left| \begin{smallmatrix} t_+ \\ t_- \end{smallmatrix} \right\rangle - \left| \begin{smallmatrix} t_- \\ t_+ \end{smallmatrix} \right\rangle \right)
\end{aligned}$$

$$(S=1, P=1, k=\pi)$$

$$\begin{aligned}
S^z &= \pm 1 : |\phi^{\perp}_{1_{\pm 1}}\rangle = \frac{1}{\sqrt{2}} \left(\left| \begin{smallmatrix} t_\pm \\ s_0 \end{smallmatrix} \right\rangle + \left| \begin{smallmatrix} s_0 \\ t_\pm \end{smallmatrix} \right\rangle \right) \\
S^z &= 0 : |\phi^{\perp}_{1_0}\rangle = \frac{1}{\sqrt{2}} \left(\left| \begin{smallmatrix} t_0 \\ s_0 \end{smallmatrix} \right\rangle + \left| \begin{smallmatrix} s_0 \\ t_0 \end{smallmatrix} \right\rangle \right)
\end{aligned} \tag{A.24}$$

$$(S=1, P=-1, k=\pi)$$

$$\begin{aligned}
S^z &= \pm 1 : |\phi^{\times}_{1_{\pm 1}}\rangle = \frac{1}{\sqrt{2}} \left(\left| \begin{smallmatrix} t_\pm \\ s_0 \end{smallmatrix} \right\rangle - \left| \begin{smallmatrix} s_0 \\ t_\pm \end{smallmatrix} \right\rangle \right) \\
S^z &= 0 : |\phi^{\times}_{1_0}\rangle = \frac{1}{\sqrt{2}} \left(\left| \begin{smallmatrix} t_0 \\ s_0 \end{smallmatrix} \right\rangle - \left| \begin{smallmatrix} s_0 \\ t_0 \end{smallmatrix} \right\rangle \right)
\end{aligned}$$

$$(S=0, P=1, k=0)$$

$$\begin{aligned}
S^z &= 0 : |\phi^{\parallel}_0\rangle = \left| \begin{smallmatrix} s_0 \\ s_0 \end{smallmatrix} \right\rangle \\
S^z &= 0 : |\phi^{\times,\perp}_0\rangle = \frac{1}{\sqrt{3}} \left(\left| \begin{smallmatrix} t_0 \\ t_0 \end{smallmatrix} \right\rangle - \left| \begin{smallmatrix} t_+ \\ t_- \end{smallmatrix} \right\rangle - \left| \begin{smallmatrix} t_- \\ t_+ \end{smallmatrix} \right\rangle \right)
\end{aligned}$$

$$|\phi^{\perp}_0\rangle = \frac{1}{2}\left(|\phi^{\parallel}_0\rangle - \sqrt{3}|\phi^{\times,\perp}_0\rangle\right), \quad |\phi^{\parallel,\times}_0\rangle = \frac{1}{2}\left(\sqrt{3}|\phi^{\parallel}_0\rangle + |\phi^{\times,\perp}_0\rangle\right) \tag{A.25}$$

Table A.1: Reasonable choice of basis states for a single plaquette, leg symmetrized.

B QCTMRG - Technical details

In this appendix, details of the implementation of the QCTMRG algorithm shall be presented. A smart choice of the matrix multiplications can drastically lower the running time. In Section B.1, we give an estimate of the resource consumption in the various QCTMRG iteration steps. A steadily-growing partition function during the iterations requires normalization of the tiles. Details are presented in Section B.2.

B.1 Running-time analysis of the QCTMRG algorithm

An essential feature of the QCTMRG-algorithm is the composition of various tiles which are mathematically implemented as tensor or matrix multiplication. Running time and storage consumption of the algorithm delicately depend on the order in which the tiles are put together.

For instance, regard a multiplication of three $n \times n$-matrices A, B, C. The straightforward computation

$$D_{a,b} = \sum_{i,j} A_{a,i} B_{i,j} C_{j,b} \tag{B.1}$$

requires four nested loops (one for each variable), giving an order $\mathcal{O}(n^4)$ for the running time. The storage consumption stays of order $\mathcal{O}(n^2)$, which is the size of the matrices. Remember that constant prefactors do not play an essential role as we choose n sufficiently high. A different approach to the matrix-multiplication problem introduces an auxiliary $n \times n$-matrix M and the computations

$$M_{a,j} = \sum_{i} A_{a,i} B_{i,j}, \quad D_{a,b} = \sum_{i} M_{a,i} B_{i,b} \tag{B.2}$$

which both include the summation over one variable only. While the order of storage used ($\mathcal{O}(n^2)$) stays the same in this case, the running time, originating from three nested loops, reduces to $\mathcal{O}(n^3)$.

Even more drastic decrease of resource consumption can be achieved by the smart choice of computational order in the case of tensor multiplication, where the number of variables is generically higher. So, in terms of efficiency, a detailed description of the tensor multiplication is an essential requirement to a successful implementation of the QCTMRG-algorithm and shall be given here.

In the following, we refer to the picture of the system consisting of two-dimensional *tiles* described above. A tile called W, e.g., will be represented by

$$\begin{array}{c} \widehat{o} \\ (l\ W\ r), \\ \underbrace{u} \end{array} \tag{B.3}$$

with the variables r, o, l, u being states at the right, upper, left and lower edge of the tile. In this description, we review the iteration part of the QCTMRG-algorithm (introduced in Section 3.4.1), providing the underlying multiplications.

i. **Construction of initial tiles**
Initial representations of the tiles

$$(\bullet \underset{u}{\overset{o}{C_L}} r), (l \underset{u}{\overset{o}{C_R}} \bullet), (\bullet \underset{u}{\overset{o}{P_L}} r), (l \underset{u}{\overset{o}{P_R}} \bullet), (l \underset{u}{\overset{o}{P_V}} r), (l \underset{u}{\overset{o}{W}} r), (l \underset{u}{\overset{o}{X}} r) \tag{B.4}$$

required in the renormalization procedure are constructed.

ii. **Composition of enlarged system tiles**

Enlarge Row-to-row-tiles:

$$(\bullet \underset{\{u_{1,2}\}}{\overset{\{o_{1,2}\}}{\tilde{P}_L}} r) = \sum_v (\bullet \underset{u_1}{\overset{o_1}{P_L}} v)(v \underset{u_2}{\overset{o_2}{W}} r) \tag{B.5}$$

($\tilde{P}_R, \tilde{P}_{LX}, \tilde{P}_{RX}$ analogously)
Storage: $\mathcal{O}(m^2S^3)$, *Running time:* $\mathcal{O}(m^2S^4)$

Enlarge Column-to-column-tile:

$$(\{l_{1,2}\} \underset{u}{\overset{o}{\tilde{P}_V}} \{r_{1,2}\}) = \sum_h \begin{matrix} (l_1 \underset{h}{\overset{o}{P_V}} r_1) \\ (l_2 \underset{u}{\overset{h}{W}} r_2) \end{matrix} \tag{B.6}$$

Storage: $\mathcal{O}(m^2S^4)$, *Running time:* $\mathcal{O}(m^2S^5)$

Create auxiliary tiles:

$$(\bullet \underset{\{u_{1,2}\}}{\overset{\{o_{1,2}\}}{T_L}} r) = \sum_v (\bullet \underset{u_1}{\overset{o_1}{C_L}} v)(v \underset{u_2}{\overset{o_2}{P_V}} r), \quad T_R \text{ analogously} \tag{B.7}$$

Storage: $\mathcal{O}(m^3S^2)$, *Running time:* $\mathcal{O}(m^4S^2)$

Compose enlarged corner tiles:

$$(\bullet \underset{\{u_{1,2}\}}{\overset{\{o_{1,2}\}}{\tilde{C}_L}} \{r_{1,2}\}) = \sum_{\{h_{1,2}\}} \begin{matrix} (\bullet \underset{\{h_{1,2}\}}{\overset{\{o_{1,2}\}}{T_L}} r_1) \\ (\bullet \underset{\{u_{1,2}\}}{\overset{\{h_{1,2}\}}{\tilde{P}_L}} r_2) \end{matrix} \tag{B.8}$$

($\tilde{C}_R, \tilde{C}_{LX}, \tilde{C}_{RX}$ analogously)
Storage: $\mathcal{O}(m^3S^3)$, *Running time:* $\mathcal{O}(m^4S^4)$

iii. **Calculation of expectation values**
a) Odd-site system
Firstly, left auxiliary tiles are build:

$$(\bullet \underset{\smile}{\overset{\frown}{V_L}} \{r_{1,2,3}\}) = \sum_{\{g_{1,2}\},\{h_{1,2}\}} (\bullet \underset{\{h_{1,2}\}}{\overset{\frown}{\tilde{C}_L}} \{r_{1,2}\}) \quad (\bullet \underset{\{g_{1,2}\}}{\overset{\frown}{T_L}} r_3 \quad), \qquad V_L X \text{ analogously} \tag{B.9}$$

Storage: $\mathcal{O}(m^2 S)$, *Running time:* $\mathcal{O}(m^4 S^3)$

Next, construct right auxiliary tiles:

$$(\{l_{1,2}\} \underset{\smile}{\overset{\frown}{CP_R}} \bullet) = \sum_{h} (l_1 \underset{\smile}{\overset{\frown}{C_R}} \bullet) \quad (l_2 \underset{\smile}{\overset{\frown}{P_R}} \bullet) \tag{B.10}$$

Storage: $\mathcal{O}(m^2 S^4)$, *Running time:* $\mathcal{O}(m^2 S^5)$

$$(\{l_{1,2,3}\} \underset{\smile}{\overset{\frown}{V_R}} \bullet) = \sum_{g,h} (\{l_{1,2}\} \underset{\smile}{\overset{\frown}{CP_R}} \bullet) \quad (\quad l_3 \underset{\smile}{\overset{\frown}{C_R}} \bullet) \tag{B.11}$$

Storage: $\mathcal{O}(m^2 S)$, *Running time:* $\mathcal{O}(m^4 S)$

Finally, get partition function:

$$Z = \sum_{\{v_{1,2,3}\}} (\bullet \underset{\smile}{\overset{\frown}{V_L}} \{v_{1,2,3}\})(\{v_{1,2,3}\} \underset{\smile}{\overset{\frown}{V_R}} \bullet) \tag{B.12}$$

(Z_{X_H} analogously)
Storage: $\mathcal{O}(1)$, *Running time:* $\mathcal{O}(m^2 S)$

Absorbing the constant S into the prefactor, we accomplish the calculation of the expectation value in a time $\mathcal{O}(m^4)$ requiring a maximum storage of order $\mathcal{O}(m^2)$.

b) Even-site system

After construction of auxiliary tiles...

$$(\bullet\ \underset{\bullet}{\overset{\bullet}{\tilde{V}_L}}\ \{r_{1,2,3,4}\}) = \sum_{\{g_{1,2}\},\{h_{1,2}\}} (\bullet\ \underset{\{h_{1,2}\}}{\overset{\{g_{1,2}\}}{\tilde{C}_L}}\ \{r_{1,2}\})\ (\bullet\ \underset{\{g_{1,2}\}}{\overset{\{h_{1,2}\}}{\tilde{C}_L}}\ \{r_{3,4}\}) \tag{B.13}$$

($\tilde{V}_{LX}, \tilde{V}_R$ analogously)
Storage: $\mathcal{O}(m^2S^2)$, *Running time:* $\mathcal{O}(m^4S^4)$

...we get the partition function:

$$Z = \sum_{\{v_{1,2,3}\}} (\bullet\ \underset{\bullet}{\overset{\bullet}{\tilde{V}_L}}\ \{v_{1,2,3}\})(\{v_{1,2,3}\}\ \underset{\bullet}{\overset{\bullet}{\tilde{V}_R}}\ \bullet) \tag{B.14}$$

(Z_{X_H} analogously)
Storage: $\mathcal{O}(1)$, *Running time:* $\mathcal{O}(m^2S)$

Here, the total time is of order $\mathcal{O}(m^4)$ and the storage of order $\mathcal{O}(m^2)$.

iv. **Construction of reduced density matrices**

After the enlarged tiles are renamed to the original name, the reduced density matrices can be build. In the following, the size of the state space at the edges of the employed tiles is mS. Initially, we again compose left and right column tiles:

$$(\bullet\ \underset{\bullet}{\overset{\bullet}{V_L}}\ \{r_{1,2}\}) = \sum_{g,h} (\bullet\ \underset{h}{\overset{g}{C_L}}\ r_1)\ (\bullet\ \underset{g}{\overset{h}{C_L}}\ r_2) \tag{B.15}$$

(V_R analogously)
Storage: $\mathcal{O}(m^2S^2)$, *Running time:* $\mathcal{O}(m^4S^4)$

With these, two auxiliary tiles are build:

$$(l\ \underset{u}{\overset{o}{H_L}}\ \bullet) = \sum_{v} (\bullet\ \underset{u}{\overset{o}{C_L}}\ v)\ (\{v,l\}\ \underset{\bullet}{\overset{\bullet}{V_R}}\ \bullet) \tag{B.16}$$

(H_R analogously)
Storage: $\mathcal{O}(m^3S^3)$, *Running time:* $\mathcal{O}(m^4S^4)$

By now, we can construct the horizontal reduced density matrices:

$$\rho_L(o,u) = \sum_{v,h} \; (\bullet \underset{u}{\overset{\widehat{h}}{C_L}} \; v) \; (v \underset{h}{\overset{\widehat{o}}{H_L}} \; \bullet) \tag{B.17}$$

(ρ_R analogously)
Storage: $\mathcal{O}(m^2S^2)$, *Running time:* $\mathcal{O}(m^4S^4)$

The vertical reduced density matrix is easily composed:

$$\rho_V(l,r) = \sum_{v} \; (\bullet \underset{\bullet}{\overset{\widehat{\bullet}}{V_L}} \; \{r,v\})(\{l,v\} \; \underset{\bullet}{\overset{\widehat{\bullet}}{V_R}} \; \bullet) \tag{B.18}$$

Storage: $\mathcal{O}(m^2S^2)$, *Running time:* $\mathcal{O}(m^3S^3)$

So, in the construction of the reduced density matrices, we keep an upper bound of $\mathcal{O}(m^4S^4)$ time steps and storage use of order $\mathcal{O}(m^3S^3)$.

v. **Diagonalization of reduced density matrices**
The diagonalization of right, left, and vertical reduced density matrix is performed by the routine DGEEVX from the cross-platform open source software "Linear Algebra Package". It takes a number of $\mathcal{O}(m^3S^3)$ time steps [175], and uses storage of order $\mathcal{O}(m^2S^2)$

vi. **Renormalization**
The renormalization process can be performed in $\mathcal{O}(m^4S^3)$ time steps with a maximum storage use of $\mathcal{O}(m^3S^3)$.

Overall, we expect the running-time to be of order $\mathcal{O}(m^4)$ and storage use of order $\mathcal{O}(m^3)$ within the QCTMRG algorithm. The local basis size S has been absorbed into the prefactor.

B.2 Normalization of growing tiles

While our interest lies in the calculation of (local) expectation values of a certain quantum mechanical system, we have to deal with the partition functions of an iteratively increased classical system in the QCTMRG-algorithm. Thus, the partition function is a rapidly growing entity, leading to several huge matrix entries in the tiles' numerical representation in the renormalization step. So, the program runs the risk of exceeding the numerical capacity of the variables of the system. To avoid this problem, a constant prefactor is extracted in each renormalization step.

Regard, for example, the corner tiles C_L^0, C_L^1 belonging to the first two iteration steps. In a normalization procedure, we divide C_L^0 by the maximum of the absolute value c_L^0 of its entries, yielding the new tile $\tilde{C}_L^0 = 1/c_L^0 C_L^0$, labeled by a tilde, with entries between 0 and

1. The same normalization procedure is applied to the tiles C_R^0, P_L^0, P_R^0 and P_V^0. Note, that the tilded tiles as well as the maximum entries are stored in each iteration step rather than keeping the original tiles.

Within the QCTMRG-algorithm,the system-tiles are successively increased, leading to *e.g.*

$$(\bullet \underbrace{C_L^1}_{\{u_{1,2}\}} \overbrace{\{o_{1,2}\}} \; \{r_{1,2}\}) = \sum_{v_1,v_2,h_1,h_2} (\bullet \underbrace{C_L^0}_{h_1} \overbrace{o_1} \; v_1)\; (v_1 \underbrace{P_V^0}_{h_2} \overbrace{o_2} \; r_1)\; (\bullet \underbrace{P_L^0}_{u_1} \overbrace{h_1} \; v_2)\; (v_2 \underbrace{W}_{u_2} \overbrace{h_2} \; r_2) \tag{B.19}$$

$$= c_L^0 p_V^0 p_L^0 \sum_{v_1,v_2,h_1,h_2} \underbrace{(\bullet \underbrace{\tilde{C}_L^0}_{h_1} \overbrace{o_1} \; v_1)\; (v_1 \underbrace{\tilde{P}_V^0}_{h_2} \overbrace{o_2} \; r_1)\; (\bullet \underbrace{\tilde{P}_L^0}_{u_1} \overbrace{h_1} \; v_2)\; (v_2 \underbrace{W}_{u_2} \overbrace{h_2} \; r_2)}_{(\bullet \underbrace{\bar{C}_L^1}_{\{u_{1,2}\}} \overbrace{\{o_{1,2}\}} \; \{r_{1,2}\})} \tag{B.20}$$

employing the stored variables. In the algorithm, the tilded tiles are composed to form the new tile $\bar{C}_L^1$, which itself has to be normalized to $\tilde{C}_L^1 = 1/c_L^1 \bar{C}_L^1$ like the tiles in the preceeding iteration step. We find as results for the first iteration steps

$$C_L^0 = c_L^0 \tilde{C}_L^0, \quad C_L^1 = c_L^1 c_L^0 p_V^0 p_L^0 \tilde{C}_L^1 \tag{B.21}$$

$$P_L^0 = p_L^0 \tilde{P}_L^0, \quad P_L^1 = p_L^1 p_L^0 \tilde{P}_L^1 \tag{B.22}$$

which can be generalized to

$$C_L^{i+1} = c_L^{i+1} \left(\prod_{j=0}^{i} c_L^j p_V^j p_L^j \right) \tilde{C}_L^{i+1} \tag{B.23}$$

$$P_L^{i+1} = \left(\prod_{j=0}^{i+1} p_L^j \right) \tilde{P}_L^{i+1}. \tag{B.24}$$

Similar considerations define the correspondence between the partition function Z and

composition of the stored corner tiles at step $i+1$:

$$Z^{i+1} = \sum_{v_1,v_2,h_1,h_2} \begin{matrix} (\bullet\ \overbrace{C_L^{i+1}}^{h_3}\ v_1) & (v_1\ \overbrace{C_R^{i+1}}^{h_4}\ \bullet) \\ (\bullet\ \underbrace{C_L^{i+1}}_{h_1}\ v_2) & (v_2\ \underbrace{C_R^{i+1}}_{h_2}\ \bullet) \end{matrix} \tag{B.25}$$

$$= z^{i+1} \underbrace{\sum_{v_1,v_2,h_1,h_2} \begin{matrix} (\bullet\ \overbrace{\tilde{C}_L^{i+1}}^{h_3}\ v_1) & (v_1\ \overbrace{\tilde{C}_R^{i+1}}^{h_4}\ \bullet) \\ (\bullet\ \underbrace{\tilde{C}_L^{i+1}}_{h_1}\ v_2) & (v_2\ \underbrace{\tilde{C}_R^{i+1}}_{h_2}\ \bullet) \end{matrix}}_{\tilde{Z}^{i+1}} \tag{B.26}$$

with

$$z^{i+1} = \left(c_L^{i+1} c_R^{i+1}\right)^2 \prod_{j=0}^{i} \left(c_L^j c_R^j p_L^j p_R^j p_V^j p_V^j\right)^2 . \tag{B.27}$$

In the calculation of thermodynamical quantities we are either interested in the logarithm of the partition function (leading to the free energy) or in the ratio of the partition function of a locally modified system and the partition function of the original system (other expectation values). In the latter case, we can completely ignore the prefactors of the system tiles, since they appear in both partition functions and, thus, only the normalized tiles are required. In the former case, it is sufficient to store the logarithm of the prefactors, then the product of large prefactors in (B.27) is commuted into a sum of smaller numbers, which is numerically easier to handle. With the logarithm of z^{i+1}, the free energy density at iteration step $i+1$

$$f^{i+1} = -\frac{T}{L} \ln Z^{i+1} = -\frac{T}{L} \left(\ln z^{i+1} + \ln \tilde{Z}^{i+1}\right) \tag{B.28}$$

is added together by the logarithm of the prefactor z^{i+1} and the logarithm of the partition function calculated by the normalized tiles.

C Reduced density matrix of the Ising chain

For testing the numerical algorithms, it is useful to make a comparison with analytical data. An easy-calculable, classical model is the antiferromagnetic Ising chain (4.5). In this appendix, we provide an exact formulation of eigenvalues and eigenvectors of the vertical transfer matrix and of the reduced density matrix. Additionally, we present a data table for direct comparison to TMRG-output at the end.

The local transfer matrix (3.7) is

$$\tau^{i,i+1}_{k,k+1} = \delta_{s^i_{k+1},s^i_k}\delta_{s^{i+1}_{k+1},s^{i+1}_k} \mathrm{e}^{-\epsilon J s^i_k s^{i+1}_k}. \tag{C.1}$$

We assume periodic boundary conditions, *i.e.* $s_{2M+1} \equiv s_1$. For simplicity, we now fix $i = 1$. Building up a vertical transfer matrix

$$\begin{aligned}\mathcal{T}(s^1_{(\mu=1..2M)}, s^3_{(\mu=1..2M)}) &:= \sum_{\substack{\{s^2_\mu\}\\ \mu=1\ldots 2M}} \prod_{k=1}^{M} \tau^{1,2}_{2k-1,2k}\tau^{2,3}_{2k,2k+1} \\ &= \sum_{\substack{\{s^2_\mu\}\\ \mu=1\ldots 2M}} \prod_{k=1}^{M} \delta_{s^1_{2k},s^1_{2k-1}}\delta_{s^2_{2k},s^2_{2k-1}}\delta_{s^2_{2k+1},s^2_{2k}}\delta_{s^3_{2k+1},s^3_{2k}} \mathrm{e}^{-\epsilon J(s^1_{2k}s^2_{2k}+s^2_{2k}s^3_{2k})} \\ &= \sum_{\{s^2\}} \prod_{k=1}^{M} \delta_{s^1_{2k},s^1_{2k-1}}\delta_{s^3_{2k+1},s^3_{2k}} \mathrm{e}^{-\epsilon J(s^1_{2k}s^2+s^2 s^3_{2k})}\end{aligned} \tag{C.2}$$

one sees that all s^2_k have the same value s^2 as a consequence of the Kronecker symbols. So the transfer matrix

$$\begin{aligned}\mathcal{T}(s^1_{(\mu=1..2M)}, s^3_{(\mu=1..2M)}) &= \sum_{\{s^2\}} \prod_{k=1}^{M} \delta_{s^1_{2k},s^1_{2k-1}}\delta_{s^3_{2k+1},s^3_{2k}} \mathrm{e}^{-\epsilon J(s^1_{2k}s^2+s^2 s^3_{2k})} \\ &= \left(\prod_{k=1}^{M} \delta_{s^1_{2k-1},s^1_{2k}}\right) \times 2\cosh\left[\epsilon JS(\sum_{k=1}^{M} s^1_{2k} + s^3_{2k})\right] \times \left(\prod_{k=1}^{M} \delta_{s^3_{2k},s^3_{2k+1}}\right)\end{aligned} \tag{C.3}$$

can be written in a much simpler way.

Alternative representation of $\mathcal{T}$

A vector in this Hilbert space $\mathcal{H}_s$ of $2M$ spins is:

$$\left|v_s\right\rangle = \sum_{\substack{\{s_\mu\}\\ \mu=1\ldots 2M}} v_s(s_1, s_2, \ldots s_{2M})\left|s_1\right\rangle \otimes \left|s_2\right\rangle \otimes \cdots \otimes \left|s_{2M}\right\rangle \tag{C.4}$$

We define a new, smaller Hilbert space $\mathcal{H}_t$ spanning the states of M spins. It consists of a tensor product of states of all spins at sites $2k$, $k = 1 \ldots M$. Here, a vector reads:

$$\left|v_t\right\rangle = \sum_{\substack{\{t_\mu\}\\ \mu=1\ldots M}} v_t(t_1, t_2, \ldots t_M)\left|t_1\right\rangle \otimes \left|t_2\right\rangle \otimes \cdots \otimes \left|t_M\right\rangle \tag{C.5}$$

In order to allow interaction between both Hilbert spaces, two projection operators are introduced:

$$\mathcal{P}_\alpha := \sum_{\{t_\mu\},\{s_\mu\}} \left|t_1, t_2, \ldots t_M\right\rangle \prod_{k=1}^{M} \delta_{t_k,s_{2k}} \delta_{s_{2k},s_{2k-1}} \left\langle s_1, s_2, \ldots s_{2M}\right| \tag{C.6}$$

$$\mathcal{P}_\beta := \sum_{\{t_\mu\},\{s_\mu\}} \left|t_1, t_2, \ldots t_M\right\rangle \prod_{k=1}^{M} \delta_{t_k,s_{2k}} \delta_{s_{2k},s_{2k+1}} \left\langle s_1, s_2, \ldots s_{2M}\right| \tag{C.7}$$

With the definition

$$\mathcal{M} = \sum_{\{t'_\mu\},\{t_\mu\}} \left|t'_1, t'_2, \ldots t'_M\right\rangle 2\cosh\left[\epsilon JS(\sum_{k=1}^{M} t'_k + t_k)\right] \left\langle t_1, t_2, \ldots t_M\right| \tag{C.8}$$

we rewrite the transfer matrix

$$\mathcal{T} = {\mathcal{P}_\alpha}^{-1} \mathcal{M} \mathcal{P}_\beta \tag{C.9}$$

as product of matrices.

Eigenvalues and eigenvectors of $\mathcal{T}$

Turning again to the problem of finding the exact eigenvalues and vectors, we argue as follows:

i. From this representation it can be seen that any non-vanishing eigenvalue $\lambda_i > 0$ has a corresponding right eigenvector of the form

$$\Psi_i^R = {\mathcal{P}_\alpha}^{-1} \Phi_i^R, \tag{C.10}$$

i.e. it can be represented as projection of a vector from $\mathcal{H}_t$ to $\mathcal{H}_s$.

ii. Ψ_i^R as a right eigenvector must fulfill

$$\mathcal{T}\Psi_i^R = \lambda_i \Psi_i^R \tag{C.11}$$

which can be rewritten as

$${\mathcal{P}_\alpha}^{-1} \mathcal{M} \mathcal{P}_\beta {\mathcal{P}_\alpha}^{-1} \Phi_i^R = {\mathcal{P}_\alpha}^{-1} \lambda_i \Phi_i^R. \tag{C.12}$$

This is, by leaving out the projection $\mathcal{P}_\alpha^{-1}$ at the left hand side, an eigenvector equation for Φ_i^R:

$$\mathcal{M} \mathcal{P}_\beta {\mathcal{P}_\alpha}^{-1} \Phi_i^R = \lambda_i \Phi_i^R. \tag{C.13}$$

iii. Forward and backward projection with both different projection operators

$$\mathcal{P}_\beta {\mathcal{P}_\alpha}^{-1} = \left|\uparrow^M\right\rangle\left\langle\uparrow^M\right| + \left|\downarrow^M\right\rangle\left\langle\downarrow^M\right| =: \mathcal{P}_{\uparrow,\downarrow} \tag{C.14}$$

projects out all states except for $\left|\uparrow^M\right\rangle := \left|\uparrow\uparrow\ldots\uparrow\right\rangle$ and $\left|\downarrow^M\right\rangle := \left|\downarrow\downarrow\ldots\downarrow\right\rangle$ in $\mathcal{H}_t$.

iv. With these considerations and $T^z = \sum_{k=1}^{M} t_k$, it follows

$$\lambda_i \Phi_i^R(\{t_\mu\})\big|\{t_\mu\}\big\rangle = \sum_{\{t'_\mu\}} \mathcal{M}\ \mathcal{P}_{\uparrow,\downarrow}\ \Phi_i^R(\{t'_\mu\})\ \big|\{t'_\mu\}\big\rangle \tag{C.15}$$

$$= \mathcal{M}\ \Big[\Phi_i^R(\uparrow^M)\ |\ \uparrow^m\big\rangle\ + \Phi_i^R(\downarrow^M)\ |\ \downarrow^M\big\rangle\Big] \tag{C.16}$$

$$= \Big\{2\Phi_i^R(\uparrow^M)\cosh\left[\epsilon JS(T^z + MS)\right] + 2\Phi_i^R(\downarrow^M)\cosh\left[\epsilon JS(T^z - MS)\right]\Big\}\big|\{t_\mu\}\big\rangle. \tag{C.17}$$

v. For $\Phi_i^R(\uparrow^M)$ and $\Phi_i^R(\uparrow^M)$ we find:

$$\lambda_i \Phi_i^R(\uparrow^M) = 2\Phi_i^R(\uparrow^M)\cosh\left[2\epsilon MJS^2\right] + 2\Phi_i^R(\downarrow^M) \tag{C.18}$$

$$\lambda_i \Phi_i^R(\downarrow^M) = 2\Phi_i^R(\uparrow^M) + 2\Phi_i^R(\downarrow^M)\cosh\left[-2\epsilon MJS^2\right] \tag{C.19}$$

This gives the eigenvalues

$$\lambda_+ = 2(\cosh\left[2\epsilon MJS^2\right] + 1) = 4\cosh^2\left[\epsilon MJS^2\right] \tag{C.20}$$

$$\lambda_- = 2(\cosh\left[2\epsilon MJS^2\right] - 1) = 4\sinh^2\left[\epsilon MJS^2\right] \tag{C.21}$$

which agree with the well-known transfer matrix solution of the Ising model [79]. Further, we find

$$\Phi_+^R(\uparrow^M) = \Phi_+^R(\downarrow^M) \tag{C.22}$$

$$\Phi_-^R(\uparrow^M) = -\Phi_-^R(\downarrow^M) \tag{C.23}$$

as a condition for the eigenvectors. For the general components $\Phi_i^R(\{t_\mu\})$ of the eigenvectors we get:

$$\Phi_+^R(\{t_\mu\}) = \frac{\cosh(\epsilon MJS^2)}{\cosh^2\left[\epsilon MJS^2\right]}\cosh(\epsilon JST^z)\Phi_+^R(\uparrow^M) \tag{C.24}$$

$$\Phi_-^R(\{t_\mu\}) = \frac{\sinh(\epsilon MJS^2)}{\sinh^2\left[\epsilon MJS^2\right]}\sinh(\epsilon JST^z)\Phi_-^R(\uparrow^M) \tag{C.25}$$

or simplified and setting $\Phi_+^R(\uparrow^M) = \Phi_-^R(\uparrow^M) = 1$:

$$\Phi_+^R(\{t_\mu\}) = \frac{\cosh(\epsilon JST^z)}{\cosh(\epsilon MJS^2)} \tag{C.26}$$

$$\Phi_-^R(\{t_\mu\}) = \frac{\sinh(\epsilon JST^z)}{\sinh(\epsilon MJS^2)} \tag{C.27}$$

The left eigenvectors can as well be represented as projection on the reduced Hilbert space $\mathcal{H}_t$:

$$\Psi_i^L(\{t_\mu\}) = \Phi_i^L(\{t_\mu\})\mathcal{P}_\beta \tag{C.28}$$

A similar procedure as in the right eigenvector case shows

$$\Phi_+^L(\{t_\mu\}) = \frac{\cosh(\epsilon JST^z)}{\cosh(\epsilon MJS^2)} \tag{C.29}$$

$$\Phi_-^L(\{t_\mu\}) = \frac{\sinh(\epsilon JST^z)}{\sinh(\epsilon MJS^2)} \tag{C.30}$$

as well.

As a solution for the eigenvector problem in $\mathcal{H}_s$, we get

$$\Psi_+^R(\{s_\mu\}) = \frac{\cosh(\epsilon JS\frac{S^z}{2})}{\cosh(\epsilon MJS^2)} \prod_{k=1}^{M} \delta_{s_{2k},s_{2k+1}} \tag{C.31}$$

$$\Psi_+^L(\{s_\mu\}) = \frac{\cosh(\epsilon JS\frac{S^z}{2})}{\cosh(\epsilon MJS^2)} \prod_{k=1}^{M} \delta_{s_{2k-1},s_{2k}} \tag{C.32}$$

$$\tag{C.33}$$

and

$$\Psi_-^R(\{s_\mu\}) = \frac{\sinh(\epsilon JS\frac{S^z}{2})}{\sinh(\epsilon MJS^2)} \prod_{k=1}^{M} \delta_{s_{2k},s_{2k+1}} \tag{C.34}$$

$$\Psi_-^L(\{s_\mu\}) = \frac{\sinh(\epsilon JS\frac{S^z}{2})}{\sinh(\epsilon MJS^2)} \prod_{k=1}^{M} \delta_{s_{2k-1},s_{2k}} \tag{C.35}$$

.

$$\Psi_+^R\Psi_+^L = \sum_{\{s_\mu\}} \Psi_+^R(\{s_\mu\})\Psi_+^L(\{s_\mu\}) \tag{C.36}$$

$$= \sum_{\{s_\mu\}} \frac{\cosh^2(\epsilon JS\frac{S^z}{2})}{\cosh^2(\epsilon MJS^2)} \prod_{k=1}^{M} \delta_{s_{2k},s_{2k+1}}\delta_{s_{2k-1},s_{2k}} \tag{C.37}$$

$$= \frac{\cosh^2(\epsilon MJS^2)}{\cosh^2(\epsilon MJS^2)} + \frac{\cosh^2(-\epsilon MJS^2)}{\cosh^2(\epsilon MJS^2)} = 2 \tag{C.38}$$

Reduced density matrix ρ

The reduced density matrix $\rho = \sum_{\{s_{M+1..2M}\}} \left|\Psi_+^L\right\rangle\left\langle\Psi_+^R\right|$ lives on the Hilbert space of the M first spins $s_1 \ldots s_M$ summing out the spins $s_{M+1} \ldots s_{2M}$.

$$\begin{aligned}\rho(s'_{(\mu=1..M)}, s_{(\mu=1..M)}) &= \sum_{\{s'_{M+1..2M}\},\{s_{M+1..2M}\}} \prod_{k=1}^{M} \delta_{s'_{2k-1},s'_{2k}} \delta_{s_{2k},s_{2k+1}} \prod_{k=M+1}^{2M} \delta_{s'_k,s_k} \\ &\quad \times \frac{\cosh(\epsilon JS\frac{1}{2}\sum_{k=1}^{2M} s'_k)\cosh(\epsilon JS\frac{1}{2}\sum_{k=1}^{2M} s_k)}{2\cosh^2(\epsilon MJS^2)} \qquad \text{(C.39)} \\ &= \sum_{\tilde{s}} \prod_{k=1}^{M} \delta_{s'_{2k-1},s'_{2k}} \delta_{s_{2k},s_{2k+1}} \\ &\quad \times \frac{\cosh(\epsilon JS\frac{1}{2}[M\tilde{s}+S'^z])\cosh(\epsilon JS\frac{1}{2}[M\tilde{s}+S^z])}{2\cosh^2(\epsilon MJS^2)} \qquad \text{(C.40)}\end{aligned}$$

The summation and the staggered arrangement of the delta symbols leads to setting all "upper" spins $s_{M+1..2M} = s_{M+1..2M} = \tilde{s}$ in (C.40). This has consequences for the "lower" spins as well.

Eigenvalues and eigenvectors of ρ

The non-vanishing eigenvalues of ρ

$$\begin{aligned}\lambda_i^\rho \psi_i^R(\{s'_\mu\}) &= \sum_{\{s_\mu\}} \sum_{\tilde{s}} \prod_{k=1}^{M} \delta_{s'_{2k-1},s'_{2k}} \delta_{s_{2k},s_{2k+1}} \\ &\quad \times \frac{\cosh(\epsilon JS\frac{1}{2}[M\tilde{s}+S'^z])\cosh(\epsilon JS\frac{1}{2}[M\tilde{s}+S^z])}{2\cosh^2(\epsilon MJS^2)} \psi_i^R(\{s_\mu\}) \qquad \text{(C.41)}\end{aligned}$$

can be found by similar considerations as above:

$$\begin{aligned}\lambda_i^\rho \psi_i^R(\{s'_\mu\}) &= \sum_{\tilde{s}} \prod_{k=1}^{M} \delta_{s'_{2k-1},s'_{2k}} \delta_{s_{2k},s_{2k+1}} \\ &\quad \times \Big\{ \frac{\cosh(\epsilon JS\frac{1}{2}[M\tilde{s}+S'^z])\cosh(\epsilon JS\frac{1}{2}[M\tilde{s}+MS])}{2\cosh^2(\epsilon MJS^2)} \psi_i^R(\uparrow^M) + \\ &\quad \frac{\cosh(\epsilon JS\frac{1}{2}[M\tilde{s}+S'^z])\cosh(\epsilon JS\frac{1}{2}[M\tilde{s}-MS])}{2\cosh^2(\epsilon MJS^2)} \psi_i^R(\downarrow^M) \Big\} \qquad \text{(C.42)}\end{aligned}$$

Now, we have to distinguish between odd and even M. For the case of odd M, we see that the density matrix has only non-vanishing elements for $s'_M = \tilde{s}$ and $s_1 = \tilde{s}$ and the

eigenvalue equation

$$\begin{aligned}\lambda_i^\rho \psi_i^R(\{s'_\mu\}) &= \prod_{k=1}^{M} \delta_{s'_{2k-1},s'_{2k}} \\ &\quad \times \frac{\cosh(\epsilon JS\frac{1}{2}[Ms'_M + S'^z])\cosh(\epsilon MJSs'_M)}{2\cosh^2(\epsilon MJS^2)} \psi_i^R([s'_M]^M) \qquad \text{(C.43)} \\ &= \prod_{k=1}^{M} \delta_{s'_{2k-1},s'_{2k}} \frac{\cosh(\epsilon JS\frac{1}{2}[Ms'_M + S'^z])}{2\cosh(\epsilon MJS^2)} \psi_i^R([s'_M]^M) \qquad \text{(C.44)}\end{aligned}$$

reduces to a more simple form. For $\psi_i^R(\uparrow^M)$ and $\psi_i^R(\downarrow^M)$ we find two decoupled equations

$$\lambda_i^\rho \psi_i^R(\uparrow^M) = \frac{1}{2}\psi_i^R(\uparrow^M), \quad \lambda_i^\rho \psi_i^R(\downarrow^M) = \frac{1}{2}\psi_i^R(\downarrow^M), \qquad \text{(C.45)}$$

leading two a two-fold degenerate eigenvalue of $\lambda_{1,2}^\rho = \frac{1}{2}$.
Considering M even, $s_M = \tilde{s}$ and $s_1 = \tilde{s}$ leads to an equation

$$\begin{aligned}\lambda_i^\rho \psi_i^R(\{s'_\mu\}) &= \prod_{k=1}^{M} \delta_{s'_{2k-1},s'_{2k}} \Big\{ \frac{\cosh(\epsilon JS\frac{1}{2}[MS + S'^z])}{2\cosh(\epsilon MJS^2)} \psi_i^R(\uparrow^M) + \\ &\quad \frac{\cosh(\epsilon JS\frac{1}{2}[-MS + S'^z])}{2\cosh(\epsilon MJS^2)} \psi_i^R(\downarrow^M) \Big\} \qquad \text{(C.46)}\end{aligned}$$

which takes us to

$$\begin{aligned}\lambda_i^\rho \psi_i^R(\uparrow^M) &= \frac{1}{2}\psi_i^R(\uparrow^M) + \frac{1}{2\cosh(\epsilon MJS^2)} \psi_i^R(\downarrow^M) \qquad \text{(C.47)} \\ \lambda_i^\rho \psi_i^R(\downarrow^M) &= \frac{1}{2\cosh(\epsilon MJS^2)} \psi_i^R(\uparrow^M) + \frac{1}{2}\psi_i^R(\downarrow^M) \qquad \text{(C.48)}\end{aligned}$$

and

$$\lambda_+^\rho = \frac{1}{2}\left[1 + \frac{1}{\cosh(\epsilon MJS^2)}\right], \quad \lambda_-^\rho = \frac{1}{2}\left[1 - \frac{1}{\cosh(\epsilon MJS^2)}\right]. \qquad \text{(C.49)}$$

In Table C.1, we give some eigenvalues of the transfer matrix and the corresponding reduced density matrix for fixed ϵ and various Trotter numbers.

M	λ_+	λ_-	λ_+^ρ	λ_-^ρ
1	4.00063	0.00063	0.50000	0.50000
2	4.00250	0.00250	0.99984	0.00016
3	4.00563	0.00563	0.50000	0.50000
4	4.01001	0.01001	0.99938	0.00062
5	4.01565	0.01565	0.50000	0.50000
6	4.02254	0.02254	0.99860	0.00140
7	4.03070	0.03070	0.50000	0.50000
8	4.04013	0.04013	0.99751	0.00249
9	4.05084	0.05084	0.50000	0.50000
10	4.06283	0.06283	0.99612	0.00388
20	4.25525	0.25525	0.98477	0.01523
50	5.77685	1.77685	0.91606	0.08394
100	14.26458	10.26458	0.76477	0.23523
200	150.41990	146.41990	0.58154	0.41846
500	268339.28652	268335.28652	0.50193	0.49807

Table C.1: Eigenvalues of transfer matrix and reduced density matrix for fixed $\epsilon = 0.05$, $J = 1$ and $S = 1/2$ for various M.

Bibliography

[1] A. Läuchli, G. Schmid, and M. Troyer: *Phase Diagram of the Spin Ladder with Cyclic Four Spin Exchange*. Phys. Rev. B **67**, 100409 (2003). 1, 2, 15, 25, 26, 27, 32, 35, 36, 86, 97, 109, 111, 114, 119, 128, 129

[2] E. Dagotto: *Experiments on ladders reveal a complex interplay between a spin-gapped normal state and superconductivity*. Rep. Prog. Phys. **62**, 1525 (1999). 7, 8, 9, 81

[3] F. Haldane: *Continuum Dynamics of the 1-D Heisenberg Antiferromagnet: Identification with the O(3) Nonlinear Sigma Model*. Phys. Lett. A **93**, 464 (1983). 7, 93

[4] F. Haldane: *Nonlinear Field Theory of Large-Spin Heisenberg Antiferromagnets: Semiclassically Quantized Solitons of the One-Dimensional Easy-Axis Néel State*. Phys. Rev. Lett. **50**, 1153 (1983). 7, 93

[5] R. Hirsch: *Diplomarbeit, Universität zu Köln* (1988). 7

[6] P. W. Anderson: *Resonating valence bonds: A new kind of insulator?* Mat. Res. Bull. **8**, 153 (1973). 7

[7] P. W. Anderson: *The resonating valence bond state in* La_2CuO_4 *and superconductivity*. Science **235**, 1196 (1987). 7, 11

[8] J. G. Bednorz and K. A. Müller: *Possible High* T_c *Superconductivity in the Ba-La-Cu-O System*. Z. Phys. B **64**, 189 (1986). 7

[9] E. Dagotto and A. Moreo: *Zero-temperature properties of the two-dimensional Heisenberg antiferromagnet: A numerical study*. Phys. Rev. B **38**, 5087 (1988). 7, 11

[10] D. C. Johnston, J. W. Johnson, D. P. Goshorn, and A. J. Jacobson: *Magnetic susceptibility of* $(VO)_2P_2O_7$*: A one-dimensional spin-1/2 Heisenberg antiferromagnet with a ladder spin configuration and a singlet ground state*. Phys. Rev. B **35**, 219 (1987). 8

[11] R. S. Eccleston, T. Barnes, J. Brody, and J. W. Johnson: *Inelastic neutron scattering from the spin ladder compound* $(VO)_2P_2O_7$. Phys. Rev. Lett. **73**, 2626 (1994). 8

[12] E. Dagotto, J. Riera, and D. Scalapino: *Superconductivity in ladders and coupled planes*. Phys. Rev. B **45**, 5744 (1992). 8, 11

[13] A. W. Garrett, S. E. Nagler, D. A. Tennant, B. C. Sales, and T. Barnes: *Magnetic Excitations in the* $S = 1/2$ *Alternating Chain Compound* $(VO)_2P_2O_7$. Phys. Rev. Lett. **79**, 745 (1997). 8

[14] M. Azuma, Z. Hiroi, M. Takano, K. Ishida, and Y. Kitaoka: *Observation of a spin gap in* $SrCu_2O_3$ *comprising spin-1/2 quasi-1D two-leg ladders*. Phys. Rev. Lett. **73**, 3463 (1994). 8

[15] K. Kojima, A. Keren, G. M. Luke, B. Nachumi, W. D. Wu, Y. J. Uemura, M. Azuma, and M. Takano: *Magnetic Behavior of the 2-Leg and 3-Leg Spin Ladder Cuprates* $Sr_{n-1}Cu_{n+1}O_{2n}$. Phys. Rev. Lett. **74**, 2812 (1995). 8

[16] M. Uehara, T. Nagata, J. Akimitsu, H. Takahashi, N. Môri, and K. Kinoshita: *Superconductivity in the Ladder Material* $Sr_{0.4}Ca_{13.6}Cu_{24}O_{41.84}$. J. Phys. Soc. Jpn. **65** (1996). 9

[17] T. Nagata, J. Goto, M. Uehara, N. Komiya, J. Akimitsu, N. Motoyama, H. Eisaki, S. Uchida, H. Takahashi, T. Nakanishi, and N. Môri: *Superconductivity in the ladder compound* $Sr_{2.5}Ca_{11.5}Cu_{24}O_{41}$ *(single crystal)*. Physica C **282**, 153 (1997). 9

[18] D. C. Johnston, M. Troyer, S. Miyahara, D. Lidsky, K. Ueda, M. Azuma, Z. Hiroi, M. Takano, M. Isobe, Y. Ueda, M. A. Korotin, V. I. Anisimov, A. V. Mahajan, and L. L. Miller: *Magnetic Susceptibilities of Spin-1/2 Antiferromagnetic Heisenberg Ladders and Applications to Ladder Oxide Compounds* (2000). cond-mat/0001147. 9, 77

[19] T. K. Kim, H. Rosner, S.-L. Drechsler, Z. Hu, C. Sekar, G. Krabbes, J. Málek, M. Knupfer, J. Fink, and H. Eschrig: *Unusual electronic structure of the pseudoladder compound* $CaCu_2O_3$. Phys. Rev. B **67**, 024516 (2003). 9

[20] S.-L. Drechsler, H. Rosner, T. K. Kim, M. Knupfer, J. Málek, and H. Eschrig: *Electronic structure and magnetism of the "pseudo-ladder" compounds* ACu_2O_3, A = Ca, Mg. Physica C **408**, 270 (2004). 9

[21] E. Dagotto and T. M. Rice: *Surprises on the Way from One- to Two-Dimensional Quantum Magnets: The Ladder Materials*. Science **271**, 618 (1996). 9

[22] M. Greiner, O. Mandel, T. Esslinger, T. W. Hänsch, and I. Bloch: *Quantum phase transition from a superfluid to a Mott insulator in a gas of ultracold atoms*. Nature **415**, 39 (2002). 9

[23] M. H. Anderson, J. R. Ensher, M. R. Matthews, C. E. Wieman, and E. A. Cornell: *Observation of Bose-Einstein Condensation in a Dilute Atomic Vapor*. Science **269**, 198 (1995). 10

[24] K. B. Davis, M.-O. Mewes, M. R. Andrews, N. J. van Druten, D. S. Durfee, D. M. Kurn, and W. Ketterle: *Bose-Einstein condensation in a gas of sodium atoms*. Phys. Rev. Lett. **75**, 3969 (1995). 10

[25] C. A. Regal, C. Ticknor, J. L. Bohn, and D. S. Jin: *Creation of ultracold molecules from a Fermi gas of atoms*. Nature **424**, 47 (2003). 10

[26] S. Jochim, M. Bartenstein, A. Altmeyer, G. Hendl, S. Riedl, C. Chin, J. Hecker Denschlag, and R. Grimm: *Bose-Einstein Condensation of Molecules*. Science **302**, 2101 (2003). 10

[27] M. Greiner, C. A. Regal, and D. S. Jin: *Fermionic Condensates*. In: *ATOMIC PHYSICS 19: XIX International Conference on Atomic Physics; ICAP 2004* (AIP, 2005), vol. 770, pp. 209–217. 10

[28] M. Theis, G. Thalhammer, K. Winkler, M. Hellwig, G. Ruff, R. Grimm, and J. H. Denschlag: *Tuning the Scattering Length with an Optically Induced Feshbach Resonance*. Phys. Rev. Lett. **93**, 123001 (2004). 10

[29] J. J. Garcia-Ripoll, M. A. Martin-Delgado, and J. I. Cirac: *Implementation of Spin Hamiltonians in Optical Lattices*. Phys. Rev. Lett. **93**, 250405 (2004). 10

[30] P. Buonsante, V. Penna, and A. Vezzani: *Fractional-filling Mott domains in two-dimensional optical superlattices*. Phys. Rev. A **72**, 031602 (2005). 10

[31] W. Heisenberg: *Zur Theorie des Ferromagnetismus*. Z. Phys. **49**, 619 (1928). 10

[32] S. P. Strong and A. J. Millis: *Competition between singlet formation and magnetic ordering in one-dimensional spin systems*. Phys. Rev. Lett. **69**, 2419 (1992). 11

[33] M. Azzouz, L. Chen, and S. Moukouri: *Calculation of the singlet-triplet gap of the antiferromagnetic Heisenberg model on a ladder*. Phys. Rev. B **50**, 6233 (1994). 11

[34] T. Barnes, E. Dagotto, J. Riera, and E. S. Swanson: *Excitation spectrum of Heisenberg spin ladders*. Phys. Rev. B **47**, 3196 (1993). 11

[35] S. R. White, R. M. Noack, and D. J. Scalapino: *Resonating valence bond theory of coupled Heisenberg chains*. Phys. Rev. Lett. **73**, 886 (1994). 11

[36] S. A. Kivelson, D. S. Rokhsar, and J. P. Sethna: *Topology of the resonating valence-bond state - Solitons and high-T(c) superconductivity*. Phys. Rev. B **35**, 8865 (1987). 11

[37] M. Troyer, H. Tsunetsugu, and D. Würtz: *Thermodynamics and spin gap of the Heisenberg ladder calculated by the look-ahead Lanczos algorithm*. Phys. Rev. B **50**, 13515 (1994). 12, 77, 89, 93, 100

[38] E. Manousakis: *The spin- 1/2 Heisenberg antiferromagnet on a square lattice and its application to the cuprous oxides*. Rev. Mod. Phys. **63**, 1 (1991). 12

[39] D. G. Shelton, A. A. Nersesyan, and A. M. Tsvelik: *Antiferromagnetic spin ladders: Crossover between spin S=1/2 and S=1 chains*. Phys. Rev. B **53**, 8521 (1996). 12

[40] K. P. Schmidt and G. S. Uhrig: *Spectral Properties of Magnetic Excitations in Cuprate Two-Leg Ladder Systems*. Mod. Phys. Lett. B **19**, 1179 (2005). 12, 93

[41] M. Takahashi: *Half-filled Hubbard model at low temperature*. J. Phys. C: Solid State Phys. **10**, 1289 (1977). 13, 14

[42] T. Momoi, T. Hikihara, M. Nakamura, and X. Hu: *Scalar chiral ground states of spin ladders with four-spin exchanges*. Phys. Rev. B **67**, 174410 (2003). 13, 16, 17, 28, 29, 111, 129, 130

[43] D. J. Thouless: *Exchange in solid ^{3}He and the Heisenberg Hamiltonian*. Proceedings of the Physical Society **86**, 893 (1965). 13

[44] M. Roger, J. H. Hetherington, and J. M. Delrieu: *Magnetism in solid ^{3}He*. Rev. Mod. Phys. **55**, 1 (1983). 13

[45] A. H. MacDonald, S. M. Girvin, and D. Yoshioka: *t/U expansion for the Hubbard model*. Phys. Rev. B **37**, 9753 (1988). 14

[46] A. H. MacDonald, S. M. Girvin, and D. Yoshioka: *Reply to "Comment on 't/U expansion for the Hubbard model' "*. Phys. Rev. B **41**, 2565 (1990). 14

[47] E. Müller-Hartmann and A. Reischl: *Derivation of effective spin models from a three band model for CuO_2-planes*. Eur. Phys. J. B **28**, 173 (2002). 14

[48] M. Matsuda, K. Katsumata, R. S. Eccleston, S. Brehmer, and H.-J. Mikeska: *Magnetic excitations and exchange interactions in the spin-1/2 two-leg ladder compound $La_6Ca_8Cu_{24}O_{41}$*. Phys. Rev. B **62**, 8903 (2000). 14

[49] T. S. Nunner, P. Brune, T. Kopp, M. Windt, and M. Grüninger: *Cyclic spin exchange in cuprate spin ladders*. Phys. Rev. B **66**, 180404 (2002). 14

[50] A. Bühler, U. Löw, K. P. Schmidt, and G. S. Uhrig: *Thermodynamic Properties of Spin Ladders with Cyclic Exchange*. Phys. Rev. B **67**, 134428 (2003). 15, 77, 93, 98, 128

[51] K. P. Schmidt, H. Monien, and G. S. Uhrig: *Rung-singlet phase of the S = (1/2) two-leg spin-ladder with four-spin cyclic exchange*. Phys. Rev. B **67**, 184413 (2003). 15, 77, 81, 93, 109, 128

[52] S. Brehmer, H.-J. Mikeska, M. Müller, N. Nagaosa, and S. Uchida: *Effects of biquadratic exchange on the spectrum of elementary excitations in spin ladders*. Phys. Rev. B **60**, 329 (1999). 15, 93, 109

[53] M. Müller, T. Vekua, , and H.-J. Mikeska: *Perturbation theories for the S = 1/2 spin ladder with a four-spin ring exchange*. Phys. Rev. B **66**, 134423 (2002). 15, 109

[54] T. Hikihara, T. Momoi, and X. Hu: *Spin-Chirality Duality in a Spin Ladder with Four-Spin Cyclic Exchange*. Phys. Rev. Lett. **90**, 087204 (2003). 15, 16, 25, 109, 111, 128, 129

[55] V. Gritsev, B. Normand, and D. Baeriswyl: *Phase diagram of the Heisenberg spin ladder with ring exchange*. Phys. Rev. B **69**, 094431 (2004). 15, 16, 111, 128, 129, 130

[56] L. A. Takhtajan: *The picture of low-lying excitations in the isotropic Heisenberg chain of arbitrary spins*. Phys. Lett. A **87**, 479 (1982). 15, 109

[57] H. M. Babujian: *Exact Solution of the One-Dimensional Isotropic Heisenberg Chain with Arbitrary Spin S*. Phys. Lett. A **90**, 479 (1982). 15, 109

[58] A. Schadschneider and J. Zittartz: *Variational study of isotropic spin-1 chains using matrix-product states*. Ann. Phys. **4**, 157 (1995). 27, 28, 135

[59] A. Klümper, A. Schadschneider, and J. Zittartz: *Groundstate properties of a generalized VBS-model*. Z. Phys. B **87**, 281 (1992). 28, 29, 127

[60] A. Klümper, A. Schadschneider, and J. Zittartz: *Matrix Produkt Ground States for One-Dimensional Spin-1 Quantum Antiferromagnets*. Europhys. Lett. **24**, 293 (1993). 28, 127

[61] M. Fannes, B. Nachtergaele, and R. F. Werner: *Finitely correlated states on quantum spin chains*. Comm. Math. Phys. **144**, 443 (1992). 28

[62] A. K. Kolezhuk and H.-J. Mikeska: *Models with exact ground states connecting smoothly the S=1 / 2 dimer and S=1 Haldane phases of one-dimensional spin chains*. Phys. Rev. B **56**, R11380 (1997). 28

[63] H. Niggemann and J. Zittartz: *Optimum ground states for spin-3/2 ladders with two legs*. J. Phys. A: Math. Gen. **31**, 9819 (1998). 28, 127

[64] A. K. Kolezhuk and H.-J. Mikeska: *Finitely Correlated Generalized Spin Ladders*. Int. J. Mod. Phys. B **12**, 2325 (1998). 28, 29

[65] M. A. Ahrens, A. Schadschneider, and J. Zittartz: *Exact ground states of spin-2 chains*. Europhys. Lett. **59**, 889 (2002). 28, 127

[66] S. Brehmer, H.-J. Mikeska, and U. Neugebauer: *The phase diagram and hidden order for generalized spin ladders*. J. Phys.: Condens. Matter **8**, 7161 (1996). 28, 29, 34

[67] A. K. Kolezhuk, H.-J. Mikeska, and S. Yamamoto: *Matrix-product-states approach to Heisenberg ferrimagnetic spin chains*. Phys. Rev. B **55**, 3336 (1997). 28, 29

[68] K. Totsuka and M. Suzuki: *Matrix formalism for the VBS-type models and hidden order* . J. Phys.: Condens. Matter **7**, 1639 (1995). 28

[69] U. Neugebauer and H.-J. Mikeska: *Domain wall theory of elementary excitations in anisotropic antiferromagnetic $S = 1$ chains*. Z. Phys. B **99**, 151 (1996). 28

[70] S. Brehmer, A. K. Kolezhuk, H.-J. Mikeska, and U. Neugebauer: *Elementary excitations in the gapped phase of a frustrated $S = 1/2$ spin ladder: from spinons to the Haldane triplet*. J. Phys.: Condens. Matter **10**, 1103 (1998). 28, 34

[71] E. Bartel, A. Schadschneider, and J. Zittartz: *Excitations of anisotropic spin-1 chains with matrix product ground state*. Eur. Phys. J. B **31**, 209 (2003). 28, 127

[72] H. Niggemann and J. Zittartz: *Optimum ground states for spin-$\frac{3}{2}$ chains*. Z. Phys. B **101**, 289 (1996). 28

[73] H. Niggemann, A. Klümper, and J. Zittartz: *Quantum phase transition in spin-$\frac{3}{2}$ systems on the hexagonal lattice - optimum ground state approach*. Z. Phys. B **104**, 103 (1997). 28

[74] H. Niggemann, A. Klümper, and J. Zittartz: *Ground state phase diagram of a spin-2 antiferromagnet on the square lattice*. Eur. Phys. J. B **13**, 15 (2000). 28

[75] M. A. Ahrens, A. Schadschneider, and J. Zittartz: *Exact ground states of quantum spin-2 models on the hexagonal lattice*. Phys. Rev. B **71**, 174432 (2005). 28

[76] I. Affleck, T. Kennedy, E. H. Lieb, and T. Tasaki: *Rigorous results on valence-bond ground states in antiferromagnets*. Phys. Rev. Lett. **59**, 799 (1987). 29

[77] I. Affleck, T. Kennedy, E. H. Lieb, and T. Tasaki: *Valence bond ground states in isotropic quantum antiferromagnets*. Comm. Math. Phys. **115**, 477 (1988). 29

[78] R. J. Baxter: *Exactly Solved Models in Statistical Mechanics* (Academic Press, London, 1982). 39, 50, 57

[79] H. A. Kramers and G. H. Wannier: *Statistics of the Two-Dimensional Ferromagnet. Part I*. Phys. Rev. **60**, 252 (1941). 39, 44, 65, 155

[80] N. Metropolis, A. W. Rosenbluth, M. N. Rosenbluth, A. H. Teller, and E. Teller: *Equation of State Calculations by Fast Computing Machines*. J. Chem. Phys. **21**, 1087 (1953). 39

[81] M. Suzuki: *Relationship between d-dimensional quantal spin systems and $(d+1)$-dimensional Ising systems*. Prog. Theor. Phys. **56**, 1454 (1976). 39, 42

[82] M. Suzuki: *Transfer-matrix method and Monte Carlo simulation in quantum spin systems*. Phys. Rev. B **31**, 2957 (1985). 39, 44

[83] M. Suzuki: *Decomposition formulas of exponential operators and Lie exponentials with some applications to quantum mechanics and statistical physics*. J. Math. Phys. **26**, 601 (1985). 39

[84] M. Suzuki: *Quantum Statistical Monte Carlo Methods and Applications to Spin Systems*. J. Stat. Phys. **43**, 883 (1986). 39

[85] H. F. Trotter: *On the product of semigroups of operators*. Proc. Am. Math. Soc. **10**, 545 (1959). 40

[86] R. M. Fye: *New results on Trotter-like approximations*. Phys. Rev. B **33**, 6271 (1986). 40

[87] J. Sirker and A. Klümper: *Temperature-driven crossover phenomena in the correlation lengths of the one-dimensional t-J model*. Europhys. Lett. **60**, 262 (2002). 42

[88] J. Sirker: *Transfer matrix approach to thermodynamics and dynamics of one-dimensional quantum systems*. Ph.D. thesis, Abteilung Physik der Universität Dortmund (2002). 42

[89] I. Peschel, W. Wang, M. Kaulke, and K. Hallberg, editors: *Density Matrix Renormalisation. A New Numerical Method in Physics*, vol. 528 of *Lecture Notes in Physics* (Springer, Berlin, 1998). 45

[90] D. Mermin and H. Wagner: *Absence of Ferromagnetism or Antiferromagnetism in One- or Two-Dimensional Isotropic Heisenberg Models*. Phys. Rev. Lett. **17**, 1133 (1966). 45

[91] E. H. Lieb and D. C. Mattis: *Mathematical Physics in one dimension* (Academic Press, New York, 1966). 45

[92] M. R. Evans: *Phase Transitions in one-dimensional nonequilibrium systems*. Braz. J. Phys **30**, 42 (2000). 45

[93] S. R. White: *Density matrix formulation for quantum renormalization groups*. Phys. Rev. Lett. **69**, 2863 (1992). 46, 47, 126

[94] S. R. White: *Density-matrix algorithms for quantum renormalization groups*. Phys. Rev. B **48**, 10345 (1993). 46, 47

[95] J. Gaite: *Entanglement Entropy And The Density Matrix Renormalization Group*. In: D. Iagolnitzer, V. Rivasseau, and J. Zinn-Justin, editors, *Proceedings of the International Congress on Theoretical Physics, Paris, July 2002* (Birkhäuser Verlag, Basel, 2004). quant-ph/0301120. 46, 47

[96] E. R. Latorre and G. Vidal: *Fine-grained entanglement loss along renormalization group flows*. Quant. Inf. Comp. **4**, 100409 (2004). 46, 47

[97] Ö. Legeza and J. Sólyom: *Optimizing the density-matrix renormalization group method using quantum information entropy*. Phys. Rev. B **68**, 195116 (2003). 46, 47

[98] Ö. Legeza and J. Sólyom: *Quantum data compression, quantum information generation, and the density-matrix renormalization-group method*. Phys. Rev. B **70**, 205118 (2004). 46, 47

[99] T. J. Osborne and M. A. Nielsen: *Entanglement, quantum phase transitions, and density matrix renormalization*. Quant. Inf. Proc. **1**, 45 (2002). quant-ph/0109024. 46, 47

[100] S. R. White: *Strongly correlated electron systems and the density matrix renormalization group*. Phys. Rep. **301**, 187 (1998). 47

[101] J. Gaite: *Angular Quantization and the Density Matrix Renormalization Group*. Modern Physics Letters A **16**, 1109 (2001). 47

[102] U. Schollwöck: *The density-matrix renormalization group*. Rev. Mod. Phys. **77**, 259 (2005). 47, 49, 57, 126

[103] C. Müller-Gugenberger: *Diplomarbeit, Universität zu Köln* (2005). 49, 126

[104] S. Östlund and S. Rommer: *Thermodynamic Limit of Density Matrix Renormalization*. Phys. Rev. Lett. **75**, 3537 (1995). 49, 50, 126

[105] T. Nishino and K. Okunishi: *Product wave function renormalization group method*. J. Phys. Soc. Jpn. **67**, 3066 (1995). 49

[106] J. Dukelsky, M. A. Martin-Delgado, T. Nishino, and G. Sierra: *Equivalence of the variational matrix product method and the density matrix renormalization group applied to spin chains*. Europhys. Lett. **43**, 457 (1998). 49

[107] G. Vidal: *Efficient Simulation of One-Dimensional Quantum Many-Body Systems*. Phys. Rev. Lett. **93**, 040502 (2004). 50

[108] A. J. Daley, C. Kollath, U. Schollwöck, and G. Vidal: *Time-dependent density-matrix renormalization-group using adaptive effective Hilbert spaces*. J. Stat. Mech. **2004**, P04005 (2004). 50

[109] S. R. White and A. E. Feiguin: *Real-Time Evolution Using the Density Matrix Renormalization Group*. Phys. Rev. Lett. **93**, 076401 (2004). 50

[110] F. Verstraete, J. J. Garcia-Ripoll, and J. I. Cirac: *Matrix Product Density Operators: Simulation of Finite-Temperature and Dissipative Systems*. Phys. Rev. Lett. **93**, 207204 (2004). 50, 126

[111] F. Verstraete and J. I. Cirac: *Renormalization algorithms for Quantum-Many Body Systems in two and higher dimensions* (2004). cond-mat/0407066. 50

[112] T. Nishino: *Density Matrix Renormalization Group Method for 2D Classical Models*. J. Phys. Soc. Jpn. **64**, 3598 (1995). 50

[113] R. J. Baxter: *Dimers on a rectangular lattice*. J. Math. Phys. **9**, 650 (1968). 50, 57

[114] R. J. Baxter: *Variational approximations for square lattice models in statistical mechanics*. J. Stat. Phys. **19**, 461 (1978). 50, 57

[115] T. Nishino and K. Okunishi: *Corner Transfer Matrix Renormalization Group Method*. J. Phys. Soc. Jpn. **65**, 891 (1996). 50, 57, 58

[116] R. J. Bursill, T. Xiang, and G. A. Gehring: *The density matrix renormalization group for a quantum spin chain at non-zero temperature*. J. Phys.: Condens. Matter **8**, L583 (1996). 50, 126

[117] X. Wang and T. Xiang: *Transfer-matrix density-matrix renormalization-group theory for thermodynamics of one-dimensional quantum systems*. Phys. Rev. B **56**, 5061 (1997). 50, 126

[118] N. Shibata: *Thermodynamics of the Anisotropic Heisenberg Chain Calculated by the Density Matrix Renormalization Group Method*. J. Phys. Soc. Jpn. **66**, 2221 (1997). 50, 126

[119] A. Kemper: *Transfermatrix-DMRG for dynamics of stochastic models and thermodynamics of fermionic models*. Ph.D. thesis, Institut für Theoretische Physik, Universität zu Köln (2003). 51, 52

[120] N. Shibata: *Application of the density matrix renormalization group method to finite temperatures and two-dimensional systems*. J. Phys. A: Math. Gen. **36** (2003). 52

[121] T. Nishino and K. Okunishi: *Corner Transfer Matrix Algorithm For Classical Renormalization Group*. J. Phys. Soc. Jpn. **66**, 3040 (1997). 57, 58, 59

[122] N. Tsushima and T. Horiguchi: *Phase Diagrams of Spin-3/2 Ising Model on a Square Lattice in Terms of Corner Transfer Matrix Renormalization Group Method*. J. Phys. Soc. Jpn. **67**, 1574 (1998). 59

[123] H. Takasaki, T. Nishino, and Y. Hieida: *Phase Diagram of a 2D Vertex Model*. J. Phys. Soc. Jpn. **70**, 1429 (2001). 59

[124] D. P. Foster and C. Pinettes: *A corner transfer matrix renormalization group investigation of the vertex-interacting self-avoiding walk model*. J. Phys. A: Math. Gen. **36**, 10279 (2003). 59

[125] D. P. Foster and C. Pinettes: *Corner-transfer-matrix renormalization-group method for two-dimensional self-avoiding walks and other O(n) models*. Phys. Rev. E **67**, 045105 (2003). 59

[126] A. Kemper, A. Gendiar, T. Nishino, A. Schadschneider, and J. Zittartz: *Stochastic light-cone CTMRG: a new DMRG approach to stochastic models*. J. Phys. A: Math. Gen. **36**, 29 (2003). 59

[127] E. Ising: *Beitrag zur Theorie des Ferromagnetismus*. Z. Phys. **31**, 253 (1925). 65, 103

[128] H. Bethe: *Zur Theorie der Metalle: Eigenwerte und Eigenfunktionen der linearen Atomkette*. Z. Phys. **71**, 205 (1931). 67

[129] B. Frischmuth, B. Ammon, and M. Troyer: *Susceptibility and low-temperature thermodynamics of spin-1/2 Heisenberg ladders*. Phys. Rev. B **54**, 3714 (1996). 77

[130] M. Hagiwara, H. A. Katori, U. Schollwöck, and H.-J. Mikeska: *Specific heat of an $S = 1/2$ Heisenberg ladder compound $Cu_2(C_5H_{12}N_2)_2Cl_4$ under magnetic fields*. Phys. Rev. B **62**, 1051 (2000). 77

[131] X. Wang and L. Yu: *Magnetic-Field Effects on Two-Leg Heisenberg Antiferromagnetic Ladders: Thermodynamic Properties*. Phys. Rev. Lett. **84**, 5399 (2000). 77, 95, 111, 129

[132] M. T. Batchelor, X. Guan, N. Oelkers, K. Sakai, Z. Tsuboi, and A. Foerster: *Exact Results for the Thermal and Magnetic Properties of Strong Coupling Ladder Compounds*. Phys. Rev. Lett. **91**, 217202 (2003). 77

[133] Z. Honda, K. Katsumata, A. Kikkawa, and K. Yamada: *Thermodynamic Properties in the Approach to the Quantum Critical Point of the Spin-Ladder Material $Na_2Co_2(C_2O_4)_3(H_2O)_2$*. Phys. Rev. Lett. **95**, 087204 (2005). 77

[134] A. Bühler: *High Temperature Series Expansions for Spin- and Spin-Phonon-Systems*. Ph.D. thesis, Institut für Theoretische Physik, Universität zu Köln (2003). 77, 93

[135] S. Furukawa, G. Misguich, and M. Oshikawa: *Systematic Derivation of Order Parameters through Reduced Density Matrices* (2005). cond-mat/0508469. 78

[136] B. Bernu and G. Misguich: *Specific heat and high-temperature series of lattice models: Interpolation scheme and examples on quantum spin systems in one and two dimensions*. Phys. Rev. B **63**, 134409 (2001). 89

[137] T. Jolicoeur and O. Golinelli: *σ-model study of Haldane-gap antiferromagnets*. Phys. Rev. B **50**, 9265 (1994). 89

[138] J. L. Cardy: *Operator content of two-dimensional conformally invariant theories*. Nuclear Physics B **270**, 186 (1986). 89

[139] I. Affleck: *Universal term in the free energy at a critical point and the conformal anomaly*. Phys. Rev. Lett. **56**, 746 (1986). 89

[140] H. W. J. Blöte, J. L. Cardy, and M. P. Nightingale: *Conformal invariance, the central charge, and universal finite-size amplitudes at criticality*. Physical Review Letters **56**, 742 (1986). 89

[141] F. D. M. Haldane: *"Θ physics" and quantum spin chains*. Journal of Applied Physics **57**, 3359 (1985). 93

[142] S. Yamamoto and S. Miyashita: *Thermodynamic properties of S=1 antiferromagnetic Heisenberg chains as Haldane systems*. Phys. Rev. B **48**, 9528 (1993). 93

[143] K. P. Schmidt, C. Knetter, and G. S. Uhrig: *Raman response in antiferromagnetic two-leg S=1/2 Heisenberg ladders*. Europhys. Lett. **56**, 877 (2001). 93

[144] A. Bühler: *Numerische Untersuchungen an niedrigdimensionalen Quanten-Spinsystemen*. In: Der Rektor der Universität zu Köln, editor, *Kooperative Informationsverarbeitung an der Universität zu Köln - Jahrbuch 2002* (Köln, 2002), pp. 168–172. 93

[145] P. Hoever and J. Zittartz: *Thermodynamics of Some Layered Ising Models*. Z. Phys. B **44**, 129 (1981). 94

[146] S. Yamamoto, S. Brehmer, and H.-J. Mikeska: *Elementary excitations of Heisenberg ferrimagnetic spin chains*. Phys. Rev. B **57**, 13610 (1998). 94

[147] S. Yamamoto, T. Fukui, K. Maisinger, and U. Schollwöck: *Combination of ferromagnetic and antiferromagnetic features in Heisenberg ferrimagnets*. J. Phys.: Condens. Matter **10**, 11033 (1998). 94

[148] K. Maisinger, U. Schollwöck, S. Brehmer, H. J. Mikeska, and S. Yamamoto: *Thermodynamics of the $(1, 1/2)$ ferrimagnet in finite magnetic fields*. Phys. Rev. B **58**, R5908 (1998). 94

[149] A. Al-Omari and A. H. Nayyar: *Thermal properties of ferrimagnetic systems* (2000). cond-mat/0008167. 94

[150] S. K. Pati, S. Ramasesha, and D. Sen: *Low-lying excited states and low-temperature properties of an alternating spin-1-spin-1/2 chain: A density-matrix renormalization-group study*. Phys. Rev. B **55**, 8894 (1997). 94

[151] N. Maeshima and K. Okunishi: *Antiferromagnetic zigzag spin chain in magnetic fields at finite temperatures*. Phys. Rev. B **62**, 934 (2000). 95

[152] Y. Yoshida, N. Tateiwa, M. Mito, T. Kawae, K. Takeda, Y. Hosokoshi, and K. Inoue: *Specific Heat Study of an S=1/2 Alternating Heisenberg Chain System: F_5PNN in a Magnetic Field*. Phys. Rev. Lett. **94**, 037203 (2005). 95

[153] G. Chaboussant, M.-H. Julien, Y. Fagot-Revurat, M. Hanson, L. P. Lévy, C. Berthier, M. Horvatic, and O. Piovesana: *Zero temperature phase transitions in spin-ladders: Phase diagram and dynamical studies of $Cu_2(C_5H_{12}N_2)_2Cl_4$*. Eur. Phys. J. B **6**, 167 (1998). 95

[154] G. Chaboussant, Y. Fagot-Revurat, M.-H. Julien, M. E. Hanson, C. Berthier, M. Horvatić, L. P. Lévy, and O. Piovesana: *Nuclear Magnetic Resonance Study of the S = 1/2 Heisenberg Ladder $Cu_2(C_5H_{12}N_2)_2Cl_4$: Quantum Phase Transition and Critical Dynamics*. Phys. Rev. Lett. **80**, 2713 (1998). 95

[155] T. Nakamura and K. Kubo: *Elementary excitations in the Δ chain*. Phys. Rev. B **53**, 6393 (1996). 95

[156] D. Sen, B. S. Shastry, R. E. Walstedt, and R. Cava: *Quantum solitons in the sawtooth lattice*. Phys. Rev. B **53**, 6401 (1996). 95

[157] K. Maisinger and U. Schollwöck: *Thermodynamics of Frustrated Quantum Spin Chains*. Phys. Rev. Lett. **81**, 445 (1998). 95, 126

[158] A. K. Kolezhuk and H.-J. Mikeska: *Non-Haldane Spin-Liquid Models with Exact Ground States*. Phys. Rev. Lett. **80**, 2709 (1998). 95, 109, 129, 130

[159] A. Läuchli: *Quantum Magnetism and Strongly Correlated Electrons in Low Dimensions*. Ph.D. thesis, Swiss Federal Institute of Technology, Zürich (2002). 100, 102, 103

[160] N. W. Ashcroft and N. D. Mermin: *Solid State Physics* (Brooks Cole, 1976). 100

[161] F. J. Dyson: *Thermodynamic Behavior of an Ideal Ferromagnet*. Phys. Rev. **102**, 1230 (1956). 100

[162] K.-J.-B. Lee and P. Schlottmann: *Critical behavior of the isotropic ferromagnetic Heisenberg chain with arbitrary spin S*. Phys. Rev. B **36**, 466 (1987). 101

[163] L. Capriotti, D. J. Scalapino, and S. R. White: *Spin-Liquid versus Dimerized Ground States in a Frustrated Heisenberg Antiferromagnet*. Phys. Rev. Lett. **93**, 177004 (2004). 102

[164] A. A. Nersesyan and A. M. Tsvelik: *One-Dimensional Spin-Liquid without Magnon Excitations*. Phys. Rev. Lett. **78**, 3939 (1997). 109

[165] M. J. Martins and B. Nienhuis: *Exact and Numerical Results for a Dimerized Coupled Spin-1/2 Chain*. Phys. Rev. Lett. **85**, 4956 (2000). 109

[166] K. Hijii and K. Nomura: *Universality class of an S=1/2 quantum spin ladder system with four-spin exchange*. Phys. Rev. B **65**, 104413 (2002). 109, 128

[167] M. Nakamura and S. Todo: *Novel Order Parameter to Characterize Valence-Bond-Solid States*. Prog. Theor. Phys. Suppl. **145**, 217 (2002). 109

[168] M. Nakamura and S. Todo: *Order Parameter to Characterize Valence-Bond-Solid States in Quantum Spin Chains*. Phys. Rev. Lett. p. 077204 (2002). 109

[169] Y. Honda and T. Horiguchi: *Quantum phase transition by cyclic four-spin exchange interaction for S=1/2 two-leg spin ladder* (2001). cond-mat/0106426. 109, 128

[170] K. Hijii, S. Qin, and K. Nomura: *Staggered dimer order and criticality in an S = 1/2 quantum spin ladder system with four-spin exchange*. Phys. Rev. B **68**, 134403 (2003). 109, 128

[171] P. N. Bibikov: *Zero-temperature magnetic phase transition between two ordered gapped phases in spin-ladders with ferromagnetic legs* (2005). cond-mat/0509556. 117

[172] T. Nishino and N. Shibata: *Efficiency of symmetric targeting for finite-T DMRG*. J. Phys. Soc. Jpn. **68**, 3501 (1999). 126

[173] T. Enss and U. Schollwöck: *On the choice of the density matrix in the stochastic TMRG*. J. Phys. A: Math. Gen. **34**, 7769 (2001). 126

[174] F. Mila: *Ladders in a magnetic field: a strong coupling approach*. Eur. Phys. J. B **6**, 201 (1998). 130

[175] Z. Bai, C. Bischof, L. S. Blackford, J. Demmel, J. Dongarra, J. D. Croz, A. Greenhaum, S. Hammarling, A. McKenney, and S. D.: *Lapack Users' Guide: Third Edition* (SIAM, Philadelphia, 2000). 147

Danksagung

Zunächst danke ich Herrn Prof. Dr. J. Zittartz sehr herzlich für die Unterstützung der vorliegenden Doktorarbeit und die Ermöglichung der hervorragenden Rahmenbedingungen.

Mein ganz besonderer Dank gilt Herrn Priv.-Doz. Dr. Andreas Schadschneider für die intensive Begleitung dieser Arbeit, für die stete Ansprechbarkeit und die hervorragende fachliche Betreuung sowie für viele hilfreiche Gespräche auch in nichtphysikalischen Bereichen.

Herzlich danke ich Herrn Prof. Dr. Achim Rosch für wichtige Anregungen und die angenehme Arbeitsatmosphäre.

Für anregende Diskussionen, die ganz wesentlich zum Gelingen dieser Arbeit beigetragen haben, möchte ich mich bei Priv.-Doz. Dr. Ute Löw, Dr. Andreas Kemper und Dr. Andreas Läuchli bedanken.

Ein großes Dankeschön an die netten Leute, die die täglichen Mensa- oder Bäckergänge, die gelegentlichen Kaffeepausen oder Grillfeste zu besonderen Highlights gemacht haben: Frank Zielen, Ansgar Kirchner, Andreas Kemper, Christian Dziurzik, Alireza Namazi, Alexander John, Inga Fischer, Clemens Müller-Gugenberger, Rolf Helmes und Nayana Shah.

An dieser Stelle richtet sich ein großer Dank an Marc André Ahrens, der in den letzten Jahren ein wichtiger Ansprechpartner nicht nur in physikalischen und musikalischen Fragen war. Ihm wünsche ich alles Gute für seine künftigen Wege.

Sehr gefreut habe ich mich über die Unterstützung durch meine Korrekturleser: Clemens Müller-Gugenberger, Rolf Helmes und Nayana Shah.

Dank an Andreas Sindermann, der zur Not auch am Wochenende Computern Beine macht.

Ganz herzlich möchte ich mich bei meinen Eltern und meiner Schwester bedanken, deren Unterstützung ich mir stets sicher sein kann.

Schließlich gilt mein lieber Dank Jörn, der auch privat einen Physiker erträgt.

Abstract

This thesis focuses on the thermodynamical properties of spin ladder systems. The interest in spin ladders has been triggered by the fact that spin ladders show some principal similarities with two-dimensional superconducting cuprate compounds. However, spin ladders are quasi one-dimensional systems and can thus be treated with the whole number of analytical and numerical methods which have been developed for one-dimensional systems. This makes spin ladders an attractive field of research in the context of strongly correlated electron systems. In the past few years, it has been noticed that spin ladder systems with an additional four-spin interaction show a rich and surprising phase diagram.

In this thesis, we calculate thermodynamic quantities for the spin ladder system with cyclic exchange by the transfer-matrix density-matrix renormalization group (TMRG). In the TMRG-method, a one dimensional quantum system with short-ranged interaction is mapped onto a two-dimensional classical lattice. The free energy of this system is determined by the highest eigenvalue of an appropriate transfer-matrix which is iteratively enlarged while unimportant degrees of freedom are truncated by the so-called density-matrix projection.

We have proposed a new variant of the TMRG approach that combines ideas of the so called corner transfer matrix approach with a two dimensional Trotter decomposition. Since this method does not require a time consuming diagonalization of large systems, the calculation of thermodynamic quantities of one dimensional quantum systems should be much faster. However, tests performed on the classical Ising model and the Heisenberg chain indicated two inherent difficulties related to the structure of the Trotter decomposition. These difficulties have not been solved up to now.

The results for the ladder systems have been obtained by implementing a TMRG code which makes use of object-oriented programming techniques in highly efficient numerical routines. In that way reliable and precise numerical data could be obtained for temperatures down to $T \approx 0.02$. Using this approach specific heat, generalized susceptibilities and thermodynamic expectation values have been determined. We found evidence for the rich phase structure of the phase diagram predicted for vanishing temperature.

In the vicinity of the first order phase transition our finite temperature results indicate a caricature of the transition in the behavior of the specific heat, i.e. a sharp maximum at low temperatures. The position of this maximum depends algebraically on the distance from the transition. Furthermore in the phases with broken discrete symmetries a characteristic shape of the specific heat with two maxima was observed. The broken symmetries were identified clearly by the divergence of the related generalized susceptibilities.

Deutsche Zusammenfassung

Die vorliegende Arbeit beschäftigt sich mit den thermodynamischen Eigenschaften von Spinleitern. Spinleitern bestehen aus zwei über Sprossenverbindungen miteinander wechselwirkenden Spinketten, die als topologische Struktur in komplexen Übergangsmetallverbindungen auftreten und die relevante Tieftemperaturphysik bestimmen. Die Tatsache, dass für eindimensionale Systeme eine ganze Reihe hochentwickelter analytischer und numerischer Methoden zur Verfügung stehen, macht Spinleitern zu einem attraktiven Forschungsgebiet im Bereich stark korrelierter Elektronensysteme. In jüngerer Zeit wurde entdeckt, dass zahlreiche experimentell realisierte Substanzen nur verlässlich durch die Einbeziehung eines zyklischen Vier-Spin-Wechselwirkungsterms (Ringaustausch) theoretisch modelliert werden können.

In der vorliegenden Arbeit wurden thermodynamische Größen für Spinleitern mit beliebigem Ringaustausch numerisch mit Hilfe der Transfermatrix-Dichtematrix-Renormierungsgruppe (TMRG) berechnet. In der TMRG-Methode wird ein eindimensionales Quantensystem mit kurzreichweitiger Wechselwirkung auf ein zweidimensionales klassisches Gittermodell abgebildet. Die freie Energie des zugrundeliegenden Systems wird durch den höchsten Eigenwert einer geeigneten Transfermatrix codiert, welche durch eine iterative Prozedur vergrößert wird. Unwichtige Freiheitsgrade werden dabei durch Dichtematrixprojektion verworfen.

Eine Weiterentwicklung der TMRG-Methode wird in dieser Arbeit vorgestellt, die die Idee der so genannten Corner-Transfermatrix-Methode für die zweidimensionale Trotterzerlegung anwendet. In dieser Methode fehlt die zeitaufwändige Berechnung von Eigenwerten großer Systeme. Im Prinzip ist daher ein hoher Geschwindigkeitsvorteil gegenüber der TMRG in der Berechnung von thermischen Eigenschaften von eindimensionalen Quantensystemen zu erwarten. Testberechnungen am klassischen Ising-Modell und am Heisenbergmodell zeigen jedoch zwei bis lang ungelöste inhärente Schwierigkeiten, die mit der Struktur der zweidimensionalen Trotterzerlegung zusammenhängen.

Im Rahmen der vorliegenden Arbeit ist ein TMRG-Programm entstanden, das sowohl die Methoden der objektorientierten Programmierung als auch hohe numerische Effizienz in den relevanten Routinen umsetzt. Verläßliche numerische Daten konnten so bis in einen Temperaturbereich von $T \approx 0,02$ mit hoher Genauigkeit erzielt werden. Mit dieser Methode wurden spezifische Wärmekapazität, verallgemeinerte Suszeptibilitäten und thermische Erwartungwerte berechnet. Wir fanden damit eine Reihe von Hinweisen, welche das reichhaltige Phasenverhalten des vorhergesagten Phasendiagramms für verschwindende Temperatur bestätigen.

In der Nähe eines Quantenphasenübergangs erster Ordnung sahen wir bei endlichen Temperaturen die Karikatur eines Phasenübergangs, das heißt ein scharfes Tieftemperaturmaximum in der spezifischen Wärme, dessen Position über ein Potenzgesetz vom Abstand zum Punkt des Phasenübergangs abhängt. Darüberhinaus ermittelten wir in den Phasen mit gebrochener diskreter Symmetrie eine charakteristische Struktur mit zwei Maxima in der spezifischen Wärme. Die gebrochenen Symmetrien konnten wir als Divergenzen in entsprechenden verallgemeinerten Suszeptibilitäten klar erkennen.

Erklärung

Ich versichere, dass ich die von mir vorgelegte Dissertation selbständig angefertigt, die benutzten Quellen und Hilfmittel vollständig angegeben und die Stellen der Arbeit – einschliesslich Tabellen, Karten, und Abbildungen –, die anderen Werken im Wortlaut oder dem Sinn nach entnommen sind, in jedem Einzelfall als Entlehnung kenntlich gemacht habe; dass diese Dissertation noch keiner anderen Fakultät oder Universität zur Prüfung vorgelegen hat; dass sie – abgesehen von unten angegegebenen Teilpublikationen – noch nicht veröffentlicht worden ist sowie, dass ich eine solche Veröffentlichung vor Abschluss des Promotionsverfahrens nicht vornehmen werde. Die Bestimmungen dieser Promotionsordnung sind mir bekannt. Die von mir vorgelegte Dissertation ist von Herrn Prof. Dr. Zittartz betreut worden.

Erik Bartel
Köln, den 24. Oktober 2005

Teilpublikationen

– keine –